A multi-harmonic finite element method for the micro-Doppler effect, with an application to radar sensing

David Gasperini

▶ **To cite this version:**

David Gasperini. A multi-harmonic finite element method for the micro-Doppler effect, with an application to radar sensing. Mathematics [math]. Université de Lorraine; Université de Liège, 2022. English. NNT : 2022LORR0026 . tel-03667895

HAL Id: tel-03667895
https://hal.univ-lorraine.fr/tel-03667895

Submitted on 13 May 2022

HAL is a multi-disciplinary open access archive for the deposit and dissemination of scientific research documents, whether they are published or not. The documents may come from teaching and research institutions in France or abroad, or from public or private research centers.

L'archive ouverte pluridisciplinaire **HAL**, est destinée au dépôt et à la diffusion de documents scientifiques de niveau recherche, publiés ou non, émanant des établissements d'enseignement et de recherche français ou étrangers, des laboratoires publics ou privés.

AVERTISSEMENT

Ce document est le fruit d'un long travail approuvé par le jury de soutenance et mis à disposition de l'ensemble de la communauté universitaire élargie.

Il est soumis à la propriété intellectuelle de l'auteur. Ceci implique une obligation de citation et de référencement lors de l'utilisation de ce document.

D'autre part, toute contrefaçon, plagiat, reproduction illicite encourt une poursuite pénale.

Contact : ddoc-theses-contact@univ-lorraine.fr

LIENS

Code de la Propriété Intellectuelle. articles L 122. 4
Code de la Propriété Intellectuelle. articles L 335.2- L 335.10
http://www.cfcopies.com/V2/leg/leg_droi.php
http://www.culture.gouv.fr/culture/infos-pratiques/droits/protection.htm

A multi-harmonic finite element method for the micro-Doppler effect, with an application to radar sensing

THÈSE

soutenue publiquement le 31 mars 2022

pour l'obtention des

Doctorats des Universités de Lorraine et de Liège

(spécialité Mathématiques)

par

David Gasperini

Composition du jury

Président	**Stéphane Bordas** - Professeur, Université du Luxembourg
Directeurs	**Xavier Antoine** - Professeur, Université de Lorraine **Christophe Geuzaine** - Professeur, Université de Liège
Rapporteurs	**Hélène Barucq** - Directrice de recherche, Inria Pau **Sébastien Pernet** - Maître de recherche, Onera Toulouse
Examinateurs	**Ingrid Lacroix-Violet** - Professeur, Université de Lorraine **Udo Schroeder** - Docteur, Iee Luxembourg **François Henrotte** - Docteur, Université de Liège

Institut Elie Cartan de Lorraine, Université de Lorraine
Department of Electrical Engineering and Computer Science, Université de Liège

Abstract

A finite element method in the spectral domain is proposed for solving wave scattering problems with moving boundaries or, more generally, deformed domains. First, the original problem is rewritten as an equivalent weak formulation set in a fixed domain. Next, this formulation is approximated as a simpler weak form based on asymptotic expansions when the amplitude of the movements or the deformations is small. Fourier series expansions of some geometrical quantities under the assumption that the movement is periodic, and of the solution are next introduced to obtain a coupled multi-harmonic frequency domain formulation. Standard finite element methods can then be applied to solve the resulting problem and a block diagonal preconditioner is proposed to accelerate the Krylov subspace solution of the linear system for high frequency problems. The efficiency of the resulting method is demonstrated on a radar sensing application for the automotive industry.

Keywords: Micro-Doppler effect, High frequency scattering, Moving boundaries, Wave equation, Multi-harmonic resolution, Finite element method, Electromagnetics.

Résumé

Nous proposons une méthode de résolution par éléments finis et en domaine spectral de problèmes de diffraction d'ondes au sein de domaines dont les frontières se déforment au cours du temps. Le problème original est exprimé sous forme faible, puis approché par une formulation simplifiée basée sur des développements asymptotiques valides lorsque l'amplitude des déformations est faible. Nous introduisons alors des développements en séries de Fourier de certaines grandeurs géométriques, ainsi que de la solution dans le cas de mouvements périodiques. Cela permet ainsi d'obtenir une formulation multi-harmoniques couplée du problème de diffraction initial. Une méthode de résolution standard par éléments finis associée à un solveur itératif, est alors appliquée afin de résoudre le système résultant, de type Helmholtz. En vue d'accélérer la solution du système linéaire, définie sur des sous-espaces de Krylov, nous proposons un préconditionneur diagonal par bloc, indispensable à la convergence de la méthode pour les problèmes hautes fréquences. L'efficacité de la méthode présentée est enfin illustrée à travers une application à la détection radar pour l'industrie automobile.

Mots-clés: Effet micro-Doppler, Diffusion haute fréquence, Frontières mobiles, Équation des ondes, Résolution multi-harmonique, Méthode des éléments finis, Électromagnétisme.

Remerciements

Xavier Antoine a été mon professeur d'EDP au cours du master au Luxembourg, à la suite duquel il a ouvert la voie à cette aventure en devenant mon directeur de thèse. C'est alors que j'ai fait la connaissance de mon second directeur, Christophe Geuzaine. Je tiens à les remercier en premier lieu pour m'avoir initié à cette branche des mathématiques siégeant à la croisée des mondes, et pour leur accompagnement particulièrement précieux au cours de cette période où aléas sociétaux et personnels se sont conjugués de façon complexe. Tous deux se sont rendus très disponibles et d'excellents conseils, méticuleux, toujours de bonne humeur et prompts à la plaisanterie. Je recommande!

J'exprime également toute ma gratitude envers le Fond National de la Recherche de Luxembourg pour avoir financé ce projet.

Mes remerciements vont ensuite aux membres du jury, qui m'ont fait l'honneur d'examiner avec attention le présent travail: Hélène Barucq pour son rôle de rapporteuse (et indirectement pour son statut de "grande-directrice de thèse" par filiation), Sébastien Pernet pour ce même rôle ainsi que sa relecture particulièrement attentive, François Henrotte, Ingrid Lacroix-Violet, Stéphane Bordas pour avoir accepté de présider ce jury, und Udo Schroeder für seine guten Ratschläge und den Arbeitsrhythmus, den er mir als Tutor seit meinem Masterabschluss vermittelt hat.

Ce travail a par ailleurs été rendu possible grâce à l'équipe d'Iee, dont l'accompagnement depuis le stage de fin d'études de master a été très appréciable. Ich möchte besonders bei Werner Bieck, Günter Gödert, Thomas Stifter und Andreas Fox für ihre Unterstützung und ihren sachkundigen Rat bedanken, Hans-Peter Beise für seine Aufsicht seit dem Masterstudium, seine Verfügbarkeit, seine gute Laune und seine äußerst wertvolle Hilfe, Una Karahasanovic za njegovu pomoć, njegovo znanje i dobre savjete, és Rita Tóth-Bencsik a segítségéért.

De Nancy, Liège et d'ailleurs, je garderai d'excellents souvenirs avec Simon pour nos débats fondamentaux, et mon co-bureau Ismail le Niçois avec qui nous avons découvert et véritablement apprécié Vienne. Un grand merci également à Bertrand Thierry, Jérémie Gaidamour, Séraphin Mefire et Antoine Lejay pour leurs conseils avisés ainsi qu'aux doctorants de *Montefiore*.

J'exprime une grande pensée à mes amis pour leur présence et conseils. Notamment Ben pour son pragmatisme, son soutien, et Charles pour veiller au maintien de la rigueur dans nos formalisations philosophiques, car c'est de toute évidence toujours délicat. Je tiens aussi vivement à remercier ma famille, et particulièrement mes parents et grand-parents pour m'avoir soutenu et encouragé dans cette aventure, dont les bases ont été érigées voilà plus de deux décennies.

Enfin et surtout, merci à toi Salima pour m'avoir accompagné, supporté, aidé, motivé, conseillé, remotivé, et pour continuer de le faire encore longtemps. Je tiens naturellement à terminer ces remerciements avec notre chère Lilya, soleil de nos journées (et de nos nuits).

Physics is mathematical not because we know so much about the physical world, but because we know so little; it is only its mathematical properties that we can discover.

Bertrand Russel

Contents

Introduction (en français) **1**

Introduction **7**

1 Presentation of the problem **10**

1.1 Motivations 11

1.1.1 VitaSense continuous waves radar 11

1.1.2 Micro-Doppler signatures 13

1.2 The wave equation for the electric scalar potential 15

2 One dimensional wave scattering with moving obstacle **18**

2.1 Problem statement and reformulation in a fixed domain 19

2.1.1 The initial boundary-value problem 19

2.1.2 The case of a motionless boundary 20

2.1.3 Reformulation of the initial problem as a fixed domain problem 22

2.2 The specific case of a boundary with sine motion 23

2.2.1 Analysis for the case of a small amplitude boundary motion 23

2.2.2 Derivation of a multi-harmonic approximate system 27

2.2.3 The case of a larger amplitude boundary motion 28

2.3 Numerical implementation of the method 36

2.3.1 Convergence of the frequency-domain solution $\widehat{w}^{\mathcal{J}^+}_{\mathrm{gen},h}$ 36

2.3.2 Influence of the number of frequency components $\sharp\mathcal{J}^+$ 38

2.3.3 Validity of the small-amplitude approximation $\widehat{w}^{\mathcal{J}^+}_h$ 39

2.4 Scattering with general boundary motions 40

2.5 Formal extension to higher dimensions 42

2.6 Conclusion 49

3 Extension of the multi-harmonic FEM to higher dimensions **50**
3.1 Problem statement and notations . . . 51
3.2 Approximate multi-harmonic Helmholtz-type weak coupled formulation . . . 52
3.2.1 Equivalent weak formulation in a fixed domain . . . 52
3.2.2 Approximate weak formulation for small deformations . . . 55
3.2.3 Coupled multi-harmonic Helmholtz-type system . . . 61
3.3 Finite element approximation . . . 66
3.4 Efficient solution of the linear system . . . 68
3.5 Application to a model problem . . . 71
3.5.1 Description of the problem . . . 71
3.5.2 Numerical resolution . . . 73
3.6 Conclusion . . . 84

4 Application of the multi-harmonic FEM to realistic configurations **85**
4.1 Definition of the extended geometries . . . 87
4.1.1 The reference configuration . . . 87
4.1.2 The different test configurations with car occupants . . . 88
4.1.3 Realistic breathing motions . . . 88
4.2 Numerical simulations . . . 92
4.2.1 Calibration of the test cases . . . 92
4.2.2 Detection of car occupants . . . 93
4.3 Discussion of the results . . . 108

General conclusion **109**

A The case of a moving antenna **112**

B Discrete Fourier transform of $|\mathbf{J}_k^{-1}|$ **115**

C Resolution of the approximate block Toeplitz system (3.46) **117**

D A weak formulation of the moving boundary problem for the EM field **122**

List of Figures **125**

Bibliography **129**

Introduction (en français)

Dans le cadre des phénomènes de propagation d'ondes, l'effet Doppler module la fréquence du signal réfléchi par un obstacle en déplacement par rapport à la source. Les dispositifs radar utilisent cette signature fréquentielle afin de détecter des cibles mobiles et de caractériser leurs déplacements. Ces équipements sont ainsi devenus incontournables dans les industries navales et aéronautiques, et occupent une place de plus en plus importante dans le secteur automobile, notamment dans les systèmes de sécurité, d'aide à la conduite et des voitures autonomes. Au cours des dernières décennies, le développement de transmetteurs hautes fréquences a d'ailleurs été largement mis à profit pour la détection radar de cibles en mouvement non uniforme. A titre d'exemple, les bandes de fréquences 24-24.5 GHz et 61-61.5 GHz (bandes ISM) sont courantes pour de nombreuses applications, et la bande 77-81 GHz est à présent abondement utilisée par l'industrie automobile. Des fréquences encore supérieures (THz) seront d'ailleurs atteintes dans un futur proche. En effet, l'avantage crucial des radars hautes fréquences réside dans leur sensibilité accrue aux micro-mouvements d'obstacles constitués de nombreuses parties mobiles, ce qui est à l'origine de l'effet micro-Doppler exploité actuellement dans de nombreuses applications (identification de cibles telles que les drones, dénombrement de passants, détection sans contact de signes vitaux, ...). Il est habituellement calculé *a posteriori* au moyen de techniques de traitement de signaux. Cependant, afin de disposer d'un outil prédictif permettant la modélisation de ce phénomène, il est nécessaire de considérer le modèle physique sous-jacent, qui conduit dans la pratique à la résolution d'un problème de propagation d'ondes en fonction du temps, dans un environnement complexe et composé de plusieurs matériaux diélectriques interagissant fortement avec l'onde émise. Il est notoirement difficile, pour ces problèmes, d'obtenir des solutions explicites et par conséquent, la modélisation mathématique naturelle implique un système d'équations aux dérivées partielles (EDP) dans les domaines temporel et fréquentiel, qui doit être résolu numériquement de manière efficace. Si la résolution de l'effet Doppler avec cibles mobiles, formulé dans un cadre d'EDP, a déjà fait l'objet d'une certaine attention de la part des mathématiciens et des ingénieurs, il est toutefois à noter que la modélisation par EDP et la résolution numérique de l'effet micro-Doppler n'ont jusqu'à présent pas été abordées dans la littérature.

C'est précisément la question traitée dans cette thèse, menée en collaboration avec la société Iee spécialisée dans le développement de capteurs électromagnétiques pour l'industrie automobile. Dans ce contexte, nous proposons une contribution au développement du dispositif radar VitaSense de Iee, conçu pour détecter des occupants d'une voiture. VitaSense est un radar à ondes continues émettant un champ de fréquence constante, ce qui rend naturel de considérer les problèmes de propagation d'ondes sous-jacents en régime harmonique. Nous avons donc choisi de nous concentrer sur le domaine fréquentiel plutôt que temporel, où les coûts de calcul seraient probablement

considérables en raison du nombre important de pas de temps à choisir dans le régime de hautes fréquences $10^9 - 10^{10}$ GHz. De plus, travailler en domaine spectral permet d'exploiter les récents développements de solveurs rapides pour les équations de Helmholtz à hauts nombres d'ondes. Nous proposons dans cette thèse une approche numérique multi-harmonique originale pour résoudre les problèmes de propagation d'ondes dans un domaine spatial mobile par la méthode des éléments finis, connue pour être flexible dans le traitement de configurations complexes.

Détection radar de la présence de passagers

Le radar VitaSense (Figure 1a) est intégré dans la garniture de toit du véhicule et détecte l'éventuelle présence d'un passager sur le siège arrière après que le contact ait été coupé. Ce système vise à apporter une solution au problème du nombre croissant d'enfants et de bébés laissés par inadvertance dans une voiture exposée au soleil, dont l'habitacle peut rapidement atteindre une température critique. Aux États-Unis, 39 enfants meurent ainsi en moyenne chaque année d'un coup de chaleur, et davantage souffrent de handicaps dus à des lésions organiques ou cérébrales. [81].

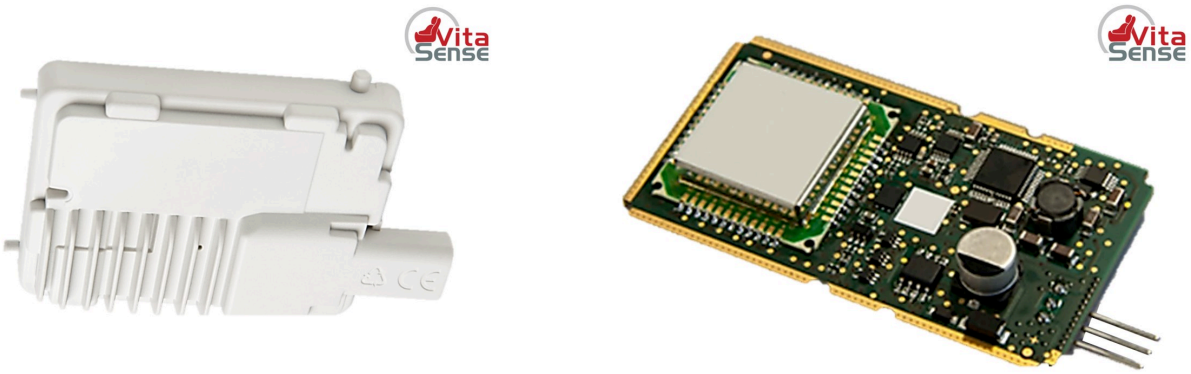

(a) (b)

Figure 1: Radar VitaSense (gauche). Unité de commande électronique (droite).

Face à la multitude de situations rencontrées (pluie, obscurité, ...), de nombreuses technologies ont été testées telles que les capteurs basés sur le siège, les capteurs thermiques ou encore les systèmes optiques. Cependant, chacun d'entre eux présente des points faibles en termes de détection, et ce même dans des situations courantes. En effet, les systèmes basés sur une caméra 2D ne fonctionnent pas dans l'obscurité ou si le champ de vision est bloqué. Les caméras infrarouges ne sont pas fiables lorsque l'intérieur de la voiture est déjà chaud. Les cellules piézoélectriques sont certes très sensibles aux battements de cœur, mais aussi aux vibrations (pluie, ...) et les capteurs à ultrasons ne parviennent pas à détecter de façon fiable un nouveau-né endormi. Comme les ondes électromagnétiques (EM) peuvent traverser les parasols et les vêtements, l'appareil en question fonctionne indépendamment des conditions de luminosité et des courants d'air. Les mouvements respiratoires peuvent alors être clairement distingués d'un éventuel bruit de fond. L'objectif de détection des passagers dans une voiture suggère l'utilisation de configurations radar pseudo-monostatiques voire monostatiques où le récepteur est positionné dans le voisinage immédiat de l'émetteur. La distance relativement courte par rapport à la cible, ainsi que la nécessité de détecter

une déformation de cette dernière en fonction du temps ne sont pas compatibles avec les radars à impulsions. D'autre part, comme la détermination précise de la distance à la cible n'est pas requise, le choix d'un radar à ondes continues modulées en fréquence n'est pas nécessaire. Ceci justifie donc le choix des radars à ondes continues, qui sont peu coûteux et simples à mettre en place.

Pour illustrer ce processus, nous reportons en Figure 2a le signal réfléchi en présence d'une déformation du domaine, et sur la Figure 2b son spectre. Ces données ont été mesurées expérimentalement par Iee en situation réelle, et sont disponibles dans [74]. Le signal présente des variations presque sinusoïdales de période environ une seconde, ce qui correspond à l'ordre de grandeur d'une respiration humaine. Ceci est cohérent avec la modulation de fréquence visible sur la Figure 2b, où l'on observe plusieurs contributions symmétriquement réparties autour de la fréquence d'émission, régulièrement espacées par la fréquence de respiration, et d'amplitudes décroissantes.

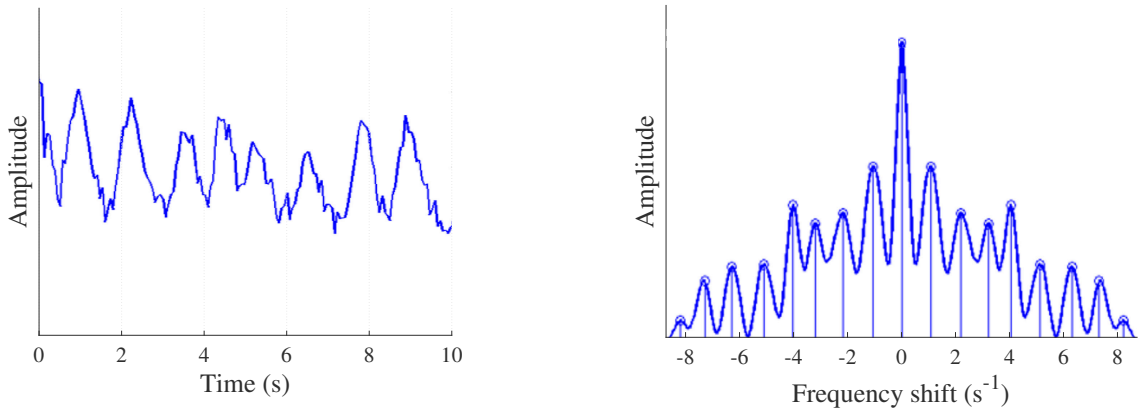

(a) (b)

Figure 2: Signal radar réfléchi (gauche). Spectre associé (droite).

Signature de l'effet micro-Doppler

Le radar considéré est à la fois capable d'émettre un signal sinusoïdal continu u^{i} de fréquence constante ν_{f} et de mesurer un signal réfléchi u^{r}. Le signal émis est partiellement réfléchi par la cible dont le mouvement, de vitesse radiale c^{target} (le long de l'axe défini par l'antenne et le diffuseur), modifie la fréquence initiale conformément à

$$\nu_{\mathrm{r}} = \nu_{\mathrm{f}} \left(\frac{c^{\mathrm{air}} + c^{\mathrm{target}}}{c^{\mathrm{air}} - c^{\mathrm{target}}} \right),$$

où c^{air} est la vitesse de la lumière dans le vide, et ν_{r} la fréquence du signal réfléchi. Il s'agit là de l'effet Doppler. Ainsi, lorsque la cible se rapproche de l'antenne émettrice on a $\nu_{\mathrm{r}} > \nu_{\mathrm{f}}$, et $\nu_{\mathrm{r}} < \nu_{\mathrm{f}}$ lorsqu'elle s'en éloigne. Pour les mouvements non relativistes, la fréquence Doppler

ν_{D} correspondant au mouvement de la cible est donnée par la différence entre les fréquences des signaux émis et reçus, pour laquelle nous avons l'approximation suivante

$$\nu_{\mathrm{D}} := \nu_{\mathrm{r}} - \nu_{\mathrm{f}} = 2\nu_{\mathrm{f}} \frac{c^{\mathrm{target}}}{c^{\mathrm{air}} - c^{\mathrm{target}}} \approx 2\nu_{\mathrm{f}} \frac{c^{\mathrm{target}}}{c^{\mathrm{air}}}.$$

Pour notre cas particulier, le mouvement radial $\ell(t)$ de la cible est produit par une respiration, ce qui en fait une fonction non linéaire du temps décrivant le mouvement relatif des parties de la cible. Comme établi dans [32], cette modulation de fréquence peut être approché en remplaçant c^{target} par la vitesse instantanée de la cible, ce qui conduit à

$$\nu_{\mathrm{D}} \approx 2\nu_{\mathrm{f}} \frac{\partial_t \ell}{c^{\mathrm{air}}}.$$

Afin d'esquisser la structure générale du champ d'ondes total dans le cas d'un mouvement ℓ borné et de faible amplitude, considérons les composantes radiales $u_x^{\mathrm{i}}(x,t)$ et $u_x^{\mathrm{r}}(x,t)$ de u^{i} et u^{r} respectivement, le long de l'axe x comme le montre la Figure 3. Sans perte de généralité, nous

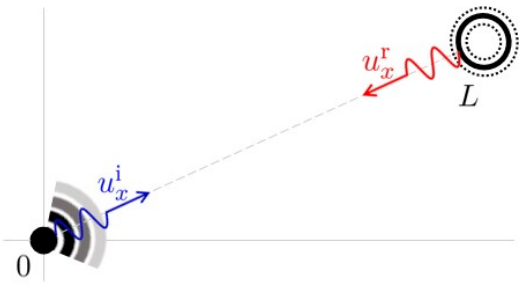

Figure 3: Champ incident et champ réfléchi par l'obstacle mobile.

supposons que le champ incident dans la direction radiale, émis à l'origine, est donné comme un signal sinusoïdal

$$u_x^{\mathrm{i}}(x,t) = \sin(\omega_{\mathrm{f}} \left(t - \frac{x}{c^{\mathrm{air}}} \right)),$$

avec une pulsation $\omega_{\mathrm{f}} := 2\pi\nu_{\mathrm{f}}$, et que la cible, située à une distance $L > 0$ du radar, réfléchit parfaitement l'onde incidente. Pour cette situation et en l'absence de mouvement de la cible, le champ réfléchi s'écrit directement

$$u_x^{\mathrm{r}}(x,t) = -\sin(\omega_{\mathrm{f}} \left(t - \frac{2L - x}{c^{\mathrm{air}}} \right)). \tag{1}$$

A présent, laissons la cible occuper ses positions successives en remplaçant formellement L par la formulation de ℓ dans (1). Ceci correspond à la méthode quasi-stationnaire [88]. Pour notre application, il est raisonnable de considérer un mouvement sinusoïdal $\ell(t) = L(1 + \epsilon \sin(\omega_\ell t))$ de faible pulsation ω_ℓ et d'amplitude relative $\epsilon \ll 1$, ce qui donne

$$
\begin{aligned}
u_x^{\mathrm{r}}(x,t) &= -\sin(\omega_{\mathrm{f}}\left(t-\frac{2L(1+\epsilon\sin(\omega_\ell t))-x}{c^{\mathrm{air}}}\right)) \\
&= -\Im\left\{e^{i\omega_{\mathrm{f}}t}e^{i\omega_{\mathrm{f}}\frac{2L-x}{c^{\mathrm{air}}}}\sum_{j=-\infty}^{\infty}e^{ij\omega_\ell t}\mathrm{J}_j\left(\frac{-2L\epsilon\omega_{\mathrm{f}}}{c^{\mathrm{air}}}\right)\right\} \qquad (2)\\
&= -\Im\left\{e^{i\omega_{\mathrm{f}}\frac{2L-x}{c^{\mathrm{air}}}}\sum_{j=-\infty}^{\infty}e^{i(\omega_{\mathrm{f}}+j\omega_\ell)t}\mathrm{J}_{-j}\left(\frac{2L\epsilon\omega_{\mathrm{f}}}{c^{\mathrm{air}}}\right)\right\},
\end{aligned}
$$

où J_j désigne la $j-$ième fonction de Bessel de première espèce définie pour $j\in\mathbb{Z}$ et $x\in\mathbb{R}$ par

$$
\mathrm{J}_j(x) := \sum_{m=0}^{\infty}\frac{(-1)^m}{m!\Gamma(m+j+1)}\left(\frac{x}{2}\right)^{2m+j},
$$

en fixant $\Gamma(\cdot)$ comme la fonction spéciale Gamma. Le spectre de u_x^{r} montré dans (2) consiste en un peigne de Dirac centré sur la fréquence d'émission ν_{f}, avec des pics également espacés de ν_ℓ et d'amplitudes décroissant rapidement pour j suffisamment grand. En effet, la multiplication de la norme de $\mathrm{J}_j(x)$ par un polynôme en $j\geq 0$ de degré arbitraire $n\in\mathbb{N}$ donne

$$
j^n|\mathrm{J}_j(x)| = \sum_{m\in\mathbb{N}}\frac{e^{n\ln(j)+(2m+j)\ln(\frac{x}{2})}}{m!\Gamma(m+j+1)} \underset{|j|\to\infty}{\sim} \sum_{m\in\mathbb{N}}\frac{e^{j\ln(\frac{x}{2})}}{m!\Gamma(m+j+1)}.
$$

La somme est absolument convergente, donc bornée, et $j\mapsto \mathrm{J}_j(x)$ est à décroissance rapide pour x fixé. De plus, une propriété directe des fonctions de Bessel est que $|\mathrm{J}_j|=|\mathrm{J}_{-j}|$. Par conséquent, nous obtenons le même résultat pour $|\mathrm{J}_{-j}|(x)$. Ce comportement est cohérent avec la structure globale du champ d'ondes mesurée expérimentalement sur la figure 2b. Cette observation fondamentale a été le point de départ de notre étude. Enfin, l'analyse de cette modulation permet de retrouver les propriétés géométriques de la cible à partir de son spectre, qui peut donc être considéré comme une signature et ainsi être utilisé comme méthode de reconnaissance.

Plan de la thèse

Le manuscrit est organisé de la façon suivante.

Dans le Chapitre 1, nous précisons le contexte industriel ayant motivé cette étude et introduisons plus en détails les observations fondamentales sur lesquelles notre méthode se base. Enfin, nous exposons les principaux objets physiques qui sous-tendent la description mathématique du problème, à savoir l'équation des ondes pour le potentiel scalaire électrique.

Nous analysons ensuite dans le Chapitre 2 le problème de propagation d'ondes dans le cas unidimensionel, qui a fait l'objet d'une publication en 2020 dans la revue *Wave Motion* [47]. Nous y exposons une première version de la méthode multi-harmonique développée dans ce travail, puis établissons quelques notations et définissons les idées principales. En particulier, nous transformons d'abord l'équation d'onde à coefficients constants en domaine mobile en une nouvelle équation d'onde en domaine fixe mais avec coefficients variables, induits par le changement de métrique associé. Puisque nous étudions un problème micro-Doppler caractérisé par des oscillations de

faibles fréquences et amplitudes, nous développons la solution sous forme de série de Fourier centrée autour de la fréquence d'émission, et modulée par la perturbation basse fréquence générée par le mouvement de la cible. Cette approche résulte alors en un système couplé d'équations de Helmholtz pour les nombres d'onde associés au développement en série de la solution, que nous résolvons avec une méthode par éléments finis de Lagrange. Finalement, l'approche est généralisée à des frontières dont les déformations ne sont pas explicitement prescrites.

Le Chapitre 3 est axé sur une refonte de la méthode multi-harmoniques par éléments finis présentée au Chapitre 2 afin de traiter de situations plus complexes, en dimensions deux et trois, et incluant notamment des géométries sophistiquées ainsi que différents matériaux. Concrètement, nous récrivons pour un domaine fixe la formulation faible du problème au moyen d'un champ vectoriel qui peut être également évalué localement par la méthode des éléments finis. En inversant de la sorte les deux premières étapes de la méthode par rapport au Chapitre 2, nous gagnons en flexibilité pour des géométries complexes avec conditions aux bords spécifiques. Une implémentation par éléments finis est ensuite développée pour le système couplé obtenu, puis nous exploitons la structure particulière du système linéaire correspondant afin de proposer un solveur itératif préconditionné efficace. Quelques résultats numériques illustrent le comportement de l'approche et ses principales caractéristiques. Cette partie de la thèse a été publiée en 2022 dans la revue *SIAM Journal on Scientific Computing* [49].

Finalement, nous proposons dans le Chapitre 4 une application de la méthode à des situations réalistes basées sur des géométries détaillées. De nombreuses configurations sont testées, en faisant varier des paramètres tels que la position des antennes et des récepteurs, l'orientation des passagers et la modulation de leurs respirations. Nous discutons alors la pertinence de certaines de ces configurations dans le cadre de la détection de la présence de passagers.

Introduction

In the framework of wave scattering problems, the Doppler effect [25, 52] characterizes the property that the motion of a target modulates the frequency of the reflected signal initially emitted by a source. For motions with uniform velocity, the Doppler frequency shift can be easily obtained [23] while for more general movements it is estimated by combining simple models and signal processing techniques [19, 20, 25, 27, 53, 67, 70]. During the last years, the radar detection of non uniformly moving scatterers was applied to a wide variety of problems because of the availability of newly designed high-frequency sensors and devices. For example, the two radar frequency ranges 24-24.5 GHz and 61-61.5 GHz (ISM bands) are now standard in many applications, and the new 77-81 GHz band is being used for applications in the automotive industry. Furthermore, the THz frequency range will be used in the coming years (e.g. at the frequency 140 GHz). A crucial advantage of high-frequency radar sensing is its sensitivity to micro movements of obstacles involving several moving parts, which results in the micro-Doppler effect [25] used nowadays in many applications [3, 17, 20, 27, 46]. In [27], the authors consider the micro-Doppler effect, and derive explicit analytical formulas for elementary micro-motions, which are then used on real radar data problems, while other works treat randomly moving scatterers [72]. This phenomenon is used with great success from drone detection [17] or the analysis of pedestrian movement [20, 27, 46] to the modeling of the effect of the rotation of helicopter rotor blades on the radar signature of the aircraft [3]. In the automotive industry, micro-Doppler sensing has recently been applied with success [36, 53, 62, 67] to the contactless detection of vital signs, in particular for the breathing of children left alone on the back seat of overheating cars. Difficult challenges are related to this kind of application as for example the analysis of random body movements or vehicle vibrations [36, 53, 67, 69, 70, 77] that can be classified thanks to their radar signature by deep learning techniques [16, 17, 29]. In the development life cycle of these new sensors, a full realistic simulation of the high frequency scenarios is therefore needed. The goal of this thesis is to design a suitable numerical modelling for this problem and to propose efficient computational solutions.

In practice, the physical model leads to solving a time-dependent wave propagation problem in a complex environment (here the interior of a car) with a complex geometry made up of several dielectric materials strongly interacting with the high frequency emitted wave. Moreover, the moving targets, such as a child located on the back seat of the car, can have nontrivial shapes, consist of different materials, and often show small amplitude displacements which usually happen at frequencies several orders of magnitude below the frequencies of the emitter. Difficulties appear in higher dimensional cases as closed form solutions are hard to derive for more complex boundary motions. Therefore, the natural mathematical modelling involves a system of partial differential equations (PDEs) both in time and frequency domain, which needs to be efficiently

solved numerically.

The solution of moving target problems formulated in a PDE framework has already received some attention from both the mathematical and engineering sides. Among them, analytical approaches for solving wave-like problems with simple motions have been developed e.g. for rotating obstacles [22, 28, 33, 87] or vibrating objects [24, 28, 57, 70]. Moreover, numerical approximation schemes based e.g. on FDTD [57, 93, 94] or fast integral equation solvers [92] have also been developed. More theoretical contributions essentially linked to one-dimensional moving boundary problems have been considered as well, e.g. by Fokas and his co-authors [42] to recast the problem as a Volterra integral equation in a fixed domain, or by Christov and Christov [32] for an asymptotic multiple-scale analysis of the Doppler effect in a half-space. To the best of the authors' knowledge, however, numerically solving the micro-Doppler PDE modeling problem has not been considered in the literature until now.

This is precisely the issue addressed in this thesis, which was conducted within the international company Iee, specialized in the development of electromagnetic sensors for the automotive industry. In this context, we propose a contribution to the development of Iee's VitaSense radar-based device which is dedicated to the detection of occupants in a car. The VitaSense design is based on continuous wave radars (CW radars), constantly emitting a fixed frequency field, which makes it natural to consider the underlying wave propagation problems in harmonic regimes. We thus chose to focus on the frequency domain rather than the time domain, where the computational costs would likely be considerable due to the number of time steps to be considered in the high frequency regime of interest ($10^9 - 10^{10}$ GHz). Moreover, working in the spectral domain allows to exploit recent advances in fast solvers for high-frequency Helmholtz equations, for which various fast direct and iterative algorithms [66, 79] have been proposed. In order to develop a frequency domain solver to tackle micro-Doppler problems, we propose in this thesis an original multi-harmonic numerical approach to solve wave propagation problems with moving or deforming boundaries by the finite element method [38], which is known to be flexible to handle two- and three-dimensional complex engineering configurations, including complex materials and shapes. This approach, based on the expansion of the unknown in the Fourier domain, can be linked to the so-called harmonic balance method [14, 21, 55, 56, 61, 71, 90]. In addition, this choice allows to consider in the future an algorithmic adaptation of efficient high-order finite element solvers based on domain decomposition [13, 37, 39, 85], where only a local resolution of the problem around the moving obstacle could be resolved.

Thesis outline

The manuscript is organised as follows.

In Chapter 1, we first present the industrial motivations behind this work and introduce the fundamental observation on which our method is based. Next, we introduce the main physical concepts required for this study and establish the link between the physical description of the wave scattering problem and its mathematical formulation, from which we develop the proposed method.

We analyze in Chapter 2 the wave scattering problem in the one-dimensional case, which corresponds to an article published in 2020 in *Wave Motion* [47]. We outline a first version of the multi-harmonic method developed in this work, set some notations and define the main ideas. In particular, we first transform the constant coefficients wave equation in the moving domain as

a new wave-like equation in a fixed domain but with variable coefficients related to the metric change (a similar approach was used for quasi-static electromagnetic models in [56]). Since we are studying the micro-Doppler problem (small amplitude and low frequency oscillations of the scatterer) for a high frequency radar, we can then expand the solution as a time Fourier series centered around the radar frequency and modulated by the low frequency perturbation induced by the scatterer movement. For small amplitude movements, the variable coefficients wave equation can be simplified thanks to the small amplitude, and the series expansion can be truncated to keep a finite number of discrete frequency components related to the small amplitude variations. The resulting approach then yields a coupled system of Helmholtz equations for the wave numbers defined by the discrete frequency components kept by the approximation. For larger amplitude movements, a similar analysis can be developed based on adding more Fourier modes since the frequency coupling is stronger, resulting in a larger system of coupled Helmholtz equations with variable coefficients. Then, we illustrate the validity of the method through numerical computations and comparisons to brute force methods, and generalise it to general boundary motions which are not explicitly prescribed.

In Chapter 3, we redesign the multi-harmonic finite element method presented in Chapter 2 to tackle more complicated engineering problems with complex geometries and inhomogeneous media, in two and three spatial dimensions. More precisely, after stating the problem we derive an approximate multi-harmonic Helmholtz-type weak coupled formulation well-adapted to the finite element method. To this end, we rewrite the moving target problem written in weak form for a fixed domain by means of a mapping that can be computed by the finite element method. This way of proceeding reverses these two steps compared to Chapter 2, significantly improving the adaptability of the method for complex geometries. Since the resulting weak formulation in the fixed domain remains complicated to solve, we propose an approximation of this formulation by a simplified weak form for small deformations. To justify this approximation, we derive some asymptotic error estimates of the bilinear forms according to the small deformation parameter setting. Then, the coupled multi-harmonic Helmholtz-type system is derived from the approximate weak formulation. Considering the time Fourier series expansions of the geometrical quantities (e.g. the Jacobian tensor) for periodic movements and the unknown wavefield, we obtain an approximate truncated finite system of coupled weak form Helmholtz equations at different equally spaced frequencies. The finite element implementation is next developed for the coupled system, and an efficient preconditioned solver that exploits the structure and properties of the resulting linear system is proposed. Finally, we present the application of the resulting method to a two-dimensional problem of the detection of a breathing baby placed on the rear seat of a car. Some numerical results illustrate the behavior of the approach and its main features. This part of the thesis has been published in 2022 in *SIAM Journal on Scientific Computing* [49].

Chapter 4 is devoted to the application of the developed method to realistic situations involving highly detailed geometries and different materials. Many configurations are considered, including varying the position of the moving target, its motion, or the position of the transmitting antenna. The relevance of certain configurations for the effectiveness of the car occupant detection is discussed, based on the results obtained.

Finally, in a general conclusion, we outline the work done and the obtained results. The conclusion of the manuscript also includes research perspectives that could follow from this thesis.

Chapter 1

Presentation of the problem

Contents

1.1 Motivations 11

1.1.1 VitaSense continuous waves radar 11

1.1.2 Micro-Doppler signatures 13

1.2 The wave equation for the electric scalar potential 15

1.1 Motivations

1.1.1 VitaSense continuous waves radar

Radar is an indispensable piece of equipment in the naval and aeronautical industries, but it is also becoming increasingly important in the automotive industry, particularly in the field of safety sensing systems, driver assistance and autonomous cars. This is the context of this work where we present an original numerical method to solve scattering problems in presence of moving boundaries. More precisely, we propose to focus on the VitaSense device of IEE, which has made important contributions in the design of sensors for the automotive, security and health sectors. VitaSense is a small (about 8cm length) radio frequency based sensor (see Figure 1.1a), integrated behind the headliner of the vehicle, that detects the presence of a passenger on the rear seat after the ignition has been switched off. Once the presence of a living being is detected, the driver can be warned. It aims to provide a solution to the problem of the increasing number of children and babies inadvertently left inside a car exposed to the sun (Forgotten Baby Syndrome), whose interior can quickly reach a critical temperature. In the US, 39 children die of vehicular heatstroke on average each year and more suffer disabilities due to organ or brain damage [81].

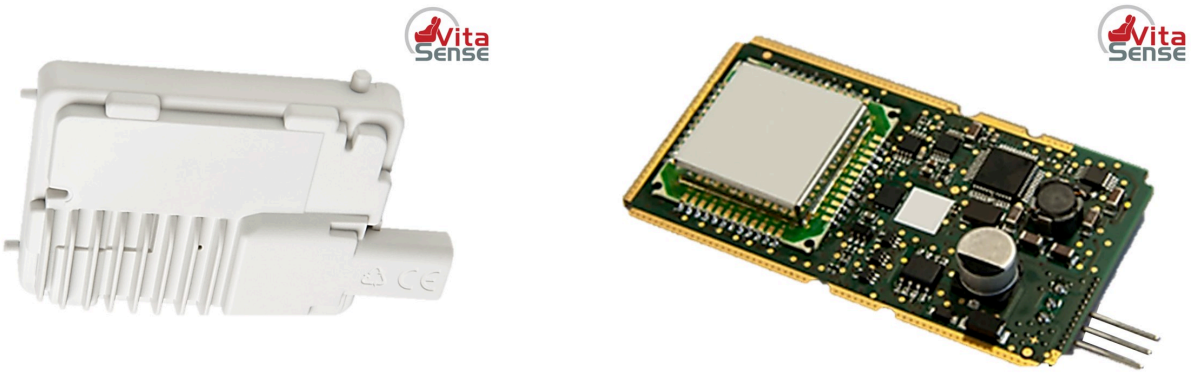

(a) (b)

Figure 1.1: Left: VitaSense device. Right: VitaSense electronic control unit (ECU).

Many technologies have been investigated in response to the multitude of situations encountered such as detection through the sunshade of a rearward-facing child seat. For instance, let us mention seat-based or thermal sensors, or even optical systems. But each of them shows certain weaknesses regarding child detection in certain normal circumstances. Indeed, 2D camera based systems do not work in the dark or if the field of view is blocked. Infrared cameras become unreliable when the car interior is already hot. Piezoelectric foils are very sensitive to heartbeats, but also to vibrations (rain, ...) and ultrasonic sensors cannot detect a sleeping newborn. Since electromagnetic (EM) waves can penetrate through sunshades and clothing, the device works independently from light conditions and air currents. The breathing motions can then be clearly distinguished from background noise.

The objective of passenger detection in a car suggests the use of pseudo-monostatic or even monostatic radar configurations where the receiver is positioned in the immediate neighborhood

of the transmitter. The relatively short distance to the target, as well as the need to detect a time dependent deformation of the latter is not compatible with pulse radars. On the other hand, since the precise determination of the distance to the target is not required, the choice of a frequency modulated continuous waves radar (FMCW) is not necessary. We therefore consider the option of CW radars, which are inexpensive and simple to set up. The VitaSense sensing unit (see Figure 1.1b) emits signals in the 60 GHz ISM band and works with a very low transmission power of 4mW, leading to a specific energy absorption rate more than 20 times below that of a cell phone (typically between 500 and 1000mW). The receiver measures the field scattered by the breathing motion of the child's abdomen while sleeping, or overall body movements when he is awake. The detection is based on the analysis of the frequency modulation of the field originating from the spatial deformation of the domain of propagation. Two sensing modes are implemented. The first one concerns large amplitude movements (displacements, playing baby), allowing immediate detection. The second one is related to a local almost periodic deformation (typically a breath). The work presented in the thesis considers this second situation. Furthermore, we point out that the first VitaSense prototype was transmitting at 24 GHz, and the change to 60 GHz was motivated by a slight reduction in the volume of the device as well as an increase in the available bandwidth (gain from 250 MHz to 4 GHz). However, due to the centimetric amplitude of the deformations in question, this change does not impact the results of our study which was mostly based on the first version of the device.

To illustrate this process, we report in Figure 1.2a the reflected signal in presence of breathing motion, and in Figure 1.2b its spectrum. These data have been experimentally measured by IEE in real situations and are available in [74]. The signal shows almost periodic variations with an average duration of about one second, which corresponds to a typical human breathing motion. This is in accordance with the frequency modulation in Figure 1.2b, where we observe a bounded cluster of peaks around the frequency of emission, regularly spaced by the breathing frequency.

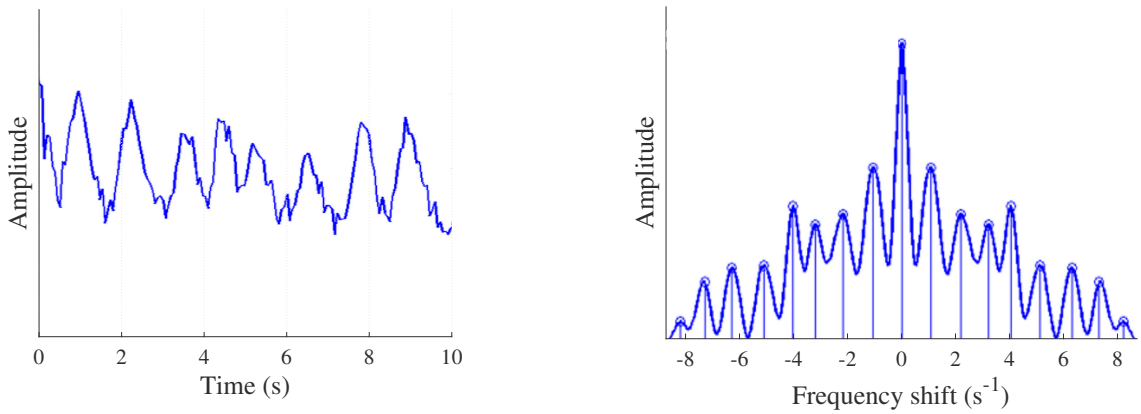

(a) (b)

Figure 1.2: Left: reflected radar signal. Right: corresponding spectrum.

1.1.2 Micro-Doppler signatures

CW radars are able to both emit a continuous sinusoidal signal u^{i} of constant frequency ν_{f} and to receive a reflected signal u^{r}. The transmitted signal is partially scattered by the target, whose motion of radial velocity c^{target} (i.e. along the axis defined by the antenna and the scatterer) modifies the initial frequency according to

$$\nu_{\mathrm{r}} = \nu_{\mathrm{f}} \left(\frac{c^{\mathrm{air}} + c^{\mathrm{target}}}{c^{\mathrm{air}} - c^{\mathrm{target}}} \right),$$

where c^{air} is the speed of light in the vacuum, and ν_{r} the frequency of the scattered signal. This is the Doppler effect. Thus, when the target moves closer to the transmitting antenna we have $\nu_{\mathrm{r}} > \nu_{\mathrm{f}}$, and $\nu_{\mathrm{r}} < \nu_{\mathrm{f}}$ when it moves away. For non-relativistic motions, the Doppler frequency ν_{D} corresponding to the target motion is given by the difference between the frequencies of the transmitted and received signals, which is approximated by

$$\nu_{\mathrm{D}} := \nu_{\mathrm{r}} - \nu_{\mathrm{f}} = 2\nu_{\mathrm{f}} \frac{c^{\mathrm{target}}}{c^{\mathrm{air}} - c^{\mathrm{target}}} \approx 2\nu_{\mathrm{f}} \frac{c^{\mathrm{target}}}{c^{\mathrm{air}}}.$$

In our particular case, the radial movement $\ell(t)$ of the target is produced by a breathing, and is therefore a nonlinear function of time, which describes the local motion of the parts of the target. It is then shown in [32] that the frequency shift can be approximated by replacing c^{target} by the instantaneous velocity of the target, leading to

$$\nu_{\mathrm{D}} \approx 2\nu_{\mathrm{f}} \frac{\partial_t \ell}{c^{\mathrm{air}}}.$$

To outline the general structure of the wave field in case of a small amplitude and bounded motion ℓ, let us consider the radial components $u_x^{\mathrm{i}}(x,t)$ and $u_x^{\mathrm{r}}(x,t)$ of u^{i} and u^{r} respectively, along the x-axis as shown in Figure 1.3. Without loss of generality, we assume that the incident field along

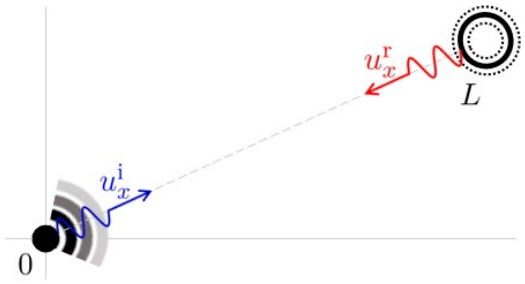

Figure 1.3: Scattered field by moving target.

the radial direction, emitted at the origin, is given as a sinusoidal signal

$$u_x^{\mathrm{i}}(x,t) = \sin(\omega_{\mathrm{f}} \left(t - \frac{x}{c^{\mathrm{air}}} \right)),$$

with pulsation $\omega_{\mathrm{f}} := 2\pi\nu_{\mathrm{f}}$, and that the target, located at a distance $L > 0$ from the radar, is perfectly reflecting the incident wave. For this situation and without motion of the target, the reflected field directly writes

$$u_x^{\mathrm{r}}(x,t) = -\sin(\omega_{\mathrm{f}}\left(t - \frac{2L-x}{c^{\mathrm{air}}}\right)). \tag{1.1}$$

Now we let the target occupy its successive positions according to the motion, i.e. we formally replace L by the formulation of ℓ in (1.1). This corresponds to the quasi-stationary method [88]. For our applications, it is reasonable to consider a sine motion $\ell(t) = L(1 + \epsilon\sin(\omega_\ell t))$ of small pulsation ω_ℓ and amplitude $\epsilon \ll 1$, which yields

$$\begin{aligned} u_x^{\mathrm{r}}(x,t) &= -\sin(\omega_{\mathrm{f}}\left(t - \frac{2L(1+\epsilon\sin(\omega_\ell t)) - x}{c^{\mathrm{air}}}\right)) \\ &= -\Im\left\{e^{i\omega_{\mathrm{f}}t}e^{i\omega_{\mathrm{f}}\frac{2L-x}{c^{\mathrm{air}}}}\sum_{j=-\infty}^{\infty} e^{ij\omega_\ell t}\mathrm{J}_j\left(\frac{-2L\epsilon\omega_{\mathrm{f}}}{c^{\mathrm{air}}}\right)\right\} \\ &= -\Im\left\{e^{i\omega_{\mathrm{f}}\frac{2L-x}{c^{\mathrm{air}}}}\sum_{j=-\infty}^{\infty} e^{i(\omega_{\mathrm{f}}+j\omega_\ell)t}\mathrm{J}_{-j}\left(\frac{2L\epsilon\omega_{\mathrm{f}}}{c^{\mathrm{air}}}\right)\right\}, \end{aligned} \tag{1.2}$$

where J_j denotes the j-th Bessel function of the first-kind defined for $j \in \mathbb{Z}$ and $x \in \mathbb{R}$ by

$$\mathrm{J}_j(x) := \sum_{m=0}^{\infty} \frac{(-1)^m}{m!\Gamma(m+j+1)}\left(\frac{x}{2}\right)^{2m+j},$$

setting $\Gamma(\cdot)$ as the Gamma special function. The spectrum of u_x^{r} shown in (1.2) consists of a Dirac comb centered on the frequency of emission ν_{f}, with peaks equally spaced by ν_ℓ and of rapid decaying amplitudes for j sufficiently large. Indeed, the multiplication of the norm of $\mathrm{J}_j(x)$ by a polynomial in $j \geq 0$ of arbitrary degree $n \in \mathbb{N}$ gives

$$j^n|\mathrm{J}_j(x)| = \sum_{m\in\mathbb{N}} \frac{e^{n\ln(j)+(2m+j)\ln(\frac{x}{2})}}{m!\Gamma(m+j+1)} \underset{|j|\to\infty}{\sim} \sum_{m\in\mathbb{N}} \frac{e^{j\ln(\frac{x}{2})}}{m!\Gamma(m+j+1)}.$$

The sum is absolutely convergent and then bounded, and $j \mapsto \mathrm{J}_j(x)$ is of fast decay for each fixed x. Moreover a direct property of Bessel functions is that $|\mathrm{J}_j| = |\mathrm{J}_{-j}|$. Hence we have the same result for $j \mapsto |\mathrm{J}_{-j}|(x)$. This behavior is illustrated in Figure 1.4, and is coherent with the global structure of the wave field experimentally measured in Figure 1.2b. This initial observation has been the starting point of our study.

Other analytical formulations for the Doppler frequency case are derived in [78, 80], depending on the acceleration of the target. However, such explicit descriptions are not satisfactory for our study. Indeed, we must take into account complex propagation phenomena (multiple reflections in the passenger compartment, non homogeneous materials, ...) as well as the nature of the perturbation we wish to report. Moreover, it is not a displacement as such, but the deformation of the target which is the passenger we want to detect. These local disturbances induce the

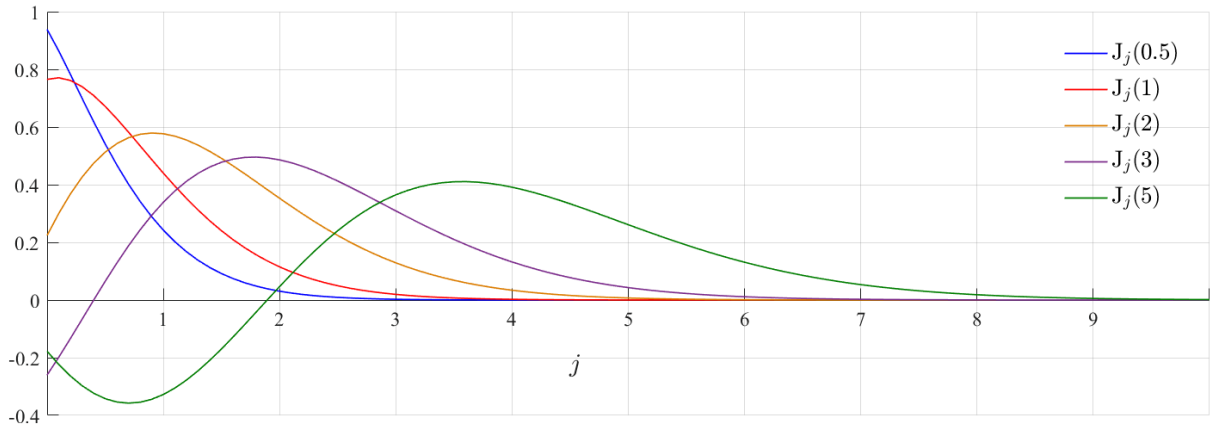

Figure 1.4: Fast decay of $\mathrm{J}_j(x)$ for fixed x and $j \to \infty$.

temporal modulation of the frequency of the received signal (while the transmitted signal keeps a fixed frequency). This comes from the different radial velocities of the separate movements of the different parts of the target, and constitutes the micro-Doppler effect.

Its analysis allows to trace the geometrical properties of the target from its spectrum, which can therefore be seen as a signature, and used as a recognition method. This phenomenon typically leads to the notion of instantaneous frequency [10]. Generally, a time-frequency representation of the micro-Doppler effect is performed using spectrograms (see for example Figure 2.14 in Section 2.5). More precisely, by decomposing the modulating signal into short time windows it is possible to estimate the temporal variation of the frequency of the latter by means of the short time Fourier transform (STFT), or even wavelet transform, which therefore provides a description of the signal through the micro-Doppler signature [26, 51]. This approach applies naturally to the study of the electromagnetic field in the context of a deforming target, and allows to infer the micro movements of its parts. This is crucial for target identification.

Throughout this thesis, we propose to develop a global approach to compute the full spectrum of the wave field by means of a coupled system of PDEs, within the framework of a periodic perturbation of the target. Therefore, we expect to obtain a frequency modulation spreading over a band on both sides of ν_{f}, with a similar structure as the form illustrated by Figure 1.2b.

1.2 The wave equation for the electric scalar potential

In the following, we specify the physical foundations of the equations in which we are interested. Let $(\mathbf{E}, \mathbf{B})$ be the electromagnetic (EM) field in a domain $\Omega^{\mathrm{ext}} \subset \mathbb{R}^3$, with position vector $\mathbf{x} = (x_1, x_2, x_3)^{\mathrm{T}} \in \Omega^{\mathrm{ext}}$. We define the electric permittivity ε_∞ and the magnetic permeability μ_∞

of the medium delimited by Ω^{ext}. In particular, ε_∞ quantifies the polarizability of the medium under the field $\mathbf{E}$, and μ_∞ is a measure of its magnetization under $\mathbf{B}$. In a source and current free isotropic medium, Maxwell's equations [6], which govern the evolution of $(\mathbf{E}, \mathbf{B})$, reduce to

$$\nabla_{\mathbf{x}} \cdot \mathbf{E} = 0, \tag{1.3}$$

$$\nabla_{\mathbf{x}} \cdot \mathbf{B} = 0, \tag{1.4}$$

$$\nabla_{\mathbf{x}} \times \mathbf{E} = -\partial_t \mathbf{B}, \tag{1.5}$$

$$\nabla_{\mathbf{x}} \times \mathbf{B} = \mu_\infty \varepsilon_\infty \partial_t \mathbf{E}, \tag{1.6}$$

with the time variable $t \in \mathbb{R}$, the gradient operator $\nabla_{\mathbf{x}} := (\partial_{x_1}, \partial_{x_2}, \partial_{x_3})^{\mathrm{T}}$, the scalar product $\cdot$ and the vector product $\times$. Let us set the Laplacian $\Delta_{\mathbf{x}} := (\nabla_{\mathbf{x}})^2 = \partial^2_{x_1} + \partial^2_{x_2} + \partial^2_{x_3}$. It is well known that using the identity $\nabla_{\mathbf{x}} \times \nabla_{\mathbf{x}} \times \mathbf{E} = \nabla_{\mathbf{x}}(\nabla_{\mathbf{x}} \cdot \mathbf{E}) - \Delta_{\mathbf{x}} \mathbf{E}$ in (1.5) and (1.6), and the divergence free conditions (1.3) and (1.4) yield the vector wave equations for both the electric and magnetic fields, with wave velocity defined as $c_\infty := 1/\sqrt{\mu_\infty \varepsilon_\infty}$. However, a useful alternative representation of the EM vector field can be derived from the scalar electric potential ψ defined from electrostatics as

$$\mathbf{E} = -\nabla_{\mathbf{x}} \psi. \tag{1.7}$$

Indeed, (1.4) implies that we can define a magnetic vector potential $\mathbf{A}$ such that

$$\mathbf{B} = \nabla_{\mathbf{x}} \times \mathbf{A}. \tag{1.8}$$

Then, injecting (1.8) in (1.5) yields $\nabla_{\mathbf{x}} \times (\mathbf{E} + \partial_t \mathbf{A}) = 0$. Hence, $\mathbf{E} + \partial_t \mathbf{A}$ is a gradient defined up to a constant, which must satisfy the static case (1.7). Then, we have

$$\mathbf{E} = -\nabla_{\mathbf{x}} \psi - \partial_t \mathbf{A},$$

and using the source free condition (1.3) one obtains

$$-\Delta_{\mathbf{x}} \psi - \partial_t \nabla_{\mathbf{x}} \cdot \mathbf{A} = 0.$$

From the arbitrariness of the determination of the scalar and vector potentials ψ and $\mathbf{A}$, let us here consider the field configurations corresponding to the Lorenz gauge. In anticipation of further extensions to inhomogeneous media, let us consider in particular the generalised Lorenz gauge [31]

$$\nabla_{\mathbf{x}} \cdot \varepsilon_\infty \mathbf{A} = -\mu_\infty \varepsilon_\infty^2 \partial_t \psi = \frac{\varepsilon_\infty}{c_\infty^2} \partial_t \psi.$$

This leads to the following equation in source free region

$$\partial_t^2 \psi - \frac{c_\infty^2}{\varepsilon_\infty} \nabla_{\mathbf{x}} \cdot \varepsilon_\infty \nabla_{\mathbf{x}} \psi = 0. \tag{1.9}$$

This corresponds to the homogeneous scalar wave equation for the electric potential studied in this work. For our purposes, the characteristic size of the domain is much larger than the emitted wavelength. Hence, we assume that the source free condition (1.3) is not violated and then we consider

the approximation stating that (1.10) governs the EM field $(\mathbf{E}, \mathbf{B})$, scattered in the propagation domain Ω^{ext} and emitted by an antenna located on its boundary $\partial\Omega^{\text{ext}}$. In the following chapter, we analyze the one dimensional wave scattering problem with moving boundary in isotropic spatial domain. In this case, (1.9) can be simplified to

$$\partial_t^2 \psi - c_\infty^2 \Delta_{\mathbf{x}} \psi = 0. \tag{1.10}$$

In the rest of the thesis, all the physical quantities will be expressed in the standard MKSA system and we will thus omit to precise the units for the numerical values.

Chapter 2

One dimensional wave scattering with moving obstacle

Contents

2.1 Problem statement and reformulation in a fixed domain 19
2.1.1 The initial boundary-value problem 19
2.1.2 The case of a motionless boundary 20
2.1.3 Reformulation of the initial problem as a fixed domain problem 22
2.2 The specific case of a boundary with sine motion 23
2.2.1 Analysis for the case of a small amplitude boundary motion 23
2.2.2 Derivation of a multi-harmonic approximate system 27
2.2.3 The case of a larger amplitude boundary motion 28
2.3 Numerical implementation of the method 36
2.3.1 Convergence of the frequency-domain solution $\widehat{w}^{\mathcal{J}^+}_{\mathrm{gen},h}$ 36
2.3.2 Influence of the number of frequency components $\sharp\mathcal{J}^+$ 38
2.3.3 Validity of the small-amplitude approximation $\widehat{w}^{\mathcal{J}^+}_{h}$ 39
2.4 Scattering with general boundary motions 40
2.5 Formal extension to higher dimensions 42
2.6 Conclusion 49

2.1 Problem statement and reformulation in a fixed domain

2.1.1 The initial boundary-value problem

We consider the one dimensional bounded spatial domain reported in Figure 2.1, and defined by $\Omega(t) = \Omega_t :=]0, \ell(t)[$, where x denotes the spatial variable.

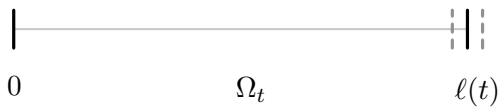

Figure 2.1: Bounded domain Ω_t with moving boundary ℓ.

As previously, the modeling of the moving boundary is described by the time-dependent function $\ell(t)$. In the context of this work, $\ell(t)$ is supposed to be smooth and bounded. For $\mathbb{R}_*^+ :=]0, \infty[$, we introduce the unknown total wave field $u := u(x,t)$, for $x \in \Omega(t)$ and $t \in \mathbb{R}_*^+$, solution to the constant coefficients scalar wave equation

$$\partial_t^2 u - c_\infty^2 \partial_x^2 u = 0, \tag{2.1}$$

where c_∞ is the constant wave velocity in the medium under consideration. Equation (2.1) corresponds to the one-dimensional formulation of (1.10), and u implicitly refers to the electric scalar potential ψ introduced in Chapter 1 and which provides a description of the total EM field. At the fixed left boundary $x = 0$ of $\Omega(t)$, we impose a single-source term $A\sin(\omega_{\mathrm{f}} t)$, with amplitude $A \in \mathbb{R}_*^+$ and angular frequency $\omega_{\mathrm{f}} := 2\pi\nu_{\mathrm{f}} > 0$. In practice, ν_{f} is expected to be very large compared to the frequency content of $\ell(t)$. For instance, ν_{f} might be in frequency range $10^9 - 10^{10}$ for realistic radar applications, which is our focus in Chapters 3 and 4. The associated inhomogeneous Dirichlet boundary condition is then set as:

$$u(0,t) = A\sin(\omega_{\mathrm{f}} t). \tag{2.2}$$

On the moving right boundary, we fix a homogeneous Dirichlet boundary condition

$$u(\ell(t), t) = 0. \tag{2.3}$$

Other boundary conditions can also be considered; for instance, in Appendix A we consider the case of a moving antenna, as also investigated in [32]. For physical applications, we consider the time origin of the problem as an emission starting at $t = 0$, and take into account the transient mode of the excited wave field. Finally, for the sake of well-posedness, we add the two initial conditions

$$u(x,0) = 0 \tag{2.4}$$

and

$$\partial_t u(x,0) = 0. \tag{2.5}$$

2.1.2 The case of a motionless boundary

Let us consider the case where the right boundary is fixed, i.e. $\ell(t) := L$. Then, we get an explicit form of the solution.

Proposition 2.1. *Let us assume that $\Omega_t = \Omega_0 :=]0, L[$, $\forall t > 0$. We define $\kappa_{\mathrm{f}} := \omega_{\mathrm{f}}/c_\infty$, $\kappa_m := m\pi/L$ and $\omega_m := c_\infty \kappa_m$, for $m \in \mathbb{N}$. We suppose that: $\omega_{\mathrm{f}} \neq \omega_m$, $\forall m \in \mathbb{N}$. Then, the solution $\widetilde{u}$ of (2.1) is given by: $\forall x \in \Omega_0$, $t > 0$,*

$$\widetilde{u} = \widetilde{u}_{\nu_{\mathrm{f}}} + \sum_{m\in\mathbb{N}} \widetilde{u}_{\nu_m} \tag{2.6}$$

where

$$\begin{cases} \widetilde{u}_{\nu_{\mathrm{f}}}(x,t) := \dfrac{A}{\sin(\kappa_{\mathrm{f}} L)} \sin(\kappa_{\mathrm{f}}(L-x)) \sin(\omega_{\mathrm{f}} t), \\ \\ \widetilde{u}_{\nu_m}(x,t) := \dfrac{2A\kappa_{\mathrm{f}}}{L(\kappa_{\mathrm{f}}^2 - \kappa_m^2)} \sin(\kappa_m x) \sin(\omega_m t)\,. \end{cases}$$

Proof. The source term of frequency ν_{f} that continuously emits into the domain at the left boundary constitutes an initial impulse that excites the eigenmodes of the system at time $t = L/c_\infty$, which are solutions to the homogeneous wave equation (2.1) with zero boundary conditions.

To separate the different contributions in the global wave field, we decompose u as the sum of the forced stationary wave coming from the source term and the free stationary waves related to the eigenmodes of the system. Hence, let us define

$$\widetilde{u} = \widetilde{u}_{\nu_{\mathrm{f}}} + \widetilde{u}_{\nu}, \tag{2.7}$$

where $\widetilde{u}_{\nu_{\mathrm{f}}}(x,t) = \widetilde{E}_{\nu_{\mathrm{f}}}(x)\sin(\omega_{\mathrm{f}} t)$, and $\widetilde{E}_{\nu_{\mathrm{f}}}$ is the stationary solution to the Helmholtz equation with wavenumber $\kappa_{\mathrm{f}} := \omega_{\mathrm{f}}/c_\infty$ in the bounded domain $]0, L[$

$$(\partial_x^2 + \kappa_{\mathrm{f}}^2)\widetilde{E}_{\nu_{\mathrm{f}}} = 0,$$

with boundary conditions $\widetilde{E}_{\nu_{\mathrm{f}}}(0) = A$ and $\widetilde{E}_{\nu_{\mathrm{f}}}(L) = 0$. A simple calculation gives $\widetilde{u}_{\nu_{\mathrm{f}}}$ as

$$\widetilde{u}_{\nu_{\mathrm{f}}}(x,t) = \frac{A}{\sin(\kappa_{\mathrm{f}} L)} \sin(\kappa_{\mathrm{f}}(L-x)) \sin(\omega_{\mathrm{f}} t). \tag{2.8}$$

Let us now compute $\widetilde{u}_\nu$. As a linear combination of stationary waves, the function $\widetilde{u}_\nu$ is characterized by independent periodicities either in space and time, leading to the direct computation of the field $\widetilde{u}_\nu$ by the separation of variables. More precisely, considering $\widetilde{u}_\nu(x,t) = \widetilde{E}(x)\widetilde{U}(t)$ into (2.1), we obtain the following Helmholtz equation

$$-\partial_x^2 \widetilde{E} = \frac{\lambda^2}{c_\infty^2}\widetilde{E},$$

on $]0, L[$, with homogeneous Dirichlet boundary conditions and for a constant $\lambda \in \mathbb{R}$. Since the spectrum of the Laplace operator in a bounded domain is discrete, the corresponding solutions for each eigenvalue λ_m such that $\lambda_m := m\pi c_\infty/L$ constitute an Hilbert basis $\{e_{\nu_m}\}_{m\in\mathbb{N}}$, with $e_{\nu_m}(x) = \sin(\frac{m\pi}{L}x) =: \sin(\kappa_m x)$ and $\omega_m := 2\pi\nu_m = \kappa_m c_\infty = \frac{m\pi c_\infty}{L}$, for $m \in \mathbb{N}$. In addition, we have the ODE

$$-\partial_t^2 \widetilde{U} = \omega_m^2 \widetilde{U},$$

for $m \in \mathbb{N}$, with $U(0) = 0$. For each frequency ν_m, the solution is then of the form

$$\widetilde{u}_{\nu_m}(t) = \phi_m \sin(\omega_m(t + \psi)),$$

where $\phi_m \in \mathbb{R}$, for $m \in \mathbb{N}$, and ψ must be determined. Since $\widetilde{u}_{\nu_\mathrm{f}}(x, 0) = 0$, (2.4) and (2.7) imply that $\widetilde{u}_{\nu_m}(x, 0) = 0$ and then $\psi = 0$. Hence, by the superposition principle, the general solution $\widetilde{u}_\nu$ for the free modes can then be written as

$$\widetilde{u}_\nu(x, t) = \sum_{m\in\mathbb{N}} \widetilde{u}_{\nu_m}(t)e_{\nu_m}(x) = \sum_{m\in\mathbb{N}} \phi_m \sin(\omega_m t)e_{\nu_m}(x),$$

which entails that

$$\partial_t \widetilde{u}_\nu(x, 0) = \sum_{m\in\mathbb{N}} \phi_m \omega_m e_{\nu_m}(x). \tag{2.9}$$

Since each stationary mode is $\mathcal{C}^\infty(\Omega(t) \times \mathbb{R}_*^+)$, the convergence of the sum is guaranteed. Moreover, (2.5) and (2.7) lead to

$$\partial_t \widetilde{u}_{\nu_m}(x, 0) = -\partial_t \widetilde{u}_{\nu_\mathrm{f}}(x, 0). \tag{2.10}$$

Hence, using (2.8) and (2.10), one gets by a direct computation

$$\partial_t \widetilde{u}_\nu(x, 0) = -\frac{A\omega_\mathrm{f}}{\sin(\kappa_\mathrm{f} L)} \sin(\kappa_\mathrm{f}(L - x)). \tag{2.11}$$

Let us consider the L-periodic odd extension of $\sin(\kappa_\mathrm{f}(L - x))$ in (2.11). Expanding it in the basis $\{e_{\nu_m}\}_{m\in\mathbb{N}}$ for $\nu_{0,\mathrm{f}} \neq \nu_m$, we obtain for $x \in]0, L[$

$$\sin(\kappa_\mathrm{f}(L - x)) = \sum_{m\in\mathbb{N}} \varphi_m e_{\nu_m}(x) = \sum_{m\in\mathbb{N}} \varphi_m \sin(\kappa_m x),$$

where it is well-known that the odd Fourier coefficient φ_m satisfies

$$\begin{aligned}
\varphi_m &= \frac{2}{L}\int_0^L \sin(\kappa_\mathrm{f}(L - x)) \sin(\kappa_m x) dx \\
&= \frac{1}{L}\int_0^L \left[\cos(x(\kappa_m + \kappa_\mathrm{f}) - \kappa_\mathrm{f} L) - \cos(x(\kappa_m - \kappa_\mathrm{f}) + \kappa_\mathrm{f} L)\right] dx \\
&= \frac{2\kappa_m \sin(\kappa_\mathrm{f} L)}{L(\kappa_m^2 - \kappa_\mathrm{f}^2)}.
\end{aligned}$$

Finally, by identification with (2.9), we conclude that

$$\phi_m = \frac{2A\kappa_\mathrm{f}}{L(\kappa_\mathrm{f}^2 - \kappa_m^2)}.$$

Finally, for $\nu_\mathrm{f} \neq \nu_m$, we obtain the result by replacing $\widetilde{u}_{\nu_\mathrm{f}}$ and $\widetilde{u}_\nu$ in (2.7). ■

Let us remark that $\widetilde{u}$ can be extended to $t \in \mathbb{R}$, if we consider the source term (2.2) emitting for $t < 0$, and the conditions (2.3), (2.4) and (2.5). Hence, this allows us to introduce $\mathcal{F}\widetilde{u}$, where the time Fourier transform $\mathcal{F}$ of a function f defined on $\mathbb{R}$ is given by duality with the Fourier transform in sense of distributions, by

$$\mathcal{F}f(x,\xi) := \int_{\mathbb{R}} f(x,t)e^{-2i\pi\xi t}dt. \tag{2.12}$$

From (2.6), one gets

$$\begin{aligned} \mathcal{F}\widetilde{u} &= \frac{A}{2i\sin(\kappa_{\mathrm{f}}L)}\sin(\kappa_{\mathrm{f}}(L-x))(\delta_{\nu_{\mathrm{f}}} - \delta_{-\nu_{\mathrm{f}}}) \\ &\quad + \sum_{m\in\mathbb{N}} A\frac{\kappa_{\mathrm{f}}}{iL(\kappa_{\mathrm{f}}^2 - \kappa_m^2)}\sin(\kappa_m x)(\delta_{\nu_m} - \delta_{-\nu_m}) \\ &=: \mathcal{F}\widetilde{u}_{\nu_{\mathrm{f}}} + \sum_{m\in\mathbb{N}} \mathcal{F}\widetilde{u}_{\nu_m}, \end{aligned} \tag{2.13}$$

where δ_a is the Dirac distribution at a point a. Considering (2.13), we observe that the amplitude of the m-th mode $\mathcal{F}\widetilde{u}_{\nu_m}$ scales like $\kappa_{\mathrm{f}}/L|\kappa_{\mathrm{f}}^2 - \kappa_m^2|$, and thus exhibits a fast decay as the frequency ν_m moves away from ν_{f} (see e.g. Figure 2.2 for an example of such a solution). When ν_{f} is close to an eigenfrequency ν_m, then the solution tends to behave like a single-mode with infinite amplitude, hence concentrating the energy of the system.

In the case of a moving boundary, we expect that the overall behavior of the solution owns similar properties: a first main contribution centered around the frequency ν_{f} and a finite discrete sum of other significant contributions centered around the resonances ν_m, most particularly for a small perturbation of the boundary oscillating at a frequency ν_ℓ such that $0 < \nu_\ell \ll \nu_{\mathrm{f}}$. However, in practical applications the domain is often partially open, has wave absorbing objects at the boundary, or involves damping factors $\alpha > 0$ in the problem formulation, by rewriting (2.1) as

$$\partial_t^2 u + \alpha\partial_t u - c_\infty^2\partial_x^2 u = 0.$$

This leads to non resonant finite amplitude solutions (in particular for the two- and three-dimensional cases). Finally, we highlight that for practical remote sensing applications based on the Doppler effect, the useful information is mainly related to perturbations around ν_{f}.

2.1.3 Reformulation of the initial problem as a fixed domain problem

Let us now focus on the resolution of (2.1), in the case of a moving reflecting boundary. We first map Ω_t to the fixed domain $\Omega_0 =]0, L[$, which corresponds to the equilibrium state of Ω_t. This results in a new wave-like equation from the metric change. The physical solution u is obtained by applying the reverse change of variable, i.e. from Ω_0 to Ω_t. More precisely, the change of space variable $x_0 : (x,t) \mapsto x_0(x,t)$ is such that $x_0(0,t) = 0$, $x_0(\ell(t),t) = L$, for all $t > 0$, and is built as a smooth mapping with respect to x and t. The spatial and time derivative operators then write

$$\partial_x u = \partial_x x_0\ \partial_{x_0}u_0, \qquad \partial_t u = \partial_t u_0 + \partial_t x_0\ \partial_{x_0}u_0, \qquad \partial_x^2 u = (\partial_x x_0)^2\,\partial_{x_0}^2 u_0 + \partial_{x_0}^2 x_0\ \partial_{x_0}u_0,$$
$$\partial_t^2 u = \partial_t^2 u_0 + (\partial_t x_0)^2\,\partial_{x_0}^2 u_0 + 2\partial_t x_0\ \partial_{x_0 t}u_0 + \partial_t^2 x_0\ \partial_{x_0}u_0.$$

Therefore, the initial scattering problem can be rewritten as follows: find $u_0(x_0,t) = u(x,t)$ that maps from $\Omega_0 \times \mathbb{R}_*^+$ to $\mathbb{R}$ and that satisfies

$$\partial_t^2 u_0 - c_\infty^2 \left[(\partial_x x_0)^2 \, \partial_{x_0}^2 u_0 + \partial_x^2 x_0 \; \partial_{x_0} u_0 \right] + (\partial_t x_0)^2 \, \partial_{x_0}^2 u_0 + 2 \partial_t x_0 \; \partial_{x_0 t} u_0 + \partial_t^2 x_0 \partial_{x_0} u_0 = 0, \quad (2.14)$$

with $u_0(0,t) = A \sin(\omega_{\mathrm{f}} t)$, $u_0(L,t) = 0$, $u_0(x_0,0) = 0$ and

$$\partial_t u_0(x_0,0) = -(\partial_t x_0 \; \partial_{x_0} u_0)(x_0,0) = 0.$$

Let us remark that, similarly to [56], the spatial Jacobian $\partial_x x_0$ of x_0 appears in (2.14). In the following, we provide a frequency domain method to solve the modified wave equation (2.14).

2.2 The specific case of a boundary with sine motion

2.2.1 Analysis for the case of a small amplitude boundary motion

Let us again consider the case where the motion of the right endpoint $\ell(t)$ of the domain Ω_t is given as in (A.2), i.e. $\ell(t) = L(1 + \epsilon f(\omega_\ell t))$, where f is smooth and periodic and with $\epsilon \ll 1$. In the one-dimensional case, we can assume that this is given by a linear relation $x = x_0 \ell(t)/L$. To be more explicit, we now focus on the special case where the boundary has a small time sinusoidal motion around L, defined by

$$\ell(t) = L(1 + \epsilon \sin(\omega_\ell t)), \quad (2.15)$$

i.e. setting $f(\omega_\ell t) := \sin(\omega_\ell t)$. This leads to

$$\begin{aligned}
\partial_x x_0 = \frac{L}{\ell} = \frac{1}{1 + \epsilon \sin(\omega_\ell t)} = \mathcal{O}(1), \qquad \partial_x^2 x_0 = 0, \\
\partial_t x_0 = -xL \frac{\ell'}{\ell^2} = -x_0 \frac{\ell'}{\ell} = -x_0 \frac{\epsilon \omega_\ell \cos(\omega_\ell t)}{1 + \epsilon \sin(\omega_\ell t)} = \mathcal{O}(\epsilon), \\
\partial_t^2 x_0 = xL \frac{2\ell'^2 - \ell'' \ell}{\ell^3} = x_0 \frac{2\ell^2 - \ell'' \ell}{\ell^2} = x_0 \frac{\epsilon \omega_\ell^2 (\sin(\omega_\ell t)(1 + \epsilon \sin(\omega_\ell t)) - 2\epsilon \cos(\omega_\ell t))}{(1 + \epsilon \sin(\omega_\ell t))^2} = \mathcal{O}(\epsilon),
\end{aligned}$$

where the composite term $\epsilon \omega_\ell$ highlights the small deformation in both space and time dimensions.

More generally, neglecting the $\mathcal{O}(\epsilon)$ terms in (2.14), we obtain the variable speed wave equation

$$\partial_t^2 v - c_\infty^2 (\partial_x x_0)^2 \partial_{x_0}^2 v = 0, \quad (2.16)$$

which can be written as

$$\frac{\ell^2}{(L c_\infty)^2} \partial_t^2 v - \partial_{x_0}^2 v = 0 \quad (2.17)$$

in $\Omega_0 \times \mathbb{R}_*^+$, with $v(0,t) = A \sin(\omega_{\mathrm{f}} t)$, $v(L,t) = 0$, $v(x_0,0) = 0$ and $\partial_t v(x_0,0) = 0$.

Let us denote by $\Box$ the d'Alembert operator

$$\Box := \frac{1}{c_\infty^2} \partial_t^2 - \partial_{x_0}^2,$$

and $\widetilde{u}(x_0,t)$ as the solution to (2.1) in the case of fixed boundaries. We consider the modified operator

$$\Box_\epsilon := \frac{\ell(t)^2}{(Lc_\infty)^2}\partial_t^2 - \partial_{x_0}^2 = \Box + \epsilon\Box_1,$$

where

$$\Box_1 := \frac{2\sin(\omega_\ell t) + \epsilon\sin(\omega_\ell t)^2}{c_\infty^2}\partial_t^2.$$

For a solution $\Box_\epsilon v = 0$, we define the perturbative part v_1 by $v = \widetilde{u} + v_1$, leading to

$$\Box_\epsilon v_1 = -\epsilon\Box_1\widetilde{u} = -\epsilon\Box_1\left(\widetilde{u}_{\nu_\mathrm{f}} + \sum_{m\in\mathbb{N}}\widetilde{u}_{\nu_m}\right),$$

according to (2.6).

Let us analyze the solutions to the equations associated to each single source term involved in the series expansion of $\widetilde{u}$, i.e.

$$\Box_\epsilon v_{1,\nu_\mathrm{f}} = -\epsilon\Box_1\widetilde{u}_{\nu_\mathrm{f}},$$

and, for $m\in\mathbb{N}$,

$$\Box_\epsilon v_{1,\nu_m} = -\epsilon\Box_1\widetilde{u}_{\nu_m}.$$

The right hand sides are $\mathcal{C}^\infty(\Omega_0\times\mathbb{R}_*^+)$ functions and the corresponding boundary conditions are homogeneous Dirichlet conditions. Thus, since these equations are of hyperbolic-type, we have the existence and uniqueness of the solutions and by superposition

$$v_1 = v_{1,\nu_\mathrm{f}} + \sum_{m\in\mathbb{N}} v_{1,\nu_m}.$$

Finally, we prove that there exist some functions v_{ν_f} and v_{ν_m}, $m\in\mathbb{N}$, in $\mathcal{C}^\infty(\Omega_0\times\mathbb{R}_*^+)$ such that the solution v of (2.17) admits the following decomposition:

$$v = v_{\nu_\mathrm{f}} + \sum_{m\in\mathbb{N}} v_{\nu_m}, \tag{2.18}$$

with $v_{\nu_\mathrm{f}} = \widetilde{u}_{\nu_\mathrm{f}} + v_{1,\nu_\mathrm{f}}$ and $v_{\nu_m} = \widetilde{u}_{\nu_m} + v_{1,\nu_m}$, for $m\in\mathbb{N}$.

This form provides a generalisation of (2.6) to the case of a moving boundary based on the approximation (2.17) of the full wave equation (2.14). Let us also remark that the previous decomposition can be extended to the case of smooth and bounded functions ℓ defined by a function f.

We now focus on the term v_{ν_f} of main contribution, appearing in the expansion (2.18). A similar approach can be adapted to the other terms v_{ν_m}, for $m\in\mathbb{N}$. Based on the method of separation of variables, we define $v_{\nu_\mathrm{f}}(x_0,t) = E(x_0)V(t)$. The time-dependent component $V(t)$ of $v_{\nu_\mathrm{f}}(x_0,t)$ is given as the solution of the variable coefficients ODE

$$\partial_t^2 V + \frac{\omega_\mathrm{f}^2 L^2}{\ell(t)^2}V = 0, \tag{2.19}$$

for which we are seeking a solution in $\mathcal{C}^\infty(\mathbb{R}_*^+)$. Since

$$\frac{\omega_{\mathrm{f}}^2 L^2}{\ell(t)^2} = \frac{\omega_{\mathrm{f}}^2}{(1+\epsilon\sin(\omega_\ell t))^2},$$

and $\epsilon\sin(\omega_\ell t) \in]-1,1[$, we have the power series expansion

$$\begin{aligned} \frac{\omega_{\mathrm{f}}^2 L^2}{\ell(t)^2} &= \omega_{\mathrm{f}}^2 \sum_{k\in\mathbb{N}} (-1)^k (k+1)\left(\epsilon\sin(\omega_\ell t)\right)^k \\ &= \omega_{\mathrm{f}}^2 \left(1 - 2\epsilon\sin(\omega_\ell t) + \mathcal{O}(\epsilon^2)\right). \end{aligned} \tag{2.20}$$

For $\epsilon \ll 1$, we consider the approximate solution W to the equation (2.19) based on the first-order truncation of (2.20), i.e.

$$\partial_t^2 W + \omega_{\mathrm{f}}^2 \left(1 - 2\epsilon\sin(\omega_\ell t)\right) W = 0. \tag{2.21}$$

Let us define the change of variable $\tau := \pi\nu_\ell t + \frac{\pi}{4}$ and the function $\widetilde{W}(\tau) := W(t)$. Then the second-order derivative writes

$$\partial_t^2 W = (\pi\nu_\ell)^2 \partial_\tau^2 \widetilde{W}.$$

From (2.21), we deduce the Mathieu's equation

$$\partial_\tau^2 \widetilde{W} + (\alpha - 2q\cos(2\tau))\widetilde{W} = 0, \tag{2.22}$$

with $\alpha = (\frac{2\nu_{\mathrm{f}}}{\nu_\ell})^2$ and $q = -\alpha\epsilon$. The solutions of (2.22) are given as linear combinations of Mathieu functions of the first-kind [2]. According to Floquet's theory [63], they can be written as $\Phi(\tau) = e^{i\mu\tau}p(\tau)$, with p a π-periodic function and μ the associated Floquet's exponent. Let us remark that the function $\Phi(-\tau)$ is also solution to the equation (2.22). Whenever $\Phi(\tau)$ and $\Phi(-\tau)$ are linearly independent, the general solution writes [2] as

$$\begin{aligned} \widetilde{W}(\tau) &= e^{i\mu\tau}\sum_{j\in\mathbb{Z}} \overline{a}_j^+ e^{2ij\tau} + e^{-i\mu\tau}\sum_{j\in\mathbb{Z}} \overline{a}_j^- e^{-2ij\tau} \\ &= \sum_{j\in\mathbb{Z}} \overline{a}_j^+ e^{2i(\frac{\mu}{2}+j)\tau} + \overline{a}_j^- e^{-2i(\frac{\mu}{2}+j)\tau}, \end{aligned} \tag{2.23}$$

with $\overline{a}_j^\pm$ being the complex valued Fourier coefficients of p. Since $\widetilde{W}(\tau)$ is a periodic $\mathcal{C}^\infty(\mathbb{R}_*^+)$ function, $|\overline{a}_j^\pm|$ has a fast decay when $|j| \to +\infty$.

As $q = \mathcal{O}(\epsilon)$, for sufficiently small perturbations ϵ, we may expand α in terms of μ and q (cf. [2], Ch. 20, p. 730)

$$\alpha = \mu^2 + \frac{q^2}{2(\mu^2-1)} + \mathcal{O}\left(\frac{q^4}{\mu^6}\right) = \mu^2 + \mathcal{O}(\epsilon^2). \tag{2.24}$$

Hence, at first-order in ϵ one gets $\mu \approx \sqrt{\alpha} = \frac{2\nu_{\mathrm{f}}}{\nu_\ell}$, and for small values of ϵ, we have the approximation

$$\widetilde{W}(\tau) \approx \sum_{j\in\mathbb{Z}} \overline{a}_j^+ e^{2i(\frac{\nu_{\mathrm{f}}}{\nu_\ell}+j)\tau} + \overline{a}_j^- e^{-2i(\frac{\nu_{\mathrm{f}}}{\nu_\ell}+j)\tau},$$

which yields, for $\tau = \pi\nu_\ell t + \frac{\pi}{4}$,

$$W(t) \approx \sum_{j\in\mathbb{Z}} i^j \overline{a}_j^+ e^{i\frac{\pi\nu_{\rm f}}{2\nu_\ell}} e^{2i\pi(\nu_{\rm f}+j\nu_\ell)t} + (-i)^j \overline{a}_j^- e^{-i\frac{\pi\nu_{\rm f}}{2\nu_\ell}} e^{-2i\pi(\nu_{\rm f}+j\nu_\ell)t}.$$

Combining $(\pm i)^j \overline{a}_j^\pm e^{\pm i\frac{\pi\nu_{\rm f}}{2\nu_\ell}}$ with the space dependent component $E(x_0)$ of v, we define the coefficients $\{a_j^\pm(x_0)\}_{j\in\mathbb{Z}}$ such that, for each integer j, we have

$$a_j^\pm(x_0) = (\pm i)^j \overline{a}_j^\pm e^{\pm i\frac{\pi\nu_{\rm f}}{2\nu_\ell}} E(x_0).$$

We formally obtain the following ansatz for small ϵ

$$v_{\nu_{\rm f}}(x_0,t) \;\approx\; \sum_{j\in\mathbb{Z}} a_j^+(x_0) e^{i(\omega_{\rm f}+j\omega_\ell)t} + a_j^-(x_0) e^{-i(\omega_{\rm f}+j\omega_\ell)t}. \tag{2.25}$$

Let us define, for fixed integers $J_1 \le 0$ and $J_2 \ge 0$ the finite sets of integers $\mathcal{J} = \mathcal{J}^- \cup \mathcal{J}^+$ and frequencies $\mathcal{I} = \mathcal{I}^- \cup \mathcal{I}^+$, where

$$\begin{array}{ll} \mathcal{J}^- := \{j\in\mathbb{Z}, -J_2 \le j \le -J_1\}, & \mathcal{J}^+ := \{j\in\mathbb{Z}, J_1 \le j \le J_2\}, \\ \mathcal{I}^- := \{-\nu_{\rm f} + j\nu_\ell\}_{j\in\mathcal{J}^-}, & \mathcal{I}^+ := \{\nu_{\rm f} + j\nu_\ell\}_{j\in\mathcal{J}^+}. \end{array} \tag{2.26}$$

We denote by $\sharp\mathcal{J}$ the cardinal of the set $\mathcal{J}$. Since $|a_j^\pm(x_0)|$ is fastly decaying for $|j|\to\infty$, (2.25) justifies that the method that we develop (most particularly for small ϵ) in the following is based on the approximation $w^{\mathcal{J}}$ of $v_{\nu_{\rm f}}$ by the finite sum

$$w^{\mathcal{J}}(x_0,t) := \sum_{j\in\mathcal{J}^+} a_j^+(x_0) e^{i(\omega_{\rm f}+j\omega_\ell)t} + a_j^-(x_0) e^{-i(\omega_{\rm f}+j\omega_\ell)t}, \tag{2.27}$$

where $\sharp\mathcal{J} = 2\sharp\mathcal{J}^+$ coefficients $a_j^\pm(x_0)$ have to be computed thanks to a coupled system of multi-harmonic Helmholtz-type equations in the Fourier domain. The two integers J_1 and J_2 must be carefully chosen to include the significant contributions to the solution.

By construction of the Fourier series expansion, we have $a_j^+ = \overline{a_j^-}$. For the sake of clarity, let us set in the following $a_j := a_j^+$. Thus, one gets

$$\begin{array}{rcl} w^{\mathcal{J}}(x_0,t) & = & \displaystyle\sum_{j\in\mathcal{J}^+} a_j(x_0) e^{i(\omega_{\rm f}+j\omega_\ell)t} + \sum_{j\in\mathcal{J}^+} \overline{a_j}(x_0) e^{-i(\omega_{\rm f}+j\omega_\ell)t} \\ & =: & w^{\mathcal{J}^+}(x_0,t) + w^{\mathcal{J}^-}(x_0,t), \end{array} \tag{2.28}$$

where the Fourier coefficients of $w^{\mathcal{J}^-}$ are the complex conjugates of the Fourier coefficients of $w^{\mathcal{J}^+}$.

Let us remark that the expression (2.18) of v also involves the functions v_{ν_m}. However, their contribution to v is less significant than $v_{\nu_{\rm f}}$. In the case where a part of the domain is open or includes some absorption materials (see Section 2.5), they are even negligible. Finally, if $\epsilon = 0$, all the above computations are exact and $J_1 = J_2 = 0$.

2.2.2 Derivation of a multi-harmonic approximate system

Let us assume that the Leibniz integral rule holds for v. Then, assuming that the time Fourier transform $\widehat{v}$ of v is defined according to (2.12), (with the extension $v = \widetilde{u}$ for $t < 0$), one gets: $\mathcal{F}\partial_{x_0}^2 v(x_0,t) = \partial_{x_0}^2 \widehat{v}(x_0,\xi)$, setting $\widehat{v}(x_0,\xi) := \mathcal{F}v(x_0,t)$.

Applying $\mathcal{F}$ to (2.15)-(2.17) gives

$$\begin{aligned}\mathcal{F}\left(\partial_{x_0}^2 v - \frac{(1+\epsilon\sin(\omega_\ell t))^2}{c_\infty^2}\partial_t^2 v\right)&\\ = \mathcal{F}\left(\partial_{x_0}^2 v - \frac{1}{c_\infty^2}\left[1+\frac{\epsilon^2}{2}+2\epsilon\sin(\omega_\ell t)-\frac{\epsilon^2}{2}\cos(2\omega_\ell t)\right]\partial_t^2 v\right)&\\ = \partial_{x_0}^2\widehat{v} + \left[\left(1+\frac{\epsilon^2}{2}\right)\delta_0 + i\epsilon(\delta_{-\nu_\ell}-\delta_{\nu_\ell}) - \frac{\epsilon^2}{4}\left(\delta_{2\nu_\ell}+\delta_{-2\nu_\ell}\right)\right] * \left[\left(\frac{2\pi\xi}{c_\infty}\right)^2\widehat{v}\right] = 0,&\end{aligned}$$

where $*$ is the convolution product. Denoting by τ_a the translation operator such that $\tau_a f(t) = f(t-a)$, we obtain the following problem: find $\widehat{v}:\Omega_0\times\mathbb{R}\to\mathbb{R}$ satisfying

$$\partial_{x_0}^2\widehat{v} + \left[\left(1+\frac{\epsilon^2}{2}\right) + i\epsilon\left(\tau_{-\nu_\ell}-\tau_{\nu_\ell}\right) - \frac{\epsilon^2}{4}\left(\tau_{2\nu_\ell}+\tau_{-2\nu_\ell}\right)\right]\left[\left(\frac{2\pi\xi}{c_\infty}\right)^2\widehat{v}\right] = 0. \tag{2.29}$$

In addition, for all $\xi\in\mathbb{R}$, we have $\widehat{v}(L,\xi)=0$, $\widehat{v}(0,\xi)=0$ if $|\xi|\neq\nu_{\mathrm{f}}$, $\widehat{v}(0,\nu_{\mathrm{f}}) = \frac{A}{2i}$ and $\widehat{v}(0,-\nu_{\mathrm{f}}) = -\frac{A}{2i}$.

Let us now compute an approximation of the contribution $\widehat{v}_{\nu_{\mathrm{f}}}$ of the solution $\widehat{v}$ to (2.29) around ν_{f}. From the ansatz (2.28), it is reasonable to look for an approximate solution $\widehat{w}^{\mathcal{J}}(x_0,\xi)$ of $\widehat{v}_{\nu_{\mathrm{f}}}(x_0,\xi)$ as

$$\widehat{w}^{\mathcal{J}} = \widehat{w}^{\mathcal{J}^+} + \widehat{w}^{\mathcal{J}^-} := \sum_{j\in\mathcal{J}^+} a_j\delta_{\nu_{\mathrm{f}}+j\nu_\ell} + \sum_{j\in\mathcal{J}^+}\overline{a_j}\delta_{-(\nu_{\mathrm{f}}+j\nu_\ell)}, \tag{2.30}$$

which is a linear combination of Dirac distributions, centered around $\pm\nu_{\mathrm{f}}$, spaced by the modulating frequency ν_ℓ, and with (unknown) spatial amplitudes $\{a_j^{\pm}\}_{\mathcal{J}^+}$. The fast decay of the coefficients $|a_j|$ for $|j|\to+\infty$ guarantees that the finite supports $\mathcal{I}^{\pm}$ of the tempered distributions $\widehat{w}^{\mathcal{J}^{\pm}}$ are disjoint. Hence, we can restrict our analysis to the contribution $\widehat{w}^{\mathcal{J}^+}$. Plugging the expansion of $\widehat{w}^{\mathcal{J}^+}(x_0,\xi)$ defined in (2.30) into (2.29) leads to

$$\begin{aligned}\sum_{j\in\mathcal{J}^+}\Bigg[\partial_{x_0}^2 a_j\delta_{\nu_{\mathrm{f}}+j\nu_\ell} + a_j\Bigg[\left(1+\frac{\epsilon^2}{2}\right)\delta_{\nu_{\mathrm{f}}+j\nu_\ell}&\\ +i\epsilon\left(\left(\frac{2\pi(\xi+\nu_\ell)}{c_\infty}\right)^2\delta_{\nu_{\mathrm{f}}+(j-1)\nu_\ell} - \left(\frac{2\pi(\xi-\nu_\ell)}{c_\infty}\right)^2\delta_{\nu_{\mathrm{f}}+(j+1)\nu_\ell}\right)&\\ -\frac{\epsilon^2}{4}\left(\left(\frac{2\pi(\xi-2\nu_\ell)}{c_\infty}\right)^2\delta_{\nu_{\mathrm{f}}+(j+2)\nu_\ell} + \left(\frac{2\pi(\xi+2\nu_\ell)}{c_\infty}\right)^2\delta_{\nu_{\mathrm{f}}+(j-2)\nu_\ell}\right)\Bigg]\Bigg] = 0.&\end{aligned}$$

Then, after identifying the coefficients in front of the Dirac distributions one obtains

$$\partial_{x_0}^2 a_j + \kappa_j^2\left(1+\frac{\epsilon^2}{2}\right)a_j + i\epsilon(\kappa_{j+1}^2 a_{j+1} - \kappa_{j-1}^2 a_{j-1}) - \frac{\epsilon^2}{4}(\kappa_{j-2}^2 a_{j-2} + \kappa_{j+2}^2 a_{j+2}) = 0, \tag{2.31}$$

for $j \in \mathcal{J}^+$, with $\kappa_j := (\omega_\mathrm{f} + j\omega_\ell)/c_\infty$ and for the boundary conditions $a_0(0) = \frac{A}{2i}$, $a_j(0) = 0$ for $j \neq 0$, $a_j(L) = 0$, and $a_j(x_0) = 0$ for $x_0 \in \Omega_0$ and $j \in \mathbb{Z} \setminus \mathcal{J}^+$.

Equation (2.31) describes the coupling between the frequency components induced by the boundary oscillations. As expected, taking $\epsilon = 0$ gives a system of uncoupled Helmholtz equations, where the coefficients vanish for $j \neq 0$, and

$$a_0(x_0) = \frac{A}{2i}\frac{\sin(\kappa_\mathrm{f}(L - x))}{\sin(\kappa_\mathrm{f} L)}.$$

In Section 2.3, we numerically solve (2.31) by means of the finite element method. To this end, we derive the following coupled weak formulation: find $a_j \in H^1_{\frac{A}{2i},0}(\Omega_0) := \{a_j \in H^1(\Omega_0) \mid a_0(0) = \frac{A}{2i}$, $a_j(0) = 0$ for $j \neq 0$, $a_j(L) = 0\}$ such that

$$\begin{aligned} -\int_{\Omega_0} \partial_{x_0} a_j \partial_{x_0}\phi dx_0 + \int_{\Omega_0} \Big[\kappa_j^2\left(1+\epsilon^2\right)a_j + i\epsilon(\kappa_{j+1}^2 a_{j+1} - \kappa_{j-1}^2 a_{j-1}) \\ -\epsilon^2(\kappa_{j-2}^2 a_{j-2} + \kappa_{j+2}^2 a_{j+2})\Big]\phi dx_0 = 0 \end{aligned} \tag{2.32}$$

holds for all test functions $\phi \in H^1_{0,0}(\Omega_0)$ and for $j \in \mathcal{J}^+$, with $a_j(x_0) = 0$ for $j \in \mathbb{Z} \setminus \mathcal{J}^+$. Here, $H^m(\Omega_0)$ designates the standard Sobolev space of solutions of finite energy on Ω_0 and $H^1_{0,0}(\Omega_0) := \{\phi \in H^1(\Omega_0) \mid \phi(0) = 0$ and $\phi(L) = 0\}$. We then consider a regular covering $\Omega_{0,h}$ of Ω_0 using n_{Ω_0} finite elements of size h. All the notations are extended with an h subscript for the discrete version of the domains as well as unknowns. We choose a linear element approximation and denote by

$$\widehat{w}_h^{\mathcal{J}^+} = \sum_{j\in\mathcal{J}^+} a_{j,h}\delta_{\nu_\mathrm{f}+j\nu_\ell}$$

the solution of the discretization of the variational coupled system (2.32), with $a_{j,h}$ belonging to the $(n_{\Omega_0} - 1)$-dimensional finite element subspace of $H^1_{\frac{A}{2i},0}(\Omega_0)$.

2.2.3 The case of a larger amplitude boundary motion

The previous method has been specifically designed for the case of small amplitude motions, according to the approximate equation (2.31). In this subsection, we focus on a more general case as we transfer the exact equation (2.14) directly to the frequency domain. The range of validity of this approach is explored with a numerical study in Section 2.3.

For $\epsilon \in]0, L[$ and a linear transformation in x, multiplying (2.14) by ℓ^2 yields

$$\ell^2\partial_t^2 u_0 + (x_0^2\ell'^2 - c_\infty^2 L^2)\partial_{x_0}^2 u_0 - 2x_0\ell\ell'\partial_{x_0 t}u_0 + x_0(2\ell'^2 - \ell\ell'')\partial_{x_0}u_0 = 0, \tag{2.33}$$

with $u_0(0,t) = A\sin(\omega_\mathrm{f} t)$, $u_0(L,t) = 0$ for $t > 0$, and $u_0(x_0,0) = 0$, $\partial_t u_0(x_0,0) = 0$, for $x_0 \in \Omega_0$. The same linear change of metric with harmonic deformation $\ell = L(1 + \epsilon\sin(\omega_\ell t))$ entails that

$$\begin{aligned} &L^2(1+\epsilon\sin(\omega_\ell t))^2\partial_t^2 u_0 + L^2(x_0^2(\epsilon\omega_\ell\cos(\omega_\ell t))^2 - c_\infty^2)\partial_{x_0}^2 u_0 \\ &\quad -2x_0 L^2(1+\epsilon\sin(\omega_\ell t))\epsilon\omega_\ell\cos(\omega_\ell t)\partial_{x_0 t}u_0 \\ &\quad +x_0(2(L\epsilon\omega_\ell\cos(\omega_\ell t))^2 - L^2(1+\epsilon\sin(\omega_\ell t))(-\epsilon\omega_\ell^2\sin(\omega_\ell t)))\partial_{x_0}u_0 = 0. \end{aligned}$$

After linearization, we obtain

$$\left(1+\frac{\epsilon^2}{2}+2\epsilon\sin(\omega_\ell t)-\epsilon^2\frac{\cos(2\omega_\ell t)}{2}\right)\partial_t^2 u_0+\left(x_0^2\epsilon^2\omega_\ell^2\frac{1+\cos(2\omega_\ell t)}{2}-c_\infty^2\right)\partial_{x_0}^2 u_0$$
$$-2x_0\epsilon\omega_\ell\left(\cos(\omega_\ell t)+\epsilon\frac{\sin(2\omega_\ell t)}{2}\right)\partial_{x_0 t}u_0$$
$$+\frac{x_0\epsilon\omega_\ell^2}{2}\left(\epsilon(3+\cos(2\omega_\ell t))+2\sin(\omega_\ell t)\right)\partial_{x_0}u_0=0. \quad (2.34)$$

Let $\widehat{u}_0(x_0,\xi):=\mathcal{F}(u_0)(x_0,\xi)$ be the time Fourier transform of a solution u_0 of (2.34). The methodology presented in the previous subsection is now applied and the time Fourier transform of (2.34) writes as

$$\left[\left(1+\frac{\epsilon^2}{2}\right)\delta_0-i\epsilon(\delta_{\omega_\ell}-\delta_{-\omega_\ell})-\frac{\epsilon^2}{4}(\delta_{2\omega_\ell}+\delta_{-2\omega_\ell})\right]*\left[-(2\pi\xi)^2\widehat{u}_0\right]$$
$$+\left[\left(\frac{x_0^2\epsilon^2\omega_\ell^2}{2}-c_\infty^2\right)\delta_0+\frac{x_0^2\epsilon^2\omega_\ell^2}{4}(\delta_{2\omega_\ell}+\delta_{-2\omega_\ell})\right]*\partial_{x_0}^2\widehat{u}_0$$
$$-2x_0\epsilon\omega_\ell\left[\frac{1}{2}(\delta_{\omega_\ell}+\delta_{-\omega_\ell})-\frac{i\epsilon}{4}(\delta_{2\omega_\ell}-\delta_{-2\omega_\ell})\right]*[2i\pi\xi\partial_{x_0}\widehat{u}_0)]$$
$$+x_0\epsilon\omega_\ell^2\left[\frac{3\epsilon}{2}\delta_0+\frac{\epsilon}{4}(\delta_{2\omega_\ell}+\delta_{-2\omega_\ell})-\frac{i}{2}(\delta_{\omega_\ell}-\delta_{-\omega_\ell})\right]*\partial_{x_0}\widehat{u}_0 \quad = \quad 0,$$

which leads to

$$-\left[\left(1+\frac{\epsilon^2}{2}\right)-i\epsilon(\tau_{\omega_\ell}-\tau_{-\omega_\ell})-\frac{\epsilon^2}{4}(\tau_{2\omega_\ell}+\tau_{-2\omega_\ell})\right]\left[(2\pi\xi)^2\widehat{u}_0\right]$$
$$+\left[\left(\frac{x_0^2\epsilon^2\omega_\ell^2}{2}-c_\infty^2\right)+\frac{x_0^2\epsilon^2\omega_\ell^2}{4}(\tau_{2\omega_\ell}+\tau_{-2\omega_\ell})\right]\partial_{x_0}^2\widehat{u}_0$$
$$-x_0\epsilon\omega_\ell\left[(\tau_{\omega_\ell}+\tau_{-\omega_\ell})-\frac{i\epsilon}{2}(\tau_{2\omega_\ell}-\tau_{-2\omega_\ell})\right][2i\pi\xi\partial_{x_0}\widehat{u}_0]$$
$$+\frac{x_0\epsilon\omega_\ell^2}{2}\left[3\epsilon+\frac{\epsilon}{2}(\tau_{2\omega_\ell}+\tau_{-2\omega_\ell})-i(\tau_{\omega_\ell}-\tau_{-\omega_\ell})\right]\partial_{x_0}\widehat{u}_0 \quad = \quad 0,$$

We assume that u_0 admits a decomposition of the form (2.18) (see also Figure 2.2). Let us now focus on the component $\widehat{u}_{0,\nu_\mathrm{f}}$ of $\widehat{u}_0$ and search for an approximation $\widehat{w}_{\mathrm{gen}}^{\mathcal{J}^+}$ of $\widehat{u}_{0,\nu_\mathrm{f}}$ for $\xi\in\mathcal{I}^+$, in the form of the ansatz (2.30) with coefficients $a_{j,\mathrm{gen}}$. Now let us define the adimensional time scale factor $\omega=\omega_\ell/\omega_\mathrm{f}$. After identifying the coefficients in front of the Dirac distributions, we divide

by ω_{f}^2 and obtain

$$
\begin{aligned}
&a_{j,\mathrm{gen}}\left(1+\frac{\epsilon^2}{2}\right)(1+j\omega)^2-\frac{3x_0\epsilon^2\omega^2}{2}\partial_{x_0}a_{j,\mathrm{gen}}-\partial_{x_0}^2 a_{j,\mathrm{gen}}\left(\frac{x_0^2\epsilon^2\omega^2}{2}-\frac{1}{\kappa_{\mathrm{f}}^2}\right)\\
&+i\epsilon\Big[a_{j+1,\mathrm{gen}}(1+\omega(j+1))^2-a_{j-1,\mathrm{gen}}(1+\omega(j-1))^2\\
&\qquad+x_0\omega\left(\partial_{x_0}a_{j+1,\mathrm{gen}}\left(1+\omega\left(j+\frac{1}{2}\right)\right)+\partial_{x_0}a_{j-1,\mathrm{gen}}\left(1+\omega\left(j-\frac{1}{2}\right)\right)\right)\Big]\\
&-\frac{\epsilon^2}{4}\Big[a_{j-2,\mathrm{gen}}(1+\omega(j-2))^2+a_{j+2,\mathrm{gen}}(1+\omega(j+2))^2\\
&\qquad-2x_0\omega\left(\partial_{x_0}a_{j-2,\mathrm{gen}}\left(1+\omega\left(j-\frac{5}{2}\right)\right)-\partial_{x_0}a_{j+2,\mathrm{gen}}\left(1+\omega\left(j+\frac{5}{2}\right)\right)\right)\\
&\qquad+x_0^2\omega^2(\partial_{x_0}^2a_{j-2,\mathrm{gen}}+\partial_{x_0}^2a_{j+2,\mathrm{gen}})\Big]=0.
\end{aligned}
$$

Defining $\omega_j=1+j\omega$, this leads to the following coupled system of equations:

$$
\begin{aligned}
&\omega_j^2\left(1+\frac{\epsilon^2}{2}\right)a_{j,\mathrm{gen}}-\frac{3x_0\epsilon^2\omega^2}{2}\partial_{x_0}a_{j,\mathrm{gen}}-\left(\frac{x_0^2\epsilon^2\omega^2}{2}-\frac{1}{\kappa_{\mathrm{f}}^2}\right)\partial_{x_0x_0}a_{j,\mathrm{gen}}\\
&\quad+i\epsilon\left[\omega_{j+1}^2a_{j+1,\mathrm{gen}}-\omega_{j-1}^2a_{j-1,\mathrm{gen}}+x_0\omega\left(\omega_{j+\frac{1}{2}}\partial_{x_0}a_{j+1,\mathrm{gen}}+\omega_{j-\frac{1}{2}}\partial_{x_0}a_{j-1,\mathrm{gen}}\right)\right]\\
&\quad-\frac{\epsilon^2}{4}\Big[\omega_{j-2}^2a_{j-2,\mathrm{gen}}+\omega_{j+2}^2a_{j+2,\mathrm{gen}}-2x_0\omega\left(\omega_{j-\frac{5}{2}}\partial_{x_0}a_{j-2,\mathrm{gen}}-\omega_{j+\frac{5}{2}}\partial_{x_0}a_{j+2,\mathrm{gen}}\right)\\
&\qquad+x_0^2\omega^2(\partial_{x_0x_0}a_{j-2,\mathrm{gen}}+\partial_{x_0x_0}a_{j+2,\mathrm{gen}})\Big]=0
\end{aligned}
\tag{2.35}
$$

for $j\in\mathcal{J}^+$, with the same boundary conditions as for system (2.31).

Remark 1. *From (2.35), different asymptotics could be analyzed, based on the dimensionless coefficients ϵ, ω, or even $\epsilon\omega$. In particular, the additional terms of* (2.35) *with respect to the small amplitude case* (2.31) *are factors of ω. Hence for high values of the emitted frequency ν_{f}, we have $\omega\ll 1$ and the difference between the models for large and small ϵ is negligible.*

As previously, in order to solve (2.35) numerically by means of the finite element method, we consider the associated weak formulation, which writes: find $a_{j,\mathrm{gen}}\in H^1_{\frac{A}{2i},0}(\Omega_0)$ such that

$$
\begin{aligned}
&\int_{\Omega_0}\left[\left(\frac{\epsilon^2\omega^2x_0^2}{2}-\frac{1}{\kappa_{\rm f}^2}\right)\partial_{x_0}a_{j,\rm gen}\partial_{x_0}\phi+\frac{\epsilon^2x_0\omega^2}{4}\left(\partial_{x_0}a_{j+2,\rm gen}+\partial_{x_0}a_{j-2,\rm gen}\right)\partial_{x_0}\phi\right]dx_0\\
&-\int_{\Omega_0}\frac{\epsilon x_0\omega}{2}\Big[\epsilon\omega\partial_{x_0}a_{j,\rm gen}\phi-2i\left(\omega_{j+\frac{1}{2}}\partial_{x_0}a_{j+1,\rm gen}+\omega_{j-\frac{1}{2}}\partial_{x_0}a_{j-1,\rm gen}\right)\phi\\
&\qquad+\epsilon\left(\omega_{j+\frac{3}{2}}\partial_{x_0}a_{j+2,\rm gen}-\omega_{j-\frac{3}{2}}\partial_{x_0}a_{j-2,\rm gen}\right)\phi\Big]dx_0 \qquad (2.36)\\
&+\int_{\Omega_0}\Bigg[\omega_j^2\left(1+\frac{\epsilon^2}{2}\right)a_{j,\rm gen}\phi+i\epsilon\left(\omega_{j+1}^2a_{j+1,\rm gen}-\omega_{j-1}^2a_{j-1,\rm gen}\right)\phi\\
&\qquad-\frac{\epsilon^2}{4}\left(\omega_{j+2}^2a_{j+2,\rm gen}+\omega_{j-2}^2a_{j-2,\rm gen}\right)\phi\Bigg]dx_0=0
\end{aligned}
$$

holds for all test functions $\phi\in H^1_{0,0}(\Omega_0)$ and $j\in\mathcal{J}^+$. We then use the same covering $\Omega_{0,h}$ of Ω_0 and denote by $\widehat{w}^{\mathcal{J}^+}_{\rm gen,h}$ the solution of the discretization of the variational coupled system (2.36).

Before proceeding to extensive numerical tests that will illustrate our approach, we report in Figure 2.2 the amplitude spectrum of the numerical solution $\widehat{u}_{0,h}$ of (2.33) at a fixed space point $x_0=0.5$ ($L=1$), without moving boundary ($\epsilon=0$, in red, where (2.33) is equivalent to (2.1) and $\widehat{u}\equiv\widehat{u}_0$) and with moving boundary ($\epsilon=0.1$, in blue). Concretely, the solution $\widehat{u}_{0,h}$ is computed by solving (2.33) numerically (with a second-order finite difference scheme in time and linear finite elements in space), leading to $u_{0,h}$, and then applying the FFT. The physical parameters are $A=1$, $c_\infty=300$, $\nu_{\rm f}=360$ and $\nu_\ell=2$. The frequencies of the eigenmodes $\widehat{u}_{0,\nu_m}$ are $\nu_m=mc_\infty/2$ and correspond to the peaks of the red curve. For $\epsilon=0$, we observe that i) there is a main contribution for $\nu_{\rm f}=360$ associated to $\widehat{u}_{0,\nu_{\rm f}}$ and ii) we have some uniformly distributed contributions $\widehat{u}_{0,\nu_m}$. This is in line with what is stated in Proposition 2.1. In the case of the oscillating boundary ($\epsilon=0.1$), we see again some contributions related to $\nu_{\rm f}$ and ν_m but with some additional new excited modes, localized around these frequencies and spaced by ν_ℓ.

Because of the modulation induced by the periodic deformation of the target, it becomes very interesting to also have a time/frequency representation of the reference field $u_{0,h}$, i.e. its STFT. As mentioned in Chapter 1, this transform allows to identify the frequency and phase contents of local sections of the scattered signal as it changes over time, and then infer knowledge about the target deformation: its micro-Doppler signature. We report in Figure 2.3a the STFT of $u_{0,h}$, with the same physical settings. The obtained spectrogram is naturally to be linked with Figure 2.2 since it brings a complementary representation of the same structure. Indeed, the horizontal curves correspond respectively to the frequencies ν_m of the eigenmodes $\widehat{u}_{0,\nu_m}$ spaced by ν_ℓ, as well as to the frequency $\nu_{\rm f}$ of the forced mode. We note the rapid decay of the amplitude of these modes as moving away from $\pm\nu_{\rm f}$. Some of these modes (here about one over two) are of very low amplitudes (see Figure 2.2) and we do not distinguish them. To zoom on these modes, we represent the logarithm of this spectrogram in Figure 2.3c. The spectrogram translates at each time the frequency component of the signal. Hence, we can identify here the sinusoidal motion of the target thanks to its micro-Doppler signature given by the ν_ℓ-periodic oscillation of the curves

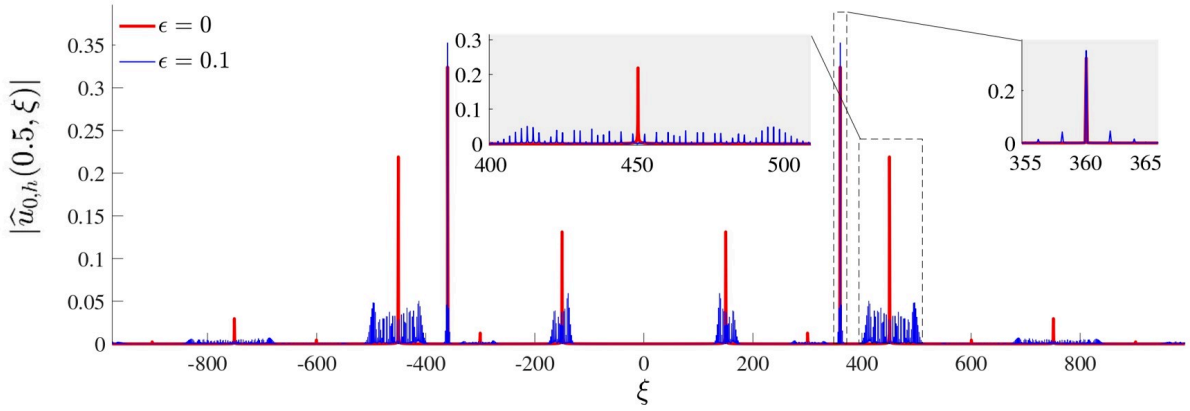

Figure 2.2: Frequency spectrum $|\widehat{u}_{0,h}(0.5,\xi)|$ without ($\epsilon = 0$, in red) and with boundary motion ($\epsilon = 0.1$, in blue). This illustrates both the assumption on the decomposition (2.18) of v and the ansatz (2.30).

corresponding to the different modes. Especially, we identify in Figure 2.3a the value $\nu_\ell = 2$. The amplitudes of these oscillations are directly related to the bandwidths of the modulations of the corresponding modes, and mainly depend on the value of ϵ as illustrated in Figure 2.6. Since the frequency shift depends on the velocity of the motion, the phase shift of $\pi/2$ observable at $t = 0$ (see zoom of Figure 2.3c) is well in agreement with the initial condition (2.4). Indeed, the target is parameterized by a sine motion which means that ℓ increases from $t = 0$ to $1/(4\nu_\ell) = 1/8$ (i.e. the target moves away from the source). This results in a negative Doppler frequency. When $t = 1/(4\nu_\ell)$, the velocity of the motion vanishes, as well as the Doppler frequency, which implies that the STFT curves cross their equilibrium positions. For $t \in [1/(4\nu_\ell), 3/(4\nu_\ell)]$, the target is getting closer and the Doppler frequency is positive. In particular, from $1/(4\nu_\ell)$ to $1/(2\nu_\ell)$, the target is accelerating and the Doppler frequency is increasing, whereas from $1/(2\nu_\ell)$ to $3/(2\nu_\ell)$ it decelerates and the Doppler frequency is decreasing, and so forth.

Let us recall that the contributions u_{0,ν_m}, $m \in \mathbb{N}$, are not significant in practice since usually the domain involves some open boundary parts and some dissipation effects. Here, since we have a Dirichlet boundary condition, we assume that ν_f is not close to an eigenfrequency ν_m. Therefore, the restriction of $\widehat{u}_{0,h}$ to $\mathcal{I}$ denoted by $\widehat{u}^{\mathcal{I}}_{0,h}$ is expected to provide a relatively accurate approximation of $\widehat{u}_{0,\nu_\mathrm{f}}$. To motivate this claim, we first report on Figure 2.3b the STFT of the restriction $u^{\mathcal{I}}_{0,h}$ of $u_{0,h}$, following the same methodology. As expected, this representation only contains the contribution from the forced mode which also appears in Figure 2.3a, showing the same periodicity and amplitudes. Accordingly to the thick bandwidth around ν_f in Figure 2.2, the amplitude of the oscillation in the spectrogram is smaller than the frequency resolution. We also report on Figure 2.4a the comparison between $u_{0,h}$ and $u^{\mathcal{I}}_{0,h}$ (defined as the inverse Fourier transform of $\widehat{u}^{\mathcal{I}}_{0,h}$) at $x_0 = 0.5$, computed by means of iFFT. We observe that the phases of the two functions are in agreement and the envelope of the signal is well reproduced, with same frequency $\nu_\ell = 2$. The difference between the signals is a consequence of the boundary movement.

Now, we introduce a second approximation which consists in validating the computation of $\widehat{u}^{\mathcal{I}}_0$ by the approximation $w^{\mathcal{J}}_{\mathrm{gen}}$. Concretely, $w^{\mathcal{J}}_{\mathrm{gen}}$ is evaluated using (2.28) after numerically solving

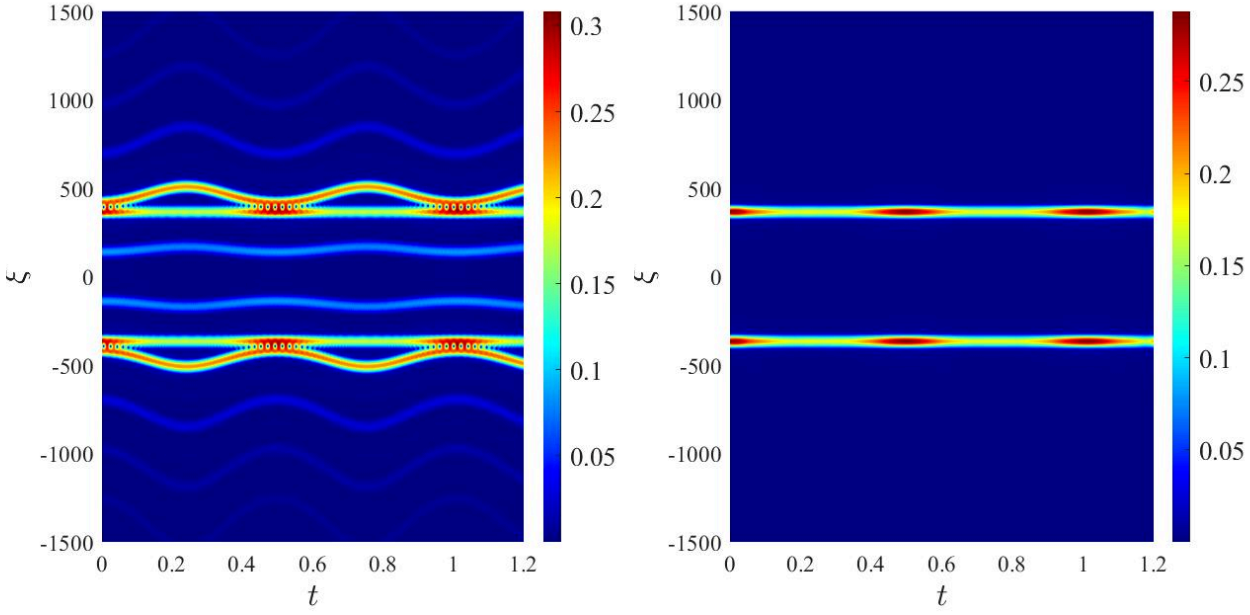

(a) $|\mathrm{STFT}(u_{0,h}(0.5,t))|$.

(b) $|\mathrm{STFT}(u^{\mathcal{I}}_{0,h}(0.5,t))|$.

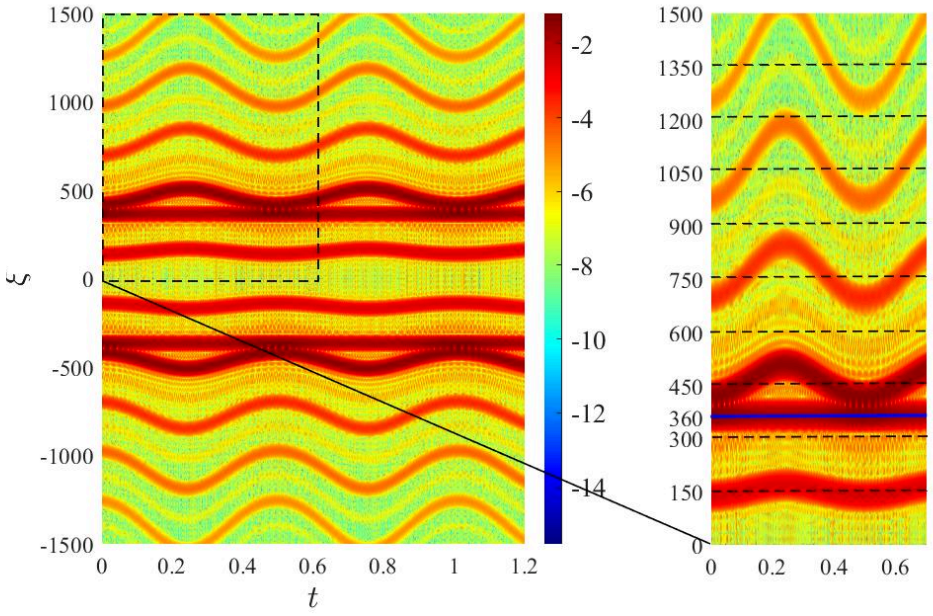

(c) $\log(|\mathrm{STFT}(u_{0,h}(0.5,t))|)$.

Figure 2.3: Spectrograms $|\mathrm{STFT}(u_{0,h}(0.5,t))|$, $|\mathrm{STFT}(u^{\mathcal{I}}_{0,h}(0.5,t))|$ and $\log(|\mathrm{STFT}(u_{0,h}(0.5,t))|)$ for $t \in]0, 1.2[$ and $\xi \in [-1500, 1500]$. The physical parameters are $\nu_{\mathrm{f}} = 360$, $\nu_{\ell} = 2$, $c_{\infty} = 300$ and $\epsilon = 0.1$.

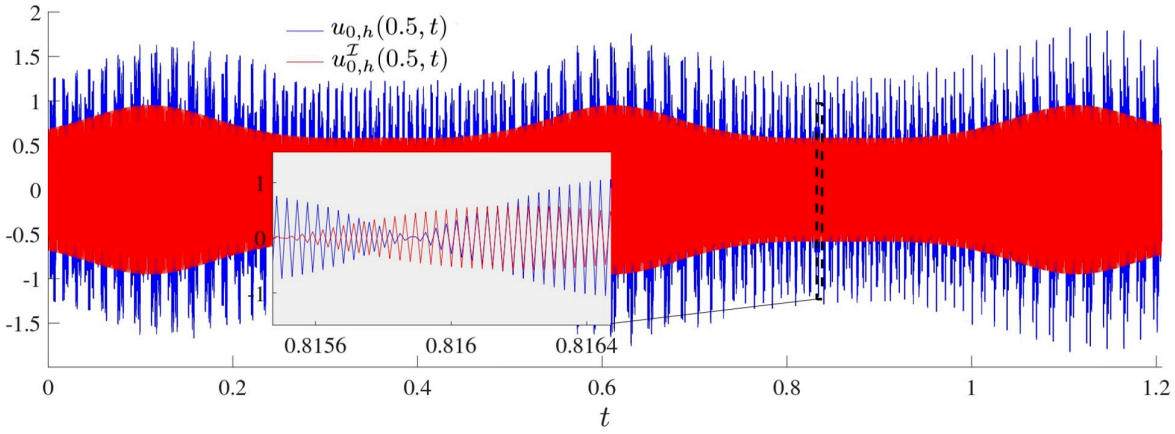

(a) $u_{0,h}(0.5,t)$ vs. t (blue) and $u^{\mathcal{I}}_{0,h}(0.5,t)$ vs. t (red).

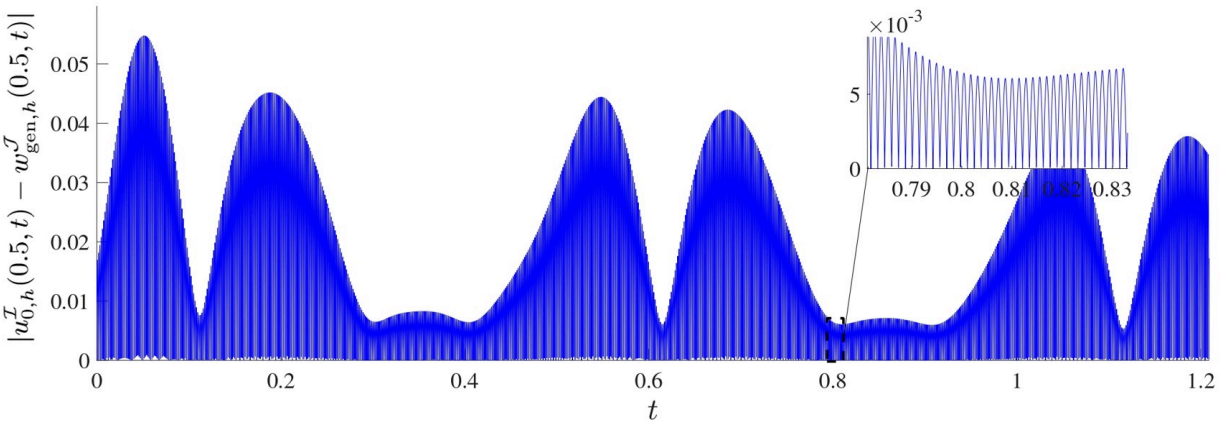

(b) $|u^{\mathcal{I}}_{0,h}(0.5,t) - w^{\mathcal{J}}_{\mathrm{gen},h}(0.5,t)|$ vs. t.

Figure 2.4: On the top figure, time signals $u_{0,h}(0.5,t)$ in blue and $u^{\mathcal{I}}_{0,h}(0.5,t)$ in red. On the bottom figure, the absolute difference between $u^{\mathcal{I}}_{0,h}(0.5,t)$ and $w^{\mathcal{J}}_{\mathrm{gen},h}(0.5,t)]$, vs. t. The physical parameters are $\nu_{\mathrm{f}} = 360$, $\nu_{\ell} = 2$, $c_{\infty} = 300$ and $\epsilon = 0.1$.

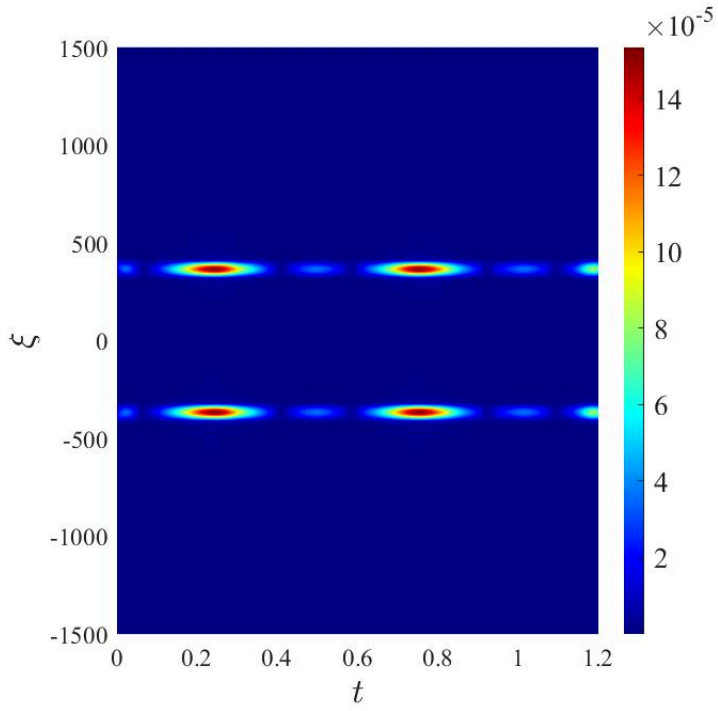

Figure 2.5: Absolute difference $|\mathrm{STFT}(u^{\mathcal{I}}_{0,h}(0.5,t)) - \mathrm{STFT}(w^{\mathcal{J}}_{\mathrm{gen},h}(0.5,t))|$. The physical parameters are $\nu_{\mathrm{f}} = 360$, $\nu_\ell = 2$, $c_\infty = 300$ and $\epsilon = 0.1$.

(2.36). To this end, we report in Fig. 2.4b the absolute error $|u^{\mathcal{I}}_{0,h}(0.5,t) - w^{\mathcal{J}}_{\mathrm{gen},h}(0.5,t)|$ for the same configuration. We observe a good agreement between the solutions, which confirms that the expected ansatz (2.30) is valid for $w^{\mathcal{J}}_{\mathrm{gen}}$. For completeness, we also report in Figure 2.5 the absolute difference $|\mathrm{STFT}(u^{\mathcal{I}}_{0,h}(0.5,t)) - \mathrm{STFT}(w^{\mathcal{J}}_{\mathrm{gen},h}(0.5,t))|$. This confirms the validity of our second approximation.

The values of J_1 and J_2 that define the interval $\mathcal{J}$ can be justified *a posteriori* by energy or numerical criteria but their *a priori* determination remains an open question. However, we discuss in Chapter 3 a first approach to answer it. In the case of a general boundary motion, the choice of J_1 and J_2 is also related to the frequency of the input signal and the perturbation amplitude ϵ. Indeed, we observe that the coefficients $|a^{\pm}_{j,\mathrm{gen}}|$ decay slower for increasing $|j|$ as ϵ gets larger. Consequently, the values of $-J_1$ and J_2 used to truncate (2.35) have to be increased, as expected. We illustrate this property in Figure 2.6 where we report the amplitude of $\widehat{u}_h(0.5,\xi)$ computed by the brute force method, for $\nu_{\mathrm{f}} = 3250$ and $c_\infty = 1280$. The values of ϵ vary from 0.01 to 0.1.

The computation of $\widehat{w}^{\mathcal{J}^+}_{\mathrm{gen},h}$ (and by extension of $\widehat{w}^{\mathcal{J}}_{\mathrm{gen},h}$) provides an accurate approximation of $\widehat{u}_{0,h}$ in the fixed domain Ω_0. Then, recovering the real field over Ω_t requires to transpose $\widehat{w}^{\mathcal{J}^+}_{\mathrm{gen},h}$ to the time domain, which is straightforward using (2.28). Finally, it remains to apply the reverse change of variable given by

$$x_0 = \frac{xL}{\ell(t)}.$$

In Chapter 3, we extend the definition of the change of metric in order to shortcut this step and

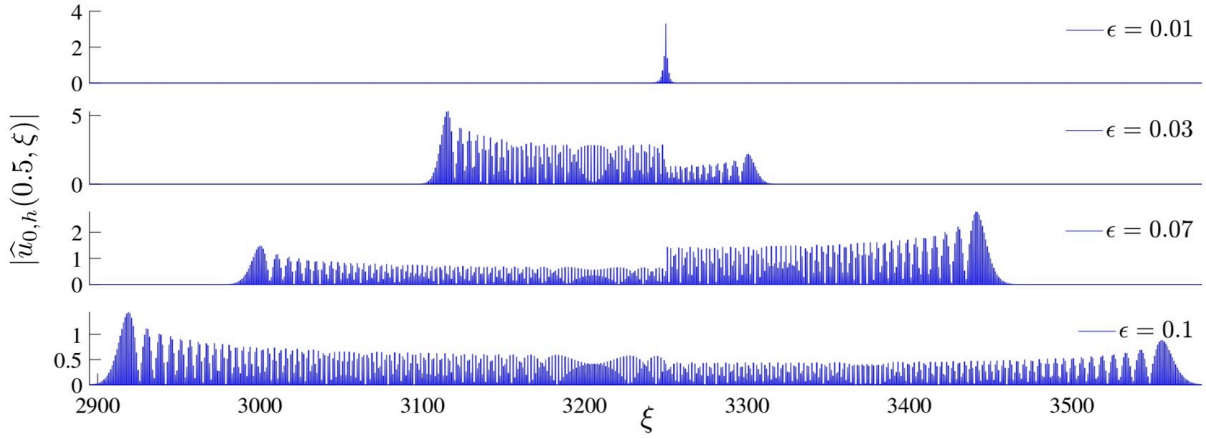

Figure 2.6: Increasing the amplitude ϵ of the sinusoidal perturbation (2.15) leads to the excitation of a larger frequency band in the solution $|\widehat{u}_{0,h}(0.5,\xi)|$, with $\nu_{\rm f} = 3250$, $c_\infty = 1280$, and $\nu_\ell = 1$.

immediately provide the real domain solution over a predefined area of the moving domain Ω_t.

2.3 Numerical implementation of the method

In the following, the amplitude of emission is set to $A = 1$, and the values of J_1 and J_2 (and thus the definition of $\mathcal{J}$ and $\mathcal{I}$, see (2.26)) are *a priori* selected relatively to the reference solution $\widehat{u}_0$ by the criterion

$$\max_{j\in\mathbb{Z}\setminus\mathcal{J}} \|\widehat{u}_{0,h}(\cdot,\nu_{\rm f}+j\nu_\ell)\|_{\infty,\Omega_{0,h}} \leq 10^{-3} \times \|\widehat{u}_{0,h}(\cdot,\nu_{\rm f})\|_{\infty,\Omega_{0,h}} \tag{2.37}$$

in such a way that $\sharp\mathcal{J}^+$ is minimized. This assumption ensures that $\widehat{u}_{0,h}^{\mathcal{I}^+}$ is restricted to the significant components of $\widehat{u}_{0,\nu_{\rm f},h}$ around $\nu_{\rm f}$, with a normalized amplitude less than 10^{-3}. Here, we set $\|f\|_{\infty,\Omega_{0,h}} = \max_{x_0\in\Omega_{0,h}} |f(x_0)|$.

2.3.1 Convergence of the frequency-domain solution $\widehat{w}_{{\rm gen},h}^{\mathcal{J}^+}$

The computational cost of the proposed frequency domain method depends on the size $\sharp\mathcal{J}^+$ of the system that we have to solve and on the number of finite elements $n_{\Omega_0} = L/h$. The corresponding algorithm requires the solution of a linear system with a sparse block pentadiagonal matrix of size $n_{\Omega_0}\sharp\mathcal{J}^+$, with tridiagonal blocks. On the other hand the brute force method used to compute the reference solution $\widehat{u}_{0,h}^{\mathcal{I}^+}$ is based on the resolution of (2.33) with a $\mathbb{P}^1$ finite element method in space and a second-order Crank-Nicolson time scheme which requires the solution of n_t tridiagonal linear systems of size n_{Ω_0}. This is followed by the computation of n_{Ω_0} FFTs of size n_t, and the truncation of $\widehat{u}_{0,h}$ to $\widehat{u}_{0,h}^{\mathcal{I}^+}$.

In order to assess the accuracy of the method, we compare the numerical solutions $\widehat{w}_{{\rm gen},h}^{\mathcal{J}^+}$ and $\widehat{u}_{0,h}^{\mathcal{I}^+}$ in different physical settings. To this end, we first define the pointwise error between the

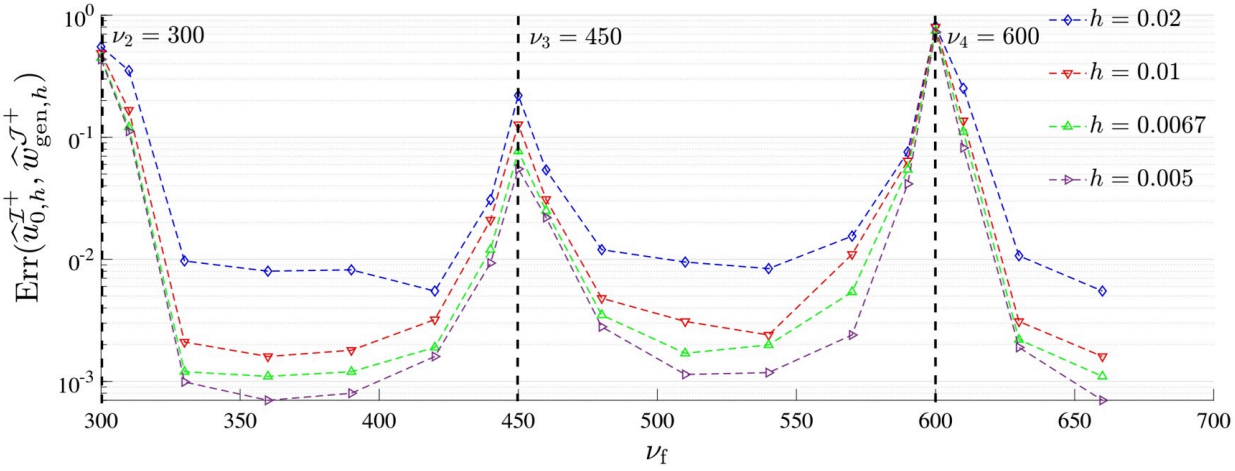

(a) $\mathrm{Err}(\widehat{u}^{\mathcal{I}^+}_{0,h}, \widehat{w}^{\mathcal{J}^+}_{\mathrm{gen},h})$ vs. ν_f for decreasing h.

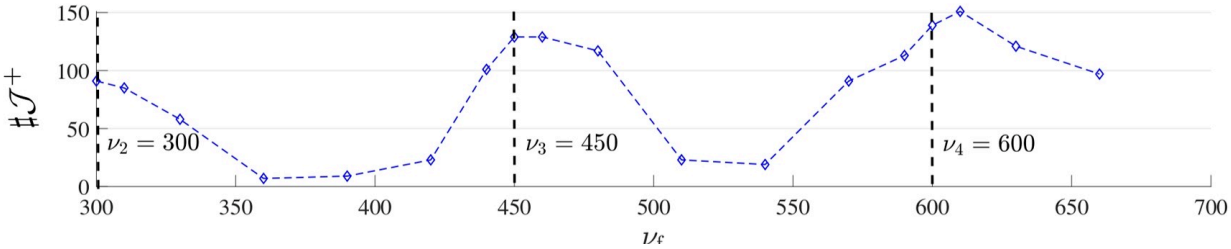

(b) $\sharp\mathcal{J}^+$ vs. ν_f.

Figure 2.7: Top: Error $\mathrm{Err}(\widehat{u}^{\mathcal{I}^+}_{0,h}, \widehat{w}^{\mathcal{J}^+}_{\mathrm{gen},h})$ depending on ν_f for increasing refinement h. Bottom: cardinal $\sharp\mathcal{J}^+$ vs. ν_f. The vertical dashed lines correspond to the eigenfrequencies $\nu_m = mc_\infty/2$ (since $L = 1$) of the spatial domain without boundary motion.

Fourier spectra $|\widehat{u}^{\mathcal{I}^+}_{0,h}|$ and $|\widehat{w}^{\mathcal{J}^+}_{\mathrm{gen},h}|$

$$\mathrm{err}(\widehat{u}^{\mathcal{I}^+}_{0,h}, \widehat{w}^{\mathcal{J}^+}_{\mathrm{gen},h}, x_0) := \frac{\big\| |\widehat{u}^{\mathcal{I}^+}_{0,h}(x_0,\cdot)| - |\widehat{w}^{\mathcal{J}^+}_{\mathrm{gen},h}(x_0,\cdot)| \big\|_{1,\mathcal{I}^+}}{\|\widehat{u}^{\mathcal{I}^+}_{0,h}(x_0,\cdot)\|_{1,\mathcal{I}^+}} \tag{2.38}$$

where $\|f\|_{1,\mathcal{I}^+} = \sum_{\xi\in\mathcal{I}^+} |f(\xi)|$.

Thanks to the non-homogeneous left boundary condition for the space-time problem (2.14), the denominator $\|\widehat{u}^{\mathcal{I}^+}_{0,h}(x_0,\cdot)\|_{1,\mathcal{I}^+}$ of (2.38) never vanishes for $x_0 \in \Omega_{0,h}$. Next, we define the overall error on the computational domain as

$$\mathrm{Err}(\widehat{u}^{\mathcal{I}^+}_{0,h}, \widehat{w}^{\mathcal{J}^+}_{\mathrm{gen},h}) := \frac{1}{L}\int_{\Omega_{0,h}} \mathrm{err}(\widehat{u}^{\mathcal{I}^+}_{0,h}, \widehat{w}^{\mathcal{J}^+}_{\mathrm{gen},h}, x_0)dx_0. \tag{2.39}$$

Figure 2.7a reports $\mathrm{Err}(\widehat{u}^{\mathcal{I}^+}_{0,h}, \widehat{w}^{\mathcal{J}^+}_{\mathrm{gen},h})$ with respect to the increasing source frequency ν_f, for different values of h. The time-domain solution $\widehat{u}^{\mathcal{I}^+}_{0,h}$ was computed on the same spatial grid

as $\widehat{w}^{\mathcal{J}^+}_{\mathrm{gen},h}$, with time discretization parameters adapted to reach the numerical convergence. In complement, we show in Figure 2.7b the size of $\mathcal{J}^+$ used to evaluate $\widehat{w}^{\mathcal{J}^+}_{\mathrm{gen},h}$ vs. ν_{f}, with $c_\infty = 300$, $\nu_\ell = 1$ and $\epsilon = 0.1$.

We observe that $\widehat{w}^{\mathcal{J}^+}_{\mathrm{gen},h}$ provides a more accurate approximation of $\widehat{u}^{\mathcal{I}^+}_{0,h}$ when the source frequency ν_{f} is not close to an eigenfrequency ν_m of the system. Otherwise, the nearest eigenmode $\widehat{u}_{0,\nu_m}$ shares components of non negligible amplitude with $\widehat{u}_{0,\nu_{\mathrm{f}}}$, which makes the error increase. This sketches validity regions for the presented method, which correspond to the assumptions made in Section 2.2.3. Moreover, Figure 2.7b illustrates that $\sharp\mathcal{J}^+$ might stay relatively small on some regions of ξ between the eigenfrequencies. In fact, the explicit determination of these precise regions is related to the *a priori* determination of $\sharp\mathcal{J}^+$ and remains an open question.

However, it is very interesting to notice that, for particular values of the ratio $\kappa_{\mathrm{f}} = 2\pi\nu_{\mathrm{f}}/c_\infty$, the minimal size $\sharp\mathcal{J}^+$ can remain small even for very large values of ν_{f}. For example, Figure 2.8 reports the spectrum $|\widehat{w}^{\mathcal{J}^+}_{\mathrm{gen},h}|$ for $\nu_{\mathrm{f}} = 3.2 \times 10^9$ and $c_\infty = 3 \times 10^8$, i.e. for a realistic radar application. In this case, 11 frequency components suffice for an accurate calculation of the solution.

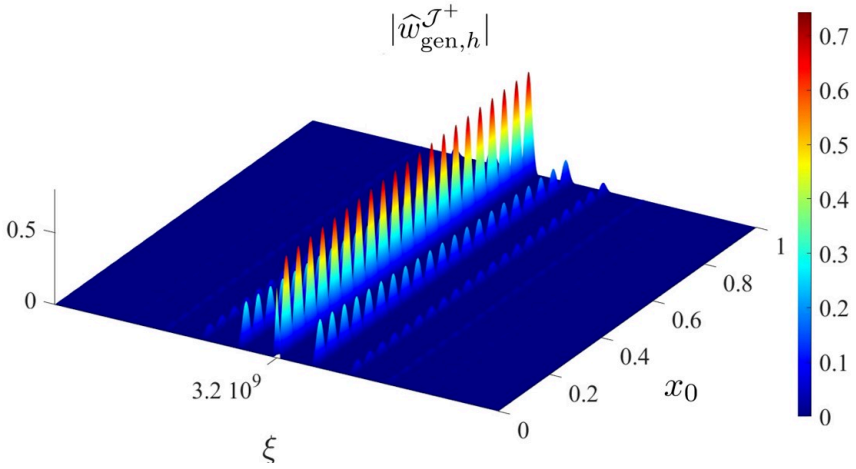

Figure 2.8: Evaluation of $|\widehat{w}^{\mathcal{J}^+}_{\mathrm{gen},h}|$ for a high frequency source, with $\nu_{\mathrm{f}} = 3.2 \times 10^9$ and $c_\infty = 3 \times 10^8$. The number of bumps along the space variable directly depends on the value of the wavenumber $\kappa_{\mathrm{f}} = 2\pi\nu_{\mathrm{f}}/c_\infty$. We use $\sharp\mathcal{J}^+ = 11$, $\epsilon = 0.01$, $\nu_\ell = 1$ and $h = 0.001$.

2.3.2 Influence of the number of frequency components $\sharp\mathcal{J}^+$

Similarly to (2.39), we report on Figure 2.9a the error $\mathrm{Err}(\widehat{u}^{\mathcal{I}^+}_{0,h}, \widehat{w}^{\mathcal{J}_1^+}_{\mathrm{gen},h})$ for different sizes $\sharp\mathcal{J}_1^+$ of the test interval $\mathcal{J}_1^+$. The reference interval $\mathcal{J}^+$ is fixed with cardinal $\sharp\mathcal{J}^+ = 111$. In addition, Figure 2.9b gives the error between $\widehat{w}^{\mathcal{J}^+}_{\mathrm{gen},h}$ and $\widehat{w}^{\mathcal{J}_1^+}_{\mathrm{gen},h}$ for $\sharp\mathcal{J}_1^+ > 111$. The parameters are $h = 0.01$, $c_\infty = 300$, $\nu_{\mathrm{f}} = 500$, $\nu_\ell = 1$ and $\epsilon = 0.1$.

The fast decay of the error is in accordance with the notion of minimal truncation interval $\sharp\mathcal{J}^+$, and $\mathrm{Err}(\widehat{u}^{\mathcal{I}^+}_{0,h}, \widehat{w}^{\mathcal{J}_1^+}_{\mathrm{gen},h})$ settles down about 3.5×10^{-3} for $\sharp\mathcal{J}_1^+ \geq 111$. In particular, for $\sharp\mathcal{J}_1^+ \geq 111$, the triangular inequality entails that

$$\mathrm{Err}(\widehat{u}^{\mathcal{I}^+}_{0,h}, \widehat{w}^{\mathcal{J}_1^+}_{\mathrm{gen},h}) \leq \mathrm{Err}(\widehat{u}^{\mathcal{I}^+}_{0,h}, \widehat{w}^{\mathcal{J}^+}_{\mathrm{gen},h}) + \mathrm{Err}(\widehat{w}^{\mathcal{J}^+}_{\mathrm{gen},h}, \widehat{w}^{\mathcal{J}_1^+}_{\mathrm{gen},h}) \approx 3.5 \times 10^{-3} + \mathrm{Err}(\widehat{w}^{\mathcal{J}^+}_{\mathrm{gen},h}, \widehat{w}^{\mathcal{J}_1^+}_{\mathrm{gen},h}),$$

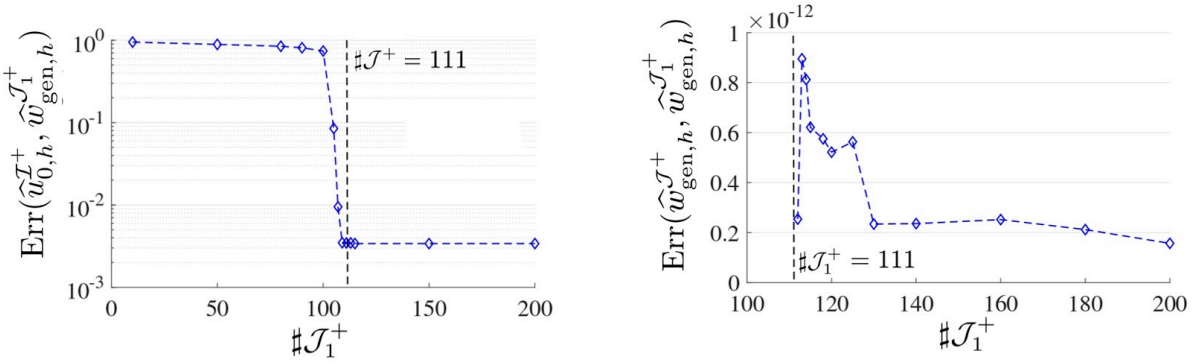

(a) $\mathrm{Err}(\widehat{u}^{\mathcal{I}^+}_{0,h}, \widehat{w}^{\mathcal{I}^+_1}_{\mathrm{gen},h})$ vs. $\sharp\mathcal{I}^+_1$

(b) $\mathrm{Err}(\widehat{w}^{\mathcal{I}^+}_{\mathrm{gen},h}, \widehat{w}^{\mathcal{I}^+_1}_{\mathrm{gen},h})$ vs. $\sharp\mathcal{I}^+_1$

Figure 2.9: Left: error $\mathrm{Err}(\widehat{u}^{\mathcal{I}^+}_{0,h}, \widehat{w}^{\mathcal{I}^+_1}_{\mathrm{gen},h})$ depending on $\sharp\mathcal{I}^+_1$. Right: $\mathrm{Err}(\widehat{w}^{\mathcal{I}^+}_{\mathrm{gen},h}, \widehat{w}^{\mathcal{I}^+_1}_{\mathrm{gen},h})$ depending on $\sharp\mathcal{I}^+_1$. The dashed line corresponds to the fixed value $\sharp\mathcal{I}^+ = 111$. The parameters are $h = 0.01$, $c_\infty = 300$, $\nu_\mathrm{f} = 500$, $\nu_\ell = 1$ and $\epsilon = 0.1$.

and, as we observe in Figure 2.9b, this stabilization is of average amplitude 10^{-13}. This illustrates the fast convergence of $\widehat{w}^{\mathcal{I}^+}_{\mathrm{gen},h}$ with respect to the parameter $\sharp\mathcal{I}^+$. This result opens up the possibility to obtain a relevant estimation of $\mathcal{I}^+$, using iteratively the algorithm which computes $\widehat{w}^{\mathcal{I}^+}_{\mathrm{gen},h}$.

2.3.3 Validity of the small-amplitude approximation $\widehat{w}^{\mathcal{I}^+}_h$

To justify the range of validity of the proposed approximate solution $\widehat{w}^{\mathcal{I}^+}$, let us compare $|\widehat{w}^{\mathcal{I}^+}_h|$ to $|\widehat{w}^{\mathcal{I}^+}_{\mathrm{gen},h}|$. In order to define $\mathcal{I}^+$ for each physical configuration $\{c, \nu_\mathrm{f}, \nu_\ell, \epsilon\}$, we again use the criterion (2.37). Now, similarly to (2.39), we consider the error

$$\mathrm{Err}(\widehat{w}^{\mathcal{I}^+}_{\mathrm{gen},h}, \widehat{w}^{\mathcal{I}^+}_h) = \frac{1}{L}\int_{\Omega_{0,h}} \mathrm{err}(\widehat{w}^{\mathcal{I}^+}_{\mathrm{gen},h}, \widehat{w}^{\mathcal{I}^+}_h, x_0)dx_0.$$

In Figure 2.10, we report the error for increasing values of ϵ ranging from 0 to 0.2 and for ν_ℓ in $[0, 4]$. The other parameters are fixed to $\nu_\mathrm{f} = 360$ and $c_\infty = 300$. The spatial discretization step is $h = 0.01$.

As expected, increasing the boundary motion amplitude ϵ and the frequency ν_ℓ increases the relative difference between the two methods. Indeed, the dropped terms in (2.17) are becoming non negligible for relatively high magnitudes of ϵ, which leads to define a region of validity of the approximation $\widehat{w}^{\mathcal{I}^+}$ around small values of ϵ. In particular, the choice of $\epsilon = 0.1$ (1/10 of the size of the domain $L = 1$) ensures a relative difference of 10^{-3} between $\widehat{w}^{\mathcal{I}^+}_h$ and $\widehat{w}^{\mathcal{I}^+}_{\mathrm{gen},h}$.

In the following section, we provide a generalisation of the frequency domain method to more complicated boundary motions, while maintaining $\epsilon \ll 1$. This assumption, in accordance to the previous discussion and Figure 2.10, allows us to focus on developing the approximate numerical method $\widehat{w}^{\mathcal{I}^+}$ for small ϵ.

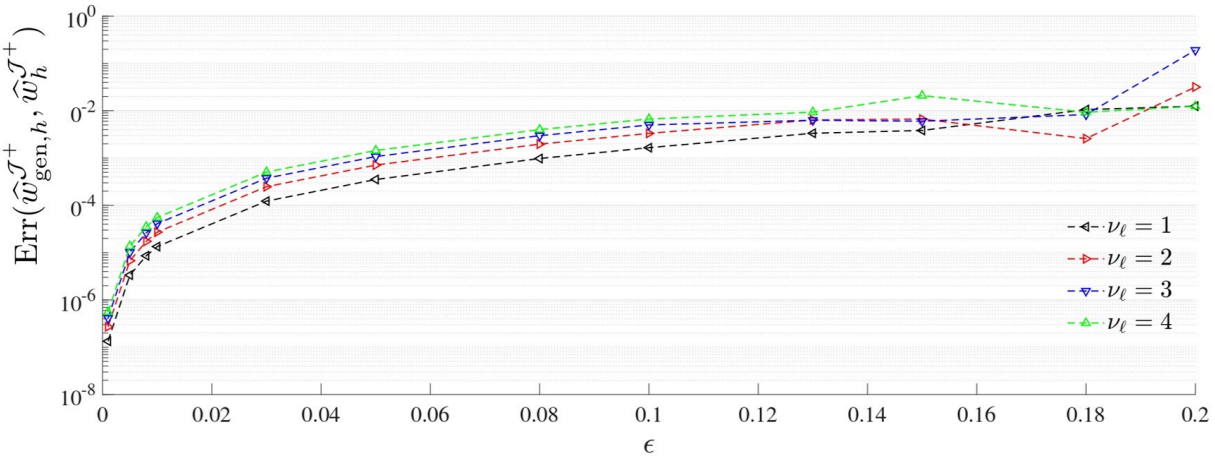

Figure 2.10: $\mathrm{Err}(\widehat{w}^{\mathcal{J}^+}_{\mathrm{gen},h}, \widehat{w}^{\mathcal{J}^+}_h)$ for increasing values of ϵ and ν_ℓ.

2.4 Scattering with general boundary motions

We introduce a generalisation of the previous approach to a motion $\ell(t)$ which has no *a priori* explicit expression. Let us denote by $u_0(x_0, t)$ the solution of (2.14). We assume that the velocity of the motion of the boundary is much smaller than the phase speed of the emitted waves. In addition, we limit the study to the case where, for fixed t, the change of variables $\Omega(t)$ to Ω_0 is linear in spatial coordinates. The motion ℓ is expected to be a $\mathcal{C}^\infty(\mathbb{R})$ periodic time-dependent function taking its values in the interval $[L - \epsilon L, L + \epsilon L]$. Let us denote by ν_ℓ the frequency of the motion.

Because ℓ never vanishes, Wiener $1/f$ theorem [76] for Fourier series entails that the application $x_0 : (x, t) \mapsto x_0(x, t)$ can be expanded as a time Fourier series around ν_ℓ. Then, by linearity of x in x_0 and due to the form of ℓ, such an expansion also holds for $(\partial_x x_0)^2$ and the corresponding time Fourier transform thus writes

$$\mathcal{F}\left(\partial_x x_0\right)^2 = \sum_{n\in\mathbb{Z}} c_n \delta_{n\nu_\ell}, \tag{2.40}$$

for some complex-valued coefficients c_n. Since ℓ is not necessarily explicitly given, the computation of the coefficients c_n of ℓ is based on the FFT in the time domain. Thanks to the linear of change of variable in x, the coefficients are constant in the spatial domain. Let us also notice that if the boundary motion is not periodic, the formulation of the Fourier transform is not a Dirac comb, which leads to a non-discrete system of equations. If it is almost-periodic in the sense of Bohr [11], a Fourier-type transform exists in the form $\sum_{n\in\mathbb{Z}} c_n \delta_{\lambda_n}$, with $c_n \in \mathbb{C}$ and $\lambda_n \in \mathbb{R}$. However, this expansion is based on the parameters λ_n which are not necessarily multiples of λ_0. We do not treat these cases here.

We now consider (2.16), which approximates (2.14) in the case of small amplitude perturbations, but with a general motion ℓ. The application of the Fourier transform on (2.16) yields

$$\frac{4\pi^2\xi^2}{c_\infty^2}\widehat{v} + \sum_{n\in\mathbb{Z}} c_n \delta_{n\nu_\ell} * \partial_{x_0}^2 \widehat{v} = 0, \tag{2.41}$$

with the boundary conditions $\widehat{v}(0,\xi)=0$ if $|\xi|\neq\nu_{\rm f}$, $\widehat{v}(0,\pm\nu_{\rm f})=\pm\frac{A}{2i}$, and $\widehat{v}(L,\xi)=0$ for all $\xi\in\mathbb{R}$. Since the boundary conditions are homogeneous with a harmonic source term, we assume that v admits a non-trivial expansion of the form (2.18). Then the arguments presented in Section 2.2 justify that we keep our focus on the component $\widehat{v}_{\nu_{\rm f}}$.

In the numerical simulations, the Fourier expansion (2.40) is truncated to $(2N+1)$ terms. Indeed, since ℓ is $\mathcal{C}^\infty(\mathbb{R})$ and never vanishes, the Fourier coefficients c_n are fastly decaying. We can therefore assume that the infinite sum (2.40) can be suitably truncated at order N as $\sum_{n=-N}^{N} c_n\delta_{n\nu_\ell}$, leading to the following approximate equation

$$\frac{4\pi^2\xi^2}{c_\infty^2}\widehat{v}+\sum_{n=-N}^{N} c_n\delta_{n\nu_\ell}*\partial_{x_0}^2\widehat{v}=0, \tag{2.42}$$

Moreover, since ℓ is periodic with fundamental frequency ν_ℓ, it is reasonable to search for an approximate solution $\widehat{w}_{\nu_{\rm f}}^{\mathcal{J}^+}$ of $\widehat{v}_{\nu_{\rm f}}$ under the form of the formal ansatz (2.30). Then, plugging the series expansion of $\widehat{w}_{\nu_{\rm f}}^{\mathcal{J}^+}$ and (2.40) truncated at order N into (2.41), and identifying the coefficients in front of the Dirac distributions leads to the following system of equations

$$\kappa_j^2 a_j+\sum_{n=-N}^{N} c_n\partial_{x_0}^2 a_{j-n}=0,\quad j\in\mathcal{J}^+, \tag{2.43}$$

where J_1 and J_2 have to be adequately chosen and $\kappa_j=(\omega_{\rm f}+j\omega_\ell)/c_\infty$. We have the boundary conditions: $a_0(0)=\frac{A}{2i}$, $a_j(0)=0$ for $j\neq 0$, $a_j(L)=0$ and $a_j(x_0)=0$ for $j\in\mathbb{Z}\setminus\mathcal{J}^+$.

As previously, to solve (2.43) by the finite element method, we use the weak formulation: find $a_j\in H^1_{\frac{A}{2i},0}(\Omega_0)$ such that, for all $j\in\mathcal{J}^+$,

$$\kappa_j^2\int_{\Omega_0} a_j\phi dx_0-\sum_{n=-N}^{N} c_n\int_{\Omega_0}\partial_{x_0}a_{j-n}\partial_{x_0}\phi dx_0=0, \tag{2.44}$$

holds for all test functions $\phi\in H^1_{0,0}(\Omega_0)$. The same covering $\Omega_{0,h}$ of Ω_0 is used. The notation $\widehat{w}_h^{\mathcal{J}^+}$ designates the solution of the discrete weak coupled system (2.44).

The case of a sine motion is already investigated in the previous sections. Let us consider the following square waves signal ℓ_{N_ℓ} that involves N_ℓ modes

$$\ell_{N_\ell}(t)=L\left(1-\frac{\epsilon\pi}{4}\sum_{k=0}^{N_\ell}\frac{\sin((2k+1)\omega_\ell t)}{2k+1}\right).$$

For the numerical simulations, the interval $\mathcal{J}^+$ is computed by using the previous criterion (2.37). For different values of $\epsilon\in[0.01,0.1]$, we report in Figure 2.11a the minimal cardinal $\sharp\mathcal{J}^+$ as a function of the number N_ℓ of modes in ℓ_{N_ℓ}. We keep the usual settings $A=1$, $c_\infty=300$, $\nu_{\rm f}=360$, $\nu_\ell=1$ and $h=0.01$. It is known that ℓ_{N_ℓ} is smooth for finite values of N_ℓ and converges to the square shaped signal $\ell_\infty(t)=L+4\,\mathrm{sign}(\sin(t))$ when $N_\ell\to+\infty$. As expected, the minimal cardinal $\sharp\mathcal{J}^+$ of the system (2.44) increases with both N_ℓ and ϵ. The error $\mathrm{Err}(\widehat{u}_{0,h}^{\mathcal{J}^+},\widehat{w}_h^{\mathcal{J}^+})$ between the solution $\widehat{w}_h^{\mathcal{J}^+}$ and the reference $\widehat{u}_{0,h}^{\mathcal{J}^+}$ is reported in Figure 2.11b for the same values of boundary

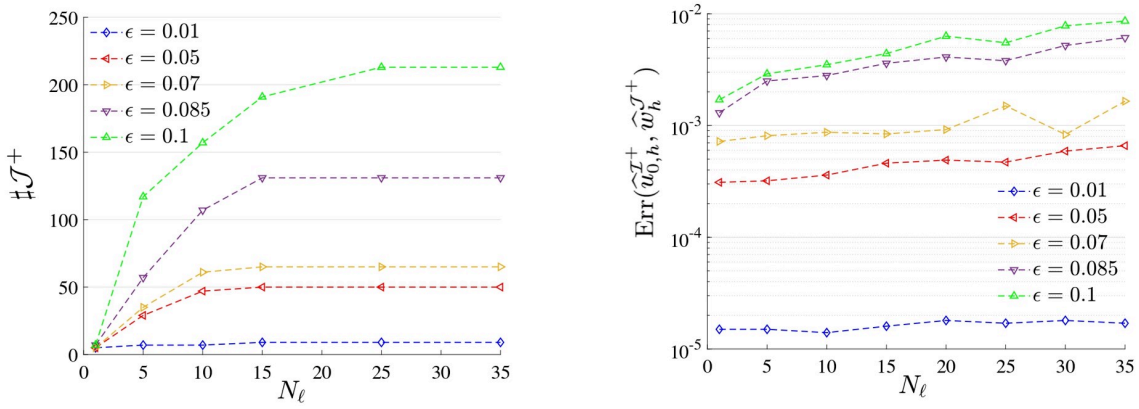

(a) $\sharp\mathcal{J}^+$ vs. N_ℓ.

(b) $\mathrm{Err}(\widehat{u}^{\mathcal{I}^+}_{0,h}, \widehat{w}^{\mathcal{J}^+}_h)$ vs. N_ℓ.

Figure 2.11: Left: $\sharp\mathcal{J}^+$ vs. N_ℓ. Right: error $\mathrm{Err}(\widehat{u}^{\mathcal{I}^+}_{0,h}, \widehat{w}^{\mathcal{J}^+}_h)$ vs. N_ℓ. The parameters are: $A = 1$, $c_\infty = 300$, $\nu_{\mathrm{f}} = 360$, and $\nu_\ell = 1$.

motion amplitudes as in Figure 2.11a. The multi-harmonic formulation exhibits stable convergence w.r.t. the number of boundary modes, the error level being simply related to the small amplitude approximation used to compute $\widehat{w}^{\mathcal{J}^+}_h$.

To illustrate the generalisation to arbitrary perturbations, let us also consider the perturbation signal $\ell^\wedge_{N_\ell}$ of order N_ℓ, which corresponds to the sawtooth waves signal

$$\ell^\wedge_{N_\ell} = L\left(1 + \frac{2\epsilon}{\pi}\sum_{k=1}^{N_\ell}(-1)^k\frac{\sin(k\omega_\ell t)}{k}\right).$$

We report in Figure 2.12a the amplitude $|\widehat{w}^{\mathcal{J}^+}_h|$ for the modulating signal ℓ_5, where we take $\sharp\mathcal{J}^+ = 31$, and in Figure 2.12b the spectrum of the field for $\ell^\wedge_5$ with $\sharp\mathcal{J}^+ = 43$. The perturbation amplitude is set to $\epsilon = 0.05$, and we fix $h = 0.001$.

The sawtooth signal is closer to a realistic breathing pattern in which inspiration is not necessarily symmetrical to expiration. These two cartographies highlight the complex frequency modulations arising from general perturbations.

2.5 Formal extension to higher dimensions

We now introduce a first natural extension of the approach developed for (2.1) to the space-time dimension $d+1$ (i.e. d in space and 1 in time). To this end, we assume that a wave is emitted by a source Ω^{s}, with boundary $\Gamma^{\mathrm{s}} = \partial\Omega^{\mathrm{s}}$, and is scattered by an obstacle $\Omega^{\mathrm{obst}}(t) = \Omega^{\mathrm{obst}}_t$ with smooth boundary $\Gamma(t) = \Gamma_t := \partial\Omega^{\mathrm{obst}}_t$, moving with frequency ν_ℓ around an equilibrium position $\Gamma_0 = \Gamma(0)$. We then define the d-dimensional domain of propagation, denoted by $\Omega^{\mathrm{ext}}_t = \Omega^{\mathrm{ext}}(t)$, as the exterior domain with boundaries Γ^{s} and Γ_t where $\Gamma^{\mathrm{s}} \cap \Gamma_t = \emptyset$ for all $t > 0$.

We remind the position vector $\mathbf{x} := (x_1, ..., x_d)^{\mathrm{T}} \in \Omega^{\mathrm{ext}}_t$ and the associated Laplace operator

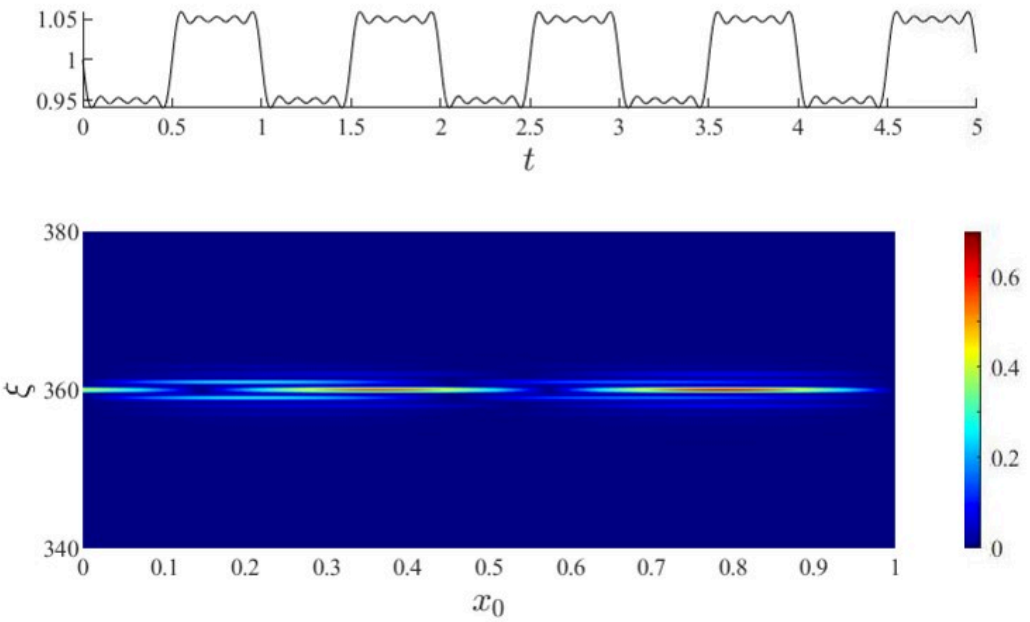

(a) $|\widehat{w}_h^{\mathcal{J}^+}|$ for ℓ_5.

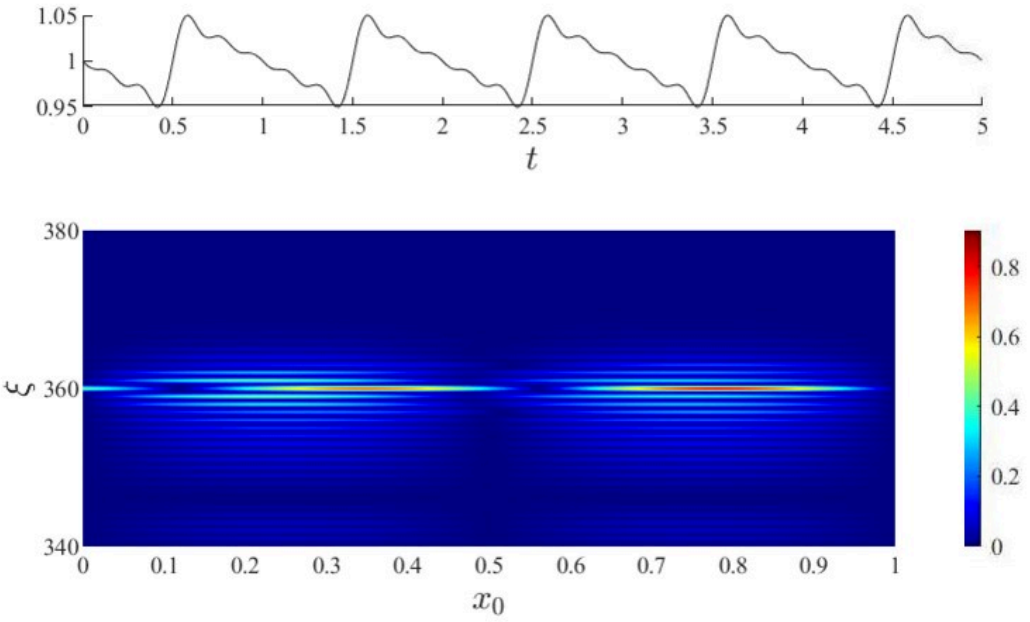

(b) $|\widehat{w}_h^{\mathcal{J}^+}|$ for $\ell_5^\wedge$.

Figure 2.12: Evaluation of $|\widehat{w}_h^{\mathcal{J}^+}|$ in $\Omega_{0,h}$ for the square shaped modulation signal in top, and for the sawtooth signal in bottom. The parameters are: $c_\infty = 300$, $\nu_\mathrm{f} = 360$, $\epsilon = 0.05$, $\nu_\ell = 1$ and $h = 0.001$.

$\Delta_{\mathbf{x}} := (\nabla_{\mathbf{x}})^2$. Then, we obtain the extension of (2.1) as

$$\partial_t^2 u - c_\infty^2 \Delta_{\mathbf{x}} u = 0 \tag{2.45}$$

with unknown total wave field $u(\mathbf{x}, t)$, for $\mathbf{x} \in \Omega_t^{\text{ext}}$ and $t \in \mathbb{R}_*^+$. The field is given on Γ^{s} by $u(\mathbf{x}, t)|_{\Gamma^{\text{s}}} = A \sin(\omega_{\text{f}} t)$. Since $\Omega^{\text{ext}}(t)$ is unbounded, the system does not have any eigenmodes and the energy of the system is concentrated around the source frequency ν_{f}. The initial conditions are $u(\mathbf{x}, 0) = 0$ and $\partial_t u(\mathbf{x}, 0) = 0$.

We first map Ω_t^{ext} to a fixed domain $\Omega_0^{\text{ext}} = \Omega^{\text{ext}}(t = 0)$ with fixed boundaries $\Gamma_0^{\text{s}} = \Gamma^{\text{s}}$ and $\Gamma_0 = \Gamma(0)$, by the change of space variable

$$\mathbf{x}_0 : (\mathbf{x}, t) \mapsto \mathbf{x}_0(\mathbf{x}, t) = (x_{01}, ..., x_{0d})^{\text{T}},$$

such that $\mathbf{x}_0(\Gamma_t, t) = \Gamma_0$ and $\mathbf{x}_0(\Gamma^{\text{s}}, t) = \Gamma_0^{\text{s}}$. Then we set: $u(\mathbf{x}, t) = u_0(\mathbf{x}_0, t)$ for $t \in \mathbb{R}_*^+$. For $\mathbf{X}_0 := (x_{01}, ..., x_{0d}, t)^{\text{T}} \in \Omega_0^{\text{ext}} \times \mathbb{R}_*^+$, let us define the gradient operators $\nabla_{\mathbf{X}_0} := (\partial_{x_{01}}, ..., \partial_{x_{0d}}, \partial_t)^{\text{T}}$ and $\nabla_{\mathbf{x}_0} := (\partial_{x_{01}}, ..., \partial_{x_{0d}})^{\text{T}}$. Then, we have $\partial_t u = \partial_t(u_0) = \partial_t \mathbf{X}_0 \cdot \nabla_{\mathbf{X}_0} u_0$, and

$$\begin{aligned} \partial_t^2 u &= \partial_t^2 \mathbf{X}_0 \cdot \nabla_{\mathbf{X}_0} u_0 + \partial_t \mathbf{X}_0 \cdot \partial_t(\nabla_{\mathbf{X}_0} u_0) \\ &= \partial_t^2 \mathbf{X}_0 \cdot \nabla_{\mathbf{X}_0} u_0 + \partial_t \mathbf{X}_0 \cdot \nabla_{\mathbf{X}_0} \partial_t(u_0) \\ &= \partial_t^2 \mathbf{X}_0 \cdot \nabla_{\mathbf{X}_0} u_0 + (\partial_t \mathbf{X}_0 \cdot \nabla_{\mathbf{X}_0})^2 u_0. \end{aligned} \tag{2.46}$$

Let us define the time dependent spatial Jacobian matrix of $(\mathbf{x}, t) \mapsto \mathbf{x}_0(\mathbf{x}, t)$ as $\mathbf{J}_t := [\partial_{x_j} x_{0i}]_{i,j \in \{1,...,d\}}$, and set $\nabla := \nabla_{\mathbf{x}_0}$ for conciseness. Then, since $\nabla_{\mathbf{x}} t = 0$, the spatial gradient and divergence write $\nabla_{\mathbf{x}} = \mathbf{J}_t^{\text{T}} \nabla$. It directly follows that:

$$\begin{aligned} \Delta_{\mathbf{x}} u &= \nabla_{\mathbf{x}} \cdot \nabla_{\mathbf{x}} u \\ &= \nabla_{\mathbf{x}} \cdot (\mathbf{J}_t^{\text{T}} \nabla u_0) \\ &= (\nabla_{\mathbf{x}} \cdot \mathbf{J}_t^{\text{T}}) \nabla u_0 + (\mathbf{J}_t^{\text{T}} \nabla)^2 u_0 \\ &= (\nabla_{\mathbf{x}} \cdot \mathbf{J}_t^{\text{T}}) \nabla u_0 + \nabla \cdot \mathbf{J}_t \mathbf{J}_t^{\text{T}} \nabla u_0, \end{aligned} \tag{2.47}$$

Hence, substituting (2.46) and (2.47) into (2.45) leads to the equation

$$\partial_t^2 \mathbf{X}_0 \cdot \nabla_{\mathbf{X}_0} u_0 + (\partial_t \mathbf{X}_0 \cdot \nabla_{\mathbf{X}_0})^2 u_0 - c_\infty^2 \left[(\nabla_{\mathbf{x}}^{\text{T}} \cdot \mathbf{J}_t^{\text{T}}) \nabla u_0 + \nabla \cdot \mathbf{J}_t \mathbf{J}_t^{\text{T}} \nabla u_0 \right] = 0. \tag{2.48}$$

As previously, if we choose x_{0i}, $i = 1, ..., d$ of first-order in x_i we get $\nabla_{\mathbf{x}} \cdot \mathbf{J}_t^{\text{T}} = 0$.

Remark 2. *The change of metric acts over the whole domain Ω_t. Hence if it is chosen linear, and unless considering particular symmetry or coordinate systems (see the vibrating disk in polar coordinates detailed in Section 3.2.2), the change of metric may not be compatible with keeping the contour Γ^{s} fixed with respect to the time coordinate. To address this issue, we choose in practice Γ^{s} sufficiently small and consider it fixed, i.e. $\Gamma^{\text{s}} \equiv \Gamma_0^{\text{s}}$. More general changes of metric are introduced in Chapter 3, in order to extend the method to complex geometries.*

If the amplitude of the movement is small and bounded by a small perturbation ϵ, we can neglect the $\mathcal{O}(\epsilon)$ terms and the function $\partial_t^2 u$ in (2.46) reduces to $\partial_t^2 u_0$. This leads to the following approximate equation for small amplitude boundary movements

$$\partial_t^2 v - c_\infty^2 \nabla \cdot \mathbf{J}_t \mathbf{J}_t^{\text{T}} \nabla v = 0, \tag{2.49}$$

which generalises (2.16). In addition, we keep the previous homogeneous boundary condition on Γ_0, the non-homogeneous boundary condition on Γ^{s}, i.e. $v(\mathbf{x}_0,t)|_{\Gamma^{\mathrm{s}}} = A\sin(\omega_{\mathrm{f}}t)$, and the initial conditions $v(\mathbf{x}_0,0) = 0$ and $\partial_t v(\mathbf{x}_0,0) = 0$. In practice, after discretization, we can choose a piecewise linear change of variable $\mathbf{x}_0$, defined on the same mesh as the finite element solution, which makes $\mathbf{J}_t$ only time dependent on each finite element.

The Fourier transform in time of (2.49) gives

$$4\pi^2\xi^2\widehat{v} + c_\infty^2\nabla\cdot(\mathcal{F}(\mathbf{J}_t\mathbf{J}_t^{\mathrm{T}}) * \nabla\widehat{v}) = 0. \tag{2.50}$$

Following (2.43), we consider the truncated Fourier series expansion of $\mathbf{J}_t\mathbf{J}_t^{\mathrm{T}}$

$$\mathcal{F}(\mathbf{J}_t\mathbf{J}_t^{\mathrm{T}})(\xi) = \sum_{n=-N}^{N}\mathbf{C}_n\delta_{n\nu_\ell}, \tag{2.51}$$

where $\mathbf{C}_n$ are some $d\times d$ complex-valued symmetric matrices. Proceeding as in Section 2.2.2, we obtain from (2.50) the following system of coupled Helmholtz-type equations in terms of the complex Fourier coefficients a_j, for $j\in\mathcal{J}^+$,

$$\kappa_j^2 a_j + \nabla\cdot\sum_{n=-N}^{N}\mathbf{C}_n\nabla a_{j-n} = 0, \tag{2.52}$$

with $\kappa_j = (\omega_{\mathrm{f}} + j\omega_\ell)/c_0$ and $a_j(x_0) = 0$ for $j\in\mathbb{Z}\setminus\mathcal{J}^+$. The boundary condition on Γ^{s} can be written as $a_0^+(\mathbf{x}_0) = \frac{A}{2i}$ and $a_j^+(\mathbf{x}_0) = 0$ for $j\neq 0$. We apply the homogeneous Dirichlet boundary condition $a_j^+(\mathbf{x}_0) = 0$ on Γ_0 for $j\in\mathcal{J}^+$.

To apply later a numerical method, e.g. the finite element method, we need to bound the exterior domain Ω_t^{ext}. To this end, we introduce a fictitious boundary Σ that delimits a finite computational domain Ω_t of Ω_t^{ext} with boundaries Σ, Γ^{s} and Γ_t. On this contour, we simply apply the Sommerfeld absorbing boundary condition

$$\partial_t u + c_\infty\partial_{\mathbf{n}}u = 0, \tag{2.53}$$

with the normal derivative $\partial_{\mathbf{n}}u := \mathbf{n}\cdot\nabla_{\mathbf{x}}u$, where $\mathbf{n}$ designates the exterior unit normal vector to Ω_t. We now introduce a fictitious boundary Σ that delimits a finite computational domain Ω_t with boundaries Σ, Γ^{s} and Γ_t. The deformation field $\mathbf{x}_0$ then maps Ω_t to the fixed domain $\Omega_0 = \Omega(0)$ with boundaries Σ_0, $\Gamma_0^{\mathrm{s}} = \Gamma^{\mathrm{s}}$ and Γ_0, and implies that the corresponding unit normal vector $\mathbf{n}_0$ to Σ_0 satisfies: $\mathbf{J}^{\mathrm{T}}\mathbf{n}_0 = \mathbf{n}$. Hence, considering the assumptions that lead to derive (2.49), we have the following equivalent absorbing boundary condition on Σ_0

$$\partial_t v + c_\infty\mathbf{n}_0\cdot\mathbf{J}\mathbf{J}^{\mathrm{T}}\nabla v = 0. \tag{2.54}$$

The time Fourier transform of (2.54) leads to

$$\frac{2i\pi\xi}{c_\infty}\widehat{v} + \mathbf{n}_0\cdot\mathcal{F}(\mathbf{J}\mathbf{J}^{\mathrm{T}}) * \nabla\widehat{v} = 0. \tag{2.55}$$

Plugging the Fourier series expansion (2.51) of $\mathbf{J}\mathbf{J}^{\mathrm{T}}(t)$ into (2.55), we obtain the following system of absorbing boundary conditions in terms of the complex Fourier coefficients a_j, associated with each single Helmholtz equation, for $j \in \mathcal{J}$:

$$i\kappa_j a_j + \mathbf{n}_0 \cdot \sum_{n=-N}^{N} \mathbf{C}_n \nabla a_{j-n} = 0, \tag{2.56}$$

with $\kappa_j = (\omega_{\mathrm{f}} + j\omega_\ell)/c_\infty$ and with $a_j(x_0) = 0$ for $j \in \mathbb{Z} \setminus \mathcal{J}^+$.

Remark 3. *We observe that Σ may also be deformed by the change of variable. Indeed, if Σ is chosen as the rectangular boundary depicted in Figure 3.1, a periodic translation of the obstacle boundary Γ_t shortens periodically the contour of Σ. This property appears in the coupled formulation* (2.56) *of the absorbing boundary condition.*

We now derive the weak formulation of (2.52): find $a_j \in H^1_{\frac{A}{2i},0}(\Omega_0) := \{a_j \in H^1(\Omega_0) \mid a_0(\mathbf{x}_0) = \frac{A}{2i}$ and $a_j(\mathbf{x}_0) = 0$, $j \neq 0$, on Γ^{s}, and $a_j(\mathbf{x}_0) = 0$ on $\Gamma_0\}$ with $a_j(x_0) = 0$ for $j \in \mathbb{Z} \setminus \mathcal{J}^+$ such that

$$\kappa_j^2 \int_{\Omega_0} a_j \phi d\Omega_0 - \int_{\Omega_0} \left(\sum_{n=-N}^{N} \mathbf{C}_n \nabla a_{j-n} \right) \cdot \nabla_{\mathbf{x}_0} \phi \, d\Omega_0 + \sum_{n=-N}^{N} \int_{\Sigma_0} \mathbf{n}_0 \cdot (\mathbf{C}_n \nabla a_{j-n}) \phi \, d\Sigma_0 = 0. \tag{2.57}$$

The boundary term in (2.57) is then replaced by the condition (2.56), leading to the following equation

$$\kappa_j^2 \int_{\Omega_0} a_j \phi d\Omega_0 - \int_{\Omega_0} \left(\sum_{n=-N}^{N} \mathbf{C}_n \nabla a_{j-n} \right) \cdot \nabla_{\mathbf{x}_0} \phi \, d\Omega_0 - i\kappa_j \int_{\Sigma_0} a_j^* \phi \, d\Sigma_0 = 0, \tag{2.58}$$

for all $\phi \in H^1_{0,0}(\Omega_0) := \{\phi \in H^1(\Omega_0) \mid \phi = 0$ on $\Gamma^{\mathrm{s}} \cup \Gamma_0\}$, where this definition of $H^1_{0,0}$ is a generalisation of the previous one in Section 2.2.2. We consider $\Omega_{0,h}$ as a covering of Ω_0 consisting of n_{Ω_0} triangular finite elements. For $j \in \mathcal{J}^+$, we denote by $a_{j,h}$ the linear finite element approximation of a_j.

We numerically illustrate the approach in the following two-dimensional ($d = 2$) model problem depicted in Figure 2.13.

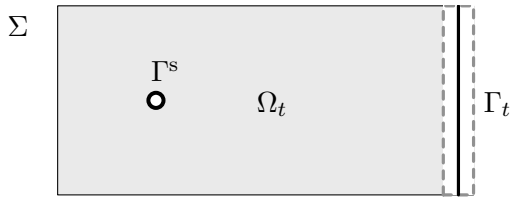

Figure 2.13: Example of a two-dimensional domain Ω_t with source boundary Γ_{s} and moving scatterer boundary $\Gamma(t)$.

The initial domain is the rectangle $]-1/3, \ell(t)[\times]-1/2, 1/2[$. The right side Γ_t of the rectangle moves according to the sine motion $\ell(t) = 1 + \epsilon \sin(2\pi\nu_\ell t)$. This first two-dimensional

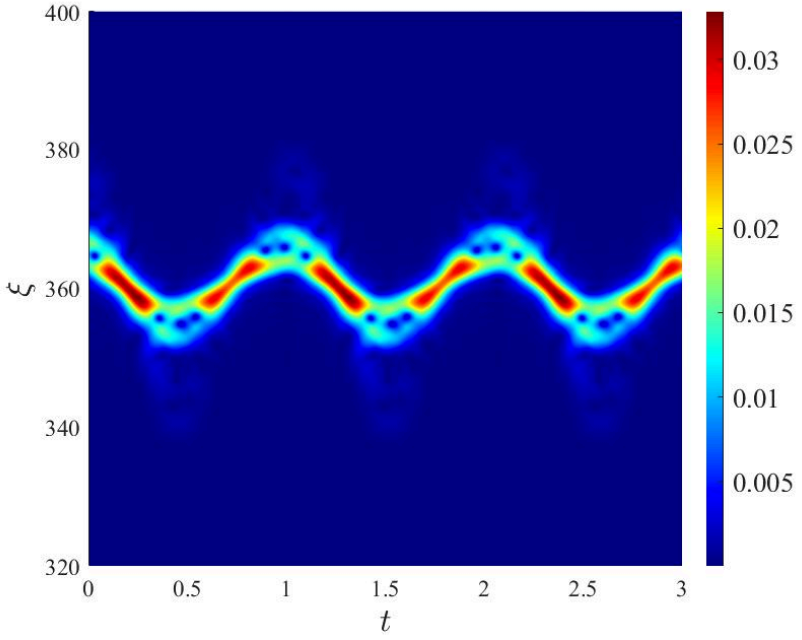

Figure 2.14: Spectrogram $|\mathrm{STFT}(w_h^{\mathcal{I}}(\mathbf{x}_0,t)|$ for $\mathbf{x}_0 = (0.5,0.5)^{\mathrm{T}}$, $t \in]0,3[$ and $\xi \in [320,400]$. The physical parameters are $\nu_{\mathrm{f}} = 360$, $\nu_\ell = 1$, $c_\infty = 300$ and $\epsilon = 0.1$

configuration is a straightforward extension of the one-dimensional problem, through longitudinal axial symmetry, and does not require further theoretical foundations. Of course, the treatment of more complex geometries needs the development of more sophisticated numerical approaches, as investigated in Chapters 3 and 4. We consider absorbing boundary conditions on the three remaining sides and a source Ω^{s} centered at $\{\mathbf{0}\}$ and modeled by a small extruded disk of boundary Γ^{s}. The change of variable constitutes an extension of the one-dimensional case (see Section 2.1.3), i.e. $\mathbf{x}_0(\mathbf{x},t) = (x_1/\ell(t), x_2)^{\mathrm{T}}$. The discretized domain $\Omega_{0,h}$ is a triangular mesh that consists of $n_{\Omega_0} = 640$ elements. As a comparison with the one-dimensional case (see Section 2.2.3), we plot in Figure 2.14 the spectrogram of $w_h^{\mathcal{I}}(\mathbf{x}_0,t)$ at $\mathbf{x}_0 = (0.5,0.5)^{\mathrm{T}}$, for the configuration $(\nu_{\mathrm{f}},\nu_\ell,c_\infty,\epsilon) = (360,1,300,0.1)$, $t \in]0,3[$ and $A = 1$. For clarity, the window has been centered around ν_{f}. Let us remark the absence of eigenmodes, as well as a significant modulation of the forced mode of frequency ν_{f}. The corresponding micro-Doppler signature allows us to identify the oscillation of the deformed boundary with a period $1/\nu_\ell = 1$.

This observation provides a first answer in dimension two to the initial problem presented in Section 1.1.1, namely the detection and identification of a motion associated with a breath from a fixed receiver.

For completeness we report in the Figures 2.15, 2.16 and 2.17 the amplitude of the four modes $|a_{0,h}(\mathbf{x}_0)|$, $|a_{1,h}(\mathbf{x}_0)|$, $|a_{2,h}(\mathbf{x}_0)|$ and $|a_{3,h}(\mathbf{x}_0)|$ of $\widehat{w}_h^{\mathcal{J}^+}(\mathbf{x}_0)$, for the configurations $(\nu_{\mathrm{f}},\nu_\ell,c_\infty,\epsilon) = (360,1,300,0)$, $(360,1,300,0.2)$ and $(3600,1,300,0.02)$, respectively. As expected, in the case without perturbation, i.e. $\epsilon = 0$ (see Figure 2.15), only the mode $|a_{0,h}(\mathbf{x}_0)|$ does not vanish, since there is no frequency modulation of the scattered wave.

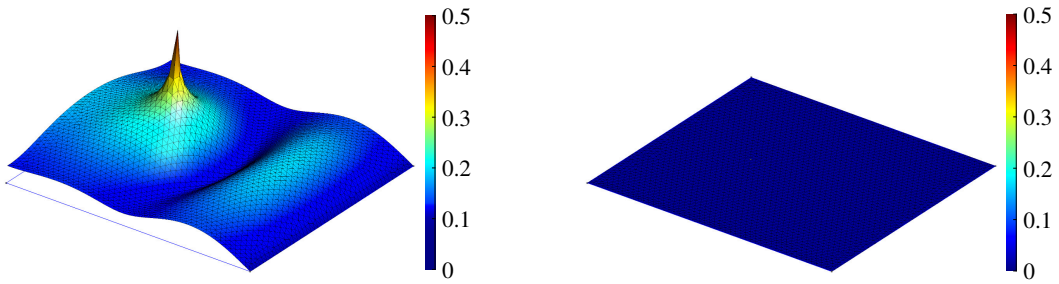

(a) $|a_{0,h}(\mathbf{x}_0)|$ (b) $|a_{1,h}(\mathbf{x}_0)|$

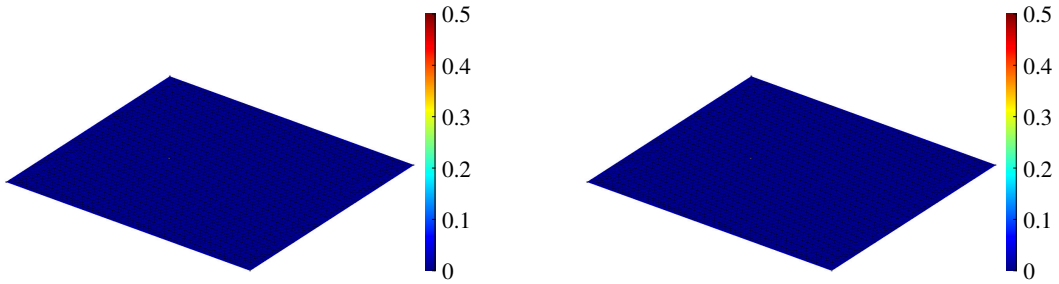

(c) $|a_{2,h}(\mathbf{x}_0)|$ (d) $|a_{3,h}(\mathbf{x}_0)|$

Figure 2.15: Four components $|a_{j,h}(\mathbf{x}_0)|$ for $j = 0, 1, 2, 3$ of $\widehat{w}_h^{\mathcal{J}^+}(\mathbf{x}_0)$, for the physical parameters $\nu_{\mathrm{f}} = 360$, $\nu_\ell = 1$, $c_\infty = 300$ and $\epsilon = 0$. This case corresponds to the standard wave propagation in a fixed domain, without frequency modulation.

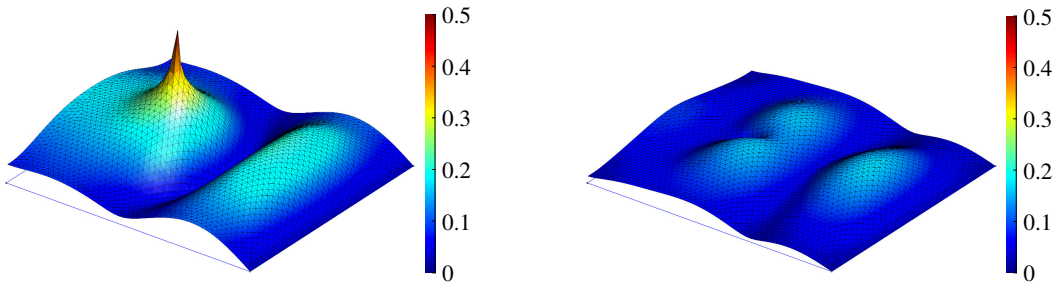

(a) $|a_{0,h}(\mathbf{x}_0)|$ (b) $|a_{1,h}(\mathbf{x}_0)|$

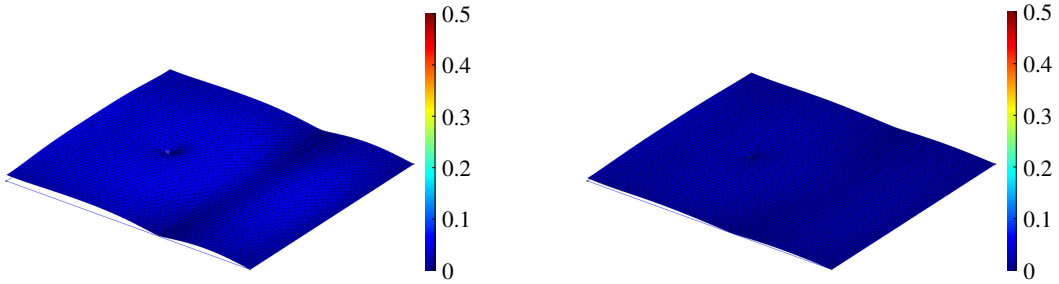

(c) $|a_{2,h}(\mathbf{x}_0)|$ (d) $|a_{3,h}(\mathbf{x}_0)|$

Figure 2.16: Four components $|a_{j,h}(\mathbf{x}_0)|$ for $j = 0, 1, 2, 3$ of $\widehat{w}_h^{\mathcal{J}^+}(\mathbf{x}_0)$, for the physical parameters $\nu_{\mathrm{f}} = 360$, $\nu_\ell = 1$, $c_\infty = 300$ and $\epsilon = 0.2$.

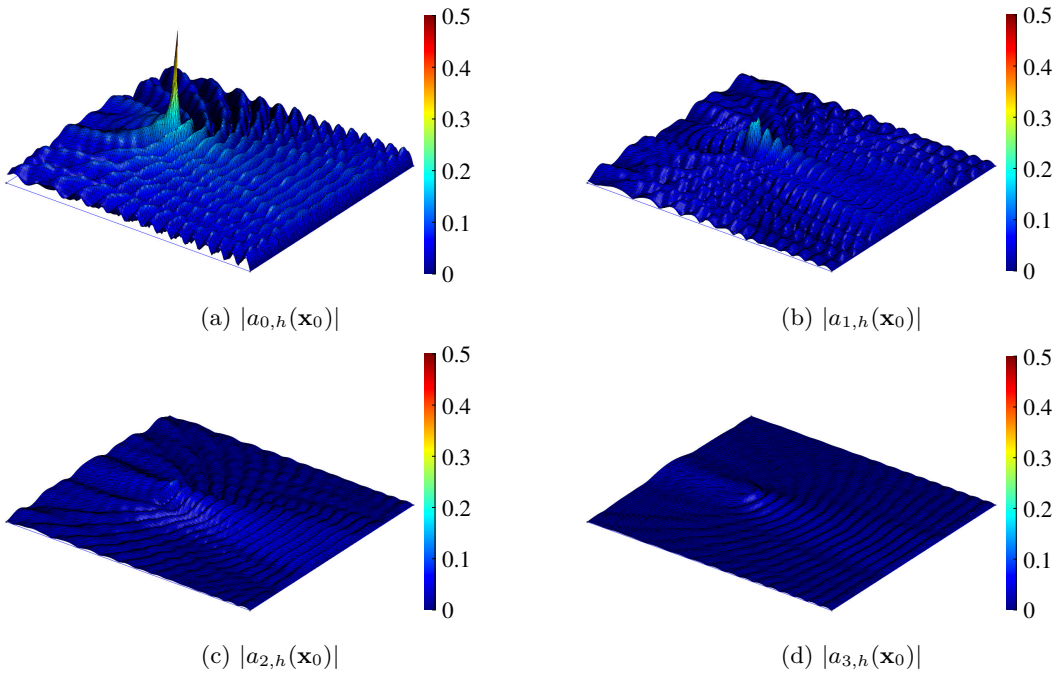

(a) $|a_{0,h}(\mathbf{x}_0)|$ (b) $|a_{1,h}(\mathbf{x}_0)|$

(c) $|a_{2,h}(\mathbf{x}_0)|$ (d) $|a_{3,h}(\mathbf{x}_0)|$

Figure 2.17: Four components $|a_{j,h}(\mathbf{x}_0)|$ for $j = 0, 1, 2, 3$ of $\widehat{w}_h^{\mathcal{J}^+}(\mathbf{x}_0)$, for the physical parameters $\nu_{\mathrm{f}} = 3600$, $\nu_\ell = 1$, $c_\infty = 300$ and $\epsilon = 0.02$.

Contrary to the one-dimensional case, and since we compute the propagation of circular waves on a plane around the source Γ^{s}, the amplitudes $|a_{j,h}(\mathbf{x}_0)|$ of the modes of the field decay like $1/|\mathbf{x}_0 - \Omega^{\mathrm{s}}|$ as $|\mathbf{x}_0 - \Omega^{\mathrm{s}}| \to \infty$. Moreover, in Figures 2.16 and 2.17, $|a_{j,h}(\mathbf{x}_0)|$ decreases as $|j|$ increases, which is in line with the fast decay of the coefficients studied in Section 2.2.1. We also observe that, in accordance with the one-dimensional case, the spatial frequency of the solution $|a_{j,h}(\mathbf{x}_0)|$ increases with the wave number κ_j.

2.6 Conclusion

In this chapter, we presented a new numerical method for solving the one dimensional scattering problem of scalar waves by a moving obstacle with general movement. The method is based on a change of variable which makes the moving domain fixed, and a multi-harmonic expansion of an approximate wave field. This results in the numerical solution of coupled systems of Helmholtz-type equations where optimized algorithms can be developed in the frequency domain. A preliminary numerical study is presented to confirm that the approach is accurate and efficient in the application domain of interest.

In the next chapter, we extend the previous methodology to tackle higher dimensional complex problems, in view of industrial implementations related to radar applications.

Chapter 3

A multi-harmonic finite element method for scattering problems with general boundary deformations in higher dimensions

Contents

3.1 Problem statement and notations 51
3.2 Approximate multi-harmonic Helmholtz-type weak coupled formulation 52
3.2.1 Equivalent weak formulation in a fixed domain 52
3.2.2 Approximate weak formulation for small deformations 55
3.2.3 Coupled multi-harmonic Helmholtz-type system 61
3.3 Finite element approximation 66
3.4 Efficient solution of the linear system 68
3.5 Application to a model problem 71
3.5.1 Description of the problem 71
3.5.2 Numerical resolution 73
3.6 Conclusion 84

3.1 Problem statement and notations

Let us keep the previous notations, where $t > 0$ is the time variable and $\mathbf{x} := (x_1, ..., x_d)^{\mathrm{T}}$ a point of $\mathbb{R}^d$ $(d = 2, 3)$. We again assume that a wave is emitted at a source with localized fixed finite support $\Omega^{\mathrm{s}} \subset \mathbb{R}^d$ of boundary Γ^{s}, and is scattered by a bounded obstacle with $\mathcal{C}^s$ $(s \geq 2)$ boundary $\partial\Omega_t^{\mathrm{obst}}$ smoothly deformed around an equilibrium position Γ_0, oscillating at a period $T_\ell = 1/\nu_\ell$ for a frequency ν_ℓ. Let us remark here that some of the stated results do not need the periodicity condition of the deformation. The d-dimensional homogeneous domain of propagation Ω_t^{ext} is bounded by $\Gamma^{\mathrm{s}} \cup \Gamma_t$, where we assume that $\Gamma^{\mathrm{s}} \cap \Gamma_t = \emptyset$ for all $t > 0$. As previously, we consider the unknown total wave field $u := u(\mathbf{x}, t)$ as the solution to the scalar wave equation

$$\partial_t^2 u - c_\infty^2 \Delta_{\mathbf{x}} u = 0, \tag{3.1}$$

for $(\mathbf{x}, t) \in \Omega_t^{\mathrm{ext}} \times \mathbb{R}_*^+$ (setting $\mathbb{R}_*^+ := \{t > 0\}$). The extension to space-dependent wave speeds will be considered later, at the discrete level. To stay general and according to the physical initial settings introduced in Section 2.5, we impose a T_{f}-periodic time-dependent complex source term supported on Γ^{s}, i.e. $u(\mathbf{x}, t)|_{\Gamma^{\mathrm{s}}} = Ae^{i\omega_{\mathrm{f}} t}$, with real-valued amplitude $A > 0$, periodicity $T_{\mathrm{f}} = 1/\nu_{\mathrm{f}}$ for a frequency ν_{f}, and angular frequency $\omega_{\mathrm{f}} := 2\pi\nu_{\mathrm{f}} > 0$. We recall that ν_{f} is supposed in practice to be very large compared to ν_ℓ. In what follows, we keep the homogeneous Dirichlet boundary condition $u(\mathbf{x}, t) = 0$ on Γ_t, but the extension to other boundary conditions (e.g. Neumann or Fourier-Robin boundary condition) is relatively direct. The two initial conditions in Ω_0^{ext} are

$$u(\mathbf{x}, 0) = 0 \quad \text{and} \quad \partial_t u(\mathbf{x}, 0) = 0. \tag{3.2}$$

Let us now introduce the fixed fictitious smooth boundary Σ enclosing Ω^{s} and Ω_t^{obst}. The resulting finite computational domain Ω_t is defined with boundary $\partial\Omega_t = \Sigma \cup \Gamma^{\mathrm{s}} \cup \Gamma_t$. Here, we consider the lower-order absorbing boundary condition on Σ

$$\partial_t u + c_\infty \partial_{\mathbf{n}} u = 0, \tag{3.3}$$

with outwardly directed unit normal vector $\mathbf{n}$. The spatial gradient operator of dimension d is given by $\nabla_{\mathbf{x}} := (\partial_{x_1}, ..., \partial_{x_d})^{\mathrm{T}}$. However, higher-order absorbing boundary conditions or PMLs could also be applied without any specific difficulty. In the sequel, we keep on denoting by u the solution to the wave equation (3.1) but set in $\Omega_t \times \mathbb{R}_*^+$, with the source term $u(\mathbf{x}, t) = Ae^{i\omega_{\mathrm{f}} t}$ on Γ^{s}, the homogeneous Dirichlet boundary condition $u(\mathbf{x}, t) = 0$ on Γ_t, the absorbing boundary condition (3.3) on Σ and with homogeneous initial data (3.2) in the compact set $\Omega(t = 0) = \Omega_0$. We schematically illustrate the configuration in Figure 3.1.

Let us remark that, in practical applications, e.g. Ω_t being the interior of a car with shape Σ, impedance boundary conditions are usually prescribed on some parts of Σ to model transparent, absorbing or reflecting materials (see also Figure 3.5 in Section 3.5). Hence, the system does not have any sharp resonance and the useful frequency information is only related to the perturbation of the wave emitted by the radar Γ^{s}, with high-frequency $\nu_{\mathrm{f}} (\gg \nu_\ell)$, by the local slowly oscillating smooth boundary Γ_t, with frequency ν_ℓ. Let us finally refer to the detailed study in Chapter 2 for the limit situation of the fully reflecting domain.

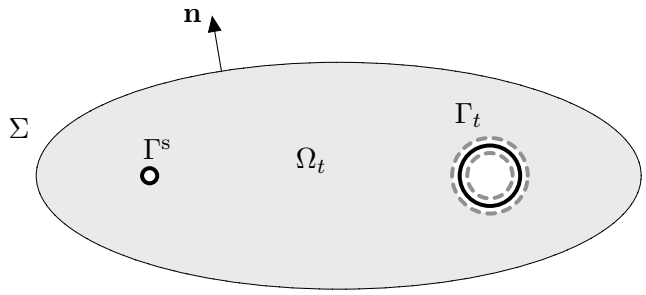

Figure 3.1: Example of a two-dimensional ($d = 2$) computational domain Ω_t with source term on the boundary Γ^{s}, with moving scattering surface Γ_t and fictitious boundary Σ.

3.2 Approximate multi-harmonic Helmholtz-type weak coupled formulation

To solve the boundary-value problem (3.1), we propose now to derive an equivalent weak formulation of the initial problem in a fixed domain. Then, an approximate variational formulation is written in Subsection 3.2.2 for small deformations. Next, in Subsection 3.2.3, a truncated Fourier series expansion of the unknown scalar field and some other geometrical quantities are considered around ν_{f} for uniformly spaced sample frequencies with step ν_ℓ. This results in the solution of a system of coupled multi-harmonic Helmholtz-type equations written under a weak form. The finite element approximation of the formulation is then discussed in Section 3.3.

3.2.1 Equivalent weak formulation in a fixed domain

The aim of this section is to write a weak form of the system in a fixed initial domain Ω_0 through a metric change parametrized by the time $t > 0$. For fixed $t > 0$, we designate by $H^m(\Omega_t)$ the standard Sobolev space of solutions of finite energy on Ω_t as

$$H^m(\Omega_t) := \left\{ u \in L^2(\Omega_t) \text{ such that } \partial^{\boldsymbol{\alpha}}_{\mathbf{x}} u(\mathbf{x}, \cdot) \in L^2(\Omega_t), 0 \leq |\boldsymbol{\alpha}| \leq m \right\}, \tag{3.4}$$

where we define the partial derivative $\partial^{\boldsymbol{\alpha}}_{\mathbf{x}} = \partial^{\alpha_1}_{x_1} \cdots \partial^{\alpha_d}_{x_d}$ in the sense of distributions, for a multi-index $\boldsymbol{\alpha} = (\alpha_1, \cdots, \alpha_d)$ of length $|\boldsymbol{\alpha}| = \alpha_1 + \cdots + \alpha_d$. The space $L^2(\Omega_t)$ is the usual space of square integrable functions on Ω_t.

Now we introduce the Sobolev space

$$H^m_{A,\omega_{\mathrm{f}}t}(\Omega_t) := \left\{ u \in H^m(\Omega_t) \mid u|_{\Gamma_t} = 0 \text{ and } u|_{\Gamma^{\mathrm{s}}} = Ae^{i\omega_{\mathrm{f}}t} \right\},$$

for $m = 1, 2$. With our notations, we have in particular that, a $t = 0$,

$$H^m_{A,0}(\Omega_0) := \left\{ u \in H^m(\Omega_0) \mid u|_{\Gamma_0} = 0 \text{ and } u|_{\Gamma^{\mathrm{s}}} = A \right\}.$$

We also need the following Sobolev space

$$H^m_{A,\omega_{\mathrm{f}}t}(\Omega_0) := \left\{ u \in H^m(\Omega_0) \mid u|_{\Gamma_0} = 0 \text{ and } u|_{\Gamma^{\mathrm{s}}} = Ae^{i\omega_{\mathrm{f}}t} \right\}. \tag{3.5}$$

All along this work, we assume that the solution $u := u(\mathbf{x}, t)$ to the initial boundary-value problem stated in Section 3.1 is an element of the space $\mathcal{C}^0([0, T_\ell], H^2_{A,\omega_{\mathfrak{f}}t}(\Omega_t))$, $\partial_t u$ is in $\mathcal{C}^0([0, T_\ell], H^1(\Omega_t))$ while $\partial_t^2 u$ is $\mathcal{C}^0([0, T_\ell], L^2(\Omega_t))$ (see e.g. [68] for regularity results of the solution of the wave equation for fixed domains).

According to these assumptions, the weak formulation in Ω_t writes: find $u(\cdot, t) \in H^1_{A,\omega_{\mathfrak{f}}t}(\Omega_t)$ such that

$$\forall \phi \in H^1_{0,0}(\Omega_t), \quad \int_{\Omega_t} \nabla_{\mathbf{x}} u \cdot \overline{\nabla_{\mathbf{x}} \phi} d\Omega_t + \int_{\Omega_t} \frac{1}{c_\infty^2} \partial_t^2 u \overline{\phi} d\Omega_t + \int_\Sigma \frac{1}{c_\infty} \partial_t u \overline{\phi}\, d\Sigma = 0, \tag{3.6}$$

for all $t \in (0, T_\ell]$, with the two initial conditions $u(\mathbf{x}, 0) = 0$ and $\partial_t u(\mathbf{x}, 0) = 0$. Here, we define $\overline{\phi}$ as the complex conjugate of the function ϕ, $\mathbf{a} \cdot \mathbf{b} := \sum_{j=1}^d a_j b_j$ for two vectors $\mathbf{a}$ and $\mathbf{b}$ in $\mathbb{C}^d$, and the norm $|\mathbf{a}|$ of $\mathbf{a}$ is: $|\mathbf{a}| = \sqrt{\mathbf{a} \cdot \overline{\mathbf{a}}}$. Equation (3.6) has been derived by dividing (3.1) and (3.3) by c_∞^2, which leads to a more convenient form of the weak formulation in the case of a non constant wave velocity investigated in Section 3.5.

In Chapter 2, the mapping between Ω_0 and Ω_t has not been detailed, leading to a restricted range of validity for the higher dimensional extension of the method. Now, we provide a rigorous and more tangible construction of this mapping. Let us consider a vector flow $\mathbf{\Phi}_t$, for $t \in \mathbb{R}^+$, defined by

$$\begin{array}{rcccl} \mathbf{\Phi}_t & : & \Omega_0 & \to & \Omega_t \subset \mathbb{R}^d \\ & & \mathbf{x}_0 & \mapsto & \mathbf{x} = (\Phi_{t1}(\mathbf{x}_0), ..., \Phi_{td}(\mathbf{x}_0))^{\mathrm{T}} = (x_1, ..., x_d)^{\mathrm{T}}, \end{array}$$

mapping the fixed initial domain Ω_0 to Ω_t in such a way that we have

$$\mathbf{\Phi}_t(\Gamma_0) = \Gamma_t, \ \mathbf{\Phi}_t(\Sigma) = \Sigma, \ \ \mathbf{\Phi}_t(\Gamma_{\mathrm{s}}) = \Gamma_{\mathrm{s}} \text{ and } \mathbf{\Phi}_0 = \mathbf{Id},$$

where $\mathbf{Id}$ is the identity map over Ω_0. For fixed $t \geq 0$, $\mathbf{\Phi}_t$ is assumed to be a $\mathcal{C}^2$-diffeomorphism with inverse map $\mathbf{\Phi}_t^{-1} : \Omega_t \to \Omega_0$, as depicted in Figure 3.2. In addition, we suppose that the vector flow $\{\mathbf{\Phi}_t\}_{t>0}$ is of class $\mathcal{C}^s$ in time, with $s \geq 2$. The vector $\mathbf{x}_0 = (x_{01}, ..., x_{0d})^{\mathrm{T}}$ denotes a point of the fixed domain Ω_0, image of $\mathbf{x} \in \Omega_t$ by the change of variables $\mathbf{\Phi}_t^{-1}$, i.e. $\mathbf{x}_0 = \mathbf{\Phi}_t^{-1}(\mathbf{x})$. Let u_0 be the unknown in Ω_0 after applying $\mathbf{\Phi}_t^{-1}$ and let us set $u(\mathbf{x}, t) = u_0(\mathbf{\Phi}_t^{-1}(\mathbf{x}), t) = u_0(\mathbf{x}_0, t)$ for $t \in \mathbb{R}^+$. We also consider the space-time vector $\mathbf{X}_0 := (\Phi_{t1}^{-1}(\mathbf{x}), ..., \Phi_{td}^{-1}(\mathbf{x}), t)^{\mathrm{T}} = (x_{01}, ..., x_{0d}, t)^{\mathrm{T}} \in \Omega_0 \times \mathbb{R}^+$. The time-dependent spatial Jacobian matrix $\mathbf{J}_t$ of $\mathbf{\Phi}_t^{-1}$ at point $\mathbf{x} \in \Omega_t$ now writes

$$\mathbf{J}_t(\mathbf{x}) = (\nabla_{\mathbf{x}} \mathbf{\Phi}_t^{-1}(\mathbf{x}))^{\mathrm{T}}.$$

By the change of metric $\mathbf{\Phi}_t^{-1}$, we have the following relations:

$$\nabla_{\mathbf{x}} u = \mathbf{J}_t^{\mathrm{T}} \nabla u_0,$$

where $\nabla := \nabla_{\mathbf{x}_0}$ and as in Section 2.5

$$\partial_t u = \partial_t \mathbf{X}_0 \cdot \nabla_{\mathbf{X}_0} u_0, \quad \partial_t^2 u = \left(\partial_t^2 \mathbf{X}_0 \cdot \nabla_{\mathbf{X}_0} + (\partial_t \mathbf{X}_0 \cdot \nabla_{\mathbf{X}_0})^2 \right) u_0.$$

Let us explain a simple construction of $\mathbf{\Phi}_t$, even if other possibilities could be alternatively considered. We introduce a smooth fixed surface Γ^{loc} enclosing Γ_t for all $t \geq 0$, such that $\Gamma^{\mathrm{loc}} \cap \Gamma_t = \emptyset$ (c.f. Figure 3.2). This defines a local neighborhood $\Omega_t^{\mathrm{loc}} := \Omega^{\mathrm{loc}}(t)$ of Γ_t in Ω_t. Let us set

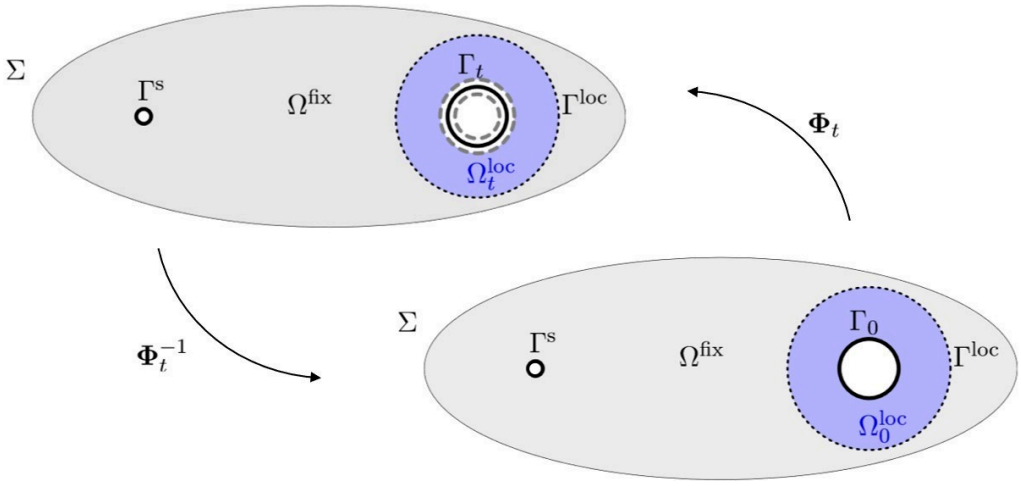

Figure 3.2: Illustration of the vector flow $\boldsymbol{\Phi}_t$.

$\Omega_0^{\text{loc}} := \Omega^{\text{loc}}(t=0)$. Therefore, we have: $\partial\Omega_0^{\text{loc}} = \overline{\Gamma_0 \cup \Gamma^{\text{loc}}}$, and the fixed complementary domain $\Omega^{\text{fix}} := \Omega_0 \setminus \Omega_0^{\text{loc}}$ is the part where the deformation is not active. In Chapter 4, we consider the particular case where Γ_0 is strictly included in Ω_0^{loc}.

It is very interesting to notice that, following Subsection 2.2.3, this particular choice ensures to recover without any additional step the approximation of the original field u over the fixed area $\Omega_t \setminus \overline{\Omega_t^{\text{loc}}}$, which also corresponds to Ω^{fix}.

Our aim is to model the impact of the local surface deformation to compute the volume coordinates changes, parametrized by $t \geq 0$. By assumption, we know that the deformation $\boldsymbol{\delta}_t$ on Γ_0 is given by $\boldsymbol{\Phi}_t - \boldsymbol{\Phi}_0 \in \mathcal{C}^2(\Gamma_0)$ and by the knowledge of Γ_t, which has $\mathcal{C}^2$ regularity. In addition, since we assume that there is no effect of the deformation on Ω^{fix}, we set: $\boldsymbol{\delta}_t = \boldsymbol{\Phi}_t - \boldsymbol{\Phi}_0 = \mathbf{0}$ on Ω^{fix}, and in particular on Γ^{loc}, for $t \geq 0$. Now, we propose to build the volume deformation

$$\boldsymbol{\delta}_t := \boldsymbol{\Phi}_t - \boldsymbol{\Phi}_0 \tag{3.7}$$

through the local unique solution $\boldsymbol{\Phi}_t$ (a proof could be obtained by the Lax-Milgram theory for example at any time $t > 0$, accordingly to the smoothness properties of the data) to the following Dirichlet problem, parametrized by $t > 0$,

$$\left\{ \begin{array}{rcll} -\Delta_{\mathbf{x}_0} \boldsymbol{\Phi}_t & = & \mathbf{0} & \text{in } \Omega_0^{\text{loc}}, \\ \boldsymbol{\Phi}_t & = & \mathbf{Id} & \text{on } \Gamma^{\text{loc}}, \\ \boldsymbol{\Phi}_t & = & \boldsymbol{\Phi}_t|_{\Gamma_0} & \text{on } \Gamma_0, \end{array} \right. \tag{3.8}$$

where $\mathbf{Id}$ is the identity operator over Γ^{loc} and $\boldsymbol{\Phi}_t|_{\Gamma_0}$ is the given deformation on Γ_0. The Laplacian is defined by $\Delta_{\mathbf{x}_0} := (\nabla)^2$. The Dirichlet problem (3.8) splits into d separated sub-problems over each component Φ_{tj} of $\boldsymbol{\Phi}_t$, $1 \leq j \leq d$. For a fixed time t, the solution to (3.8) provides $\boldsymbol{\Phi}_t$ which has components in $\mathcal{C}^2(\Omega_0^{\text{loc}}) \cap \mathcal{C}^0(\overline{\Omega_0^{\text{loc}}})$, and by extension in $\mathcal{C}^2(\Omega_0) \cap \mathcal{C}^0(\overline{\Omega_0})$. Finally, we recover $\boldsymbol{\Phi}_t$ directly from $\boldsymbol{\delta}_t$ by using (3.7). Now, we can compute the Jacobian $\mathbf{J}_t$ of $\boldsymbol{\Phi}_t^{-1}$ as from $\boldsymbol{\Phi}_t$. Since $\boldsymbol{\Phi}_t^{-1}$ is the inverse map of $\boldsymbol{\Phi}_t$, we have $\boldsymbol{\Phi}_t(\boldsymbol{\Phi}_t^{-1}(\mathbf{x})) = \mathbf{x}$, for all $\mathbf{x} \in \Omega_t$. This implies that

$\mathrm{Jac}(\mathbf{\Phi}_t)(\mathbf{x}_0)\mathbf{J}_t(\mathbf{x}) = \mathbf{I}_d$, where $\mathrm{Jac}(\mathbf{\Phi}_t)(\mathbf{x}_0)$ denotes the Jacobian matrix of $\mathbf{\Phi}_t$ taken at $\mathbf{x}_0 = \Phi_t^{-1}(\mathbf{x})$ and $\mathbf{I}_d$ is the $d \times d$ identity matrix. Thus, we compute $\mathbf{J}_t$ by the relation

$$\mathbf{J}_t = \mathrm{Jac}(\mathbf{\Phi}_t)^{-1}. \tag{3.9}$$

For a fixed $t > 0$, the coefficients of $\mathbf{J}_t$ are $\mathcal{C}^1(\Omega_0)$ functions defined as spatial derivatives of the $\mathcal{C}^2$ mapping $\mathbf{\Phi}_t$ based on the Jacobian expression. Practically, a finite collection of the local deformations at some uniformly distributed discrete times will be computed through the solution of the boundary-value problem (3.8) by the finite element method. Through (3.9), we obtain a way to compute $\mathbf{J}_t$ by derivation (again numerically realized later by the finite element method) in Ω_0^{loc}. The tensor $\mathbf{J}_t$ is trivially equal to the identity matrix in Ω^{fix}. While we chose to model the deformation by (3.8), more advanced e.g. elastic deformations could also be used. While we chose to model the deformation in a simple way by (3.8), which is also used e.g. in the context of shape optimization [64], more advanced elastic deformations could be considered without difficulty [45].

Let us recall that the Sobolev space $H^1_{A,\omega_{\mathrm{f}}t}(\Omega_0)$ is given from definition (3.5) for $m = 1$. Then, the variational formulation (3.6) writes in the fixed domain Ω_0, for fixed $t > 0$: find $u_0(\cdot, t) \in H^1_{A,\omega_{\mathrm{f}}t}(\Omega_0)$ such that, $\forall \phi \in H^1_{0,0}(\Omega_0)$,

$$\begin{aligned}\int_{\Omega_0} &\mathbf{J}_t\mathbf{J}_t^{\mathrm{T}}\nabla u_0 \cdot \overline{\nabla\phi}|\mathbf{J}_t^{-1}|d\Omega_0 \\ &+ \int_{\Omega_0} \frac{1}{c_\infty^2}\left(\partial_t^2\mathbf{X}_0 \cdot \nabla_{\mathbf{X}_0} + (\partial_t\mathbf{X}_0 \cdot \nabla_{\mathbf{X}_0})^2\right) u_0\overline{\phi}|\mathbf{J}_t^{-1}|d\Omega_0 + \int_\Sigma \frac{1}{c_\infty}\partial_t u_0\overline{\phi}\, d\Sigma = 0,\end{aligned} \tag{3.10}$$

since (see also expression (3.14))

$$(\partial_t\mathbf{X}_0 \cdot \nabla_{\mathbf{X}_0})u_0 = \partial_t u_0, \quad \text{on } \Sigma,$$

and where $|\mathbf{J}_t^{-1}|$ denotes the determinant of $\mathbf{J}_t^{-1}$, which in particular is equal to 1 on Σ. Finally, we also have the two initial conditions $u_0(\mathbf{x}_0, 0) = 0$ and $\partial_t u_0(\mathbf{x}_0, 0) = 0$ in Ω_0. From the assumptions on the smoothness of $\partial_t u$ and $\partial_t^2 u$, we deduce that $\partial_t u_0$ is an element of $H^1(\Omega_0)$ while $\partial_t^2 u_0$ is in $L^2(\Omega_0)$.

Remark 4. *Conversely to the methodology introduced in Chapter 2, we first write here the weak formulation and then apply a change of coordinates so that the problem is set in a time independent domain with a metric that depends on the parameter $t \geq 0$. This considerably improves the versatility of the method with respect to the different geometries. However, let us highlight that in Chapter 2, the change of coordinates was first applied and then the weak form was stated, which may provide a different formulation according to the algebraic calculations. However, the weak formulation of this previous approach is equivalent to* (3.10) *when applied to specific test functions of the form $\widetilde{\phi} = |\mathbf{J}_t^{-1}|\phi$.*

3.2.2 Approximate weak formulation for small deformations

In practice, the exact formulation (3.10) could be used for a numerical computation. However, in the case of a small deformation of the moving interface, an accurate approximate formulation can be used to simplify the calculations. Indeed, the careful analysis developed in Chapter 2 for the one-dimensional case, and formally extended to higher-dimensional problems, shows that the following

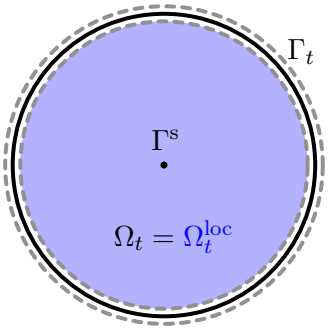

Figure 3.3: Example of a vibrating disk Ω_t with source term Γ^{s} and boundary Γ_t.

simplified weak formulation (3.11) provides an accurate approximate solution v of u_0 that satisfies (3.10). More precisely, the formulation writes: for a fixed time $t > 0$, find $v := v(\cdot, t) \in H^1_{A,\omega_{\mathrm{f}}t}(\Omega_0)$ such that, for any test-function $\phi \in H^1_{0,0}(\Omega_0)$,

$$\int_{\Omega_0} \mathbf{J}_t \mathbf{J}_t^{\mathrm{T}} \nabla v \cdot \overline{\nabla \phi} |\mathbf{J}_t^{-1}| d\Omega_0 + \int_{\Omega_0} \frac{1}{c_\infty^2} \partial_t^2 v \overline{\phi} |\mathbf{J}_t^{-1}| d\Omega_0 + \int_{\Sigma} \frac{1}{c_\infty} \partial_t v \overline{\phi} d\Sigma = 0, \tag{3.11}$$

with the two initial conditions $v(\mathbf{x}_0, 0) = 0$ and $\partial_t v(\mathbf{x}_0, 0) = 0$. The derivation of (3.11) is based on the following formal approximation

$$(\partial_t^2 \mathbf{X}_0 \cdot \nabla_{\mathbf{X}_0} + (\partial_t \mathbf{X}_0 \cdot \nabla_{\mathbf{X}_0})^2) u_0 \approx \partial_t^2 v \quad \text{in } \Omega_0. \tag{3.12}$$

To motivate (3.12), let us consider the simplified and pedagogical case of a vibrating disk Ω_t with circular boundary Γ_t of initial radius $L > 0$ ($d = 2$) at $t = 0$. As depicted in Figure 3.3, the disk is centered on a point source located at the origin, i.e. $\Gamma^{\mathrm{s}} := \{\mathbf{0}\}$, supporting the Dirichlet condition $u(\mathbf{x}, t) = Ae^{i\omega_{\mathrm{f}} t}\delta_{\mathbf{0}}$. We consider for the boundary sine oscillations of frequency $\nu_\ell = \omega_\ell/(2\pi)$ and of small relative amplitude $0 < \epsilon \ll 1$. Whereas the deformed rectangle investigated in Section 2.5 was a trivial extension along the second cartesian dimension of the one dimensional scattering problem with moving boundaries, this configuration involves a more interesting generalisation, based on circular symmetry and through which we also exhibit the validity of our assumption (3.12). The vibrating surface is defined by

$$\Gamma_t := \left\{ \mathbf{x} = \begin{pmatrix} r\cos(\theta) \\ r\sin(\theta) \end{pmatrix} \mid r = \ell(t), \theta \in [0, 2\pi[\right\},$$

where $\ell(t) := L(1 + \epsilon \sin(\omega_\ell t))$, delimiting then Ω_t. For this configuration, we have no fictitious boundary, i.e. $\Sigma = \emptyset$ and the initial setting for the moving boundary Γ_t is given by

$$\Gamma_0 = \left\{ \mathbf{x}_0 = \begin{pmatrix} r\cos(\theta) \\ r\sin(\theta) \end{pmatrix} \mid r = L, \theta \in [0, 2\pi) \right\}.$$

A natural way to build a metric change $\mathbf{\Phi}_t$ is to consider the simple linear mapping between $\mathbf{x} \in \Omega_t$ and $\mathbf{x}_0 \in \Omega_0$ as

$$\mathbf{\Phi}_t : \mathbf{x}_0 \mapsto \mathbf{x} = \frac{\ell(t)}{L} \mathbf{x}_0.$$

Let us observe that such a configuration in polar coordinates also allows to set for $\Gamma^{\rm s}$ a small fixed circle of radius $r^{\rm s}$, provided that we consider the following affine change of metric

$$\mathbf{\Phi}_t : \mathbf{x}_0 \mapsto \mathbf{x} = \frac{\ell(t) - r^s}{L - r^{\rm s}}(\mathbf{x}_0 - \mathbf{r}^{\rm s}(\mathbf{x}_0)) + \mathbf{r}^{\rm s}(\mathbf{x}_0),$$

where

$$\mathbf{r}^{\rm s}(\mathbf{x}_0) := r^{\rm s}\frac{\mathbf{x}_0}{\|\mathbf{x}_0\|}.$$

This adaptation does not fundamentally modify the approach below.

According to (3.7), the time dependent deformation $\boldsymbol{\delta}_t$ is then defined on Ω_0, and in particular on Γ_0, by

$$\boldsymbol{\delta}_t(\mathbf{x}_0) = \mathbf{\Phi}_t(\mathbf{x}_0) - \mathbf{\Phi}_0(\mathbf{x}_0) = \epsilon\sin(\omega_\ell t)\mathbf{x}_0.$$

Here, $\Gamma^{\rm loc}$ is reduced to $\Gamma^{\rm s} = \{\mathbf{0}\}$ and we observe, accordingly to (3.8), that we have

$$-\Delta\boldsymbol{\delta}_t = -\begin{pmatrix}\partial^2_{x_{01}}\delta_{t1} + \partial^2_{x_{02}}\delta_{t1}\\ \partial^2_{x_{01}}\delta_{t2} + \partial^2_{x_{02}}\delta_{t2}\end{pmatrix} = \mathbf{0}.$$

Moreover, we find for this particular case and for all $\mathbf{x}_0 \in \Omega_0$ that

$$\partial_t\mathbf{X}_0 = \partial_t\begin{pmatrix}\Phi^{-1}_{t1}(\mathbf{x})\\ \Phi^{-1}_{t2}(\mathbf{x})\\ t\end{pmatrix} = \begin{pmatrix}\partial_t\dfrac{L}{\ell(t)}x_1\\ \partial_t\dfrac{L}{\ell(t)}x_2\\ 1\end{pmatrix} = \begin{pmatrix}-\dfrac{\ell(t)}{L}x_{01}\dfrac{\epsilon\omega_\ell\cos(\omega_\ell t)}{(1+\epsilon\sin(\omega_\ell t))^2}\\ -\dfrac{\ell(t)}{L}x_{02}\dfrac{\epsilon\omega_\ell\cos(\omega_\ell t)}{(1+\epsilon\sin(\omega_\ell t))^2}\\ 1\end{pmatrix} = \begin{pmatrix}\mathcal{O}(\epsilon)\\ \mathcal{O}(\epsilon)\\ 1\end{pmatrix},$$

and

$$\partial^2_t\mathbf{X}_0 = \begin{pmatrix}x_{01}\dfrac{\epsilon\omega^2_\ell(\sin(\omega_\ell t)(1+\epsilon\sin(\omega_\ell t)) - 2\epsilon\cos(\omega_\ell t))}{(1+\epsilon\sin(\omega_\ell t))^2}\\ x_{02}\dfrac{\epsilon\omega^2_\ell(\sin(\omega_\ell t)(1+\epsilon\sin(\omega_\ell t)) - 2\epsilon\cos(\omega_\ell t))}{(1+\epsilon\sin(\omega_\ell t))^2}\\ 0\end{pmatrix} = \begin{pmatrix}\mathcal{O}(\epsilon)\\ \mathcal{O}(\epsilon)\\ 0\end{pmatrix}.$$

Hence, for small values of ϵ, we directly have

$$\partial_t\mathbf{X}_0\cdot\nabla_{\mathbf{X}_0}u_0 = (\partial_t + \mathcal{O}(\epsilon)(\partial_{x_{01}} + \partial_{x_{02}}))u_0 \underset{\epsilon\to 0}{\approx} \partial_t u_0,$$

$$\partial^2_t\mathbf{X}_0\cdot\nabla_{\mathbf{X}_0}u_0 = \mathcal{O}(\epsilon)(\partial_{x_{01}} + \partial_{x_{02}})u_0 \underset{\epsilon\to 0}{\approx} 0,$$

and

$$(\partial_t\mathbf{X}_0\cdot\nabla_{\mathbf{X}_0})^2u_0 = (\partial^2_t + \mathcal{O}(\epsilon)(\partial_{tx_{01}} + \partial_{tx_{02}}) + +\mathcal{O}(\epsilon^2)(\partial^2_{x_{01}} + \partial^2_{x_{02}}))u_0 \underset{\epsilon\to 0}{\simeq} \partial^2_t u_0.$$

For $\epsilon \ll 1$, these specific approximations are hence compatible with the general case (3.12). In addition, the time-dependent Jacobian is given by the expression: $\mathbf{J}_t = (1+\epsilon\sin(\omega_\ell t))^{-1}\mathbf{I}_2$. Therefore, the determinant of $\mathbf{J}_t^{-1}$ is such that $|\mathbf{J}_t^{-1}| := (1+\epsilon\sin(\omega_\ell t))^2$ and we have $\mathbf{J}_t\mathbf{J}_t^{\rm T} := (1+\epsilon\sin(\omega_\ell t))^{-2}\mathbf{I}_2$. Finally, the third integral over Σ arising in (3.11) reduces to zero.

Now, let us give a more rigorous understanding on how (3.12) leads to (3.11) as a correct approximation of (3.10). Without loss of generality, we rewrite the application $\mathbf{\Phi}_t$ with a small smooth perturbation $\epsilon \ll 1$ under the form

$$\mathbf{x} = \mathbf{\Phi}_t(\mathbf{x}_0) = \mathbf{x}_0 + \epsilon \boldsymbol{\delta}_t(\mathbf{x}_0), \tag{3.13}$$

where $(\boldsymbol{\delta}_t)_{t>0} \in \mathcal{C}^2(]0;T_{\max}], \mathcal{C}^2(\overline{\Omega_0}, \mathbb{R}^d))$, and $T_{\max}$ is a finite maximal time of computation. Then, for $t \in]0;T_{\max}]$, the time derivatives of $\boldsymbol{\delta}_t$ up to the second-order are uniformly bounded, i.e. there exist a constant d_ℓ such that, for any $t \in]0;T_{\max}]$, for $\ell = 0, 1, 2$, we have

$$d_{\ell,t} := \|\partial_t^\ell \boldsymbol{\delta}_t\|_{L^\infty_d(\Omega_0)} \leq d_\ell := \sup_{t\in]0;T_{\max}]} d_{\ell,t},$$

with $L^\infty_d(\Omega_0) := (L^\infty(\Omega_0))^d$. Here, $\boldsymbol{\delta}_t$ may be oscillating but this is not yet mandatory. In the case of a periodic deformation, we can fix: $T_{\max} = T_\ell$. Now, since $\mathbf{x}_0 = \mathbf{\Phi}_t^{-1}(\mathbf{x})$, we have from (3.13)

$$\mathbf{x}_0 = \mathbf{\Phi}_t^{-1}(\mathbf{x}) = \mathbf{x} - \epsilon \boldsymbol{\delta}_t(\mathbf{\Phi}_t^{-1}(\mathbf{x})).$$

Based on this expression, we get

$$\partial_t \mathbf{\Phi}_t^{-1}(\mathbf{x}) = -\epsilon \partial_t \boldsymbol{\delta}_t(\mathbf{\Phi}_t^{-1}(\mathbf{x})) =: -\epsilon \mathbf{A}(\mathbf{x}_0, t),$$

with $\mathbf{A} := \partial_t \boldsymbol{\delta}_t(\mathbf{\Phi}_t^{-1}(\mathbf{x}))$, and then

$$\partial_t \mathbf{X}_0 = \partial_t \begin{pmatrix} \mathbf{\Phi}_t^{-1}(\mathbf{x}) \\ t \end{pmatrix} = \begin{pmatrix} -\epsilon \mathbf{A} \\ 1 \end{pmatrix}.$$

Consequently, we have the following expansion in Ω_0

$$(\partial_t \mathbf{X}_0 \cdot \nabla_{\mathbf{X}_0}) u_0 = \begin{pmatrix} -\epsilon \mathbf{A} \\ 1 \end{pmatrix} \cdot \begin{pmatrix} \nabla \\ \partial_t \end{pmatrix} u_0 = (\partial_t - \epsilon \mathbf{A} \cdot \nabla) u_0. \tag{3.14}$$

Now, we obtain

$$\begin{aligned} &(\partial_t^2 \mathbf{X}_0 \cdot \nabla_{\mathbf{X}_0} + (\partial_t \mathbf{X}_0 \cdot \nabla_{\mathbf{X}_0})^2) u_0 \\ &\qquad = \begin{pmatrix} -\epsilon \partial_t \mathbf{A} \\ 0 \end{pmatrix} \cdot \begin{pmatrix} \nabla u_0 \\ \partial_t u_0 \end{pmatrix} + \begin{pmatrix} -\epsilon \mathbf{A} \\ 1 \end{pmatrix} \cdot \begin{pmatrix} \nabla \\ \partial_t \end{pmatrix} \left(\begin{pmatrix} -\epsilon \mathbf{A} \\ 1 \end{pmatrix} \cdot \begin{pmatrix} \nabla u_0 \\ \partial_t u_0 \end{pmatrix} \right). \end{aligned}$$

By using (3.14), we deduce that

$$\begin{aligned} (\partial_t^2 \mathbf{X}_0 \cdot \nabla_{\mathbf{X}_0} + (\partial_t \mathbf{X}_0 \cdot \nabla_{\mathbf{X}_0})^2) u_0 &= -\epsilon \partial_t \mathbf{A} \cdot \nabla u_0 + (\partial_t - \epsilon \mathbf{A} \cdot \nabla)^2 u_0 \\ &= \partial_t^2 u_0 - 2\epsilon \partial_t (\mathbf{A} \cdot \nabla u_0) + \epsilon^2 \ \mathbf{A} \cdot \nabla (\mathbf{A} \cdot \nabla u_0). \end{aligned} \tag{3.15}$$

Now, to prove Proposition 3.1 which justifies the approximation (3.11), let us consider the second term in (3.10) and introduce the following bilinear forms from the decomposition (3.15)

$$\mathcal{A}_{\epsilon,t}(u_0, \phi) = \mathcal{A}_{0,t}(u_0, \phi) + \epsilon \mathcal{A}_{1,t}(u_0, \phi) + \epsilon^2 \mathcal{A}_{2,t}(u_0, \phi), \tag{3.16}$$

with

$$\mathcal{A}_{\epsilon,t}(u_0,\phi) := \int_{\Omega_0} \frac{1}{c_\infty^2}\left(\partial_t^2 \mathbf{X}_0 \cdot \nabla_{\mathbf{X}_0} + (\partial_t \mathbf{X}_0 \cdot \nabla_{\mathbf{X}_0})^2\right) u_0 \overline{\phi} |\mathbf{J}_t^{-1}| d\Omega_0, \tag{3.17}$$

$$\mathcal{A}_{0,t}(u_0,\phi) := \int_{\Omega_0} \frac{1}{c_\infty^2} \partial_t^2 u_0 \overline{\phi} |\mathbf{J}_t^{-1}| d\Omega_0, \tag{3.18}$$

$$\mathcal{A}_{1,t}(u_0,\phi) := -2\int_{\Omega_0} \frac{1}{c_\infty^2} \partial_t (\mathbf{A} \cdot \nabla u_0) \overline{\phi} |\mathbf{J}_t^{-1}| d\Omega_0, \tag{3.19}$$

and

$$\mathcal{A}_{2,t}(u_0,\phi) := \int_{\Omega_0} \frac{1}{c_\infty^2} \mathbf{A} \cdot \nabla \left(\mathbf{A} \cdot \nabla u_0\right) \overline{\phi} |\mathbf{J}_t^{-1}| d\Omega_0. \tag{3.20}$$

As a consequence, the real-time weak formulation (3.10) writes

$$\int_{\Omega_0} \mathbf{J}_t \mathbf{J}_t^{\mathrm{T}} \nabla v \cdot \overline{\nabla \phi} |\mathbf{J}_t^{-1}| d\Omega_0 + \mathcal{A}_{\epsilon,t}(u_0,\phi) + \int_\Sigma \frac{1}{c_\infty} \partial_t v \overline{\phi} d\Sigma = 0,$$

or even

$$\mathcal{A}_{\epsilon,t}(u_0,\phi) + \mathcal{R}_t(u_0,\phi) = 0, \tag{3.21}$$

with the bilinear term

$$\mathcal{R}_t(u_0,\phi) := \int_{\Omega_0} \mathbf{J}_t \mathbf{J}_t^{\mathrm{T}} \nabla v \cdot \overline{\nabla \phi} |\mathbf{J}_t^{-1}| d\Omega_0 + \int_\Sigma \frac{1}{c_\infty} \partial_t v \overline{\phi} d\Sigma$$

containing the boundary integral and the stiffness term of the formulation. Now, let us first consider $\mathcal{A}_{1,t}$ given by (3.19). Then, the Cauchy-Schwarz inequality implies that

$$|\mathcal{A}_{1,t}(u_0,\phi)| \leq 2\gamma_t ||\partial_t(\mathbf{A} \cdot \nabla u_0)||_{L^2(\Omega_0)} ||\phi||_{L^2(\Omega_0)}, \tag{3.22}$$

where

$$\gamma_t := \left|\left| \frac{|\mathbf{J}_t^{-1}|}{c_\infty^2} \right|\right|_{L^\infty(\Omega_0)}.$$

If we develop the right hand side derivative term we obtain

$$\begin{array}{rcl} ||\partial_t(\mathbf{A} \cdot \nabla u_0)||_{L^2(\Omega_0)} & = & ||\partial_t \mathbf{A} \cdot \nabla u_0 + \mathbf{A} \cdot \nabla \partial_t u_0||_{L^2(\Omega_0)} \\ & \leq & ||\partial_t \mathbf{A} \cdot \nabla u_0||_{L^2(\Omega_0)} + ||\mathbf{A} \cdot \nabla \partial_t u_0||_{L^2(\Omega_0)}. \end{array} \tag{3.23}$$

Since $\mathbf{A}$ has continuous first-order time derivative, then we can deduce that there exist a constant $C_{0,t}$ which depends on $d_{2,t} = ||\partial_t \mathbf{A}||_{L_d^\infty(\Omega_0)}$ such that

$$||\partial_t \mathbf{A} \cdot \nabla u_0||_{L^2(\Omega_0)} \leq C_{0,t} ||\nabla u_0||_{L_d^2(\Omega_0)} \leq C_{0,t} ||u_0||_{H^1(\Omega_0)} \tag{3.24}$$

and a constant $C_{1,t}$ depending on $d_{1,t} = ||\mathbf{A}||_{L_d^\infty(\Omega_0)}$ such that

$$||\mathbf{A} \cdot \nabla \partial_t u_0||_{L^2(\Omega_0)} \leq C_{1,t} ||\nabla \partial_t u_0||_{L_d^2(\Omega_0)} \leq C_{1,t} ||\partial_t u_0||_{H^1(\Omega_0)}. \tag{3.25}$$

If one collects (3.22)-(3.25), we obtain

$$|\mathcal{A}_{1,t}(u_0,\phi)| \leq 2\gamma_t(C_{0,t}||u_0||_{H^1(\Omega_0)} + C_{1,t}||\partial_t u_0||_{H^1(\Omega_0)})||\phi||_{L^2(\Omega_0)}.$$

For the term $\mathcal{A}_{2,t}$, let us first set: $\widetilde{\mathbf{A}} := c_\infty^{-2}|\mathbf{J}_t^{-1}|\mathbf{A}$, which leads to

$$\begin{aligned} \mathcal{A}_{2,t}(u_0,\phi) &= \int_{\Omega_0} (\widetilde{\mathbf{A}}\overline{\phi}) \cdot \nabla(\mathbf{A}\cdot\nabla u_0) d\Omega_0 \\ &= \int_{\partial\Omega_0} (\widetilde{\mathbf{A}}\cdot\mathbf{n}_0)(\mathbf{A}\cdot\nabla u_0)\overline{\phi} d(\partial\Omega_0) - \int_{\Omega_0} ((\nabla\cdot\widetilde{\mathbf{A}})\overline{\phi} + \widetilde{\mathbf{A}}\cdot\nabla\overline{\phi})(\mathbf{A}\cdot\nabla u_0) d\Omega_0. \end{aligned} \tag{3.26}$$

By assumption, we have: $\partial\Omega_0 = \Sigma \cup \Gamma^{\mathrm{s}} \cup \Gamma_0$. On $\Sigma \cup \Gamma^{\mathrm{s}}$, since there is no deformation, $\mathbf{A}$ is identically equal to $\mathbf{0}$. In addition, the test-functions ϕ are in the space $H^1_{0,0}(\Omega_0)$ and vanish on Γ_0 (as well as on Γ^{s}). Therefore, the boundary term in (3.26) is equal to zero. For the second term, we have

$$\begin{aligned} |\mathcal{A}_{2,t}(u_0,\phi)| &= \left| \int_{\Omega_0} ((\nabla\cdot\widetilde{\mathbf{A}})\overline{\phi} + \widetilde{\mathbf{A}}\cdot\nabla\overline{\phi})(\mathbf{A}\cdot\nabla u_0) d\Omega_0 \right| \\ &\leq \left| \int_{\Omega_0} ((\nabla\cdot\widetilde{\mathbf{A}})\overline{\phi})(\mathbf{A}\cdot\nabla u_0) d\Omega_0 \right| + \left| \int_{\Omega_0} (\widetilde{\mathbf{A}}\cdot\nabla\overline{\phi})(\mathbf{A}\cdot\nabla u_0) d\Omega_0 \right|. \end{aligned} \tag{3.27}$$

For the first term on the right hand side of the above inequality, one gets

$$\left| \int_{\Omega_0} ((\nabla\cdot\widetilde{\mathbf{A}})\overline{\phi})(\mathbf{A}\cdot\nabla u_0) d\Omega_0 \right| \leq C_{3,t}\|u_0\|_{H^1(\Omega_0)}\|\phi\|_{L^2(\Omega_0)}, \tag{3.28}$$

where $C_{3,t}$ is a constant that depends on $\nabla\cdot\widetilde{\mathbf{A}}$ and $\mathbf{A}$. Concerning the second term, we obtain

$$\left| \int_{\Omega_0} (\widetilde{\mathbf{A}}\cdot\nabla\overline{\phi})(\mathbf{A}\cdot\nabla u_0) d\Omega_0 \right| \leq C_{4,t}\|u_0\|_{H^1(\Omega_0)}\|\phi\|_{H^1(\Omega_0)}, \tag{3.29}$$

where the positive constant $C_{4,t}$ is related to $\widetilde{\mathbf{A}}$ and $\mathbf{A}$. Combining (3.27)-(3.29), we deduce that

$$\begin{aligned} |\mathcal{A}_{2,t}(u_0,\phi)| &\leq C_{3,t}\|u_0\|_{H^1(\Omega_0)}\|\phi\|_{L^2(\Omega_0)} + C_{4,t}\|u_0\|_{H^1(\Omega_0)}\|\phi\|_{H^1(\Omega_0)} \\ &\leq C_{2,t}\|u_0\|_{H^1(\Omega_0)}\|\phi\|_{H^1(\Omega_0)}, \end{aligned}$$

with $C_{2,t} = C_{3,t} + C_{4,t}$. Finally, this directly proves the following proposition.

Proposition 3.1. *Let us define $\mathcal{A}_{\epsilon,t}$ $\mathcal{A}_{0,t}$, $\mathcal{A}_{1,t}$ and $\mathcal{A}_{2,t}$, by* (3.17), (3.18), (3.19) *and* (3.20), *respectively, such that* (3.16) *holds. Then, for the solution $u_0 \in C^0([0,T_\ell], H^2_{A,\omega_{\mathrm{f}}t}(\Omega_0))$ such that $\partial_t u_0 \in C^0([0,T_\ell], H^1(\Omega_0))$ and $\partial_t^2 u_0 \in C^0([0,T_\ell], L^2(\Omega_0))$, and for any test-function $\phi \in H^1_{0,0}(\Omega_0)$, we have the following error bounds, for $t > 0$,*

$$\begin{aligned} |\mathcal{A}_{\epsilon,t}(u_0,\phi) - \mathcal{A}_{0,t}(u_0,\phi)| &\leq \epsilon|\mathcal{A}_{1,t}(u_0,\phi)| + \epsilon^2|\mathcal{A}_{2,t}(u_0,\phi)| \\ &\leq \epsilon(C^1_{0,t}\|u_0\|_{H^1(\Omega_0)} + C^1_{1,t}\|\partial_t u_0\|_{L^2(\Omega_0)})\|\phi\|_{H^1(\Omega_0)} \\ &\quad + \epsilon^2 C_{2,t}\|u_0\|_{H^1(\Omega_0)}\|\phi\|_{H^1(\Omega_0)} \end{aligned} \tag{3.30}$$

and

$$\begin{aligned} |\mathcal{A}_{\epsilon,t}(u_0,\phi) - \mathcal{A}_{0,t}(u_0,\phi) - \epsilon\mathcal{A}_{1,t}(u_0,\phi)| &\leq \epsilon^2|\mathcal{A}_{2,t}(u_0,\phi)| \\ &\leq \epsilon^2 C_{2,t}\|u_0\|_{H^1(\Omega_0)}\|\phi\|_{H^1(\Omega_0)}, \end{aligned} \tag{3.31}$$

where we define: $C^1_{0,t} := 2\gamma_t C_{0,t}$, $C^1_{1,t} := 2\gamma_t C_{1,t}$.

From this we conclude that solving the weak formulation (3.11) provides an approximation v of u_0 solution to (3.10) up to a bounded error of order $\mathcal{O}(\epsilon)$. Let us remark that the estimates (3.30) and (3.31) also hold uniformly in time since one can take the maximum of $C^1_{0,t}$, $C^1_{1,t}$ and $C_{2,t}$ over $[0, T_{\max}]$.

In addition, the decompositions (3.21) and (3.16) applied to the formulation (3.11) implies, for $u_0,\ v \in H^1_{A,\omega_{\mathrm{f}}t}(\Omega_0)$ that

$$\mathcal{A}_{\epsilon,t}(u_0,\phi) + \mathcal{R}_t(u_0,\phi) = \mathcal{A}_{0,t}(v,\phi) + \mathcal{R}_t(v,\phi),\ \forall \phi \in H^1_{0,0}(\Omega_0),$$

from which one obtains

$$\mathcal{A}_{0,t}(u_0,\phi) + \epsilon\mathcal{A}_{1,t}(u_0,\phi) + \epsilon^2\mathcal{A}_{2,t}(u_0,\phi) = \mathcal{A}_{0,t}(v,\phi) - \mathcal{R}_t(u_0 - v,\phi).$$

Hence we note that $(u_0 - v) \in H^1_{0,0}(\Omega_0)$ satisfies for all test function $\phi \in H^1_{0,0}(\Omega_0)$

$$\begin{aligned}\mathcal{A}_{0,t}(u_0 - v,\phi) &= -\epsilon\mathcal{A}_{1,t}(u_0,\phi) - \epsilon^2\mathcal{A}_{2,t}(u_0,\phi) - \mathcal{R}_t(u_0 - v,\phi)\\ &= \mathcal{A}_{0,t}(u_0,\phi) - \mathcal{A}_{\epsilon,t}(u_0,\phi) - \mathcal{R}_t(u_0 - v,\phi),\end{aligned}$$

since then Proposition 3.1 provides the expected error estimate if any solution to the above variational problem is continuous with respect to the data. Furthemore, an improved first-order formulation can be obtained thanks to the bilinear form $\mathcal{A}_{0,t} + \epsilon\mathcal{A}_{1,t}$ up to an error $\mathcal{O}(\epsilon^2)$. More precisely, one could replace the bilinear form in (3.11) by $\mathcal{A}_{0,t} + \epsilon\mathcal{A}_{1,t})(v,\phi)$ with

$$\mathcal{A}_{1,t}(v,\phi) = 2\int_{\Omega_0} \frac{1}{c_\infty^2}\partial_t\left(\partial_t\mathbf{\Phi}_t^{-1}\cdot\nabla v\right)\overline{\phi}|\mathbf{J}_t^{-1}|d\Omega_0.$$

However, in the present analysis, we restrict our analysis to (3.11). In the following, we provide a suitable formulation to (3.11) when the motion of the boundary is T_ℓ-periodic in time.

3.2.3 Coupled multi-harmonic Helmholtz-type system

We now assume that the parametrization of Γ_t is periodic with periodicity T_ℓ. Then, the smooth Jacobian $\mathbf{J}_t$ is also a T_ℓ-periodic tensor of class $\mathcal{C}^s$ in time, with $\nu_\ell \ll \nu_{\mathrm{f}}$. Consequently, both $\mathbf{J}_t^{\mathrm{T}}$, $\mathbf{J}_t\mathbf{J}_t^{\mathrm{T}}$, $|\mathbf{J}_t^{-1}|$ and $|\mathbf{J}_t^{-1}|\mathbf{J}_t\mathbf{J}_t^{\mathrm{T}}$ are also time-dependent function/tensors with time periodicity T_ℓ with $\mathcal{C}^s$ regularity according to $t > 0$ and $\mathcal{C}^1$ smoothness in Ω_0 (since the quantities can be expressed as sums and products of T_ℓ-periodic smooth functions). In particular, we have the Fourier series expansions

$$|\mathbf{J}_t^{-1}|\mathbf{J}_t\mathbf{J}_t^{\mathrm{T}} =: \mathbf{C}(\mathbf{x}_0,t) = \sum_{n\in\mathbb{Z}}\mathbf{C}_n(\mathbf{x}_0)e^{in\omega_\ell t} \quad\text{and}\quad |\mathbf{J}_t^{-1}| =: c(\mathbf{x}_0,t) = \sum_{n\in\mathbb{Z}} c_n(\mathbf{x}_0)e^{in\omega_\ell t}, \tag{3.32}$$

for $\mathbf{x}_0 \in \Omega_0$, where

$$\mathbf{C}_n(\mathbf{x}_0) := \frac{1}{T_\ell}\int_{-T_\ell/2}^{T_\ell/2}|\mathbf{J}_t^{-1}|\mathbf{J}_t\mathbf{J}_t^{\mathrm{T}}e^{-in\omega_\ell t}dt \quad\text{and}\quad c_n(\mathbf{x}_0) := \frac{1}{T_\ell}\int_{-T_\ell/2}^{T_\ell/2}|\mathbf{J}_t^{-1}|e^{-in\omega_\ell t}dt.$$

The tensor fields $\mathbf{C}_n$ satisfy $\mathbf{C}_n = \overline{\mathbf{C}_{-n}}$ since $|\mathbf{J}_t^{-1}|\mathbf{J}_t\mathbf{J}_t^{\mathrm{T}}$ is a real-valued matrix. In addition, we have $c_n = \overline{c_{-n}}$ because $|\mathbf{J}_t^{-1}|$ is real-valued. Finally, these two quantities have a $\mathcal{C}^1(\Omega_0)$ regularity.

In view of a numerical implementation of the coefficients $\mathbf{C}_n$ and c_n, we discretize the T_ℓ-periodic motion of Γ_t at $2N+1$ equally spaced sampling times $t_k = k\Delta t_\ell$, $0 \leq k \leq 2N$, at frequency $(2N+1)\nu_\ell$, with time step $\Delta t_\ell := T_\ell/(2N+1)$. This is a natural choice since it avoids any aliasing effect and provides a uniform discretization over one period T_ℓ. In practical applications, the knowledge of ν_ℓ often requires a preliminary analysis and the sampling frequency then has to be chosen carrefully. Moreover, to satisfy the Nyquist-Shannon sampling theorem, $(2\Delta t_\ell)^{-1}$ has to be larger than the maximal frequency arising in $|\mathbf{J}_t^{-1}|\mathbf{J}_t\mathbf{J}_t^{\mathrm{T}}$ and $|\mathbf{J}_t^{-1}|$, represented as (3.32). Thus, we obtain a sequence $\{\Gamma_k\}_{0\leq k\leq 2N}$ of boundaries sampling Γ_t at the discrete times t_k, $0 \leq k \leq 2N$, described through the maps $\mathbf{\Phi}_k := \mathbf{\Phi}_{t_k}$. Therefore, based on the numerical solution of the $2N+1$ local boundary value problems (3.8), we can compute both $\mathbf{C}^k := \mathbf{C}(t_k)$ and $c^k := c(t_k)$ from the discrete Fourier transform (DFT) of $\mathbf{J}_k := \mathbf{J}(t_k)$, evaluated at the discrete times t_k, $0 \leq k \leq 2N$. Consequently, the approximations of $\mathbf{C}$ and c (defined by (3.32)) are given by the following truncated tensor $\mathbf{C}^{\mathcal{N}}$ and function $c^{\mathcal{N}}$

$$\mathbf{C}^{\mathcal{N}}(\mathbf{x}_0,t) := \sum_{n\in\mathcal{N}} \mathbf{C}_n(\mathbf{x}_0)e^{in\omega_\ell t} \quad \text{and} \quad c^{\mathcal{N}}(\mathbf{x}_0,t) := \sum_{n\in\mathcal{N}} c_n(\mathbf{x}_0)e^{in\omega_\ell t}, \tag{3.33}$$

which are all well-defined at any point $\mathbf{x}_0$ in Ω_0. Here, we set $\mathcal{N} := \{n \in \mathbb{Z}; -N \leq n \leq N\}$. We provide in Appendix B the formal relation from the DFT of $|\mathbf{J}_t^{-1}|\mathbf{J}_t\mathbf{J}_t^{\mathrm{T}}$ and $|\mathbf{J}_t^{-1}|$ to the truncated Fourier expansions $\mathbf{C}^{\mathcal{N}}$ and $c^{\mathcal{N}}$.

Since we assumed that $\mathbf{\Phi}_t$ is a T_ℓ-periodic diffeomorphism of class $\mathcal{C}^s$ in time, with $s \geq 2$, then one gets for example for the function c (but a similar property arises for the tensor $\mathbf{C}$), for $j = 0, ..., s$, that it is such that

$$\partial_t^j c(\mathbf{x}_0,t) := \sum_{n\in\mathbb{Z}} \left(\frac{2i\pi n}{T_\ell}\right)^j c_n(\mathbf{x}_0)e^{in\omega_\ell t},$$

for $\mathbf{x}_0 \in \Omega_0$. This implies that $\|c_n\|_{L^\infty(\Omega_0)} = o(|n|^{-s})$, justifying hence that (3.33) are suitable approximations of (3.32) if N is chosen large enough. In particular, if the mapping is $\mathcal{C}^\infty$, then one gets rapidly decaying coefficients since the $o(|n|^{-s})$ asymptotic holds for any $s > 0$ (see Section 3.5 for an illustrative numerical example). Concretely, in a finite element context, the tensor fields $\mathbf{C}_n$ and functions c_n are obtained by using some FFTs, locally on each element of the finite element triangulation, then leading to piecewise constant tensors and functions (see e.g. Sections 3.3 and 3.5.1).

Now and similarly to Chapter 2, we focus on the forced mode $v_{\nu_{\mathrm{f}}}$ of the scattered field, which provides its main contribution. Hence, and without loss of generality, we identify $v_{\nu_{\mathrm{f}}}$ with the solution v of (3.11) which we develop as a Fourier series expansion with complex Fourier coefficients a_j

$$v(\mathbf{x}_0,t) = \sum_{j\in\mathbb{Z}} a_j(\mathbf{x}_0)e^{i\omega_j t} = e^{i\omega_{\mathrm{f}} t}\sum_{j\in\mathbb{Z}} a_j e^{ij\omega_\ell t}, \tag{3.34}$$

for $\mathbf{x}_0 \in \Omega_0$, where $\omega_j := \omega_{\mathrm{f}} + j\omega_\ell = 2\pi\nu_j$, with $\nu_j := \nu_{\mathrm{f}} + j\nu_\ell$. Here, we assume that $a_j \in H^1_{0,0}(\Omega_0)$, meaning that $a_j(\mathbf{x}_0) = 0$ on Γ^{s} for $j \in \mathbb{Z} - \{0\}$, and $a_0 \in H^1_{A,0}(\Omega_0)$, i.e. $a_0(\mathbf{x}_0) = A$ on Γ^{s}. Let us remark that, when v is computed thanks to (3.34), we can deduce the main stationary part of v given by

$$|v_0(\mathbf{x}_0)|^2 = \sum_{j\in\mathbb{Z}} |a_j(\mathbf{x}_0)|^2,$$

since all the remaining terms are slowly oscillating at least relatively to $e^{i\omega_\ell t}$. In view of a numerical procedure, we have to truncate the Fourier series expansion of the unknown v. To this end, let us introduce the finite sets of integers $\mathcal{J} := \{j \in \mathbb{Z} \ ; \ -J \leq j \leq J\}$ and $\mathcal{J}_* := \mathcal{J} - \{0\}$, for a fixed truncation index $J \geq 0$. We denote by $w^{\mathcal{J}}$ the Fourier series expansion (3.34) truncated with $\sharp\mathcal{J} := 2J+1$ terms, i.e.

$$w^{\mathcal{J}}(\mathbf{x}_0, t) = \sum_{j\in\mathcal{J}} a_j(\mathbf{x}_0) e^{i\omega_j t}, \tag{3.35}$$

with $a_j \in H^1_{0,0}(\Omega_0)$, for $j \in \mathcal{J}_*$, and $a_0 \in H^1_{A,0}(\Omega_0)$. The parameter J must be carefully chosen to include the significant contributions to the solution. Let us remark that, similarly to (2.30), the Fourier transform of (3.35) in the sense of distributions is given as a finite sum of Dirac distributions δ_{ν_j} located at the discrete frequencies $\{\nu_j\}_{j\in\mathcal{J}}$, modulated by the functions a_j, i.e. using the definition (2.12)

$$\widehat{w}^{\mathcal{J}} = \sum_{j\in\mathcal{J}} a_j \delta_{\nu_j}.$$

We stress that the global solution $w^{\mathcal{J}}$ in (3.35) is a time dependent expansion, as for (2.28) in Chapter 2, whose (Fourier) coefficients are analogous to the coefficients of the solution $\widehat{w}^{\mathcal{J}}$ of (2.30). This time dependent frequency modes expansion allows to reconstruct directly the wave field. Setting $w^{\mathcal{J}}(\mathbf{x}_0, 0) = 0$ and $\partial_t w^{\mathcal{J}}(\mathbf{x}_0, 0) = 0$ as initial conditions, we obtain, by derivation of (3.35),

$$\partial_t w^{\mathcal{J}}(\mathbf{x}_0, t) = \sum_{j\in\mathcal{J}} i\omega_j a_j e^{i\omega_j t} \quad \text{and} \quad \partial_t^2 w^{\mathcal{J}}(\mathbf{x}_0, t) = -\sum_{j\in\mathcal{J}} \omega_j^2 a_j e^{i\omega_j t}. \tag{3.36}$$

Considering the approximations (3.33) and (3.36), we have

$$\begin{aligned}
c^{\mathcal{N}} \partial_t^2 w^{\mathcal{J}} &= -e^{i\omega_{\mathrm{f}} t} \sum_{n\in\mathcal{N}} c_n e^{in\omega_\ell t} \sum_{j\in\mathcal{J}} \omega_j^2 a_j e^{ij\omega_\ell t} \\
&= -e^{i\omega_{\mathrm{f}} t} \sum_{m=-(J+N)}^{J+N} \Big(\sum_{\substack{j=-J \\ -N\leq m-j\leq N}}^{J} c_{m-j}\omega_j^2 a_j \Big) e^{im\omega_\ell t} \\
&= -\sum_{m=-(J+N)}^{J+N} \Big(\sum_{\substack{j=-J \\ -N\leq m-j\leq N}}^{J} c_{m-j}\omega_j^2 a_j \Big) e^{i\omega_m t},
\end{aligned}$$

with $\omega_m = \omega_{\mathrm{f}} + m\omega_\ell$, since the following identity holds

$$\sum_{n=-N}^{N} \alpha_n \sum_{j=-J}^{J} \beta_j = \sum_{m=-(J+N)}^{J+N} \Big(\sum_{\substack{j=-J \\ -N\leq m-j\leq N}}^{J} \alpha_{m-j}\beta_j \Big).$$

Similarly, one gets in Ω_0

$$\begin{aligned}
\mathbf{C}^{\mathcal{N}} \nabla w^{\mathcal{J}} &= e^{i\omega_{\mathrm{f}} t} \sum_{n\in\mathcal{N}} \mathbf{C}_n e^{in\omega_\ell t} \sum_{j\in\mathcal{J}} \nabla a_j e^{ij\omega_\ell t} \\
&= \sum_{m=-(J+N)}^{J+N} \Big(\sum_{\substack{j=-J \\ -N\leq m-j\leq N}}^{J} \mathbf{C}_{m-j} \nabla a_j \Big) e^{i\omega_m t}.
\end{aligned}$$

Based on these truncated Fourier series expansions and from the previous calculations, we obtain the following approximation of the weak form (3.11): find $a_j \in H^1_{0,0}(\Omega_0)$, for $j \in \mathcal{J}_*$, and $a_0 \in H^1_{A,0}(\Omega_0)$ such that, for any $\phi \in H^1_{0,0}(\Omega_0)$,

$$\sum_{m=-(J+N)}^{J+N} \Big(\sum_{\substack{j=-J \\ -N\leq m-j\leq N}}^{J} \int_{\Omega_0} \mathbf{C}_{m-j}\nabla a_j \cdot \overline{\nabla\phi} d\Omega_0 - \omega_j^2 \int_{\Omega_0} \frac{c_{m-j}}{c_\infty^2} a_j \overline{\phi} d\Omega_0 + \delta_{m-j} \int_\Sigma \frac{i\omega_j}{c_\infty} a_j \overline{\phi} d\Sigma \Big)\, e^{i\omega_m t} \;=\; 0, \tag{3.37}$$

where δ_{m-j} is the delta Kronecker symbol, i.e. $\delta_{m-j} = 1$ if $m = j$, and zero otherwise. Finally, by projecting (3.37) onto the Fourier modes $-J \leq n \leq J$ in the outer sum over m, we obtain the square set of $(2J+1)$ equations with $(2J+1)$ unknowns $\{a\}_{j\in\mathcal{J}}$, for $n \in \mathcal{J}$,

$$\sum_{\substack{j=-J \\ -N\leq n-j\leq N}}^{J} \int_{\Omega_0} \mathbf{C}_{n-j}\nabla a_j \cdot \overline{\nabla\phi} d\Omega_0 - \omega_j^2 \int_{\Omega_0} \frac{c_{n-j}}{c_\infty^2} a_j \overline{\phi} d\Omega_0 + \delta_{n-j} \int_\Sigma \frac{i\omega_j}{c_\infty} a_j \overline{\phi} d\Sigma = 0. \tag{3.38}$$

A first possibility consists in assuming that we fix $N = 2J$ to get access to the $(4J+1)$ Fourier coefficients $(\mathbf{C}_n)_{-2J\leq n\leq 2J}$ and $(c_n)_{-2J\leq n\leq 2J}$. Then, (3.38) writes, for $n \in \mathcal{J}$,

$$\sum_{\substack{j=-J \\ -2J\leq n-j\leq 2J}}^{J} \int_{\Omega_0} \mathbf{C}_{n-j}\nabla a_j \cdot \overline{\nabla\phi} d\Omega_0 - \omega_j^2 \int_{\Omega_0} \frac{c_{n-j}}{c_\infty^2} a_j \overline{\phi} d\Omega_0 + \delta_{n-j} \int_\Sigma \frac{i\omega_j}{c_\infty} a_j \overline{\phi} d\Sigma = 0.$$

This first choice leads to a global weak form with $(2J+1) \times (2J+1)$ blocks involving sparse matrices. Let us now assume that we compute the $(2J+1)$ first Fourier coefficients in (3.33), i.e. $N = J$. This has the advantage of considering less modal coupling between the geometry and the unknown expansions when computing their products. As a consequence, the resulting $(2J+1) \times (2J+1)$ system is given by a $2J+1$ band limited coupled system, for $n \in \mathcal{J}$,

$$\sum_{\substack{j=-J \\ -J\leq n-j\leq J}}^{J} \int_{\Omega_0} \mathbf{C}_{n-j}\nabla a_j \cdot \overline{\nabla\phi} d\Omega_0 - \omega_j^2 \int_{\Omega_0} \frac{c_{n-j}}{c_\infty^2} a_j \overline{\phi} d\Omega_0 + \delta_{n-j} \int_\Sigma \frac{i\omega_j}{c_\infty} a_j \overline{\phi} d\Sigma = 0,$$

involving $3J^2 + 3J + 1$ blocks, instead of $4J^2 + 4J + 1$ for the first approach.

More generally, if one only retains $2N+1$ terms in the Fourier expansions (3.33), leading to indices $-N \leq n - j \leq N$ in (3.38), then the global system is still block banded, with band length $2N-1$, and requires $n_{(N,J)} := (4N+2)J + (1+N-N^2)$ blocks. From these remarks, we will say that the Fourier approximation is of order (N, J) when we consider an approximation of the unknown $w^{\mathcal{J}}$ given by (3.35) with $2J+1$ Fourier terms, and $2N+1$ ($0 \leq N \leq 2J$) Fourier coefficients for the geometrical quantities, based on (3.33). The $(2J+1) \times (2J+1)$ system to be solved is then given by (3.38), for $n \in \mathcal{J}$, and writes

$$\mathcal{A}_j(a_j, \phi) = \mathcal{L}_j(\phi), \tag{3.39}$$

with the bilinear form

$$\mathcal{A}_j(a_j,\phi) := \sum_{\substack{j=-J \\ -N\leq n-j\leq N}}^{J} \int_{\Omega_0} \mathbf{C}_{n-j}\nabla a_j \cdot \overline{\nabla\phi} d\Omega_0 - \omega_j^2 \int_{\Omega_0} \frac{c_{n-j}}{c_\infty^2} a_j \overline{\phi} d\Omega_0 + \delta_{n-j} \int_\Sigma \frac{i\omega_j}{c_\infty} a_j \overline{\phi} d\Sigma,$$

and

$$\mathcal{L}_j(\phi) := -\mathcal{A}_j(a_{\mathrm{g},j},\phi).$$

Here we introduced the natural lift $\{a_{\mathrm{g},j}\}_{j\in\mathcal{J}}$ where $a_{\mathrm{g},j} \in H^1_{0,0}(\Omega_0)$ for $j \neq 0$ and $a_{g,0} \in H^1_{A,0}(\Omega_0)$, such that $a_{\mathrm{g},j} = 0$ on $\Omega_0 \cup \Sigma$. This choice justifies that, for the sake of conciseness, we kept the same notations for the unknowns of (3.38) and (3.39), considering the direct sum $H^1_{A,0}(\Omega_0) = a_{g,0} \bigoplus H^1_{0,0}(\Omega_0)$.

When solving (3.38), the approximation of order (N,J) of the solution $w^{\mathcal{J}}$ is defined by

$$w^{(N,J)}(\mathbf{x}_0,t) = \sum_{j\in\mathcal{J}} a_j^{(N,J)}(\mathbf{x}_0) e^{i\omega_j t}, \tag{3.40}$$

where the $a_j^{(N,J)}$, $j \in \mathcal{J}$, are the $2J+1$ unknown functions associated to (3.38). Similarly, one defines the approximation $\widehat{w}^{(N,J)}$ of order (N,J) of the frequency domain solution $\widehat{w}^{\mathcal{J}}$.

Finally, let us remark that the case of inhomogeneous media, i.e. when the speed is space dependent ($c_\infty = c_\infty(\mathbf{x}_0)$), is considered in Sections 3.3 and 3.5. To this end, we directly adapt the previous formulation by considering a piecewise constant finite element approximation of the velocity, according to the local properties of the media.

Now, it is very interesting to have an overview of the link between the solution $\widehat{w}^{(N,J)}$ of order (N,J) in Ω_0 proposed by the multi-harmonic finite element method, and the real solution u of the initial problem (3.1) in the moving domain Ω_t. In particular, the process of recovering u from $\widehat{w}^{(N,J)}$ is detailed in Figure 3.4.

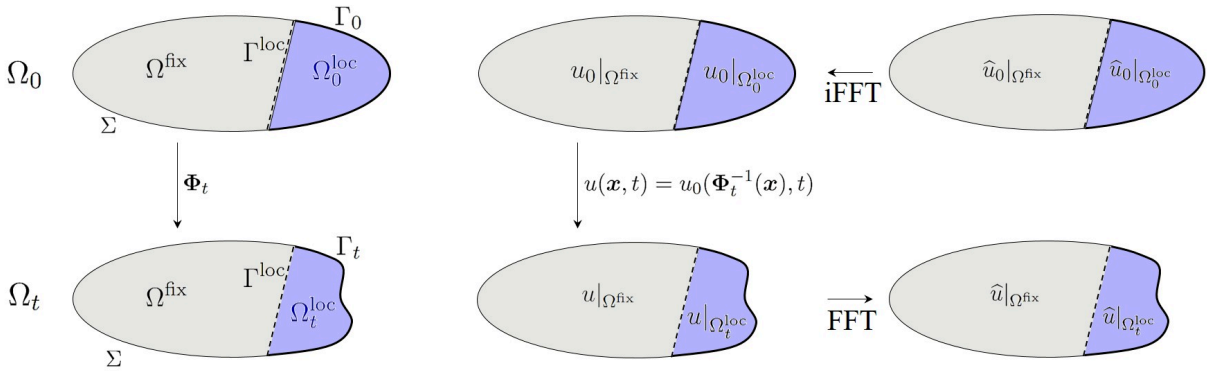

Figure 3.4: Overall scheme representing the solution of the moving boundary problem, in frequency and time domains and evaluated in both moving and fixed domains Ω_t and Ω_0.

We first recall that the vector flow $\mathbf{\Phi}_t$ acts as the identity over the common static part Ω^{fix} of both moving and fixed domains Ω_t and Ω_0. Hence, and as highlighted in Section 3.2.1, we trivially

have

$$u_0|_{\Omega^{\text{fix}}} \equiv u|_{\Omega^{\text{fix}}},$$

where $u|_{\Omega^{\text{fix}}}$ and $u_0|_{\Omega^{\text{fix}}}$ are respectively the restrictions to Ω^{fix} of the solutions u of (3.1) and u_0 of (3.10). Of course, the same holds for the restrictions $\widehat{u}|_{\Omega^{\text{fix}}}$ and $\widehat{u}_0|_{\Omega^{\text{fix}}}$ of the Fourier transforms of u and u_0. At the same time, we recover $u|_{\Omega_t^{\text{loc}}}$ from $u_0|_{\Omega_0^{\text{loc}}}$ by applying the previous definition

$$u(\boldsymbol{x}, t) = u_0(\boldsymbol{\Phi}_t^{-1}(\boldsymbol{x}), t).$$

Finally, since $\widehat{w}^{(N,J)}$ is designed as an approximation of $\widehat{u}_0$, then it immediately provides an approximation of the spectrum $\widehat{u}$ of u in Ω^{fix}. This observation is of great importance because, in practice, the position of the receiver where we evaluate the spectrum of the scattered field is located in the fixed area Ω^{fix}. Otherwise, we remark that the restriction $\widehat{w}^{(N,J)}|_{\Omega_0^{\text{loc}}}$ leads to the desired solution $\widehat{u}|_{\Omega_t^{\text{loc}}}$ in the deformed area Ω_t^{loc} by applying successively the iFFT, the inverse change of metric $\boldsymbol{\Phi}_t^{-1}$ and the FFT as described in Figure 3.4.

3.3 Finite element approximation

Let us consider a fixed covering $\Omega_{0,h} = \Omega_h(0)$ of Ω_0 with $n_{0,h}$ triangular/tetrahedral elements in 2D/3D. We also set $n_{0,h}^{\text{loc}}$ as the number of elements involved in the discrete domain $\Omega_{0,h}^{\text{loc}}$ interpolating Ω_0^{loc}. The basis functions of the $\mathbb{P}_1$ finite element approximation are denoted by $\{\phi_j\}_{1 \leq j \leq n_{\text{dof}}}$, where n_{dof} is the number of degrees of freedom for the Lagrange finite element approximation of $H^1_{0,0}(\Omega_0)$. For $j \in \mathcal{J}$, we designate by $a_{j,h}^{(N,J)}$ the $\mathbb{P}_1$ finite element approximation of $a_j^{(N,J)}$ and define the interpolated field $w_h^{(N,J)}$ in $\Omega_{0,h}$ approximating (3.40)

$$w_h^{(N,J)}(\mathbf{x}_{0,h}, t) = \sum_{j \in \mathcal{J}} a_{j,h}^{(N,J)}(\mathbf{x}_{0,h}) e^{i\omega_j t}. \tag{3.41}$$

Higher-order finite element methods (or alternative spatial discretization methods) could be used to increase the accuracy as well as to minimize the dispersion/pollution error related to high frequency time-harmonic wave problems [59]. The representation in the finite element basis of the unknown wave field $w_h^{(N,J)}$ built from the (N,J)-approximation is given by the vector $\boldsymbol{w}^{(N,J)} = (\boldsymbol{a}_{-J}^{(N,J)}, ..., \boldsymbol{a}_0^{(N,J)}, ..., \boldsymbol{a}_J^{(N,J)})^{\mathrm{T}}$, with vector components $\boldsymbol{a}_j^{(N,J)} \in \mathbb{C}^{n_{\text{dof}}}$, $j \in \mathcal{J}$. Therefore, $\boldsymbol{w}^{(N,J)}$ is an element of $\mathbb{C}^{n_{\text{dof}}^J}$, with $n_{\text{dof}}^J = (2J+1)n_{\text{dof}}$.

Let us briefly explain how to build the linear system related to (3.38). To compute $\mathbf{J}_{k,h}$, which is the $\mathbb{P}_0$ finite element approximation of $\mathbf{J}_k$ on $\Omega_{0,h}$, we solve (3.8) under its weak form. This leads to the solution of $(2N+1)$ variational problems with unknown discrete d-dimensional deformations $\boldsymbol{\Phi}_{k,h}$, $0 \leq k \leq 2N$, in the small local fixed domain $\Omega_{0,h}^{\text{loc}}$, where only the boundary condition on $\Gamma_{0,h}$ changes at index k. This means that the matrix associated with the linear system resulting from the discretization of (3.8) remains unchanged while the contribution of the boundary conditions modifies the right-hand side of the linear system to solve. To this end, a Cholesky factorization of the sparse symmetrical positive definite matrix (here, the stiffness matrix for the Laplacian) can be used before the time loop over k while only $2d$ sparse triangular linear systems can next be efficiently solved for each new right-hand side at step k, with $k = 0, ..., 2N$. Based on $\mathbb{P}_1$ finite elements,

one gets the finite sequence of discretized deformations $\mathbf{\Phi}_{k,h}$, $0 \leq k \leq 2N$. Then $\mathbf{J}_{k,h}$ is obtained by a simple numerical derivation through the discrete gradients and based on (3.9), corresponding to $\mathbb{P}_0$ approximations of the sequence of Jacobians, and piecewise constant tensors/functions $\mathbf{C}_h^k$ and c_h^k. As a consequence, on each element in $\Omega_{0,h}^{\text{loc}}$, a Fourier series expansion can be computed locally to get $\mathbf{C}_{n,h}$ and $c_{n,h}$, $-N \leq n \leq N$, from the sampling $\mathbf{C}_h^k$ and c_h^k, $0 \leq k \leq 2N$. The main computational cost in this procedure is related to the FFT computations locally on each element of the domain $\Omega_{0,h}^{\text{loc}}$ to obtain $\mathbf{C}_{n,h}$ and $c_{n,h}$, $-N \leq n \leq N$, which means $\mathcal{O}(n_{0,h}^{\text{loc}} N \log(N))$ operations.

Let us now introduce the generalised finite element stiffness matrix $\mathbf{K}_n$ and mass matrix $\mathbf{M}_n$, for $-N \leq n \leq N$, respectively given by the $n_{\text{dof}} \times n_{\text{dof}}$ matrices

$$(\mathbf{K}_n)_{\imath,\jmath} := \int_{\Omega_{0,h}} \mathbf{C}_{n,h} \nabla \phi_\imath \cdot \overline{\nabla \phi_\jmath} d\Omega_{0,h}, \quad (\mathbf{M}_n)_{\imath,\jmath} := \int_{\Omega_{0,h}} \frac{c_{n,h}}{c_\infty^2} \phi_\imath \overline{\phi_\jmath} d\Omega_{0,h}, \quad 1 \leq \imath, \jmath \leq n_{\text{dof}}.$$

These two symmetrical complex-valued sparse matrices are such that: $\mathbf{K}_n = \overline{\mathbf{K}_{-n}}$, $\mathbf{M}_n = \overline{\mathbf{M}_{-n}}$ (if c_∞ is real-valued). In addition, we need the real-valued highly sparse generalised mass matrix $\mathbf{M}_\Sigma$ on the fixed interpolated fictitious boundary Σ_h (but considered as a $n_{\text{dof}} \times n_{\text{dof}}$ matrix)

$$(\mathbf{M}_\Sigma)_{\imath,\jmath} := \int_{\Sigma_h} \frac{1}{c_\infty} \phi_\imath \overline{\phi_\jmath} \, d\Sigma_h, \quad 1 \leq \imath, \jmath \leq n_{\text{dof}},$$

where c_∞ can be assumed to be defined constant by element, i.e. as the $\mathbb{P}_0$ approximation of the space-dependent velocity c_∞. Let us remark that considering a non-homogeneous medium inside the domain (i.e. different physical materials) leads to non constant velocity c_∞ according to the space variable, and therefore to additional coupled terms due to the metric change. For the $\mathbb{P}_0$ approximation, both approaches are identical.

We now introduce some block banded matrix notations (i.e. apart from a fixed number of block diagonals, the block sub-matrices are vanishing). We define $\mathbf{S}^{(N,J)}$ as the block Toeplitz matrix, with $(2J+1) \times (2J+1)$ blocks and bandwidth equal to $2N+1$, based on a collection of $n_{\text{dof}} \times n_{\text{dof}}$ sparse complex-valued elementary matrices $\mathbf{S}_n$, $-N \leq n \leq N$, such that

$$\mathbf{S}^{(N,J)} = \begin{pmatrix} \mathbf{S}_0 & \cdots & \mathbf{S}_{-N} & \mathbf{0} & \cdots & \mathbf{0} \\ \vdots & \ddots & & \ddots & \ddots & \vdots \\ \mathbf{S}_N & & \ddots & & \ddots & \mathbf{0} \\ \mathbf{0} & \ddots & & \ddots & & \mathbf{S}_{-N} \\ \vdots & & \ddots & & \ddots & \vdots \\ \mathbf{0} & \cdots & \mathbf{0} & \mathbf{S}_N & \cdots & \mathbf{S}_0 \end{pmatrix}.$$

Let us consider the global stiffness matrix $\mathbf{K}^{(N,J)}$ associated with $\mathbf{K}_n$, $n \in \mathcal{N}$, which is a block Toeplitz matrix, with bandwidth $2N+1$. In addition, it is generated by the $N+1$ elementary matrices $\mathbf{K}_n$, $n = 0, ..., N$, since $\mathbf{K}_{-n} = \overline{\mathbf{K}_n}$. If the storage of one elementary stiffness matrix is γn_{dof}, with $\gamma > 0$ a small constant that depends on the mesh interconnections, then storing $\mathbf{K}^{(N,J)}$ needs $\gamma(N+1)n_{\text{dof}}$ coefficients. Similarly, we can introduce the global mass matrix $\mathbf{M}^{(N,J)}$, based on the elementary blocks $\mathbf{M}_n$, $n = 0, ..., N$, with similar properties as $\mathbf{K}^{(N,J)}$. To simplify the explanations, we assume that storing $\mathbf{M}_n$ also needs γn_{dof} complex values. Now, let us consider

the two diagonal matrices

$$\boldsymbol{\omega}^{(J)} = \mathrm{diag}(\omega_j)_{j\in\mathcal{J}} \otimes \mathbf{I}_{n_{\mathrm{dof}}} = \begin{pmatrix} \omega_{-J}\mathbf{I}_{n_{\mathrm{dof}}} & \mathbf{0} & \cdots & \mathbf{0} \\ \mathbf{0} & \ddots & \ddots & \vdots \\ \vdots & \ddots & \ddots & \mathbf{0} \\ \mathbf{0} & \cdots & \mathbf{0} & \omega_J\mathbf{I}_{n_{\mathrm{dof}}} \end{pmatrix}$$

and similarly

$$\boldsymbol{\omega}^{2,(J)} = \mathrm{diag}(\omega_j^2)_{j\in\mathcal{J}} \otimes \mathbf{I}_{n_{\mathrm{dof}}},$$

where $\mathbf{I}_{n_{\mathrm{dof}}}$ designates the unitary matrix of size $n_{\mathrm{dof}} \times n_{\mathrm{dof}}$. We also need the matrix $\mathbf{M}_\Sigma^{(J)}$, where $\mathbf{M}_\Sigma$ is repeated $(2J+1)$ times on the diagonal, i.e.:

$$\mathbf{M}_{\Sigma_h}^{(J)} = \mathbf{I}_{2J+1} \otimes \mathbf{M}_{\Sigma_h} = \begin{pmatrix} \mathbf{M}_{\Sigma_h} & \mathbf{0} & \cdots & \mathbf{0} \\ \mathbf{0} & \ddots & \ddots & \vdots \\ \vdots & \ddots & \ddots & \mathbf{0} \\ \mathbf{0} & \cdots & \mathbf{0} & \mathbf{M}_{\Sigma_h} \end{pmatrix}.$$

Both its construction cost and memory storage are negligible compared with $\mathbf{K}^{(N,J)}$ and $\mathbf{M}^{(N,J)}$ since $\mathbf{M}_\Sigma$ is only related to the boundary nodes on Σ_h.

Now we set

$$\mathbf{A}_{\boldsymbol{\omega}^{(J)}}^{(N,J)} := \mathbf{K}^{(N,J)} - \mathbf{M}^{(N,J)}\boldsymbol{\omega}^{2,(J)} + i\boldsymbol{\omega}^{(J)}\mathbf{M}_\Sigma^{(J)}, \tag{3.42}$$

where $\mathbf{A}_{\boldsymbol{\omega}^{(J)}}^{(N,J)} := \left(\mathbf{A}_{\boldsymbol{\omega}^{(J)},j,n}^{(N,J)}\right)_{(j,n)\in\mathcal{J}\times\mathcal{J}}$ which is a block banded and near block Toeplitz matrix (each descending block diagonal from left to right is almost constant), due to the presence of the matrices $\mathbf{M}^{(N,J)}\boldsymbol{\omega}^{(J),2}$ and $\boldsymbol{\omega}^{(J)}\mathbf{M}_\Sigma^{(J)}$. In addition, we have the block hermitian property: $\mathbf{A}_{\boldsymbol{\omega}^{(J)},j,n}^{(N,J)} = \overline{\mathbf{A}_{\boldsymbol{\omega}^{(J)},n,j}^{(N,J)}}$, for $(j,n) \in \mathcal{J}_* \times \mathcal{J}_*$. Hence, the finite element solution of (3.38) implies that the boundary conditions generate a right hand side vector $\mathbf{b}^{(N,J)} \in \mathbb{C}^{n_{\mathrm{dof}}^J}$ based on the collection $\{\mathcal{L}_j(\phi)\}_{j\in\mathcal{J}}$. Finally, this yields the block linear system

$$\mathbf{A}_{\boldsymbol{\omega}^{(J)}}^{(N,J)}\boldsymbol{w}^{(N,J)} = \mathbf{b}^{(N,J)}. \tag{3.43}$$

3.4 Efficient solution of the linear system

Let us now focus on the efficient numerical solution of the linear system (3.43). The storage of the matrix $\mathbf{A}_{\boldsymbol{\omega}^{(J)}}^{(N,J)}$ is given by the matrices $\mathbf{K}^{(N,J)}$, $\mathbf{M}^{(N,J)}$ and $\mathbf{M}_\Sigma^{(J)}$, and the brute-force application of a direct solver is not computationally tractable in the high-frequency regime even for moderate values of N and J, as each single high-frequency Helmholtz-type problem is already known to be extremely challenging, requiring the use of advanced solvers [41, 66].

Here, our aim is to show that solving (3.43) scales as $(2J+1)$ calls to robust single high-frequency Helmholtz-type solvers through an iterative process based on a preconditioned GMRES [82, 83]. One of the key ingredients of GMRES is to compute the Matrix-Vector Products (MVPs) $\boldsymbol{y} \leftarrow \mathbf{A}_{\boldsymbol{\omega}^{(J)}}^{(N,J)}\boldsymbol{x}$, where $\boldsymbol{x}$ and $\boldsymbol{y}$ are some complex-valued vectors in $\mathbb{C}^{n_{\mathrm{dof}}^J}$. In our situation, this can

be easily achieved blockwise, based on the Toeplitz storage. Since $\mathbf{A}^{(N,J)}_{\boldsymbol{\omega}^{(J)}}$ has $n_{(N,J)} := (4N+2)J + (1+N-N^2)$ blocks, then each global MVP has a cost $2\gamma n_{\rm dof} n_{(N,J)}$. In practice, N is often smaller than J (see Section 3.5). Therefore, asymptotically, the cost of a MVP is about $8\gamma n_{\rm dof} NJ$, which means that it scales linearly with J. Another crucial point of the acceleration of the GMRES is to use a preconditioner. Here, we build a left preconditioner $\mathbf{P}$ such that $\mathbf{P}\mathbf{A}^{(N,J)}_{\boldsymbol{\omega}^{(J)}} \approx \mathbf{I} := \mathbf{I}_{n_{\rm dof}(2J+1)}$ to improve the convergence rate of the Krylov method. A robust preconditioner $\mathbf{P}$ for GMRES must yield a clustering of the eigenvalues of $\mathbf{P}\mathbf{A}^{(N,J)}_{\boldsymbol{\omega}^{(J)}}$ around $(1,0)$ in the complex plane [82]. Since we have a Toeplitz storage of $\mathbf{A}^{(N,J)}_{\boldsymbol{\omega}^{(J)}}$, we cannot easily build an approximation of $(\mathbf{A}^{(N,J)}_{\boldsymbol{\omega}^{(J)}})^{-1}$. Let us instead consider the splitting: $\mathbf{A}^{(N,J)}_{\boldsymbol{\omega}^{(J)}} = \mathbf{A}^{(0,J)}_{\boldsymbol{\omega}^{(J)}} + \Delta\mathbf{A}^{(N,J)}_{\boldsymbol{\omega}^{(J)}}$, where $\mathbf{A}^{(0,J)}_{\boldsymbol{\omega}^{(J)}} := \mathrm{diag}(\mathbf{A}^{(0,J)}_{\omega_j})_{j\in\mathcal{J}}$ is the static part of $\mathbf{A}^{(N,J)}_{\boldsymbol{\omega}^{(J)}}$, i.e. the block $\mathbf{A}^{(0,J)}_{\omega_j} := \left(\mathbf{A}^{(0,J)}_{\boldsymbol{\omega}^{(J)},j,j}\right) = \mathbf{K}_0 - \omega_j^2\mathbf{M}_0 + i\omega_j\mathbf{M}_\Sigma$, for $j \in \mathcal{J}$, which is a Helmholtz-type problem associated to the zeroth-order terms $\mathbf{C}_0$ and c_0 in the Fourier expansions (3.33). Let us assume that we have access to an efficient solver for each linear system associated to the j-th block matrix $\mathbf{A}^{(0,J)}_{\omega_j}$. Then, we could consider a preconditioner $\mathbf{P}$ based on the "inversion" of the $2J+1$ diagonal blocks, which means solving an associated linear system for each $j \in \mathcal{J}$. Nevertheless, since j is changing, the linear systems are j-dependent. Let us recall that: $\omega_j = \omega_{\rm f} + j\omega_\ell$, with $\omega_{\rm f} \gg \omega_\ell$. This means that we can consider the high-frequency approximation $\omega_j \approx \omega_{\rm f} = \omega_0$ with associated block diagonal preconditioner $\mathbf{P} := \mathrm{diag}((\mathbf{A}^{(0,J)}_{\omega_0})^{-1})_{j\in\mathcal{J}} = \mathbf{A}^{-(0,J)}_{\boldsymbol{\omega}^{(0)}}$. Since we are solving the preconditioned linear system

$$\mathbf{P}\mathbf{A}^{(N,J)}_{\boldsymbol{\omega}^{(J)}}\boldsymbol{w}^{(N,J)} = \mathbf{P}\mathbf{b}^{(N,J)}, \tag{3.44}$$

we then have $\mathbf{P}\mathbf{A}^{(N,J)}_{\boldsymbol{\omega}^{(J)}} = \mathbf{I} + \mathbf{Q}^{(N,J)}_{\boldsymbol{\omega}^{(J)}}$, where $\mathbf{Q}^{(N,J)}_{\boldsymbol{\omega}^{(J)}}$ is expected to be a small perturbation of the identity matrix $\mathbf{I}$. The application of the preconditioner $\mathbf{P}$ at each GMRES iteration requires to solve the linear system

$$\mathbf{A}^{(0,J)}_{\omega_0}\mathbf{x}_j = \mathbf{b}_j, \tag{3.45}$$

for $2J+1$ right hand sides $\mathbf{b}_j$, $j \in \mathcal{J}$. Therefore, the cost for the application of the preconditioner in each iteration is equal to $(2J+1)$ times the cost of solving (3.45). In practice, a sparse LU factorization of $\mathbf{P}$ is computed before entering into the GMRES iteration loop after reordering the unknowns by a Cuthill-MacKee algorithm. This then leads to an exact factorization $\mathbf{A}^{(0,J)}_{\omega_0} = \mathbf{L}_{\omega_0}\mathbf{U}_{\omega_0}$ and block LU preconditioner $\mathbf{P}$. Let us remark that incomplete LU factorizations $\mathbf{A}^{(0,J)}_{\omega_0} \simeq \widetilde{\mathbf{L}}_{\omega_0}\widetilde{\mathbf{U}}_{\omega_0}$ (or possibly other single-frequency more advanced preconditioners) can alternatively be used [82]. Applying such LU preconditioners $\mathbf{P}$ requires the solution to $2(2J+1)$ decoupled upper/lower sparse complex-valued triangular systems.

Remark 5. *Let us remark that, under the high-frequency assumption $\omega_j \approx \omega_0 = \omega_f$, $j \in \mathcal{J}$, for $\omega_\ell \ll \omega_f$, the linear system (3.43)-(3.42) can be approximated by*

$$\mathbf{A}^{(N,J)}_{\boldsymbol{\omega}^{(0)}}\boldsymbol{w}^{(N,J)}_{\boldsymbol{\omega}^{(0)}} = \mathbf{b}^{(N,J)}, \tag{3.46}$$

setting

$$\mathbf{A}^{(N,J)}_{\boldsymbol{\omega}^{(0)}} := \mathbf{K}^{(N,J)} - \omega_f^2\mathbf{M}^{(N,J)} + i\omega_f\mathbf{M}^{(J)}_\Sigma.$$

The matrix $\mathbf{A}_{\boldsymbol{\omega}^{(0)}}^{(N,J)}$ *has* $(2J+1)\times(2J+1)$ *blocks, each one being* ω_j *independent (unlike* $\mathbf{A}_{\boldsymbol{\omega}^{(J)}}^{(N,J)}$*), leading to a block Toeplitz structure. More precisely, the matrix writes*

$$\mathbf{A}_{\boldsymbol{\omega}^{(0)}}^{(N,J)} = \begin{pmatrix} \mathbf{T}_0 & \cdots & \mathbf{T}_{-N} & \mathbf{0} & \cdots & \mathbf{0} \\ \vdots & \ddots & & \ddots & \ddots & \vdots \\ \mathbf{T}_N & & \ddots & & \ddots & \mathbf{0} \\ \mathbf{0} & \ddots & & \ddots & & \mathbf{T}_{-N} \\ \vdots & & \ddots & & \ddots & \vdots \\ \mathbf{0} & \cdots & \mathbf{0} & \mathbf{T}_N & \cdots & \mathbf{T}_0 \end{pmatrix},$$

with $\mathbf{T}_0 = \mathbf{A}_{\omega_0}^{(0,J)}$, $\mathbf{T}_n = \mathbf{A}_{\omega_0}^{(n,J)} = \mathbf{K}_n - \omega_f^2 \mathbf{M}_n$ *and* $\mathbf{T}_{-n} = \overline{\mathbf{T}_n}$, $0 \leq n \leq N$. *Therefore, one gets*

$$\mathbf{A}_{\boldsymbol{\omega}^{(J)}}^{(N,J)} = \mathbf{A}_{\boldsymbol{\omega}^{(0)}}^{(N,J)} + \frac{\omega_\ell \omega_f}{c_\infty^2} \mathbf{Q}^{(N,J)},$$

where $\mathbf{Q}^{(N,J)}$ *can be expressed in terms of mass matrices that can then be bounded in norms. Gathering* (3.43) *and* (3.46) *yields*

$$\begin{aligned} \left(\boldsymbol{w}^{(N,J)} - \boldsymbol{w}_{\boldsymbol{\omega}^{(0)}}^{(N,J)}\right) &= -\left(\mathbf{A}_{\boldsymbol{\omega}^{(J)}}^{(N,J)}\right)^{-1} \left(\mathbf{A}_{\boldsymbol{\omega}^{(J)}}^{(N,J)} - \mathbf{A}_{\boldsymbol{\omega}^{(0)}}^{(N,J)}\right) \boldsymbol{w}_{\boldsymbol{\omega}^{(0)}}^{(N,J)} \\ &= -\left(\mathbf{A}_{\boldsymbol{\omega}^{(J)}}^{(N,J)}\right)^{-1} \frac{\omega_\ell \omega_f}{c_\infty^2} \mathbf{Q}^{(N,J)} \boldsymbol{w}_{\boldsymbol{\omega}^{(0)}}^{(N,J)} \end{aligned}$$

and a direct computation shows that we have

$$\frac{\|\boldsymbol{w}^{(N,J)} - \boldsymbol{w}_{\boldsymbol{\omega}^{(0)}}^{(N,J)}\|}{\|\boldsymbol{w}_{\boldsymbol{\omega}^{(0)}}^{(N,J)}\|} \leq \frac{\omega_\ell \omega_f}{c_\infty^2} \mathrm{cond}\left(\mathbf{A}_{\boldsymbol{\omega}^{(J)}}^{(N,J)}\right) \frac{\|\mathbf{Q}^{(N,J)}\|}{\|\mathbf{A}_{\boldsymbol{\omega}^{(J)}}^{(N,J)}\|}$$

for a given matrix norm $\|\mathbf{A}\|$ *of a matrix* $\mathbf{A}$ *and where the condition number is defined by* $\mathrm{cond}(\mathbf{A}) = \|\mathbf{A}\| \times \|\mathbf{A}^{-1}\|$. *Storing* $\mathbf{A}_{\boldsymbol{\omega}^{(0)}}^{(N,J)}$ *still requires* $\gamma(N+1)n_{dof}$ *complex coefficients. Solving (3.46) can be expected to provide a suitable solution to the problem, under the assumption* $\frac{\omega_\ell \omega_f}{c_\infty^2} \ll 1$*, by using an algorithm based on fast block Toeplitz solvers [5]. In particular, we propose in Appendix C an alternative approach to handle the resolution of (3.46), tacking into account the block Toeplitz storage of the matrices and based on the circulant extensions. In addition, one may also use* $\mathbf{A}_{\boldsymbol{\omega}^{(0)}}^{(N,J)}$ *to build a banded limited preconditioner by dropping some off-diagonal blocks* $\mathbf{T}_n$ *for solving (3.42), then generalising* $\mathbf{P} = \mathbf{A}_{\boldsymbol{\omega}^{(0)}}^{-(0,J)}$.

More generally, we refer to [44] for block Toeplitz matrix preconditioning techniques, mostly based on circulant and block-circulant preconditioners [9, 60] which are very efficiently invertible as they are diagonalisable by the DFT matrices. We notably make use of this property in the approach proposed in Appendix C. It can also be interesting to consider the preconditioning of the linear system (3.46) *by* $\mathbf{P} = \mathbf{A}_{\boldsymbol{\omega}^{(0)}}^{-(0,J)}$. *This leads to a particular block Toeplitz system for which we propose in Appendix C an approach based on Neumann series expansion.*

3.5 Application to a model problem

3.5.1 Description of the problem

We now apply the proposed method to a simplified two-dimensional test-case motivated by the high-frequency radar detection of a breathing baby installed in a child seat located on the rear seat of a car. Let us consider the initial geometry at $t = 0$ depicted in Figure 3.5, which represents the two-dimensional longitudinal section of the interior of a car. The computational domain Ω_0 is delimited by the shape of the car, including the surface of the body of the baby in his seat, facing the road. We assume that the red parts of the car, called Σ_0, are Perfectly Electric Conductors (PEC), i.e. we impose a homogeneous Dirichlet boundary condition. In addition, the belly of the baby Γ_0 (black part on Figure 3.5) is also considered as a PEC assuming e.g. that the baby is wearing a perfectly conducting jacket which reflects the wave field created by an antenna modeled by an extruded circle Γ_s placed near the roof of the car, above the rear seat. This antenna is assumed to be isotropic, and emits a transverse electromagnetic (TEM) field of amplitude $A > 0$ and high-frequency ν_f. The belly of the baby is the part Γ_t of the boundary that moves in the modeling. At $t = 0$, Γ_0 is a curved segment with two endpoints $\mathbf{p}_1$ and $\mathbf{p}_2$. Finally, the rest of the surface of the car, called Σ_1 (blue part on Figure 3.5), is considered to be non-reflecting as a rough approximation, assuming that it is constituted e.g. of glass or synthetic materials. This is modelled by the zeroth-order absorbing boundary condition (3.3). Therefore, within our notations, Ω_0 is the domain with boundary $\Gamma_0 \cup \Gamma^s \cup \Sigma_0 \cup \Sigma_1$, while $\partial\Omega_t := \Gamma_t \cup \Gamma^s \cup \Sigma_0 \cup \Sigma_1$. In Ω_0, we consider that, except in the seats (grey parts), we have some air. Therefore, we model the propagation of the wave in Ω_0^{air} by the velocity c^{air} of the light in the air. In the seats Ω_0^{seat}, we have specific dielectric materials where the velocity takes different values, depending on the refraction index. More precisely, Ω_0^{seat} models the seat foam (gray volume in Figure 3.5) with complex-valued constant velocity c^{seat} and refractive coefficient (with the air) η^{seat}, obtained from (3.48)

In accordance with Section 1.2, we recall that $c^{\text{air}} = 1/\sqrt{\mu^{\text{air}}\varepsilon^{\text{air}}}$ and $c^{\text{seat}} = 1/\sqrt{\mu^{\text{seat}}\varepsilon^{\text{seat}}}$, where $\mu^{\text{air,seat}}$ and $\varepsilon^{\text{air,seat}}$ are respectively the magnetic permeability and electric permittivity of the vacuum and the seat foam. By definition of the refractive index η^{seat} at the interface air/seat, one has

$$\eta^{\text{seat}} := \frac{c^{\text{air}}}{c^{\text{seat}}} = \sqrt{\mu_{\text{r}}^{\text{seat}}\varepsilon_{\text{r}}^{\text{seat}}},$$

where $\sqrt{\cdot}$ denotes the principal determination of the square-root with branch-cut along the negative real-axis. Here $\mu_{\text{r}}^{\text{seat}}$ and $\varepsilon_{\text{r}}^{\text{seat}}$ are respectively the relative magnetic permeability and electric permittivity of the medium Ω_0^{seat}, defined as

$$\mu_{\text{r}}^{\text{seat}} := \frac{\mu^{\text{seat}}}{\mu^{\text{air}}} \quad \text{and} \quad \varepsilon_{\text{r}}^{\text{seat}} := \frac{\varepsilon^{\text{seat}}}{\varepsilon^{\text{air}}}.$$

We consider the seat foam as an imperfect dielectric material with conductivity θ^{seat}, which gives rise to partial wave absorption. The corresponding permittivity is complex and may be rewritten $\underline{\varepsilon}^{\text{seat}}$. Then, we have [58]

$$\underline{\varepsilon}^{\text{seat}} = \varepsilon^{\text{seat}} + i\frac{\theta^{\text{seat}}}{\nu_{\text{f}}}, \tag{3.47}$$

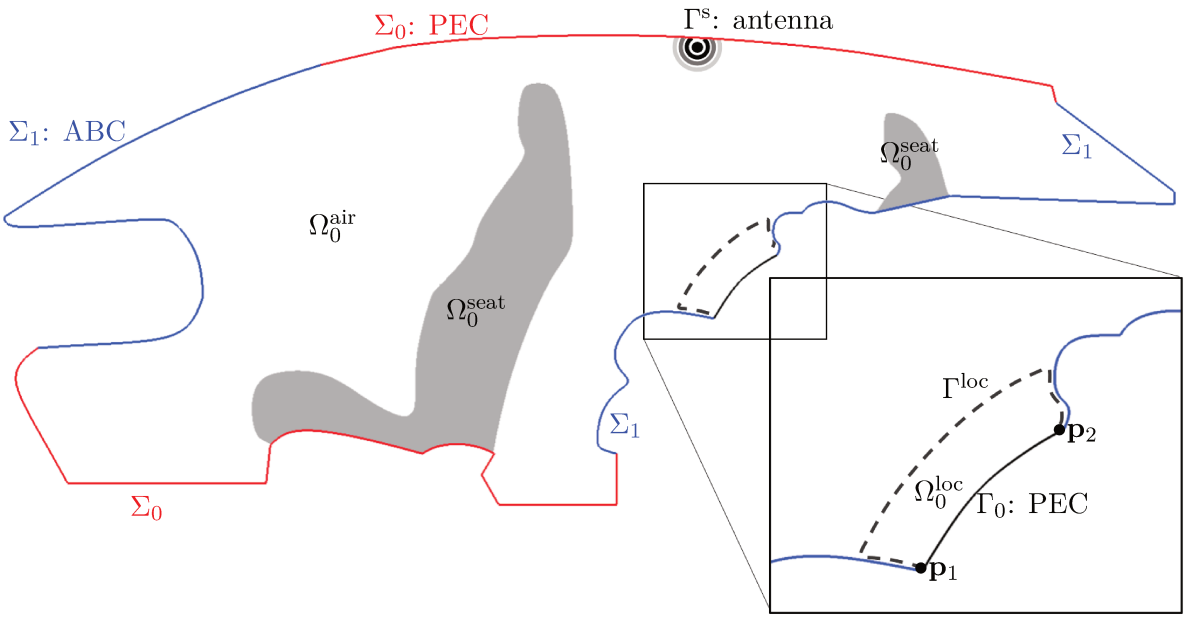

Figure 3.5: Schematic description of the 2D model problem.

with the corresponding complex relative permittivity $\underline{\varepsilon}_r^{seat} := \underline{\varepsilon}^{seat}/\varepsilon^{air}$, leading to $\eta^{seat} = \sqrt{\mu_r^{seat}\underline{\varepsilon}_r^{seat}}$. Hence, using (3.47) one obtains

$$\eta^{seat} = \sqrt{\mu_r^{seat}\left(\varepsilon_r^{seat} + i\frac{\theta^{seat}}{\nu_f \varepsilon^{air}}\right)}. \tag{3.48}$$

Let us remark that these physical parameters are chosen only according to the emission frequency ν_f. Finally, we assume as first approximation that the medium Ω_0^{seat} is non-dispersive. Therefore, we extend the model to the anisotropic case by defining c_∞ as piecewise constant, i.e. $c_\infty := c^{air,seat}$ in $\Omega_0^{air,seat}$, and $\Omega_0 = \Omega_0^{air} \cup \Omega_0^{seat}$.

Now, we need to introduce the contour Γ^{loc} to define the domain of computation of the metric change. Here, we choose a fixed polygonal open curve included inside Ω_0 with endpoints $\mathbf{p}_1$ and $\mathbf{p}_2$ (dashed black line on Figure 3.5). Therefore, this delimits the domain Ω_0^{loc} with boundary $\overline{\Gamma_0 \cup \Gamma^{loc}}$. When the baby is breathing, Γ_0 is deformed to Γ_t, but the two points $\mathbf{p}_1$ and $\mathbf{p}_2$ stay fixed. Here, we consider a small deformation of size $\epsilon \ll 1$ described by a simple T_ℓ-periodic sine mapping deforming the initial configuration Γ_0 into Γ_t in the normal direction. More precisely, for $\mathbf{x}_0 \in \Gamma_0$ and $t \geq 0$, we consider (3.13) to which we associate the deformation

$$\boldsymbol{\delta}_t(\mathbf{x}_0) = \sin\left(\pi\frac{l(\mathbf{p}_1\mathbf{x}_0)}{l(\Gamma_0)}\right)\sin(\omega_\ell t)\mathbf{n}_0(\mathbf{x}_0), \tag{3.49}$$

assuming $\omega_\ell \ll \omega_f$. Trivially, one gets $\|\boldsymbol{\delta}_t(\mathbf{x}_0)\| \leq 1$ for all $\mathbf{x}_0 \in \Gamma_0$ and $t \geq 0$. Here, $l(\mathbf{p}_1\mathbf{x}_0)$ is the arclength over Γ_0 from $\mathbf{p}_1$ to $\mathbf{x}_0$, and $l(\Gamma_0)$ denotes the length of Γ_0. The unit normal vector $\mathbf{n}_0(\mathbf{x}_0)$ at $\mathbf{x}_0 \in \Gamma_0$ is outwardly directed to Ω_0. More complex breathing models are described in [36, 62]. In our framework, considering general movements is easy since only the moving of the surface finite

element interpolation nodes on Γ_0 is needed. In addition, we have: $\Omega_0^{\rm fix} := \Omega_0 \setminus \Omega_0^{\rm loc}$, which is the part of Ω_0 where the deformation is not active. Finally, the problem under consideration is given by: find the total wave field u in Ω_t, $t > 0$, such that

$$\left\{\begin{array}{rcll} \dfrac{1}{c_\infty^2}\partial_t^2 u - \Delta_{\mathbf{x}} u &=& 0 & \text{in } \Omega_t, \\ \dfrac{1}{c_\infty}\partial_t u + \partial_{\mathbf{n}} u &=& 0 & \text{on } \Sigma_1, \\ u &=& 0 & \text{on } \Sigma_0 \cup \Gamma_t, \\ u &=& Ae^{i\omega_{\rm f} t} & \text{at } \Gamma^{\rm s}, \\ u(\mathbf{x},0) &=& 0 & \text{in } \Omega_0, \\ \partial_t u(\mathbf{x},0) &=& 0 & \text{in } \Omega_0. \end{array}\right.$$

We now consider the discrete times $\{t_k\}_{0\le k\le 2N}$, where $N \ge 1$. Since $\mathbf{\Phi}_t$ is given following (3.13) and (3.49), we can alternatively compute simultaneously the sequence of discrete deformations $\boldsymbol{\delta}_k$ in the layer $\Omega_0^{\rm loc}$ as the solutions to

$$\left\{\begin{array}{rcll} -\Delta\boldsymbol{\delta}_k &=& \mathbf{0} & \text{in } \Omega_0^{\rm loc}, \\ \boldsymbol{\delta}_k &=& \mathbf{0} & \text{on } \Gamma^{\rm loc}, \\ \boldsymbol{\delta}_k &=& \sin\left(\pi\dfrac{l(\mathbf{p}_1\mathbf{x}_0)}{l(\Gamma_0)}\right)\sin\left(\dfrac{2\pi k}{2N+1}\right)\mathbf{n}_0(\mathbf{x}_0) & \text{for } \mathbf{x}_0 \in \Gamma_0, \end{array}\right. \tag{3.50}$$

for $0 \le k \le 2N$. The solution $\boldsymbol{\delta}_{k,h}$ to (3.50) is realized by a $\mathbb{P}_1$ finite element method for the corresponding weak form in $\Omega_{0,h}^{\rm loc}$ (with $n_{0,h}^{\rm loc}$ triangles), providing hence $\mathbf{\Phi}_{k,h}(\mathbf{x}_{0,h}) = \mathbf{x}_{0,h} + \epsilon\boldsymbol{\delta}_{k,h}(\mathbf{x}_{0,h})$. A second step allows to calculate the $\mathbb{P}_0$ approximation of $\mathbf{J}_{k,h}$ by a weak derivation. The solution to the linear systems is obtained by computing once the Cholesky factorization of the stiffness matrix related to the problem (3.50) and then by a forward-backward solution for each of the $2(2N+1)$ right hand sides.

Let us remark that the size L of the layer $\Omega_{0,h}^{\rm loc}$ along the normal direction must be sufficiently large compared to ϵ so that the deformation does not flatten too much the triangulation related to $\Omega_{0,h}^{\rm loc}$. At the same time, the mesh in $\Omega_{0,h}$ must also be sufficiently refined to correctly capture the high oscillations of the solution due to $\omega_{\rm f}$. The coefficients $\mathbf{C}_n$ and c_n, $-N \le n \le N$, are finally evaluated as piecewise constant on each triangle from the Jacobian $\mathbf{J}_{k,h}$, $0 \le k \le 2N$, using (3.9) and FFTs.

The overall algorithmic implementation is summarized in Algorithm 1 (which also holds for higher-order finite element approximations of the solution).

3.5.2 Numerical resolution

We consider the following physical parameters corresponding to realistic applications of radar detection of car occupants [18, 40]: $c_\infty = 3\times 10^8$ in $\Omega_0^{\rm air}$, $\mu_{\rm r} = 1$, $\varepsilon_{\rm r} = 1.2$, $\varepsilon^{\rm air} = 8.85\times 10^{-12}$ and $\theta = 2.7\times 10^{-3}$. These values yield $c^{\rm seat} = 2.7\times 10^8 - 1.2\times 10^6 i$ according to (3.48). The emission frequency and amplitude, and the breathing motion frequency are respectively $\nu_{\rm f} = 3\times 10^9$, $A = 1$ and $\nu_\ell = 1$. The layer $\Omega_{0,h}^{\rm loc}$ is chosen with thickness $L = 0.1$. The tuning parameters ϵ, N and J are varying parameters of the study.

Let us first illustrate through an example the construction of the function $c_{n,h}$ and tensor $\mathbf{C}_{n,h}$ from the metric computation, which is a pre-processing step of the method. We fix $\epsilon = 0.01$

Algorithm 1 Pseudo-code of the method.

1. **Geometry meshing** (Input: geometrical domain Ω_0)
   Generate the mesh $\Omega_{0,h}$ of Ω_0

2. **Identification of the fixed and the local deforming parts, and FEM matrix assembly of the fixed part** (Input: thickness L of $\Omega_{0,h}^{\text{loc}}$ and $(\varepsilon_{\text{r}}, \mu_{\text{r}}, \theta)$ for each material)
   Identify $\Omega_{0,h}^{\text{loc}}$ and $\Omega_{0,h}^{\text{fix}}$ in $\Omega_{0,h}$
   Compute the matrices $\mathbf{M}_n$, $\mathbf{M}_\Sigma$ and $\mathbf{K}_n$ over $\Omega_{0,h}^{\text{fix}}$

3. **FEM matrix assembly of the local deforming part** $\Omega_{0,h}^{\text{loc}}$ (Input: N and the boundary deformations $\boldsymbol{\delta}_{k,h}|_{\Gamma_{0,h}}$ for $0 \leq k \leq 2N$)
   Compute the Cholesky factorization associated to (3.50)
   for $k \in \{0, ..., 2N\}$
      Solve (3.50) for the k-th right hand side
      Retrieve the updated node positions $\mathbf{x}_h \in \Omega_{0,h}^{\text{loc}}$ at time t_k using (3.13)
      Compute the discrete Jacobians $\mathbf{J}_{k,h}$ using (3.9)
   end for
   Compute the tensors $\mathbf{C}_{n,h}$ and the functions $c_{n,h}$, $0 \leq n \leq 2N$ by means of FFTs of $\mathbf{J}_{k,h}$
   Compute $\mathbf{M}_n$, $\mathbf{M}_\Sigma$ and $\mathbf{K}_n$ over $\Omega_{0,h}^{\text{loc}}$

4. **Assembly of the multi-harmonic linear system** (Input: $J \geq N$, ν_{f})
   Build the global block matrix $\mathbf{A}_{\boldsymbol{\omega}^{(J)}}^{(N,J)}$ from (3.42)
   Compute the right hand side $\mathbf{b}^{(N,J)}$ of (3.43)

5. **Solution and post-processing** (Input: $\mathbf{A}_{\boldsymbol{\omega}^{(J)}}^{(N,J)}$, $\mathbf{b}^{(N,J)}$)
   Solve (3.43) using a direct or iterative solver
   Compute the quantities of interest (spectrograms, RCS, ...)

Case	ϵ	N	$n=0$	$n=1$	$n=2$	$n=3$	$n=4$
$\mathtt{nnz}((\mathbf{A}^{(N,J)}_{\boldsymbol{\omega}^{(J)}})_{0,n})$	0.01	4	27982288	468181	220590	19467	0
	0.02	5	27982288	470036	306880	50530	382
$\|(\mathbf{A}^{(N,J)}_{\boldsymbol{\omega}^{(J)}})_{0,n}\|_{\mathrm{F}}$	0.01	4	7.50×10^{3}	20.4	6.24×10^{-1}	1.07×10^{-1}	0
	0.02	5	7.50×10^{3}	41.4	3.57	4.65×10^{-1}	1.48×10^{-1}

Table 3.1: nnz and Frobenius norms of the matrices $(\mathbf{A}^{(N,J)}_{\boldsymbol{\omega}^{(J)}})_{0,n}$, $n=0,...,4$, with $J=8$.

and $N=4$ (see below for this choice), which means that the time interval $[0,T_\ell]=[0,1]$ is discretized by $2N+1=9$ equally spaced points. We report on Figure 3.6a the triangulation $\Omega_{0,h}$ (gray mesh) zoomed around the rear seat. For the sake of clarity, we consider a relatively large element size (triangle edge length) of 6×10^{-3} (leading to $n_{0,h}=115702$). We superimpose on $\Omega_{0,h}$ (colored circles) the nodes of the initial triangulation mapped by $\boldsymbol{\Phi}_{k,h}$, for $k=6$ (i.e. $t_k=0.67$), resulting from the finite element approximation to (3.50). From this calculation, we can deduce the piecewise constant function $c_{n,h}$ and tensor $\mathbf{C}_{n,h}$. We represent in Figures 3.6b-3.6e the amplitude of $(\mathbf{C}_{n,h})_{1,1}$, $n=0,\cdots,3$. In particular, we observe that $(\mathbf{C}_{0,h})_{1,1}=1$ and $(\mathbf{C}_{n,h})_{1,1}=0$ $(n=1,2,3)$ outside $\Omega^{\mathrm{loc}}_{k,h}$. One of the main points of the method is to correctly adjust the value of N in (3.33) to have an accurate representation of the moving geometry but also to avoid enlarging the bandwidth of the linear system (3.43) more than necessary.

Now, for a given calculation, the mesh size must be fixed to capture the small oscillations of the wave field related to the high frequency signal (with usual wavelength in the range 0.01-0.1). For $\nu_{\mathrm{f}}=3\times10^{9}$, the element size in the triangulation $\Omega_{0,h}$ is fixed at 7×10^{-4}, which leads to $n_{0,h}=8001827$ triangular elements and $n_{\mathrm{dof}}=4000778$ nodes. For $n\in\mathbb{N}$, we set

$$m_n:=\frac{\|c_{n,h}\|_{L^\infty(\Omega^{\mathrm{loc}}_{0,h})}}{\|c_{0,h}\|_{L^\infty(\Omega^{\mathrm{loc}}_{0,h})}},\quad M_n:=\frac{\max_{1\le\imath,\jmath\le2}\|(\mathbf{C}_n)_{\imath,\jmath}\|_{L^\infty(\Omega^{\mathrm{loc}}_{0,h})}}{\max_{1\le\imath,\jmath\le2}\|(\mathbf{C}_0)_{\imath,\jmath}\|_{L^\infty(\Omega^{\mathrm{loc}}_{0,h})}}.$$

Then, we fix N as the smallest positive integer such that: $m_N\le\mathfrak{T}$ and $M_N\le\mathfrak{T}$, where $\mathfrak{T}$ is a small tolerance parameter. Usually, because of the expressions of c_n and $\mathbf{C}_n$, and from numerical simulations (see also Figure 3.7 (Left)), the most important point is to check the criterion on M_n. We report M_n and m_n, for $0\le n\le8$, in Figure 3.7 and see that $N=4$ (respectively $N=5$) for $\mathfrak{T}=10^{-2}$ and $\epsilon=0.01$ (respectively $\epsilon=0.02$). In practice, we define an initial value for N and adjust it to fulfill the above criterion. The associated local cost per element in $\Omega^{\mathrm{loc}}_{0,h}$ is however low, for a global cost of about $N\log(N)n^{\mathrm{loc}}_{0,h}$. This pre-processing step is important since it impacts the block structure of the matrix $\mathbf{A}^{(N,J)}_{\boldsymbol{\omega}^{(J)}}$. In addition, we observe that the ratios M_n (as well as m_n) are rapidly decaying and behave as $e^{-\kappa\epsilon n}$ when $n>n_0$, for some constants $n_0\in\mathbb{N}$ and $\kappa>0$, i.e.

$$\max_{1\le\imath,\jmath\le2}\|(\mathbf{C}_n)_{\imath,\jmath}\|_{L^\infty(\Omega^{\mathrm{loc}}_{0,h})}\approx\max_{1\le\imath,\jmath\le2}\|(\mathbf{C}_0)_{\imath,\jmath}\|_{L^\infty(\Omega^{\mathrm{loc}}_{0,h})}e^{-\kappa\epsilon n},$$

which is due to the fact that we use a smooth mapping.

For N fixed, since the computation of $c_{n,h}$ and $\mathbf{C}_{n,h}$ is spatially localized near the moving boundary as corrections of the static case ($n=0$) and their maximal amplitude decays with n, we can expect that the blocks $(\mathbf{A}^{(N,J)}_{\boldsymbol{\omega}^{(J)}})_{j,n}$ of $\mathbf{A}^{(N,J)}_{\boldsymbol{\omega}^{(J)}}$, $(j,n)\in\mathcal{J}_*\times\mathcal{J}_*$, have a sparser profile with smaller coefficients when n increases. We report on Table 3.1 the number of nonzero elements

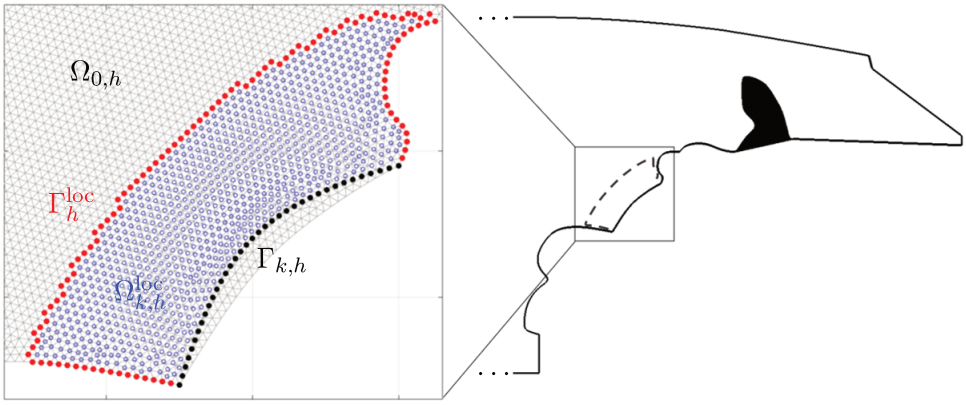

(a) Finite element triangulation and its local deformation for $k = 6$.

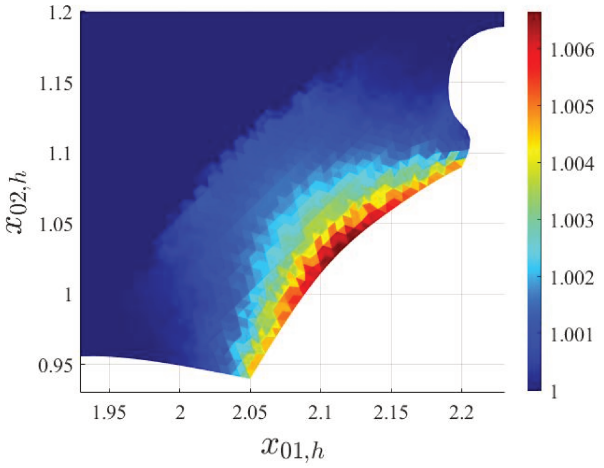

(b) $|(\mathbf{C}_{0,h})_{1,1}|$

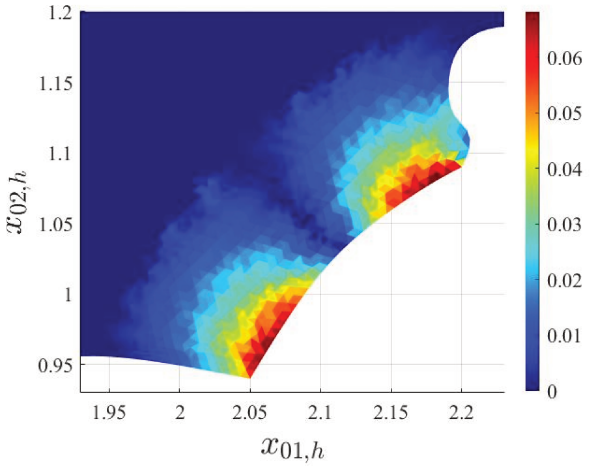

(c) $|(\mathbf{C}_{1,h})_{1,1}|$

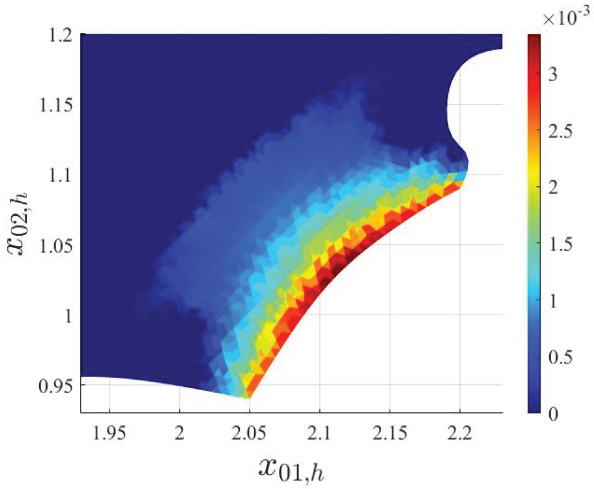

(d) $|(\mathbf{C}_{2,h})_{1,1}|$

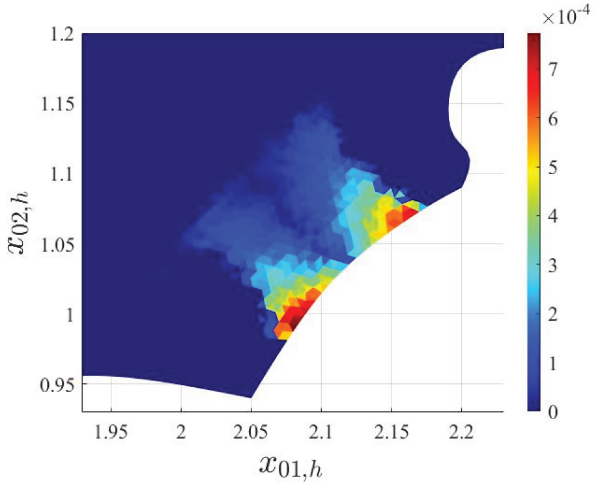

(e) $|(\mathbf{C}_{3,h})_{1,1}|$

Figure 3.6: Computation of the local deformation and piecewise constant tensor $\mathbf{C}_{n,h}$ for $0 \leq n \leq 3$.

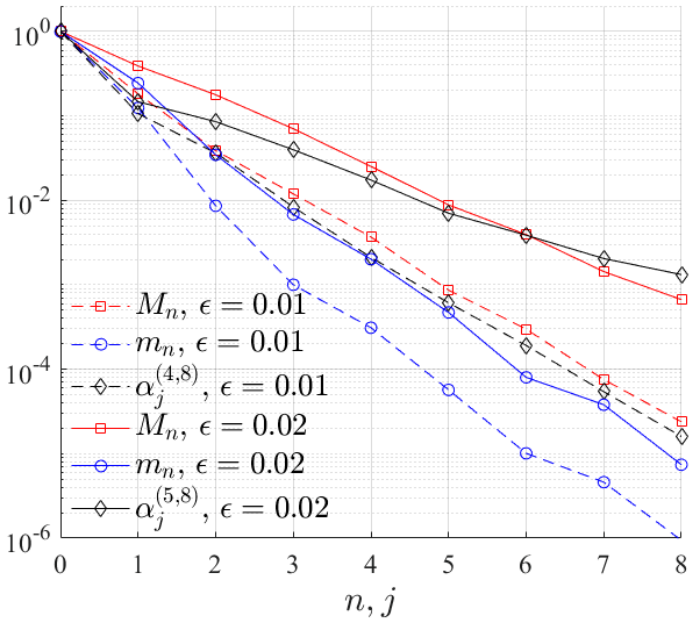

Figure 3.7: M_n, m_n and $\alpha_j^{(N,8)}$, for $0 \leq n, j \leq 8$ (threshold $\mathfrak{T} = 10^{-2}$).

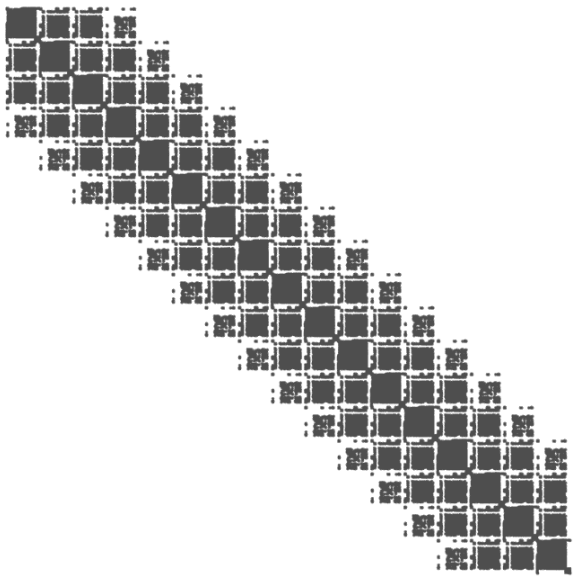

Figure 3.8: Sparsity pattern of the matrix $\mathbf{A}^{(4,8)}_{\boldsymbol{\omega}^{(8)}}$.

(`nnz`) and the Frobenius norm $\|\cdot\|_{\mathrm{F}}$ of these blocks, for $j = 0$ and $n = 0, ..., 4$, fixing $J = 8$ and for $\epsilon = 0.01$ and $\epsilon = 0.02$ (N is obtained thanks to the above truncation criterion).

This is in accordance with Figure 3.8, where the number of elements and the Frobenius norm of the blocks get smaller as k grows. In addition, a larger value of ϵ implies that N must be taken larger and that both the number of elements and the norm of the blocks is slightly larger.

Let us now analyze the selection of the truncation parameter $J \geq N$ for the unknown expansion (3.41). In Figure 3.7, we report $\alpha_j^{(N,J)} := \|a_{j,h}^{(N,J)}\|_{L^\infty(\Omega_{0,h})} / \|a_{0,h}^{(N,J)}\|_{L^\infty(\Omega_{0,h})}$, for $0 \leq j \leq J = 8$, and $\epsilon = 0.01$ ($N = 4$) and $\epsilon = 0.02$ ($N = 5$). We observe that the behaviour of $\alpha_j^{(N,J)}$ is similar to the behavior of M_n in both situations, i.e. we have rapidly decaying coefficients according to j. We recommend in practice to take J a little bit larger than N, e.g. $J = N + 3$. While it would be very interesting to have *a priori* and *a posteriori* error estimators for the expansion of the solution, this is not trivial as it depends on the global regularity of the procedure, and in particular of the mapping.

A possible strategy is to apply the method for the first empirical guess J discussed above, and *a posteriori* increase it to $J_1 > J$ if needed. To justify this approach, let us consider the convergence of $w^{(N,J)}$ for increasing J. Formally, we have

$$\|w^{(N,J+1)} - w^{(N,J)}\|_{L^2(\Omega_0)} \leq \|a_{J+1}^{(N,J+1)}\|_{L^2(\Omega_0)} + \|a_{-(J+1)}^{(N,J+1)}\|_{L^2(\Omega_0)} + S(N,J),$$

with

$$S(N,J) := \sum_{j=-J}^{J} \|a_j^{(N,J+1)} - a_j^{(N,J)}\|_{L^2(\Omega_0)}.$$

The solution $w^{(N,J+1)}$ of (3.43), computed for $J+1$, is comprised of two additional terms $a_{\pm(J+1)}^{(N,J+1)}$ and an approximation of $w^{(N,J)}$, whose difference with $w^{(N,J)}$ is bounded by $S(N,J)$. In particular, we expect that the solution of (3.43) is getting more accurate when increasing the parameter J, which means that both additional terms and $S(N,J)$ converge to zero according to J. Indeed, since $a_{\pm(J+1)}^{(N,J+1)}$ is square integrable on Ω_0, the fast decay of the corrective terms $\|a_{\pm(J+1)}^{(N,J+1)}\|_{L^\infty(\Omega_0)}$ (as a Fourier coefficient of a periodic function $\mathcal{C}^\infty$ in time) implies that $\lim_{J\to\infty} \|a_{\pm(J+1)}^{(N,J+1)}\|_{L^2(\Omega_0)} = 0$. Finally, the sum $S(N,J)$ meaures the accuracy gain for the modes $0 \leq j \leq J$ of the solution $w^{(N,J+1)}$ with respect to $w^{(N,J)}$. Then, in order to quantify the convergence of each mode $a_j^{(N,J)}$ for increasing J, let us define the relative difference

$$\mathrm{Err}_j(N,J) := \frac{\|a_j^{(N,J+1)} - a_j^{(N,J)}\|_{L^2(\Omega_0)}}{\|a_j^{(N,J)}\|_{L^2(\Omega_0)}}.$$

We report in Figure 3.9 the corresponding finite element approximations $S_h(4,J)$ and $\mathrm{Err}_{j,h}(4,J)$ for $0 \leq j \leq 6$, $5 \leq J \leq 9$ and $\epsilon = 0.01$. We first observe the fast decay of the bound $S_h(4,J)$ (black curve) and of the relative differences $\mathrm{Err}_{j,h}$ according to J, thus the convergence of the $a_j^{(N,J)}$, for fixed $j \leq J$, to the real solution. This confirms the gain of accuracy of the solution when increasing the size of the linear system (3.43). We also observe that for fixed J, the error grows while increasing j.

For completeness we report the amplitudes of the four first functions $|a_{j,h}^{(4,8)}(\mathbf{x}_0)|$, $0 \leq j \leq 3$, in $\Omega_{0,h}$ when $\epsilon = 0.01$, for $\nu_{\mathrm{f}} = 3 \times 10^9$ on Figures 3.10 to 3.13 and $\nu_{\mathrm{f}} = 1.5 \times 10^{10}$ on Figures 3.14

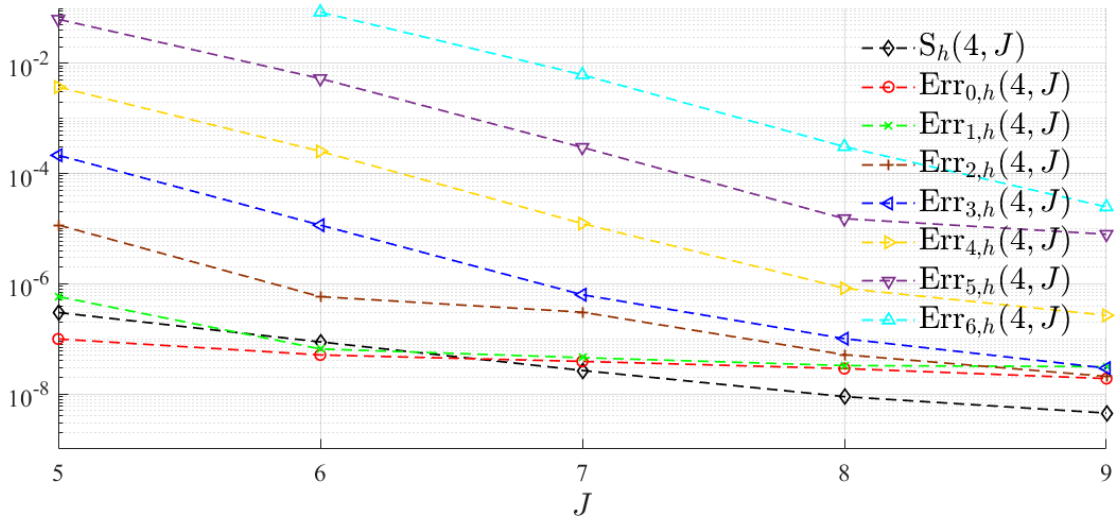

Figure 3.9: $S_h(N,J)$ and $\mathrm{Err}_{j,h}(N,J)$ for $N=4$, $0\leq j\leq 6$ and $5\leq J\leq 9$.

to 3.14. The parameters are set to $c_\infty = 3\times 10^8$, $\varepsilon_\mathrm{r}=1.2$, $\theta = 2.7\times 10^{-3}$, $A=1$, $\nu_\ell = 1$, $\epsilon = 0.01$ and $L=0.1$. Let us remark that when the radar frequency increases, the first modes contribute more to the scattering problem, leading to the Doppler effect.

We now consider the solution of the linear system (3.43) and its preconditioned version (3.44) by using the GMRES without restart. The computations were performed using `Matlab` on a laptop with Intel Core i7-10510U CPU at 2.30 GHz. The LU decomposition $\mathbf{A}_{\omega_0}^{(0,8)} = \mathbf{L}_{\omega_0}\mathbf{U}_{\omega_0}$ defining $\mathbf{P}$ is used to solve (3.45) for $j\in\mathcal{J}$, as explained in Section 3.4. The resulting upper and lower $n_\mathrm{dof}\times n_\mathrm{dof}$ triangular matrices are highly sparse for $\mathtt{nnz}/n_\mathrm{dof}^2 = 2.2\times 10^{-3}\%$ (with $\mathtt{nnz}(\mathbf{L}_{\omega_0}) = 351090973$). We report in Figure 3.18 the residual history for solving (3.43) and (3.44), for $5\leq J\leq 8$, with $\epsilon=0.01$ and $\epsilon=0.02$. The parameter settings are the same as before. Without the preconditioner, the convergence is very slow (the maximum number of iterations is fixed to 50) and may even breakdown for some configurations. When using the preconditioner $\mathbf{P}$, we obtain a very good convergence rate which seems to be independent of J. In addition, the slope of the convergence rate increases with ϵ which is natural since the boundary movement perturbates more the static configuration, which penalizes the preconditioner efficiency. In Table 3.2, we can observe that the CPU time for the iterative solution scales linearly with the parameter J and is faster than the direct `Matlab` solver for $\epsilon=0.01$. We expect that this difference will be much more important for higher frequencies or/and for three-dimensional problems.

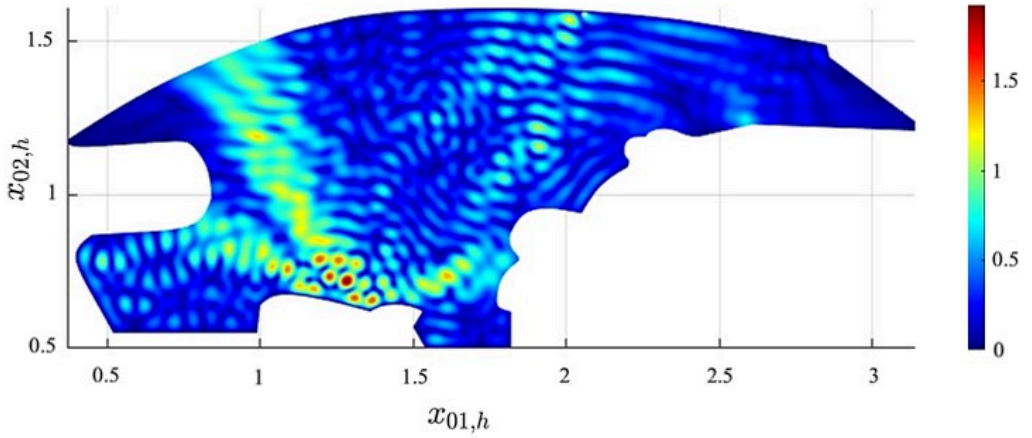

Figure 3.10: Amplitude $|a_{0,h}^{(4,8)}(\mathbf{x}_{0,h})|$ for $\nu_{\mathrm{f}} = 3 \times 10^9$.

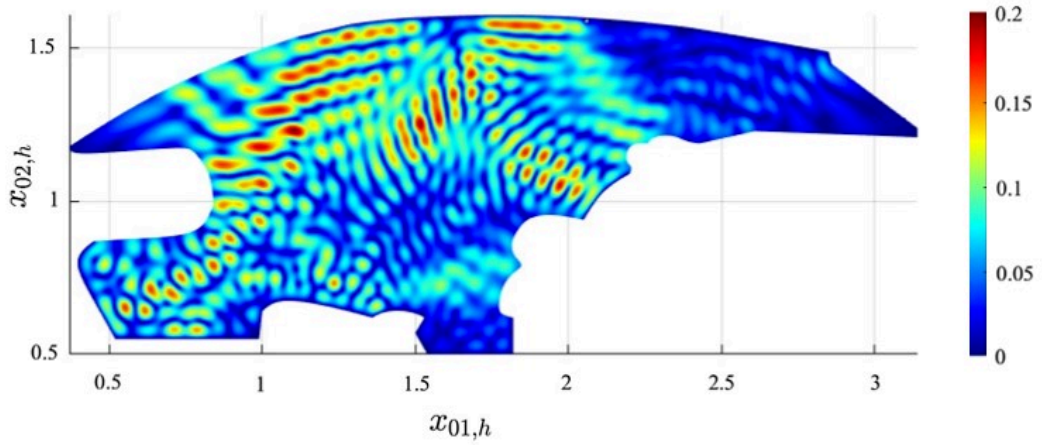

Figure 3.11: Amplitude $|a_{1,h}^{(4,8)}(\mathbf{x}_{0,h})|$ for $\nu_{\mathrm{f}} = 3 \times 10^9$.

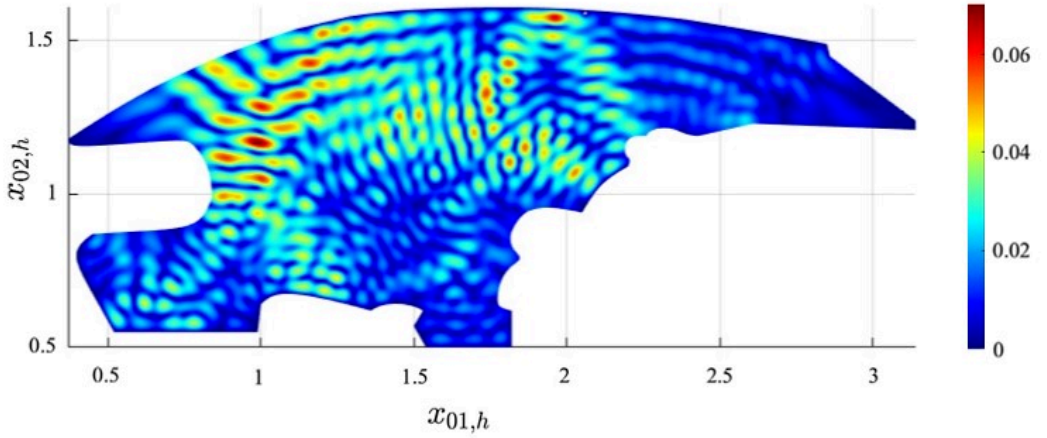

Figure 3.12: Amplitude $|a_{2,h}^{(4,8)}(\mathbf{x}_{0,h})|$ for $\nu_{\mathrm{f}} = 3 \times 10^9$.

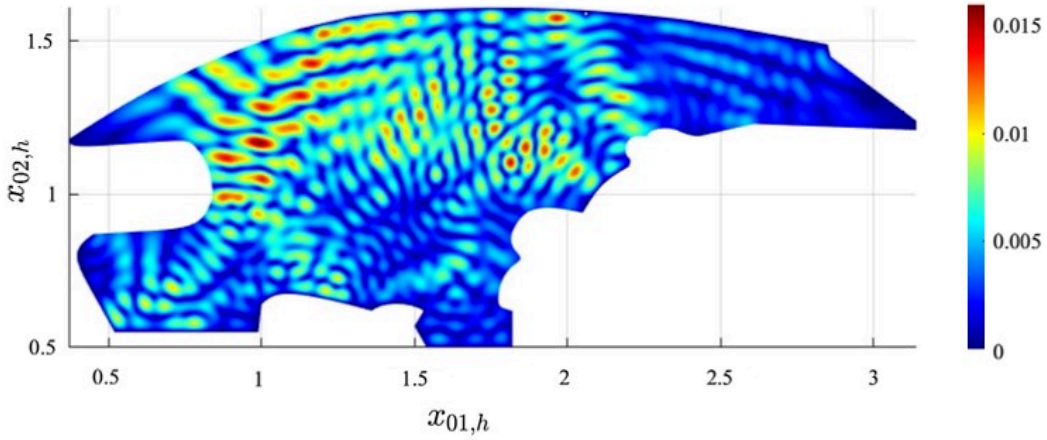

Figure 3.13: Amplitude $|a_{3,h}^{(4,8)}(\mathbf{x}_{0,h})|$ for $\nu_{\mathrm{f}} = 3 \times 10^9$.

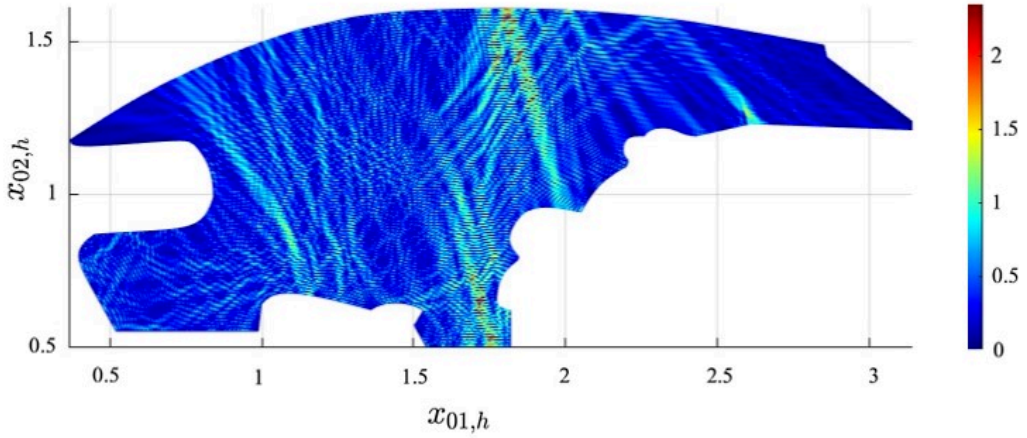

Figure 3.14: Amplitude $|a_{0,h}^{(4,8)}(\mathbf{x}_{0,h})|$ for $\nu_{\mathrm{f}} = 1.5 \times 10^{10}$.

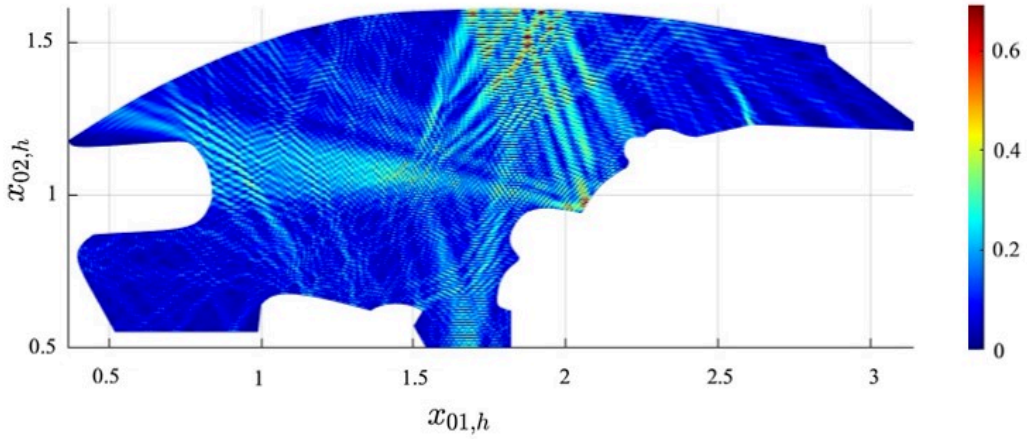

Figure 3.15: Amplitude $|a_{1,h}^{(4,8)}(\mathbf{x}_{0,h})|$ for $\nu_{\mathrm{f}} = 1.5 \times 10^{10}$.

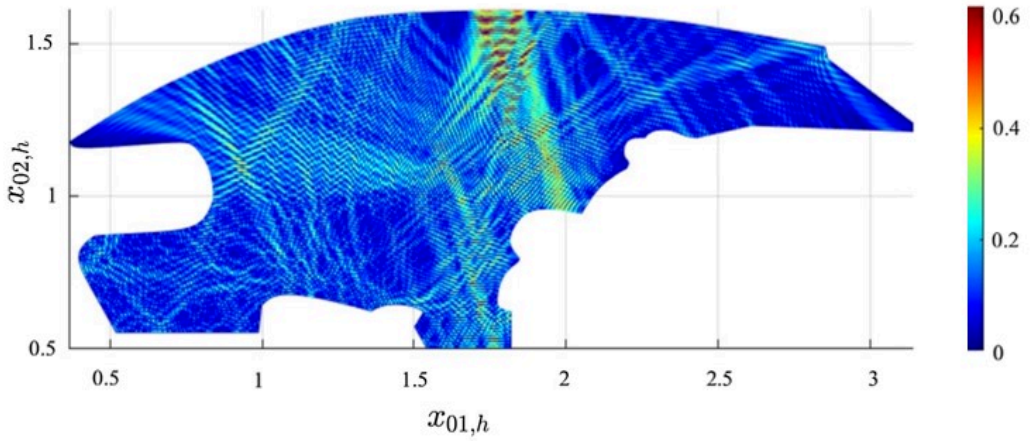

Figure 3.16: Amplitude $|a_{2,h}^{(4,8)}(\mathbf{x}_{0,h})|$ for $\nu_{\mathrm{f}} = 1.5 \times 10^{10}$.

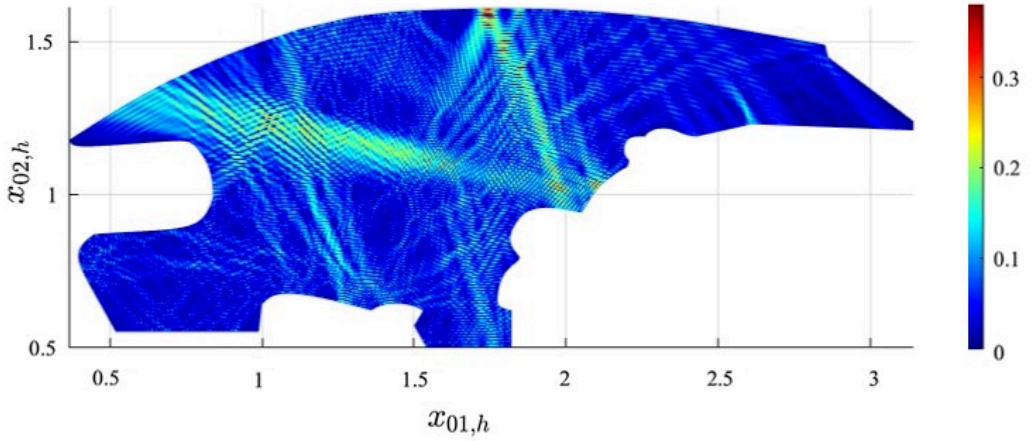

Figure 3.17: Amplitude $|a_{3,h}^{(4,8)}(\mathbf{x}_{0,h})|$ for $\nu_{\mathrm{f}} = 1.5 \times 10^{10}$.

Case	ϵ	$J=5$	$J=6$	$J=7$	$J=8$
Preconditioned GMRES	0.01	1124	1276	1450	1719
	0.02	1709	1893	2304	2627
Direct `Matlab` solver	0.01	1667	1924	2371	2743
	0.02	1680	2028	2489	2858

Table 3.2: CPU time for solving (3.43) with a direct solver and (3.44) with the preconditioned GMRES.

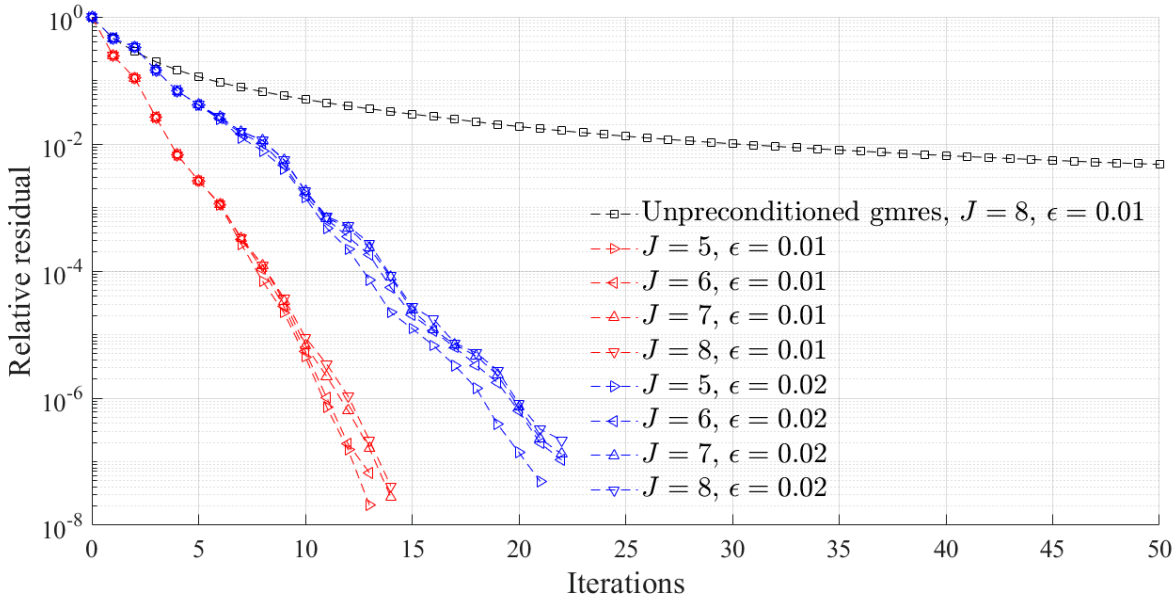

Figure 3.18: Convergence history of GMRES for solving (3.43) (black) and (3.44) with increasing J, for $\epsilon = 0.01$ (red) and $\epsilon = 0.02$ (blue).

3.6 Conclusion

This chapter proposes a general approach for computing the solution to two- and three-dimensional scattering problems by moving boundaries. To this end, the initial boundary value problem is rewritten in a fixed domain thanks to a well-adapted mapping that can be computed by a finite element method. Next, approximations are introduced according to the small deformation of the boundary, and some geometrical quantities as well as the solution are expanded in terms of truncated Fourier series. This leads to the solution of a finite coupled system of Helmholtz-type equations, that can be solved by the finite element method. The numerical implementation of the method is fully detailed on a simplified model example arising from the automotive industry. This shows the potentiality of the approach for solving moving boundary problems for wave scattering, with applications to Doppler effects. In the following chapter, we apply the presented methodology to detailed realistic geometries, multiple sources and moving targets with different materials.

Chapter 4

Application of the multi-harmonic FEM to realistic configurations

Contents

4.1 Definition of the extended geometries 87
4.1.1 The reference configuration 87
4.1.2 The different test configurations with car occupants 88
4.1.3 Realistic breathing motions 88
4.2 Numerical simulations 92
4.2.1 Calibration of the test cases 92
4.2.2 Detection of car occupants 93
4.3 Discussion of the results 108

4.1 Definition of the extended geometries

4.1.1 The reference configuration

We presented in Chapter 3 the numerical implementation of the method on a model involving a simplified car. We propose here to extend it to more realistic configurations in line with the industrial motivations sketched out in Section 1.1.1. Indeed, in the context of radar detection of occupants using micro-Doppler signatures from breathing, we have to take into account realistic geometries with several different materials. In addition, we are interested in the total EM field for different antenna locations, child seat orientations and various breathing patterns.

Thus, we consider the extended domain Ω_0 representing a two-dimensional detailed longitudinal car section, inspired from a Renault Mégane model [1] (see Figure 4.1), with an empty child seat located at the rear and facing the road as depicted in Figure 4.2. A trade-off has been chosen in order to set a sufficient level of details to capture realistic scattering behaviors without unnecessarily complexifying the geometry. The domain Ω_0 includes four different regions corresponding to the most prevalent materials inside a car. More precisely, we have $\Omega_0 = \Omega_0^{\text{air}} \cup \Omega_0^{\text{seat}} \cup \Omega_0^{\text{plas}} \cup \Omega_0^{\text{ins}}$ where Ω_0^{air} models the free space domain, Ω_0^{seat} is related to the seat foam (seats and child seat), Ω_0^{plas} is related to the plastic components and Ω_0^{ins} is related to the insulating layers. The associated complex-valued velocities $c^{\text{air,seat,plas,ins}}$ are computed using (3.48), from the corresponding conductivities $\theta^{\text{seat,plas,ins}}$, relative permittivities $\varepsilon_{\text{r}}^{\text{seat,plas,ins}}$ and permeabilities $\nu_{\text{r}}^{\text{seat,plas,ins}}$. We report the corresponding values in Table 4.1. As a first approximation, the relative magnetic permeability of the materials has been set to 1. The physical coefficients for the insulation have been measured by IEE's laboratory. The coefficients related to cloth, plastic PP and PU foam are generic values available in [1], and the human tissue properties are taken from the database [43] [2].

Physical quantity	Seat foam	Plastic	Insulation	Child	Clothes
Relative permittivity	$\varepsilon_{\text{r}}^{\text{seat}}$ 1.20	$\varepsilon_{\text{r}}^{\text{plas}}$ 1.40	$\varepsilon_{\text{r}}^{\text{ins}}$ 1.12	$\varepsilon_{\text{r}}^{\text{child}}$ 40.0	$\varepsilon_{\text{r}}^{\text{cloth}}$ 1.18
Conductivity	θ^{seat} 2.70×10^{-3}	θ^{plas} 8.00×10^{-3}	θ^{ins} $2.47.00 \times 10^{-2}$	θ^{child} 2.90×10^{-2}	θ^{cloth} 1.50×10^{-2}

Table 4.1: Reference values of the conductivities and relative permittivities of the materials that constitute the car model.

For our study, we fix the emission frequency to $\nu_{\text{f}} = 10^{10}$ and set four predefined locations $\{\Gamma_i^{\text{s}}\}_{1 \leq i \leq 4}$ for the source Γ^{s} in the roof lining (red dots in Figures 4.2 to 4.6). As previously, the red boundary, denoted by Σ_0, represents a PEC and models the metallic structure of the car. The blue boundary Σ_1 is related to glass and supports the zeroth-order absorbing boundary condition (3.3) and the antenna Γ^{s}, emitting the field of amplitude A and frequency ν_{f}. Let us remind that in the previous section we had $\partial\Omega_t = \Gamma_t \cup \Gamma^{\text{s}} \cup \Sigma_0 \cup \Sigma_1$, where Γ_t is mapped to the boundary Γ_0 of Ω_0. However, we now entirely bound Ω_0 with Γ^{s}, Σ_0 and Σ_1 such that $\partial\Omega_0 = \Gamma^{\text{s}} \cup \Sigma_0 \cup \Sigma_1$. This configuration, called C0, represents the car without any occupant.

The antenna Γ^{s} is not necessarily unique, and its geometry can be quite complex (e.g. a patch

[1] https://www.renault.ps/en/cars/MeganeBfbRsPh1/dimensions.html

[2] https://itis.swiss/virtual-population/tissue-properties/downloads/database-v4-0/

antenna made of several patches). To allow for some generality, we consider the case of disjoint circular sources simultaneously emitting in the domain. Since (3.1) is linear, the superposition principle states that we can consider the field emitted by different sources as the summation of the fields emitted by each source. Hence, we distinguish two cases. If two sources $\Gamma^{\mathrm{s},1}$ and $\Gamma^{\mathrm{s},2}$ are emitting waves with the same frequency ν_{f}, then the two disjoint sources respectively support the Dirichlet boundary conditions $u(\mathbf{x},t)|_{\Gamma^{\mathrm{s},1}} = A^1 e^{i\omega_{\mathrm{f}}t}$ and $u(\mathbf{x},t)|_{\Gamma^{\mathrm{s},2}} = A^2 e^{i\omega_{\mathrm{f}}t}$, where $A^1, A^2 \in \mathbb{R}_*^+$. This compatibility rises from the fact that the global field can still be written under the form (3.35), and the presented method is directly applicable with the previous boundary conditions. On the other hand, since our approach requires to use an expansion of the unknown around a fixed main mode of frequency ν_{f}, the case where several waves of different frequencies are emitted imposes to compute the assembly and resolution processes from (3.42) as many times as there are frequencies.

4.1.2 The different test configurations with car occupants

We now consider the presence of a dressed breathing child in the car. Hence, we introduce a first extension C1a of C0 by considering the additional subdomain $\Omega_0^{\mathrm{child1}} \cup \Omega_0^{\mathrm{cloth1}}$ of Ω_0, where $\Omega_0^{\mathrm{child1}}$ models the breathing child and $\Omega_0^{\mathrm{cloth1}}$ its layer of clothing, as illustrated in Figure 4.3. They are associated to the corresponding physical parameters $\varepsilon_{\mathrm{r}}^{\mathrm{child,cloth}}$, $\theta^{\mathrm{child,cloth}}$ and then $c^{\mathrm{child,cloth}}$. The chosen values for these coefficients are also reported in Table 4.1. The belly Γ_0^1 of the baby (curve with endpoints $\mathbf{p}_1^1$ and $\mathbf{p}_2^1$ on Figure 3.5) is no longer considered as a boundary of the domain, and only represents the curve for which we explicitly know the deformation. Now we need to introduce a new closed contour $\Gamma^{\mathrm{loc},1}$ including Γ_0^1 to delimit the domain $\Omega_0^{\mathrm{loc},1}$ of computation of the metric change. As previously, when the baby is breathing, Γ_0^1 is deformed to Γ_t^1 but the endpoints $\mathbf{p}_1^1$ and $\mathbf{p}_2^1$ remain fixed. Here, we consider a small deformation of Γ_0^1 described by the mapping $\mathbf{\Phi}_t^1$, such that for $\mathbf{x}_0 \in \Gamma_0^1$ and $t \geq 0$,

$$\mathbf{x} = \mathbf{\Phi}_t^1(\mathbf{x}_0) := \mathbf{x}_0 + \epsilon \boldsymbol{\delta}_t^1(\mathbf{x}), \tag{4.1}$$

where $\boldsymbol{\delta}_t^1$ is a bounded smooth T_ℓ-periodic odd function defined subsequently. In Figure 4.4, we introduce the configuration C1b, based on C1a, and with a rearward-facing child safety seat.

It is also interesting to observe the micro-Doppler signature generated by more than one breathing occupant in the car. To this end, we define a fourth configuration C2a based on C1a and including a second child seat at the front of the vehicle. More precisely, we set a second subdomain $\Omega_0^{\mathrm{child2}} \cup \Omega_0^{\mathrm{cloth2}}$ of Ω_0 as illustrated in Figure 4.5, for which we keep the same physical parameters $\varepsilon_{\mathrm{r}}^{\mathrm{child,cloth}}$, $\theta^{\mathrm{child,cloth}}$ and $c^{\mathrm{child,cloth}}$. Now we have to define the corresponding contour $\Gamma^{\mathrm{loc},2} = \partial\Omega_0^{\mathrm{loc},2}$ enclosing the moving curve Γ_0^2 with endpoints $\mathbf{p}_1^2$ and $\mathbf{p}_2^2$, which models the belly of the second child. We also define a mapping $\mathbf{\Phi}_t^2$ such that for $\mathbf{x}_0 \in \Gamma_0^2$ and $t \geq 0$

$$\mathbf{x} = \mathbf{\Phi}_t^2(\mathbf{x}_0) := \mathbf{x}_0 + \epsilon \boldsymbol{\delta}_t^2(\mathbf{x}).$$

Similarly, we build the variant C2b of C1b, reported in Figure 4.6.

4.1.3 Realistic breathing motions

The tolerance parameter $\mathfrak{T}$ of the Fourier expansion (see Section 3.5.2) being defined, our framework allows to implement general movements since we only need $2N+1$ regularly sampled positions of each finite element interpolation nodes of $\Gamma_{k,h}$. This leads to the space-time discretization of

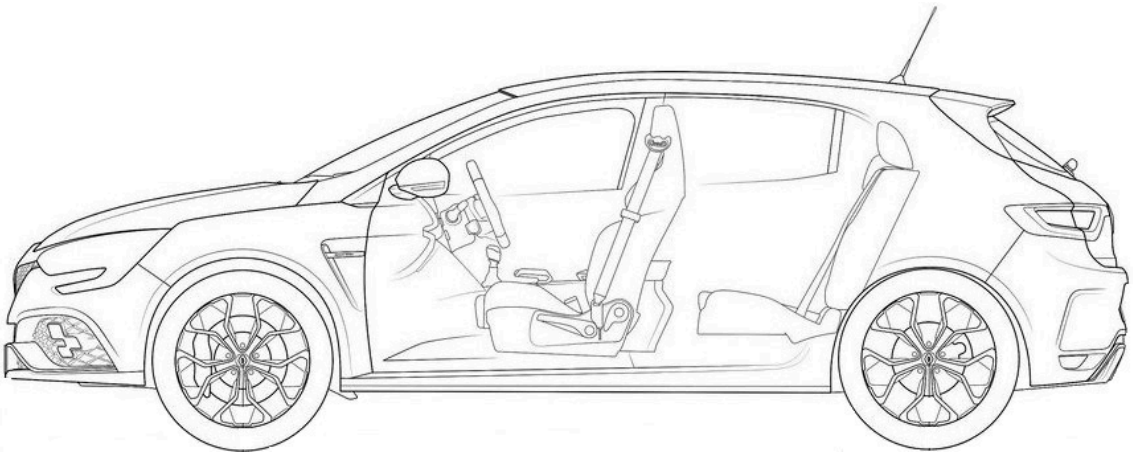

Figure 4.1: 2D schematic of a Renault Mégane.

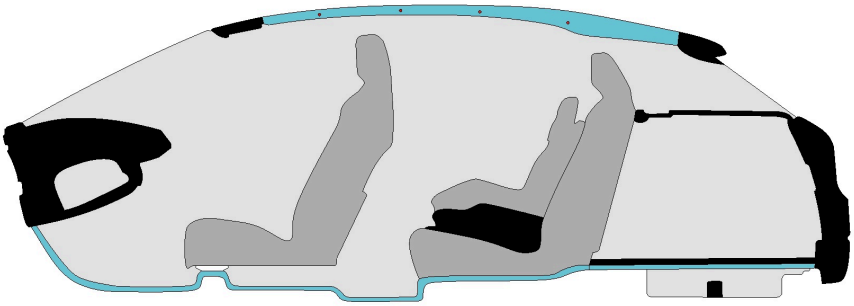

Figure 4.2: Configuration C0.

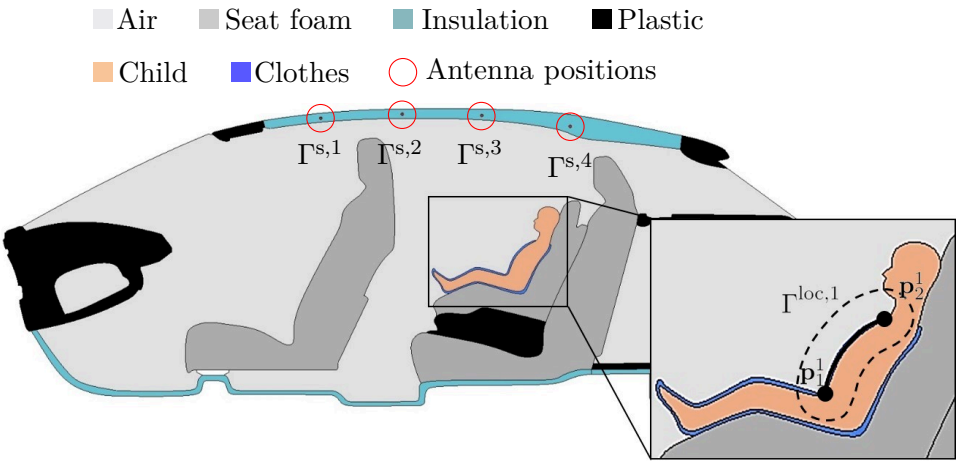

Figure 4.3: Configuration C1a.

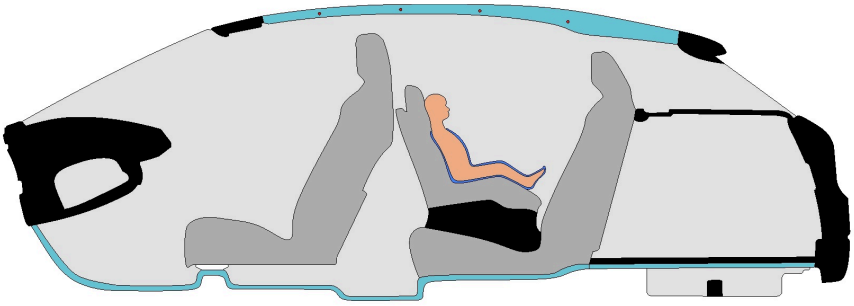

Figure 4.4: Configuration C1b.

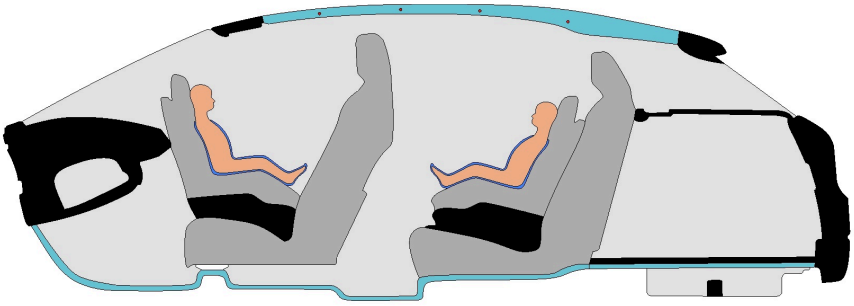

Figure 4.5: Configuration C2a.

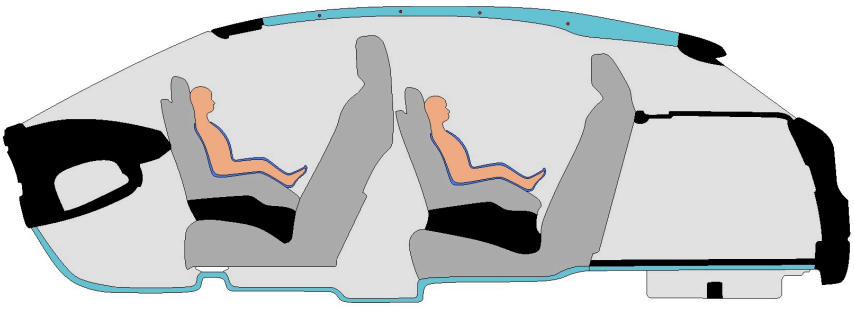

Figure 4.6: Configuration C2b.

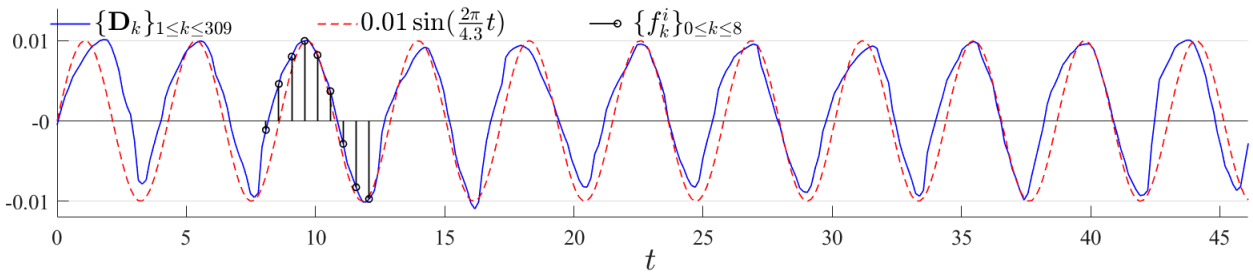

Figure 4.7: Recorded breathing motion through 309 frames in blue, sine motion of amplitude 0.01 and frequency 4.3 in red. The finite length sample $\{f_k^i\}_{0\leq k\leq 8}$ is reported with black stems.

the mapping $\mathbf{\Phi}_t$ over the sampling times $t_k = kT_\ell/(2N+1)$, $0 \leq k \leq 2N$ and the finite element triangulation of the domain. In order to extend (3.49) to various breathing patterns, the discretized deformation $\boldsymbol{\delta}_{k,h}^i|_{\Gamma_{0,h}i}$ of the boundary $\Gamma_{0,h}^i$, $i = 1, 2$ and $0 \leq k \leq 2N$, can be generalised to the following more parametrizable form

$$\begin{aligned}
\boldsymbol{\delta}_{k,h}^i|_{\Gamma_{0,h}^i}(\mathbf{x}_{0,h}) &:= \sin\left(\beta^i\pi\frac{l(\mathbf{p}_1^i\mathbf{x}_{0,h})}{l(\Gamma_{0,h}^i)}\right) f^i(\omega_\ell t_k+\varphi^i)\mathbf{n}_0(\mathbf{x}_{0,h}) \\
&= \sin\left(\beta^i\pi\frac{l(\mathbf{p}_1^i\mathbf{x}_{0,h})}{l(\Gamma_{0,h}^i)}\right) f^i\left(\omega_\ell\frac{kT_\ell}{2N+1}+\varphi^i\right)\mathbf{n}_0(\mathbf{x}_{0,h}) \qquad (4.2)\\
&=: \sin\left(\beta^i\pi\frac{l(\mathbf{p}_1^i\mathbf{x}_{0,h})}{l(\Gamma_{0,h}^i)}\right) f_k^i\mathbf{n}_0(\mathbf{x}_{0,h}).
\end{aligned}$$

In (4.2), the phase $\varphi^i \in [0, 2\pi[$ allows an offset between the rear and front breathings when $\varphi^1 \neq \varphi^2$ mod (2π). The "shape" parameter $\beta^i \in \mathbb{N}$ enables to decompose the spatial pattern of the breathing into different components. For instance setting $\beta^i = 2$ leads to an "s" motion where the belly is split into the chest and abdomen parts which are moving separately. Here the unit normal vector $\mathbf{n}_0(\mathbf{x}_{0,h})$ at $\mathbf{x}_{0,h} \in \Gamma_{0,h}^i$ is oriented such that $\mathbf{n}_0 \cdot d\mathbf{v} > 0$, where $d\mathbf{v}$ is the unit tangent vector at $\mathbf{x}_{0,h}$ of $\Gamma_{0,h}^i$ and oriented from $\mathbf{p}_1^i$ to $\mathbf{p}_2^i$. The function f^i is a general smooth T_ℓ-periodic odd function of amplitude 1, describing the time evolution of the motion. For example, we considered in Section 3.5 the sine function $f^1 := \sin$.

Let us now consider a genuine breathing sample $\{\mathbf{D}_k\}_{1\leq k\leq M}$ from [89], recorded by a small sensor centered on a human belly over $M = 309$ frames, and with sampling frequency 0.149. The duration of the breathing record then equals 46.1 and its oscillations are reported in Figure 4.7. We observe that the average breathing pattern lasts $T_\ell = 4.3$, and the average amplitude of deformation is equal to 0.01. As a comparison, we also plot in red the sine motion used in Chapters 2 and 3, centered at the origin, with amplitude $\epsilon = 0.01$ and updated frequency $\nu_\ell = 1/T_\ell = 1/4.3$.

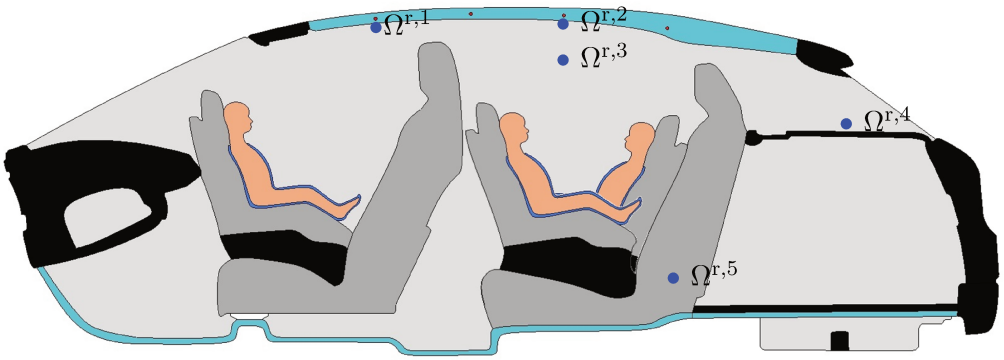

Figure 4.8: Locations of the five receiver positions $\Omega^{r,i}$, $1 \leq i \leq 5$.

Therefore, it may be interesting to use this dataset to calibrate a realistic breathing pattern for our study. To this end, let us isolate and discretize a single period of the breathing pattern into $2N+1$ time steps, as described in Section 3.2. A priori, the original sampling into M frames does not fit with our one-period sampling over $2N+1$ nodes, which is then based on the discretization of a continuous interpolation of $\{\mathbf{D}_k\}_{1\leq k\leq M}$. In view of (3.50), (4.1) and (4.2), since we have $\mathbf{\Phi}^i_{k,h}(\mathbf{x}_{0,h}) = \mathbf{x}_{0,h} + \epsilon\boldsymbol{\delta}^i_{k,h}(\mathbf{x}_{0,h})$, this provides the discretization $\epsilon\{f^i_k\}_{0\leq k\leq 2N}$ of the time dependent component ϵf^i of $\epsilon\boldsymbol{\delta}^i_{k,h}$, that we also report in Figure 4.7 for $N = 4$.

4.2 Numerical simulations

4.2.1 Calibration of the test cases

In the previous section, we defined different configurations on which we propose to apply the developed method. In order to make a comparative study of these test cases and to study the micro-Doppler signature resulting from the target motion, let us consider two kinds of representations of the calculated solutions. Firstly, we have the mapping of the field for a given harmonic $-J \leq j \leq J$, and secondly the spectrum of this field at some fixed spatial points corresponding to the receiver positions. For the sake of clarity, we plot the spectra in logarithmic scale where necessary. In accordance with the previous notations of the source, let us denote by $\{\Omega^{r,i}\}_{1\leq i\leq 5}$ the predefined positions for the receiver, considering a progressive distance from the different antenna locations. More precisely, we set $\Omega^{r,1} = (1.14, 1.53)^{\mathrm{T}}$, $\Omega^{r,2} = (2.04, 1.57)^{\mathrm{T}}$, $\Omega^{r,3} = (2.04, 1.46)^{\mathrm{T}}$, $\Omega^{r,4} = (2.9, 1.23)^{\mathrm{T}}$ and $\Omega^{r,5} = (2.37, 0.75)^{\mathrm{T}}$. We report these points on Figure 4.8.

The calculation of the reflected field in the configuration C0 corresponds to the solution of a standard Helmholtz problem for the frequency ν_f (i.e. choosing $J = 0$), on the stationary geometry of the car. In the context of occupant detection inside the car, it may then be interesting to consider this configuration as a reference. Indeed, it is preferable to consider upstream the detection of the presence of a breathing passenger rather than the detection of the absence of breathing of the passenger.

In order to fix the ideas, let us represent on Figure 4.9 the amplitude $|a^{(0,0)}_{0,h}|$ of the wave field in the stationary case, emitted from the antenna $\Gamma^{s,3}$ with amplitude $A^3 = 1$ and for $\nu_f = 10^{10}$. The

positions of the antennas are again marked by the red circles. Let us precise that for the following tests, the average element size is still fixed at 7×10^{-4}.

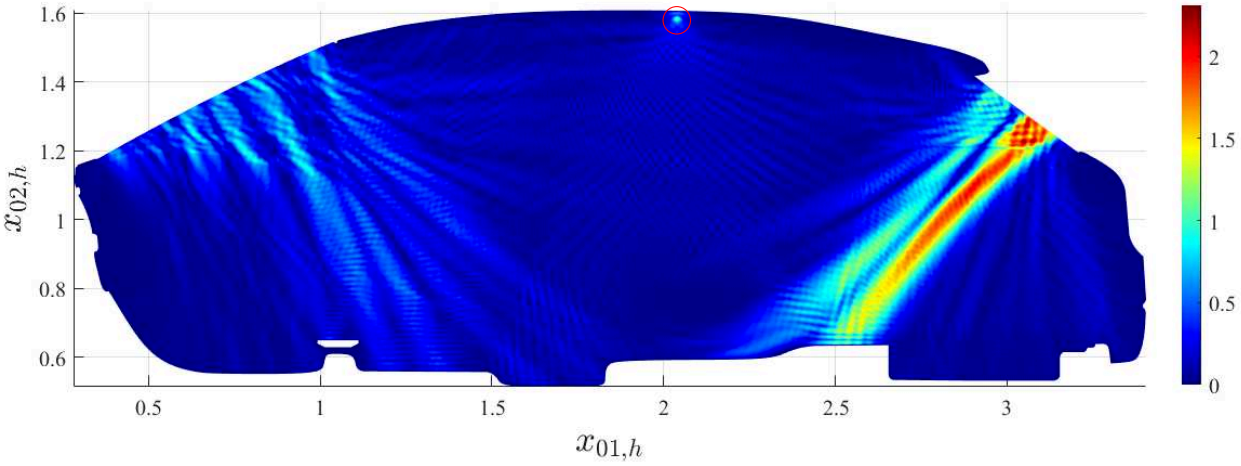

Figure 4.9: Amplitude $|a_{0,h}^{(0,0)}(\mathbf{x}_{0,h})|$ of the field emitted from $\Gamma^{s,3}$ for the configuration C0.

We observe the influence of different materials on the wavelength of the field, which makes it possible to discern some of the car components such as seats or the back deck. In addition, we make a second observation concerning the scattering of the field, showing a reflecting cavity phenomenon. Indeed, the domain appears as a reflecting cavity on all its borders, except for the front and rear windows where the boundary condition is transparent. Thus, like a light beam reflected by a light source surrounded by a mirrored sphere and pierced by an aperture (headlights, torch, etc.), the constructive interferences of the wave field produce two regions of greater amplitude, forming an axis perpendicular to each of the "apertures" of the domain boundary (front and rear windows). Let us now consider a second position $\Gamma^{s,1}$ for the emitting antenna, keeping the same settings. We report in Figure 4.10 the amplitude $|a_{0,h}^{(0,0)}|$ of the wave field over the domain.

We remark for this configuration a significant increase of maximum of amplitude of $|a_{0,h}^{(0,0)}|$, reaching a maximal amplitude of about 8 while for the position $\Gamma^{s,3}$ we obtain about 2.3. This suggests that, given the geometry of the domain, a source located at this position induces some resonance phenomena. Finally, to illustrate the previous discussion in Subsection 4.1.1 concerning the compatibility of the method with several sources, let us consider in Figure 4.11 a simultaneous emission from the two antennas $\Gamma^{s,1}$ and $\Gamma^{s,3}$, with respective amplitudes $A^1 = 1$ and $A^3 = 2$.

The resulting field corresponds to the amplitude of the sum of the fields emitted by each of the antennas $\Gamma^{s,1}$ and $\Gamma^{s,3}$.

4.2.2 Detection of car occupants

We precise that, for all the following tests, the main parameters are kept the same. More precisely, the frequency of emission is fixed to $\nu_f = 10^{10}$ with amplitude $A^i = 1$ for $1 \leq i \leq 4$, the size of the

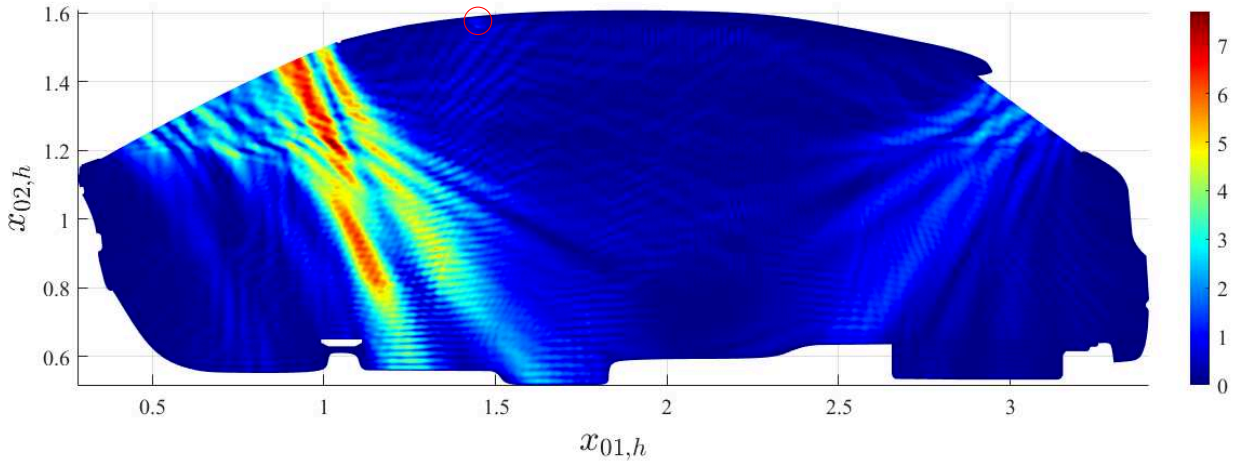

Figure 4.10: Amplitude $|a_{0,h}^{(0,0)}(\mathbf{x}_{0,h})|$ of the field emitted from $\Gamma^{s,1}$ for the configuration C0.

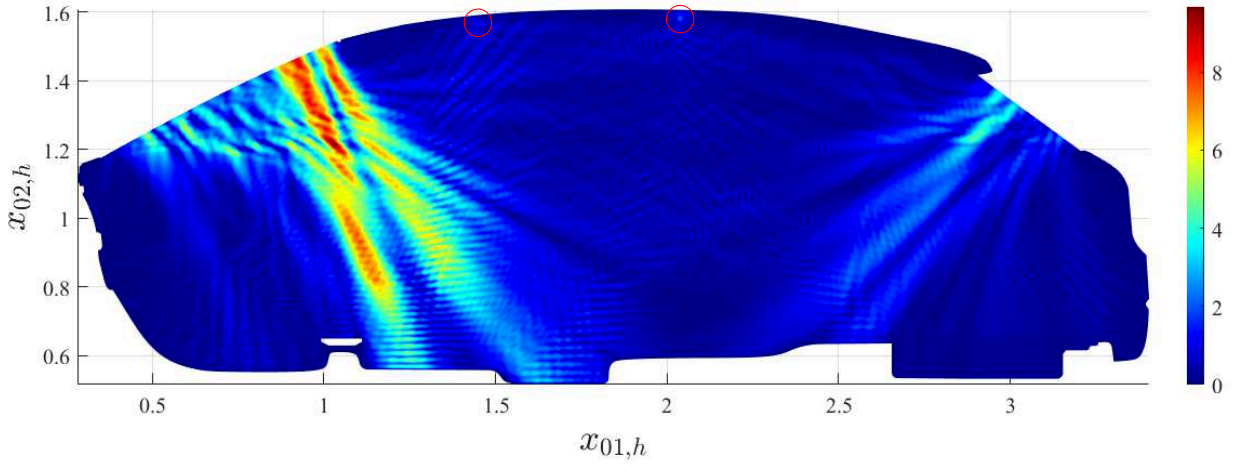

Figure 4.11: Amplitude $|a_{0,h}^{(0,0)}(\mathbf{x}_{0,h})|$ of the field emitted simultaneously from $\Gamma^{s,1}$ and $\Gamma^{s,3}$, with amplitudes $A^1 = 1$ and $A^3 = 2$, respectively, for the configuration C0.

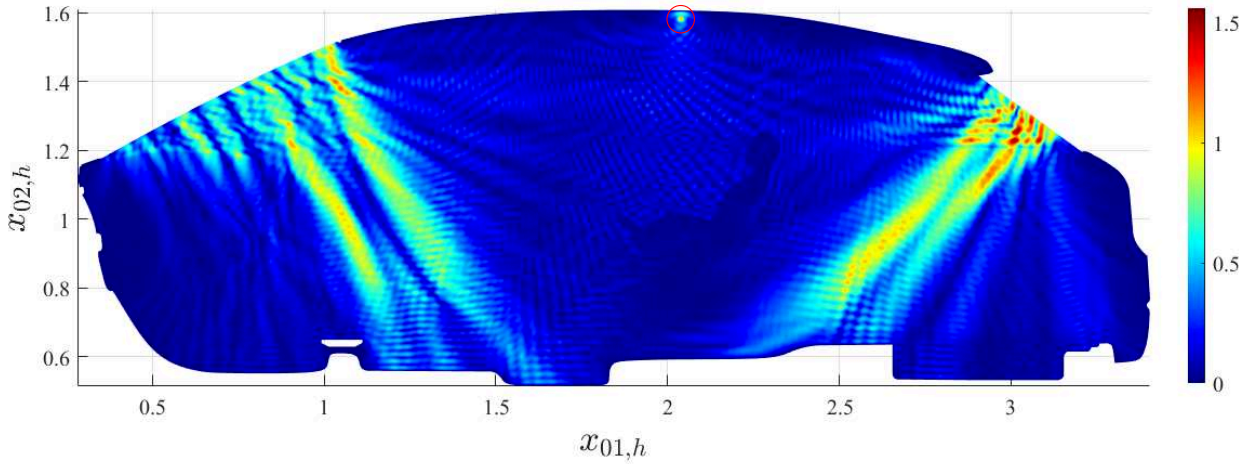

Figure 4.12: Amplitude $|a_{0,h}^{(4,10)}(\mathbf{x}_{0,h})|$ of the field emitted from $\Gamma^{\mathrm{s},3}$ for the configuration C1a.

rear (and front, if applicable) layer is $L = 0.1$ and we set $J = 10$ and $N = 4$.

The case of a passenger in the rear seat

Let us now consider a situation where a baby is sitting in the back of the car, inside a road facing seat and breathing as described in Subsection 4.1.3 (i.e. sampled by the series $\{f_k^1\}_{0\leq k\leq 8}$). The induced deformation of the moving boundary is then described by $\boldsymbol{\delta}_{k,h}^1$ through (4.2). We first consider $\beta^1 = 1$ and $\varphi^1 = 0$, i.e. a full breathing where chest and belly are moving in the same direction, and we set an emitting antenna at position $\Gamma^{\mathrm{s},3}$. We report on Figure 4.12 the amplitude $|a_{0,h}^{(4,10)}|$.

We first observe a significant absorption of the EM field by the baby as well as a substantial increasing of the wavenumber of the wavefield in the baby, due to the much higher permittivity of the human body. Indeed, according to (3.48), the higher the permittivity of the medium, the lowest the corresponding wave velocity, which is inversely proportional to the wavenumber. This is particularly visible in Figure 4.13, which corresponds to the representation of Figure 4.12 in logarithmic scale.

However, the resolution of the calculated field over this area is relatively low (some artifacts are also visible), due to the refinement of the used mesh used. For completeness, let us also represent the amplitudes of the harmonics $a_{1,h}^{(4,10)}$, $a_{2,h}^{(4,10)}$, $a_{5,h}^{(4,10)}$ and $a_{10,h}^{(4,10)}$ in Figures 4.14-4.17 respectively.

Now we can highlight the micro-Doppler signature induced by the presence of a breathing passenger. We compare in Figure 4.18 the spectrum $|\widehat{w}_h^{(4,10)}(\Omega^{\mathrm{r},4})|$ of the total field, measured at the receiver $\Omega^{\mathrm{r},4}$ for the configurations C0 (in red) and C1a (in blue) respectively, and considering the same emitting antenna $\Gamma^{\mathrm{s},3}$. According to the theory, the periodic deformation of the geometry induces a modulation of the emission frequency, over a bandwidth centered at ν_{f}, and composed of peaks spaced by the frequency of the breathing movement, i.e. $\nu_\ell = 1/T_\ell \simeq 0.23$. This is the micro-Doppler signature of the rear passenger's breathing.

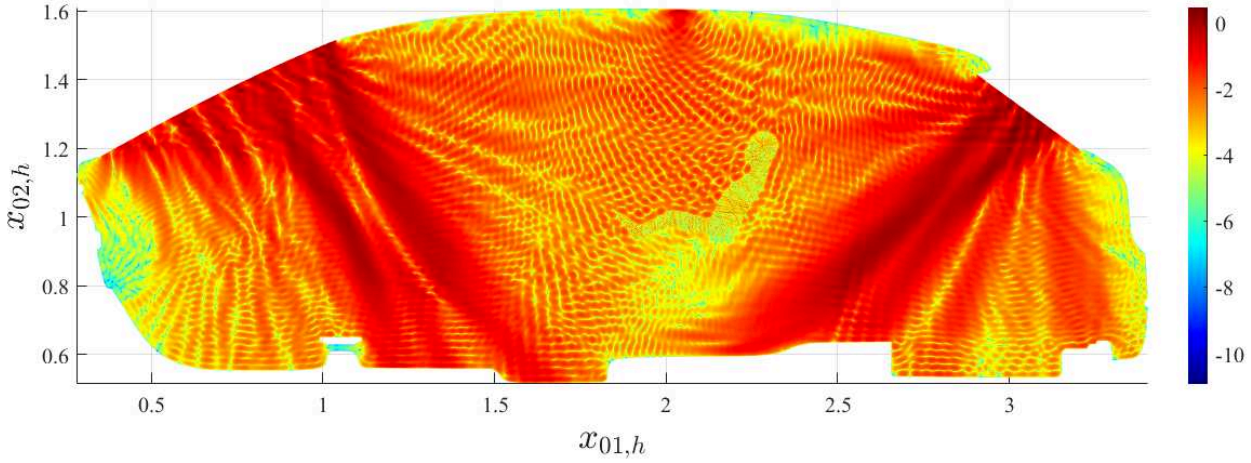

Figure 4.13: Magnitude $\log(|a_{0,h}^{(4,10)}(\mathbf{x}_{0,h})|)$ of the field emitted from $\Gamma^{s,3}$ for the configuration C1a.

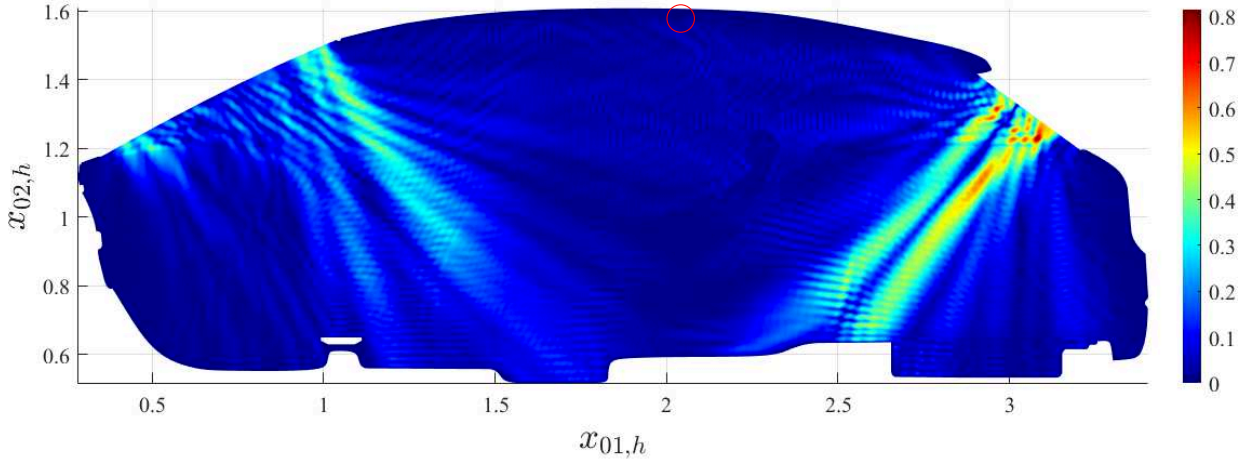

Figure 4.14: Amplitude $|a_{1,h}^{(4,10)}(\mathbf{x}_{0,h})|$ of the field emitted from $\Gamma^{s,3}$ for the configuration C1a.

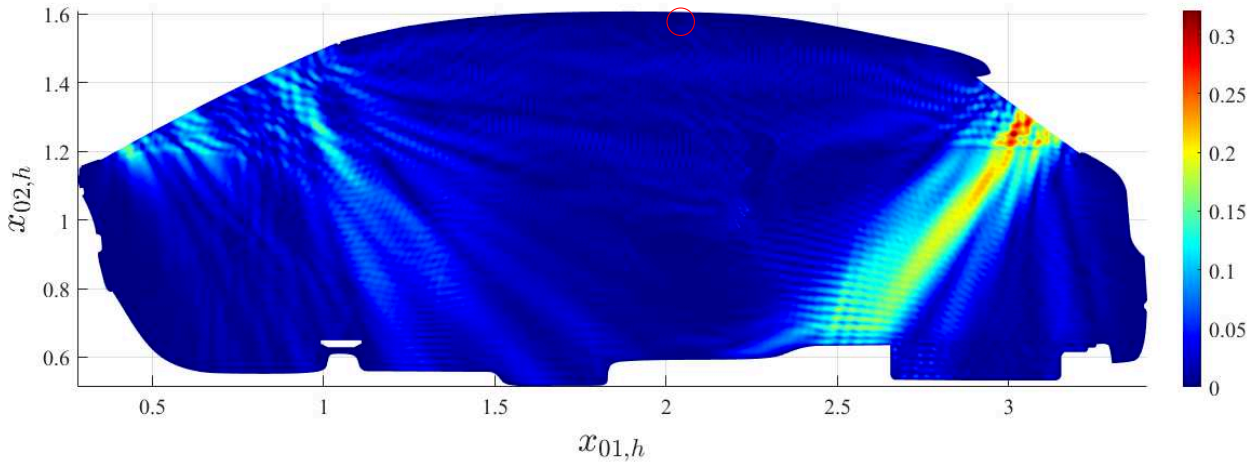

Figure 4.15: Amplitude $|a_{2,h}^{(4,10)}(\mathbf{x}_{0,h})|$ of the field emitted from $\Gamma^{s,3}$ for the configuration C1a.

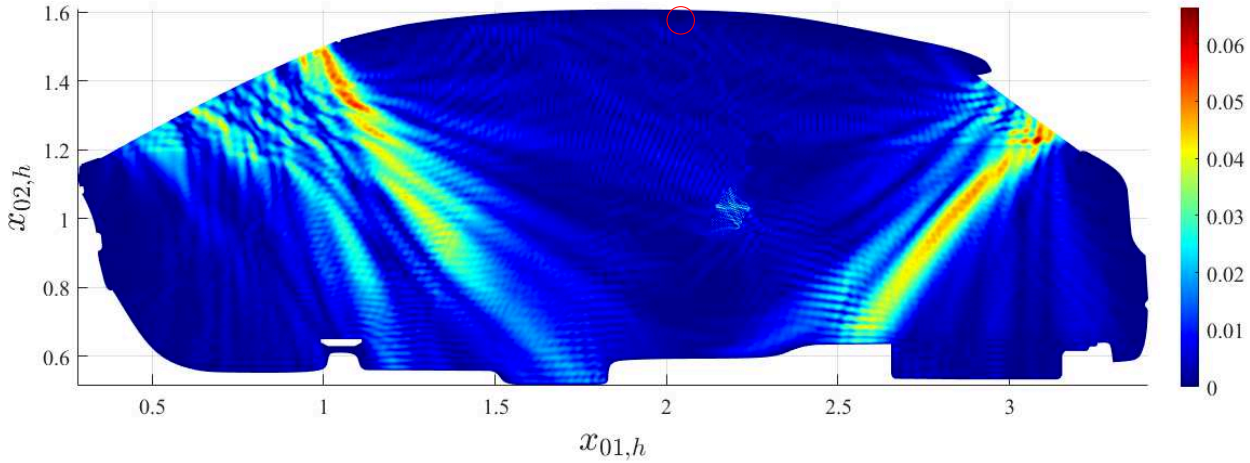

Figure 4.16: Amplitude $|a_{5,h}^{(4,10)}(\mathbf{x}_{0,h})|$ of the field emitted from $\Gamma^{s,3}$ for the configuration C1a.

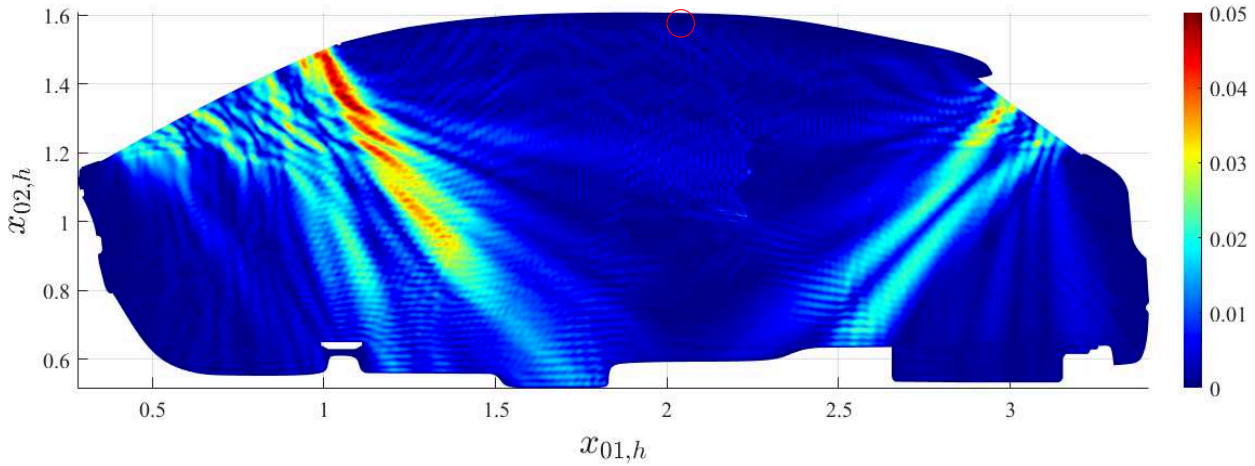

Figure 4.17: Amplitude $|a_{10,h}^{(4,10)}(\mathbf{x}_{0,h})|$ of the field emitted from $\Gamma^{s,3}$ for the configuration C1a.

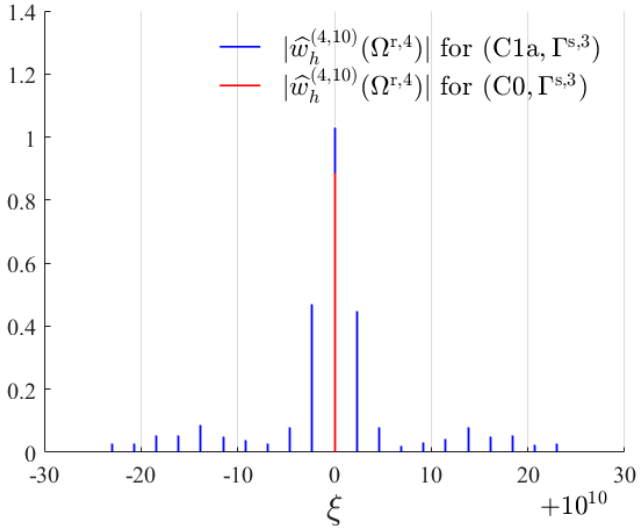

Figure 4.18: Spectrum $|\widehat{w}_h^{(4,10)}(\Omega^{r,4})|$ at $\Omega^{r,4}$ of the field, emitted from $\Gamma^{s,3}$, for C0 (red) and C1a (blue).

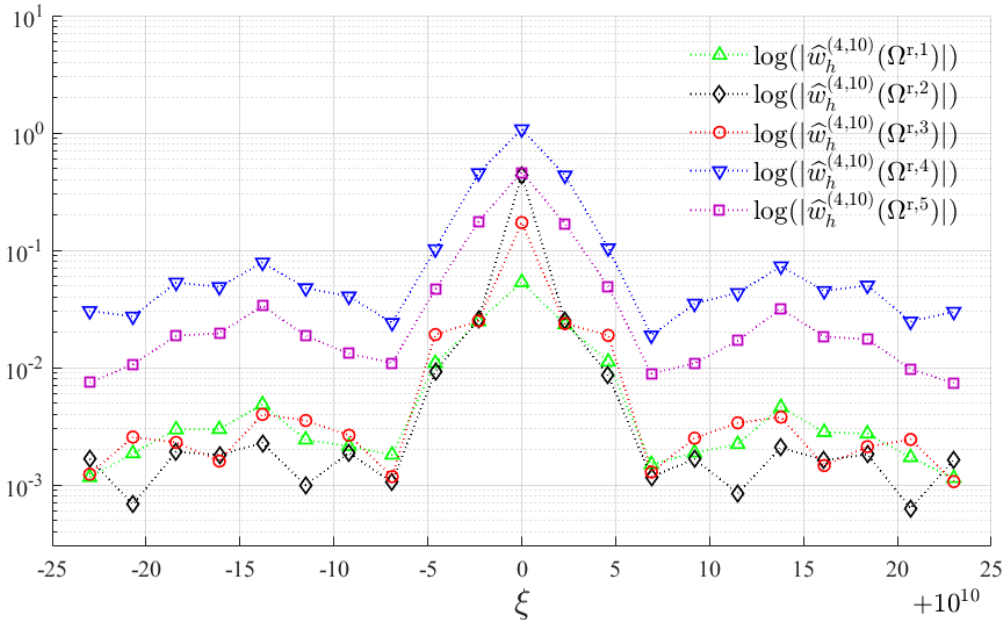

Figure 4.19: Spectrum $\log(|\widehat{w}_h^{(4,10)}|)$ of the field emitted from $\Gamma^{s,3}$ in C1a, measured at positions $\Omega^{r,i}$ for $1 \leq i \leq 5$.

Furthermore, let us remark that the previously described beam phenomenon also appears for the other harmonics of the field. This observation suggests that there are more favourable positions than others for positioning a receiver and measuring the spectrum of the reflected signal. This is illustrated in Figure 4.19 where we report the amplitudes of the spectra $\widehat{w}_h^{(4,10)}(\Omega^{r,i})$ in log scale, for $1 \leq i \leq 5$. We observe a significantly higher excitation of the harmonics in the area illuminated by the beam (receivers $\Omega^{r,4}$ and $\Omega^{r,5}$, see Figure 4.8), while elsewhere the readability of the micro-Doppler signature is lower. Although the main mode (in ν_f) is correctly represented in the neighborhood of the emission source (receiver $\Omega^{r,2}$), we note that this neighborhood does not allow an easier reading of the other harmonics.

The next interesting parameter to vary is the position of the source, in order to evaluate whether a different illumination of the domain improves the detection of the frequency modulation. Still considering the geometry C1a, we consider the sca fields emitted from the antennas $\Gamma^{s,1}$, $\Gamma^{s,2}$, $\Gamma^{s,3}$ and $\Gamma^{s,4}$ respectively. Let us report in Figures 4.20-4.22 the corresponding field cartography for $\Gamma^{s,1}$, $\Gamma^{s,2}$ and $\Gamma^{s,4}$ (the case with $\Gamma^{s,3}$ is given in Figure 4.12).

As a first observation, the structure of the illumination remains globally similar, and we find the significant increase of the solution amplitude in the case of the source $\Gamma^{s,1}$, as discussed in Subsection 4.2.1. We can also notice the attenuation of the maximum amplitude in the case of the antenna $\Gamma^{s,4}$, which can be explained by the direct proximity of the passenger whose body is highly absorbing.

Let us now compare for the fixed position $\Omega^{r,4}$ the spectra from the different antenna positions

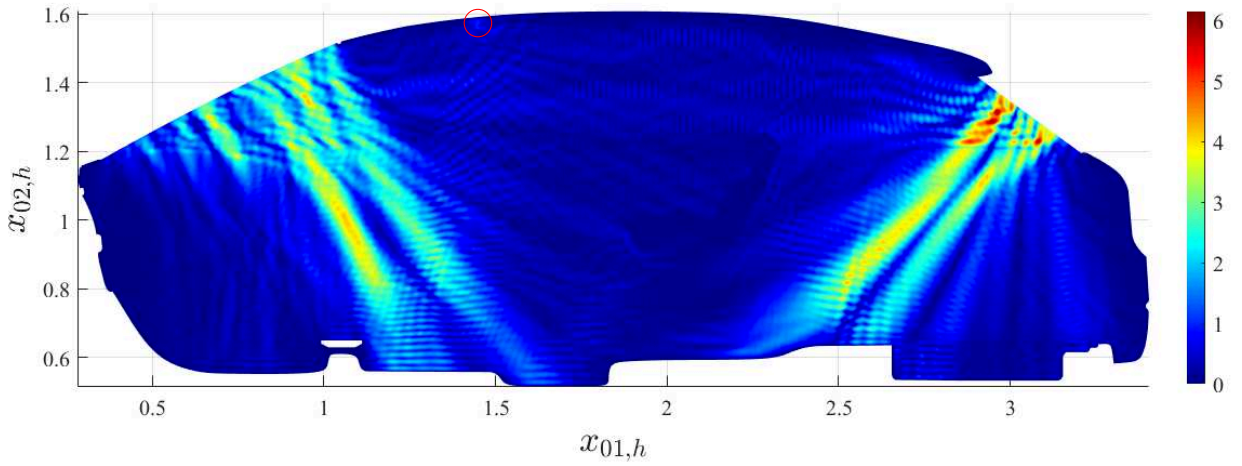

Figure 4.20: Amplitude $|a_{0,h}^{(4,10)}(\mathbf{x}_{0,h})|$ of the field emitted from $\Gamma^{s,1}$ for the configuration C1a.

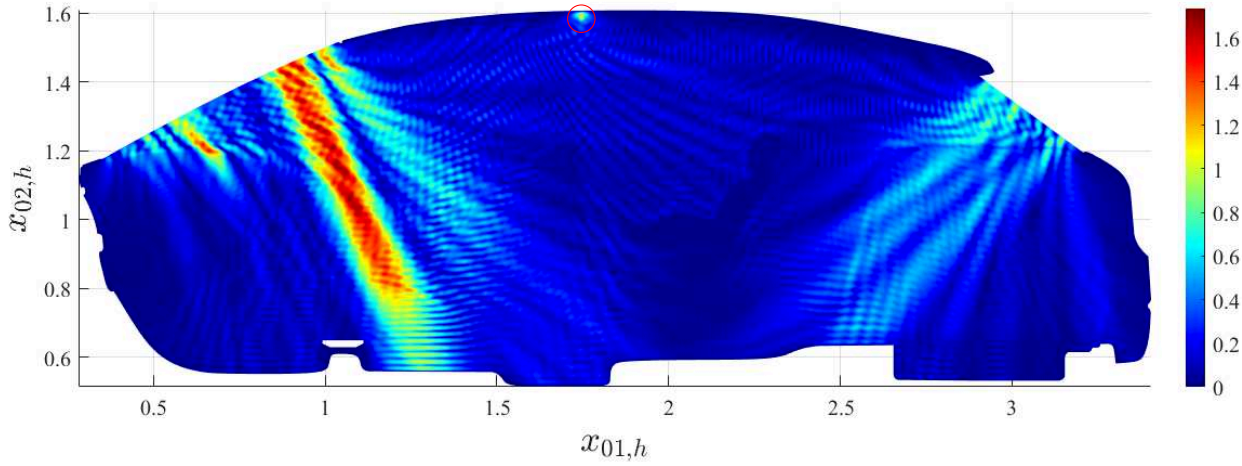

Figure 4.21: Amplitude $|a_{0,h}^{(4,10)}(\mathbf{x}_{0,h})|$ of the field emitted from $\Gamma^{s,2}$ for the configuration C1a.

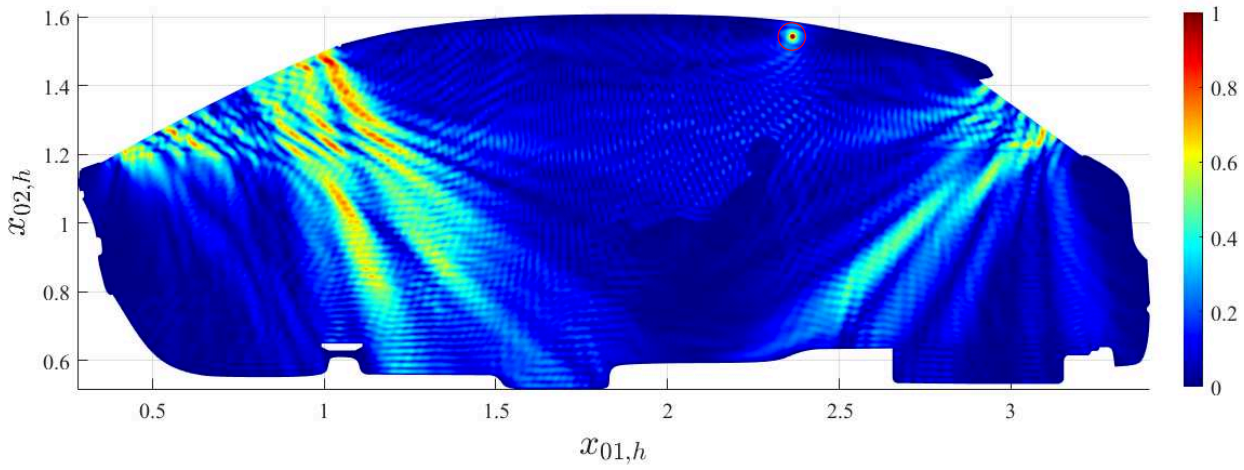

Figure 4.22: Amplitude $|a_{0,h}^{(4,10)}(\mathbf{x}_{0,h})|$ of the field emitted from $\Gamma^{\mathrm{s},4}$ for the configuration C1a.

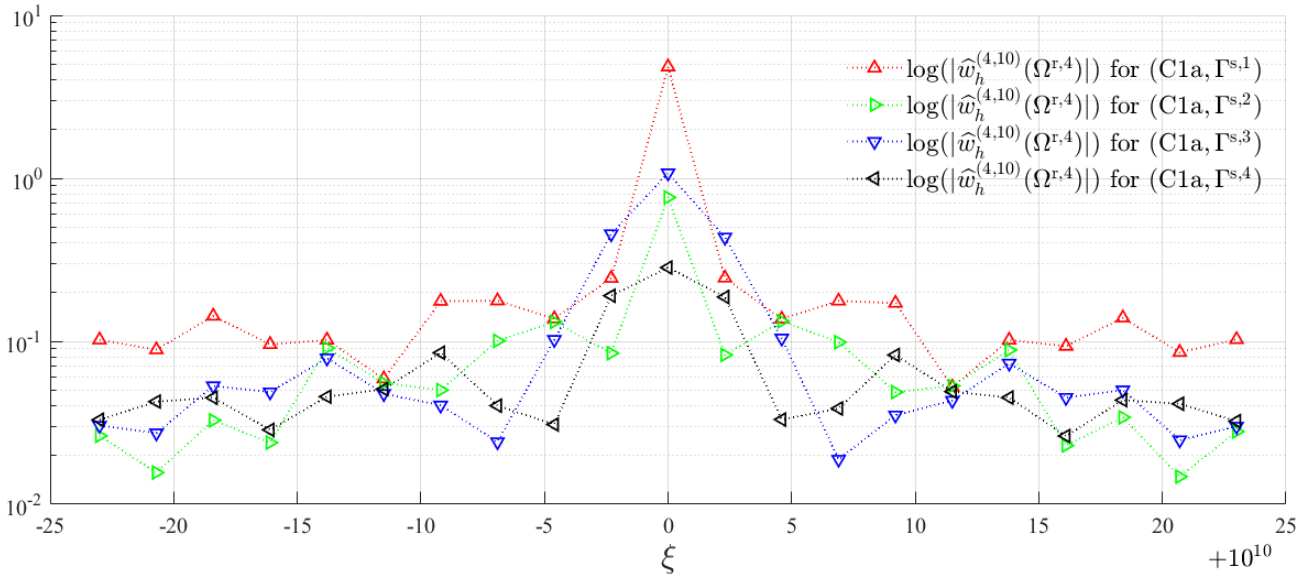

Figure 4.23: Spectrum $|\widehat{w}_h^{(4,10)}(\Omega^{\mathrm{r},4})|$ at $\Omega^{\mathrm{r},4}$ of the wave field in C1a, emitted from $\Gamma^{\mathrm{s},i}$, for $1 \leq i \leq 4$.

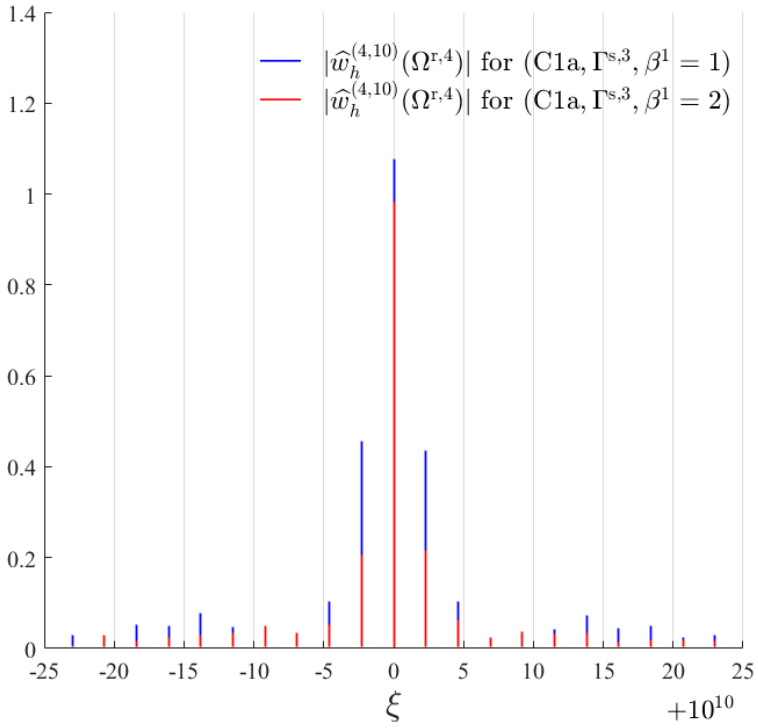

Figure 4.24: Comparison between the spectrum of the field in C1a emitted from $\Gamma^{s,3}$, at $\Omega^{r,4}$ for $\beta^1 = 1$ (blue) and $\beta^1 = 2$ (red).

in Figure 4.23 (in log scale). In agreement with the previous observations, the most excited coupled modes correspond to those of the field emitted by $\Gamma^{s,1}$ while the case of the source located at $\Gamma^{s,4}$ leads to the weaker modes excitation. This suggests that the use of antennas $\Gamma^{s,1}$, $\Gamma^{s,2}$ and $\Gamma^{s,3}$, within the C1a geometry, is preferable.

The formulation (4.2) also allows us to modulate the breathing pattern, i.e. to generate an asynchronous movement of the chest and the belly, by choosing for example $\beta^1 = 2$. We represent in Figure 4.24 the amplitude $\widehat{w}_h^{(4,10)}(\Omega^{r,4})$ in the cases $\beta^1 = 1$ (in blue) and $\beta^1 = 2$ (in red), for the configuration C1a with a source located at $\Gamma^{s,3}$. It appears that the amplitude of the modes is lower for $\beta^1 = 2$, which corresponds to the case of an asynchronous breathing. Indeed, such a movement induces a decay of the maximal amplitude of the deformation, which results in a lower excitation of the modes in accordance with Figure 2.6 in Chapter 2.

We now focus on the third configuration C1b in which the baby is facing back to the road, as shown in Figure 4.4. To illustrate the situation, we plot on Figure 4.25 the amplitude of the reflected field over the domain with an emitting antenna located at $\Gamma^{s,2}$. The calculation parameters are maintained, and we consider $\beta^1 = 1$ by default. In order to compare the micro-Doppler signatures obtained for this third configuration C1b according to the different antenna positions, we plot in Figure 4.26 the spectra of the fields emitted from antennas $\Gamma^{s,1}$, $\Gamma^{s,2}$, $\Gamma^{s,3}$ and $\Gamma^{s,4}$. These spectra are measured at position $\Omega^{r,4}$, and we also plot the reference curve, i.e. the spectrum at $\Omega^{r,4}$ of

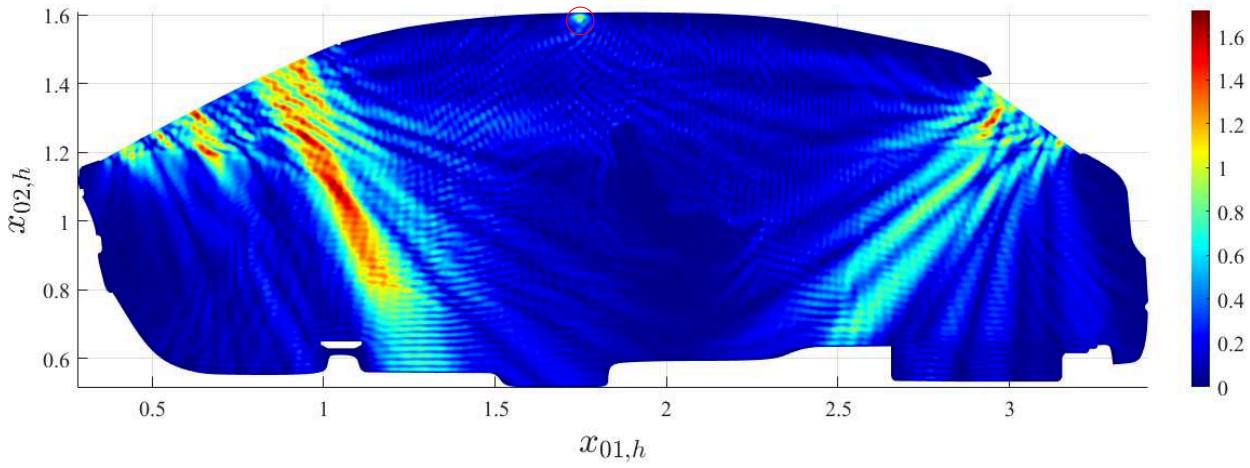

Figure 4.25: Amplitude $|a_{0,h}^{(4,10)}(\mathbf{x}_{0,h})|$ of the field emitted from $\Gamma^{s,2}$ for the configuration C1b.

the field emitted from $\Gamma^{s,3}$ in configuration C1a.

The third antenna $\Gamma^{s,3}$ results in a significantly higher excitation of the coupled modes, unlike positions $\Gamma^{s,2}$ and $\Gamma^{s,4}$. This is consistent with the previously formulated hypothesis concerning the amplitude decay linked to the presence of a highly absorbing material in the neighborhood of the emitting antenna $\Gamma^{s,2}$. Moreover, even if the choice of antenna $\Gamma^{s,1}$ seems to allow an easier reading of the Doppler modes, this is possibly due to the geometry of the domain itself, as suggested before. This makes it an *a priori* difficult choice to generalise. However, the antenna $\Gamma^{s,3}$ leads to a significant excitation for each of the two configurations C1a and C1b. The intermediate position of this antenna, facing the passenger whatever its orientation, probably explains this efficiency.

The case of two passengers in both rear and front seats

We now introduce a generalisation of the geometry by considering a second passenger on the front seat, oriented back to the road. This situation corresponds to the configurations C2a and C2b illustrated in Figures 4.5 and 4.6. Let us investigate first the total wave field when emitted in C2a, i.e. when the rear passenger faces the road. As an indication, we show in Figure 4.27 the map of the field emitted from the reference antenna $\Gamma^{s,3}$, on C2a.

We also observe the contour of the passenger, marked by a sharp decrease in amplitude as well as a clear increase of the wave number. Finally, the solution highlights the attenuation of the beam perpendicular to the front window, due to the presence of the absorbing material of the second passenger. Furthermore, we keep the spectrum at $\Omega^{r,4}$ of the field emitted by $\Gamma^{s,3}$ on C1a as a standard and compare it, with Figure 4.28, to the one obtained under the same conditions with the addition of the front passenger (i.e. configuration C2a). This allows a first evaluation of the modification of the micro-Doppler signature. In order to test the usefulness of a second transmitting antenna in the case of a second passenger, we also plot in Figure 4.28 the spectrum of the field emitted simultaneously from $\Gamma^{s,1}$ and $\Gamma^{s,3}$, with constant amplitudes $A^1 = A^3 = 1$.

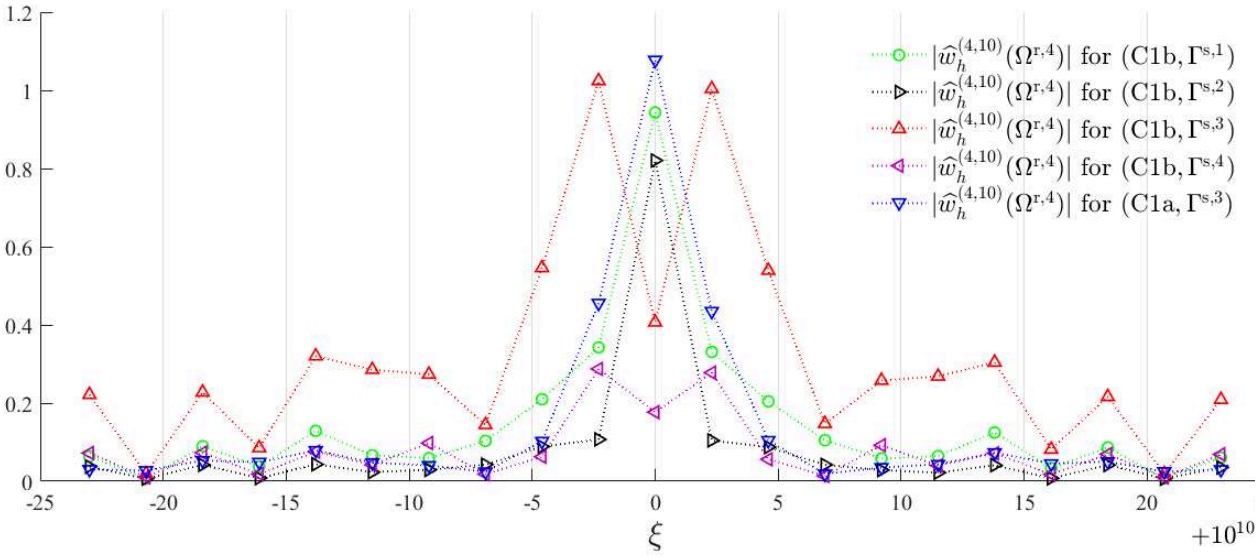

Figure 4.26: Spectrum $|\widehat{w}_h^{(4,10)}(\Omega^{r,4})|$ of the field in C1b, emitted from $\Gamma^{s,i}$, for $1 \leq i \leq 4$, vs. the reference spectrum for C1a at $\Gamma^{s,3}$.

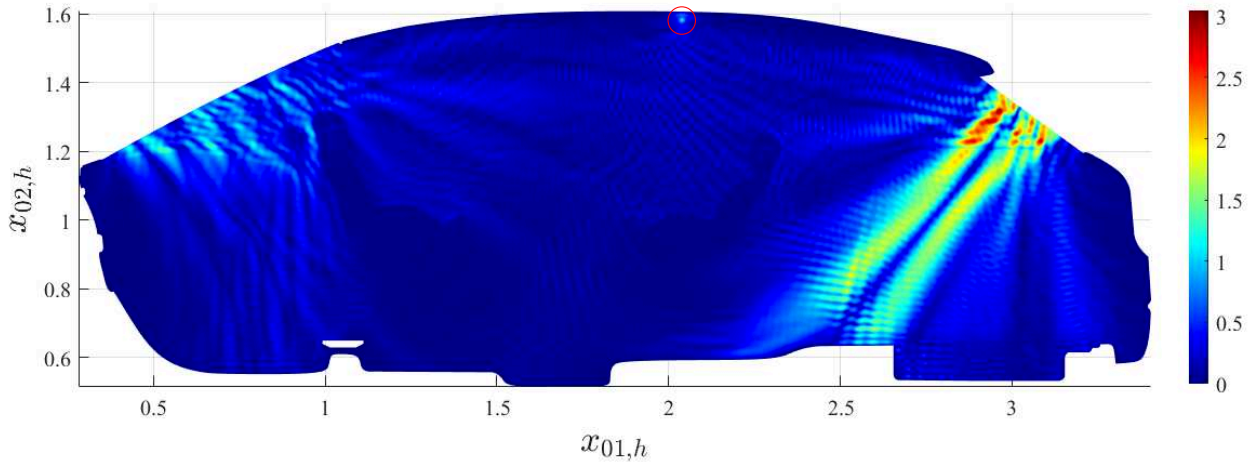

Figure 4.27: Amplitude $|a_{0,h}^{(4,10)}(\mathbf{x}_{0,h})|$ of the field emitted from $\Gamma^{s,3}$ for the configuration C2a.

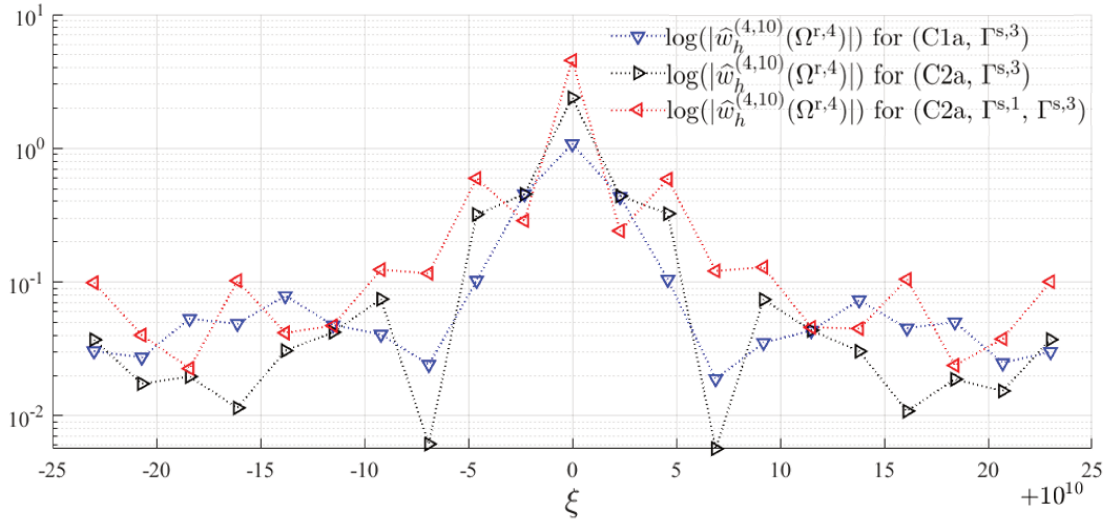

Figure 4.28: Spectrum $\log(|\widehat{w}_h^{(4,10)}(\Omega^{r,4})|)$ emitted from $\Gamma^{s,3}$ in C1a (blue), in C2a (black) and from both antennas $\Gamma^{s,1}$ and $\Gamma^{s,3}$ in C2a (red).

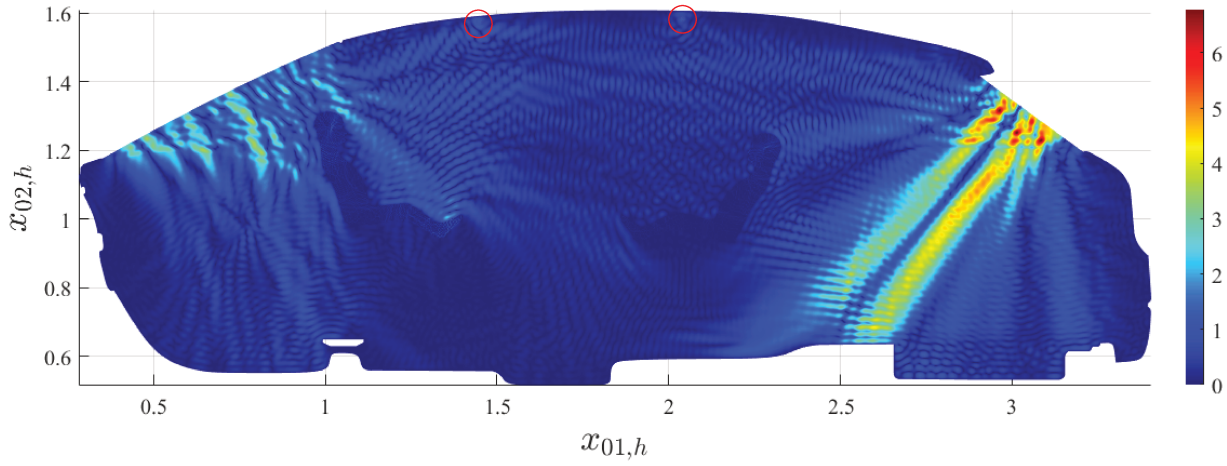

Figure 4.29: Amplitude $|a_{0,h}^{(4,10)}(\mathbf{x}_{0,h})|$ of the field emitted from $\Gamma^{s,1}$ and $\Gamma^{s,3}$ for the configuration C2a.

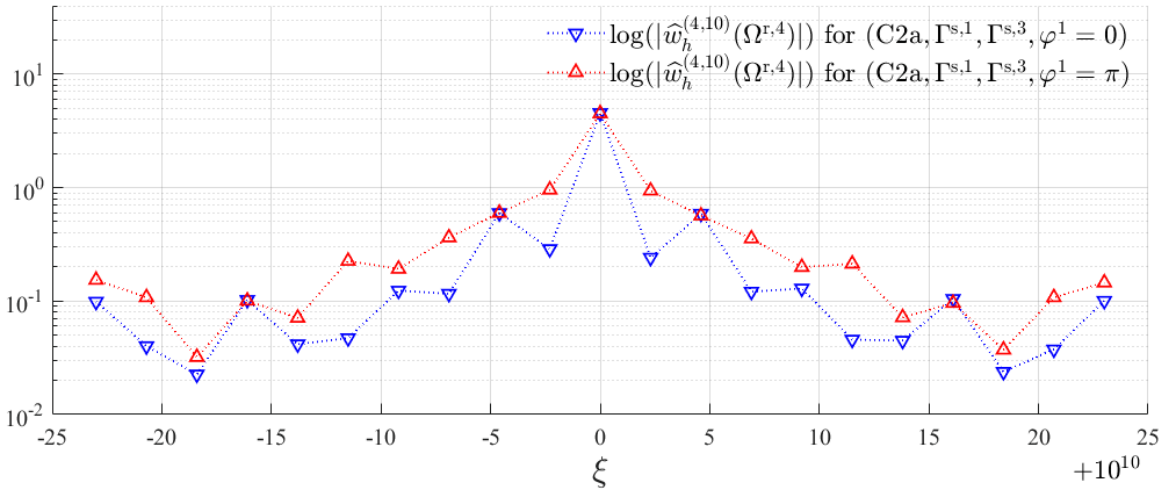

Figure 4.30: Spectrum $\log(|\widehat{w}_h^{(4,10)}(\Omega^{r,4})|)$ emitted from both $\Gamma^{s,1}$ and $\Gamma^{s,3}$ in C2a, with $\varphi^1 = 0$ (blue) and $\varphi^1 = \pi$ (red).

Let us illustrate this adjustment in Figure 4.29, where we plot the corresponding map over C2a. Firstly, the excitation of the modes is comparatively slightly lower, for a constant emission on $\Gamma^{s,3}$, when a second passenger is present. This may seem contradictory as this one "doubles" the domain deformation. However, the amplitude of this deformation does not increase, and we have seen on the contrary that the front area of the vehicle is less well illuminated by the antenna $\Gamma^{s,3}$. Secondly, we see that the addition of an extra antenna ($\Gamma^{s,1}$) illuminating this front area significantly improves the detection of the micro-Doppler signature of the deformation. This is also due to the fact that the emitted field has a higher maximum amplitude, because of the constructive interference produced by the two sources $\Gamma^{s,1}$ and $\Gamma^{s,3}$. This observation suggests the possibility of tuning the detection by modulating/refining the emission amplitude of the second antenna.

Let us now introduce a slight variation of the configuration C2a, by considering asynchronous breaths of the two passengers. More precisely, we introduce a phase opposition by choosing $\varphi^1 = \pi$ while $\varphi^2 = 0$. We report this experiment on Figure 4.30 with the spectrum of the field emitted from both antennas $\Gamma^{s,1}$ and $\Gamma^{s,3}$, with $\varphi^1 = 0$ (blue) and $\varphi^1 = \pi$ (red). We find that for a fixed configuration, the phase shift between the forward and backward deformations of the domain results in a noticeable increase in amplitude of about each one of two micro-Doppler mode. However, it is impossible to distinguish this shift without further benchmarks for comparison.

Finally, let us focus on the last configuration C2b in which the rear passenger is facing away from the road, without phase shift between the breathing motions. This situation is illustrated in Figure 4.31, with two emitting sources. We note that for this configuration, the maximum field amplitude of the fundamental mode is twice as low as in the case C2a at equal emission. It is however difficult to explain this observation precisely. In Figure 4.32 we compare the micro-Doppler response of this new configuration with the previous one C2a, for identical physical parameters. We see on this graph that the amplitude of the harmonics is less attenuated than for the fundamental. The latter therefore produces a detectable signature comparable to the previous ones.

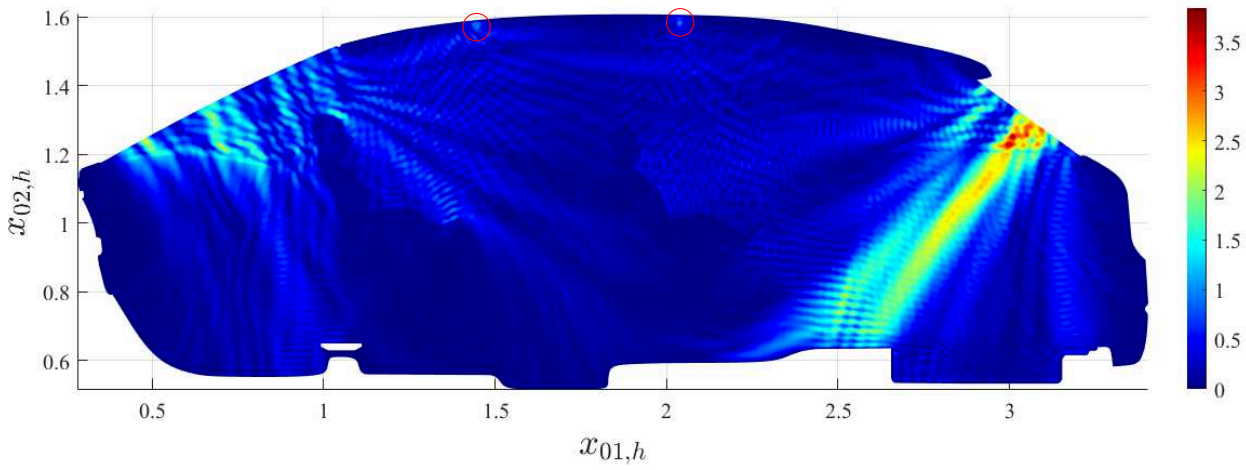

Figure 4.31: Amplitude $|a_{0,h}^{(4,10)}(\mathbf{x}_{0,h})|$ of the field emitted from $\Gamma^{s,1}$ and $\Gamma^{s,3}$ for the configuration C2b.

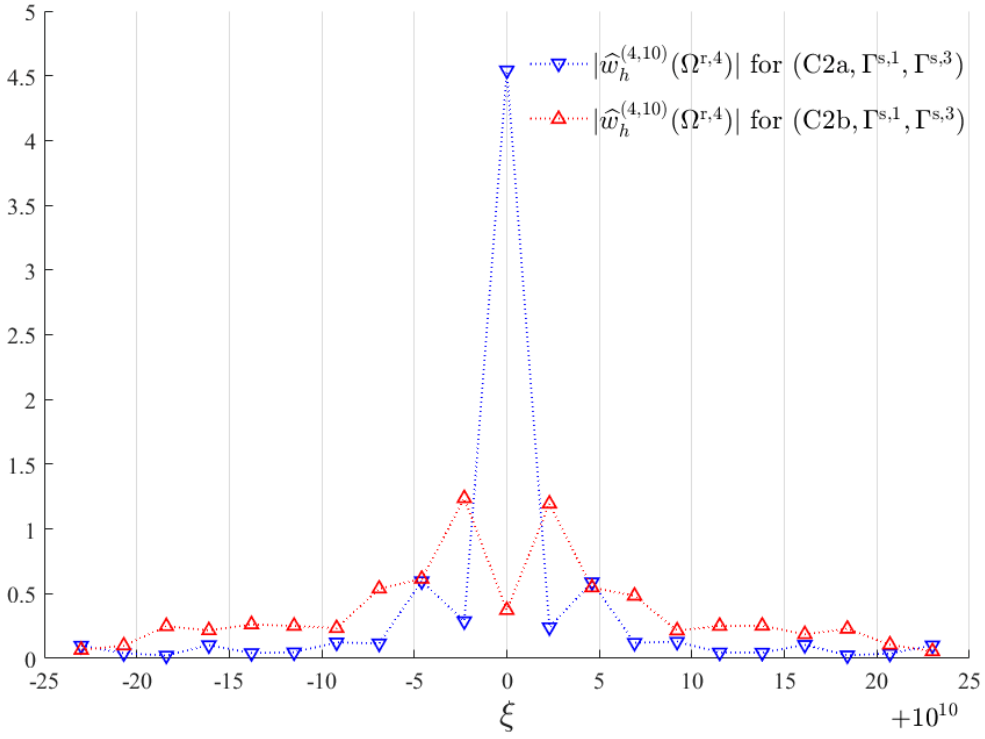

Figure 4.32: Spectrum $|\widehat{w}_h^{(4,10)}(\Omega^{r,4})|$ emitted from both $\Gamma^{s,1}$ and $\Gamma^{s,3}$ in C2a (blue) and C2b (red).

4.3 Discussion of the results

This chapter focused on the application of the method developed in this thesis to simulate the micro-Doppler signature generated by the presence of car passengers in different situations, and on a first analysis of this signature. To do this, we defined different geometries corresponding to the situations we wish to study. We then calculated the corresponding solutions by varying parameters such as the position of the antenna(s), or even the type of breathing considered. We have explicited in the previous chapters how the presence of modes around the emission frequency ν_{f} in the spectrum of the wave field is the genuine manifestation of a domain deformation. In this chapter, we showed to what extent the proposed method allows to highlight the presence of this modulation. However, important issues remain open, in particular the refinement of this detection in order to be able to differentiate the configurations, i.e. to identify a front or rear passenger, or its orientation, etc. A significant improvement in the realism of the modelled wave field follows from Chapter 1 and consists in the generalisation of the method to the three-dimensional vector case, in order to address the full Maxwell system. In particular, we set out the starting point for this extension in Appendix D. This allows the introduction of field polarization, which would be especially useful in discriminating the different perturbations according to their directions. In this more general setting we foresee that the use of two antennas might no longer be necessary for a correct reading of the micro-Doppler signature. Of course, in all cases, increasing the frequency would make the field less sensitive to absorption phenomena caused by the different materials and, above all, produce a more precise micro-Doppler signature, with a wider frequency modulation band.

General conclusion

In this thesis, we studied a two-dimensional wave scattering problem in an inhomogeneous and partially reflective medium, whose geometry is periodically deformed. Our aim was to propose an innovative modelling of the frequency modulation of the total field, i.e. the micro-Doppler signature of the domain deformation. This study is part of the very concrete framework of the detection of passengers inside a car via their breathing, using VitaSense, the radar based sensor developed by IEE.

Summary of the main findings

In the first chapter, we described the industrial context in which this work was carried out. In particular, we presented the general operating procedures of the VitaSense sensor, as well as some theoretical reminders concerning the Doppler effect theory. In doing so, we were able to highlight a particular structure of frequency modulation, specific to the harmonic deformation characteristic of a breathing motion. This observation, heuristically justified at first, allowed us to predict the structure of the unknown solution, namely a Dirac comb centred on the emission frequency and whose teeth are separated by the oscillation frequency of the deformation. Finally, we introduced the physical foundations to write this wave propagation problem using Maxwell's equations, and then derived the scalar equation governing the evolution of the electric potential.

In the second chapter, we introduced our multi-harmonic finite element method, based on the electric potential equation. The first step was to define a simplified one-dimensional context for the model, i.e. a segment bounded by a fixed source and a fully reflecting obstacle in oscillating motion. In order to address this problem, we first rewrote the system in a fixed domain with space-time coordinates by means of an appropriate metric change, resulting in a new wave-like equation, from which we set the weak formulation. An analytical resolution in the stationary case allowed us to identify the general structure in terms of eigen and forced modes of the solution. In order to propose a more intuitive interpretation of the latter, we also introduced a spectrogram representation allowing to observe the harmonic evolution of the total field spectrum (when evaluated over local time windows), generated by the oscillation of the moving boundary. This first model problem corresponds to the most constrained case, i.e. the closed domain supporting a continuous emission. This situation induces the notion of resonance, which made us restrict the method to non-resonant cases. The introduction of an oscillating motion of the reflecting boundary then naturally resulted in the appearance of a frequency modulation of the various constituent modes of the solution, which were confirmed numerically. Hence, the strategy adopted with the multi-harmonic method was to solve this harmonic problem in the frequency domain, by means of a finite element procedure. We therefore rewrote the system via a Fourier transform. The particular structure of the frequency

modulation of the different modes then led us to inject into the system a judicious form of the unknown solution, as a suitably truncated Dirac comb centered around the frequency of emission. This particular determination is based, in the case of small amplitude sine perturbations, on the theory of Mathieu functions and we showed that this is consistent with the previous observations. Thus, we ended up with a coupled Helmholtz-like system with variable coefficients. We then continued the analysis by proposing a first extension of the approach in the case of disturbances of arbitrary amplitudes explicitly defined, then in the case of any periodic disturbance, from which we directly recovered the Fourier coefficients. In order to establish the validity and to quantify the accuracy of the method introduced in the simplified framework of the one-dimensional segment, we compared it numerically to a brute force reference solution obtained by space-time resolution followed by an FFT algorithm. This comparative study allowed us to evaluate the reliability of the method and to measure its limits (resonance, maximum amplitude allowed, etc.). Finally, we proposed a first introduction to the two-dimensional case by extending the method to a simple rectangular geometry, obtained by extruding the previous one-dimensional domain.

In the third chapter, we focused on an efficient implementation of the multi-harmonic finite element method in the case of realistic geometries, composed of inhomogeneous materials and mixed boundary conditions. We first redefined the methodology by rewriting the moving target problem in a weak formulation for the moving domain, before reaching the fixed one. This approach is the reverse of that presented in Chapter 2, and significantly improves the adaptability of the method for complex geometries. The change of metric was then established in a general way in the form of a vector flow on the domain, and we chose to limit its action over a layer covering the deformed area. A judicious choice of the thickness of this layer allowed us to limit the cost of calculating successive deformations, and to produce a zone of the cabin (outside the layer) over which the calculated field corresponds to the one in the (realistic) moving domain. The problem was then rewritten taking into account the change of metric, and we showed by means of error estimates that the obtained Helmholtz-type system can be simplified in the case of perturbations of small amplitudes compared to the characteristic dimensions of the domain, which corresponds to our case of interest related to a breathing motion. The procedure can then be carried out in the same way as in Chapter 2. Indeed, we considered the Fourier series expansion of the geometrical quantities and the unknown wave field, which led to an approximate truncated finite system of coupled Helmholtz-like weak form equations at different equidistant frequencies. The finite element implementation was then developed, and we exploited the quasi-Toeplitz structure of the resulting coupled linear system to propose an efficient preconditioner. Finally, we considered a first application for passenger detection inside a simplified car geometry, with two materials of different permittivity and conductivity. We also discussed, through numerical results, the behaviour of the method, its efficiency and main characteristics.

In the fourth chapter we turned to using the method in a realistic context, in order to test its detection capability. To this end, we built a finely detailed two-dimensional geometry of the interior of a car, taking into account six different materials (air, seat foam, plastics, insulation, human tissue and clothing). This model also includes several important refinements compared to the simplified model used in Chapter 3. Firstly, the passenger in the cabin is now a full component of the domain, whose volume deformation produces the micro-Doppler signature we want to identify. Next, the model is compatible with the presence of a second passenger, which can be oriented differently, thus creating a certain number of configurations to be tested. Finally, several

possible locations for the transmitting antenna can be considered, as well as the possibility of using several antennas simultaneously. After detailing the process of obtaining a convincing breathing signal, we performed a parameter sweep to assess the micro-Doppler signature for many different configurations. In particular, this study enabled us to select some relevant useful "settings", in particular the location of the antennas.

As a general conclusion, we believe that the methodology developed in this thesis is well-adapted to solve micro-Doppler problems in complex environments, such as for radar sensing applications in the automotive industry. The proposed multi-harmonic approach, combined with an efficient preconditioner for the resulting coupled Helmholtz-type systems, has proved very efficient in a two-dimensional setting. However, many avenues for further improvements and future work exit.

Perspectives for future work

The first perspective is a direct follow-up to the experiments in Chapter 4. Indeed, if the method as-is allowed us to identify the micro-Doppler signatures in all the situations that we have considered, the identification of the *nature* of the disturbances remains difficult. Clearly, this capability is of interest if one wishes to recognise where the breathings are coming from, what objects are causing them or what their orientations are. A natural approach to this problem is to extend, on the basis of Appendix D, the method to the vector case, i.e. to the initial Maxwell system described in Chapter 1. Indeed, taking into account the polarisation of the wave field introduces the notion of propagation direction. This would a priori favour the localisation of the deformed areas as well as the identification of their topologies. The methodology developed in the thesis can be naturally applied to the vector Maxwell's equations, up to technical details. Furthermore, we can note that the chosen assumption of isotropic antennas is in practice unrealistic. Indeed, the radiated energy is unevenly distributed in space, some directions being privileged: these are the "main lobes", giving the directivity of the antenna. This property can also be taken into account in our model and used to improve the detection process.

The next step, if one wishes to reach real industrial applications, is to generalise the method to the third dimension. Again, this extension does not introduce any additional steps inside the method. However, even with e.g. high-order finite element discretizations (using for example spectral elements), the resulting computational cost will dramatically increase, simply due to the number of unknowns in 3D cases at the frequencies of interest. Indeed, the 2D geometries currently used have about 6 million nodes (average size of an element fixed at 7×10^{-4}) which, extrapolating to three dimensions, brings us to several billion degrees of freedom. Solving the associated linear systems is known to still be very challenging, even on large high-performance scientific computing systems. Recent developments in fast solvers for high-frequency time-harmonic problems provide one way forward, using e.g. Laplace-shifted preconditioners or optimized domain decomposition methods for the block system [66]. A complementary approach for high-frequency problems would be to reduce the number of degrees of freedom by introducing some asymptotic expansions in the formulation of the underlying wave propagation problems, such as ray tracing [34], geometrical optics, and its extension according to physical optics [12, 84] that can be coupled with steepest descent methods [48].

Appendix A

The case of a moving antenna

In this work, we address the problem of a wave emitted from a fixed position and scattered by an oscillating boundary. When the target is moving, the resulting field describes the frequency modulation of the wave from the point of view of the emitter (and any other fixed observation point in the domain), taken as the origin of the referential. In particular, the frequencies of the incident and reflected fields, perceived in the respective reference frames of the antenna or the obstacle, do not change according to the way the problem is presented. Indeed, on the one hand, the target always reflects a wave with, from its point of view, the same frequency as the one perceived from the incident wave. On the second hand, whether or not the transmitter is moving relative to the reference domain, the target is always moving relative to the source. Thus, it encounters the wave fronts at a higher frequency (for instance if it is approaching the source) and then reflects the wave at this new frequency, while still moving. This results in a doubling of this frequency shift (from the point of view of the emitter and any fixed point relative to it), leading to the Doppler frequency ν_{D}, which explains the factor 2 in the right hand side of (**??**). Then, we see that there is no no preferred frame of reference because of the symmetry of the situation. Hence, it may now be interesting to consider the referential centered on the oscillating boundary, for which the emitting antenna is moving.

By a simple reversal of the system, this amounts to equipping the wave propagation problem (2.1) with new boundary conditions, in order to obtain the problem: find $u = u(x,t)$, for $x \in \Omega_t =]0, \ell(t)[$ and $t > 0$, solution to (2.1):

$$\partial_t^2 u - c_\infty^2 \partial_x^2 u = 0, \tag{A.1}$$

and such that $u(\ell(t),t) = A\sin(\omega_{\mathrm{t}} t)$ and $u(0,t) = 0$, keeping the same homogeneous initial conditions (2.4) and (2.5). Let us consider the case where the motion of the right endpoint $\ell(t)$ of the domain Ω_t is given by a small smooth time-dependent perturbation $L\epsilon f(\omega_\ell t)$ of L, where f is a smooth bounded function with bounded derivatives $f^{(p)}$, oscillating with a frequency $\nu_\ell = \omega_\ell/(2\pi)$ small compared to the emitter frequency ν_{f}, that is $0 < \nu_\ell \ll \nu_{\mathrm{f}}$. Therefore, we have

$$\ell(t) = L(1 + \epsilon f(\omega_\ell t)), \tag{A.2}$$

with $\epsilon \ll 1$. This still corresponds to a sharp case where the field is scattered infinitely many times in the bounded domain, leading to eigenfrequencies and causing resonance phenomena if the

emitted frequency is badly chosen. Hence, it can also be interesting to impose different boundary conditions at $x = 0$. Let us update (A.1) with the following parametrized Fourier-Robin condition

$$[1 + \alpha(\partial_t - c_\infty \partial_x - 1)]u = 0, \tag{A.3}$$

where $\alpha \in [0, 1]$. This composite boundary condition is continuous on α and quantifies the energy of the wave passing through the boundary $x = 0$. Indeed, when $\alpha = 0$, (A.3) becomes the previous homogeneous Dirichlet boundary condition $u(0, t) = 0$, $t > 0$. Otherwise, if $\alpha = 1$, we find the standard one-dimensional transparent boundary condition $\partial_t u = c_\infty \partial_x u$ coming from the "left propagation" transport equation. To illustrate the condition (A.3), we report in Figure A.1 the absolute value of u_h, the numerical approximation of the solution u of (A.1) in the case of a motionless boundary (i.e. $u = \widetilde{u}$), where $\ell(t) \equiv L$, and with varying α in $[0, 1]$.

The physical parameters are set to $\nu_\mathrm{f} = 360$, $c_\infty = 300$, $A = 1$ and $L = 1$. As expected, for $\alpha = 1$, Figure A.1a depicts the propagation of the boundary condition $u(L, t) = A \sin(\omega_\mathrm{f} t)$. Figures A.1b ($\alpha = 0.92$) and A.1c ($\alpha = 0.75$) show, through the growing interference pattern, the increasing contribution of the scattered component of the wave. Finally, Figure A.1d ($\alpha = 0$) represents the total wave field inside the bounded domain Ω_t with fully reflecting boundaries. This pattern is periodic, in accordance with the Fourier expansion (2.13). We highlight that the presented frequency domain method is also applicable to this specific configuration without particular adaptations.

Alternatively, the problem (A.1) is analytically investigated in [32], where the solution is based on a multiple scale expansion of the solution. This leads to an explicit formulation for the approximation of the solution u, which writes as the product of amplitude and frequency modulation factors.

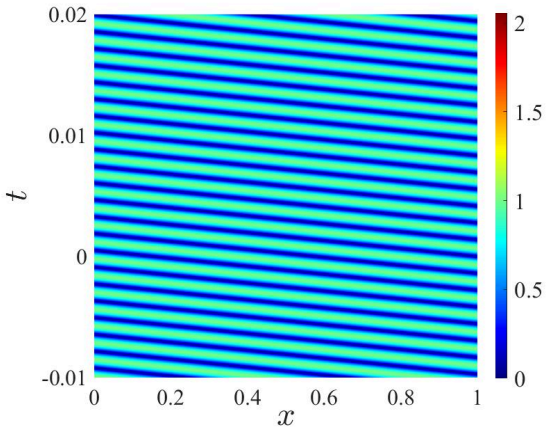

(a) $\alpha = 1$.

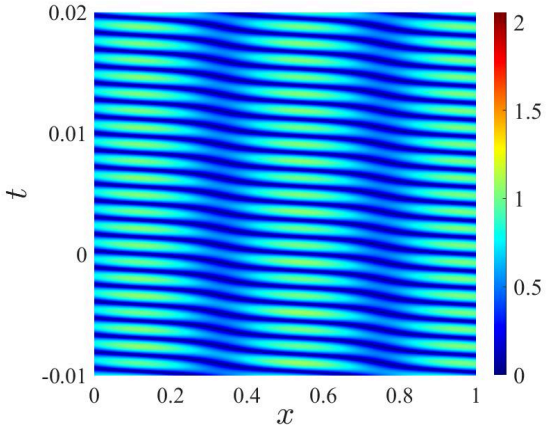

(b) $\alpha = 0.92$.

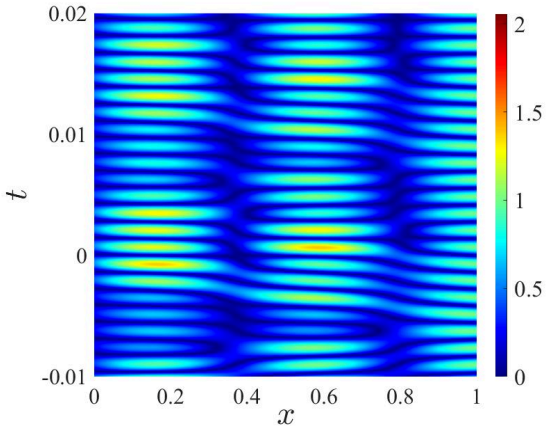

(c) $\alpha = 0.75$.

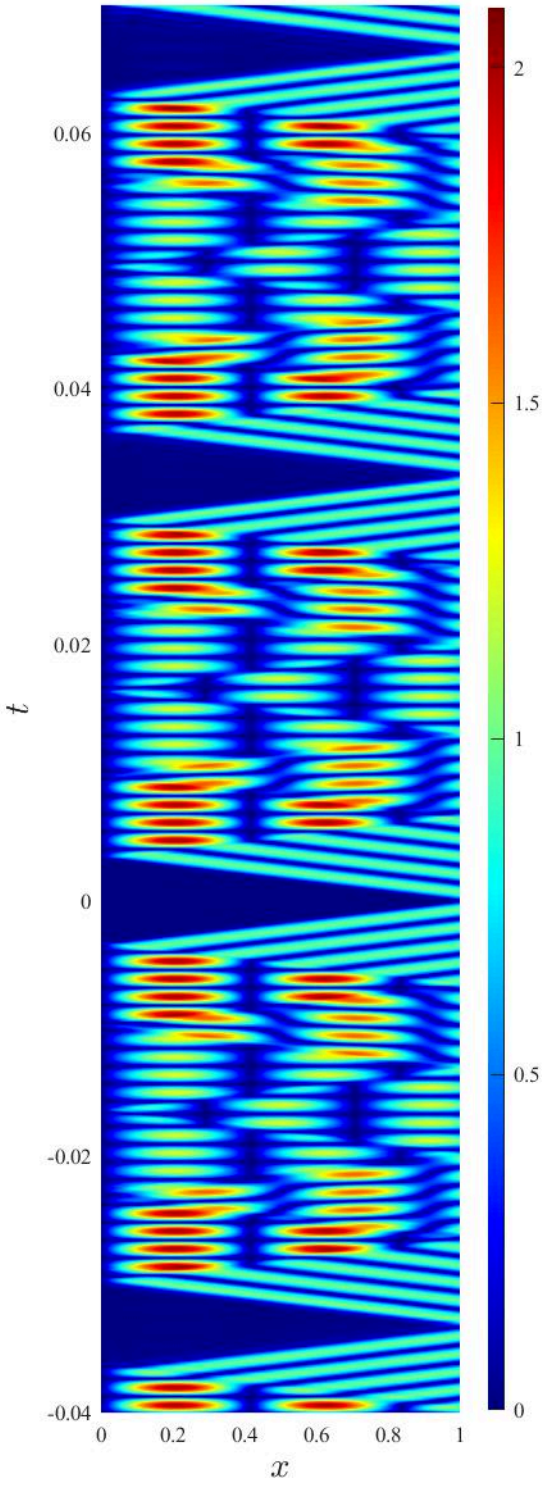

(d) $\alpha = 0$.

Figure A.1: Amplitude $|u_h|$ for decreasing values of α from 1 (transparent left boundary in top, left) to 0 (reflecting boundary in bottom, right). The parameters are $\nu_\mathrm{f} = 360$, $c_\infty = 300$, $A = 1$ and $L = 1$.

Appendix B

Discrete Fourier transform of $|\mathbf{J}_k^{-1}|$

Without loss of generality, let us analyze the link between the discrete Fourier transform $\mathrm{DFT}(|\mathbf{J}_k^{-1}|)$ of $|\mathbf{J}_k^{-1}|$ and the Fourier coefficients c_n, $n \in \mathcal{N}$. The extension to the tensors $|\mathbf{J}_t^{-1}|\mathbf{J}_t\mathbf{J}_t^{\mathrm{T}}$ and $\mathbf{C}_n$ is direct. We first sample $|\mathbf{J}_t^{-1}|$ at frequency $\Delta t_\ell^{-1} = (2N+1)\nu_\ell$ and obtain the infinite sequence for $t > 0$

$$(|\mathbf{J}_t^{-1}|)_{\mathrm{e}} = \sum_{k\in\mathbb{Z}} \left|\mathbf{J}_t^{-1}\right| \delta\left(t - \frac{k}{(2N+1)\nu_\ell}\right),$$

which is then truncated to the $2N+1$ points $\{t_k\}_{0\le k\le 2N}$, such that

$$(|\mathbf{J}_t|^{-1})_{\mathrm{tr}} := \sum_{k=0}^{2N} \left|\mathbf{J}_t^{-1}\right| \delta\left(t - \frac{k}{(2N+1)\nu_\ell}\right) = \left\{|\mathbf{J}^{-1}{}_{\frac{k}{(2N+1)\nu_\ell}}|\right\}_{0\le k\le 2N} =: \left\{|\mathbf{J}_k^{-1}|\right\}_{0\le k\le 2N}. \tag{B.1}$$

By definition of the DFT of the finite signal $(|\mathbf{J}_t^{-1}|)_{\mathrm{tr}}$, we have, for $n \in \mathcal{N}$

$$\mathrm{DFT}(|\mathbf{J}_t^{-1}|)_{\mathrm{tr}}(n) := \sum_{k=0}^{2N} |\mathbf{J}^{-1}{}_{\frac{k}{(2N+1)\nu_\ell}}| e^{-2i\pi\frac{kn}{2N+1}} \tag{B.2}$$

which is a complex sequence of size $2N+1$. Let us remark that we have the identity

$$\mathrm{DFT}(|\mathbf{J}_t^{-1}|)_{\mathrm{tr}}(n) = \mathcal{F}(|\mathbf{J}_t^{-1}|)_{\mathrm{tr}}(n\nu_\ell)$$

since the Fourier transform of (B.1) in the sense of distributions is formally given, for all $\xi \in \mathbb{R}$, by

$$\mathcal{F}(|\mathbf{J}_t^{-1}|)_{\mathrm{tr}}(\xi) = \int_{\mathbb{R}} \sum_{k=0}^{2N} \left|\mathbf{J}_t^{-1}\right| \delta\left(t - \frac{k}{(2N+1)\nu_\ell}\right) e^{-2i\pi\xi t} dt = \sum_{k=0}^{2N} |\mathbf{J}^{-1}{}_{\frac{k}{(2N+1)\nu_\ell}}| e^{-2i\pi\xi\frac{k}{(2N+1)\nu_\ell}}.$$

Now, injecting (3.32) in (B.2) yields

$$\mathrm{DFT}(|\mathbf{J}^{-1}|)_{\mathrm{tr}}(n) = \sum_{k=0}^{2N}\sum_{l\in\mathbb{Z}} c_l e^{2i\pi l\nu_\ell\frac{k}{(2N+1)\nu_\ell}} e^{-2i\pi\frac{kn}{2N+1}} = \sum_{l\in\mathbb{Z}} c_l \sum_{k=0}^{2N} e^{2i\pi\frac{k}{2N+1}(l-n)} = (2N+1)c_n.$$

Indeed, if $l = n$ we have

$$\sum_{k=0}^{2N} e^{2i\pi\frac{k}{2N+1}(l-n)} = 2N+1$$

and otherwise

$$\sum_{k=0}^{2N} e^{2i\pi \frac{k}{2N+1}(l-n)} = 0,$$

since the sum of the roots of unity vanishes. In addition, the cyclic group of the $(2N+1)$ roots of unity implies that

$$\mathrm{DFT}(|\mathbf{J}_t^{-1}|)_{\mathrm{tr}}(n) = \mathrm{DFT}(|\mathbf{J}_t^{-1}|)_{\mathrm{tr}}(n+2N+1) = \overline{\mathrm{DFT}(|\mathbf{J}^{-1}|)_{\mathrm{tr}}}(2N+1-n).$$

A similar approach applies for $|\mathbf{J}_t^{-1}|\mathbf{J}_t\mathbf{J}_t^{\mathrm{T}}$ and leads to

$$\mathrm{DFT}(|\mathbf{J}_t^{-1}|\mathbf{J}_t\mathbf{J}_t^{\mathrm{T}})_{\mathrm{tr}}(n) = (2N+1)\mathbf{C}_n,$$

for $0 \leq n \leq N$. Finally, the DFT provides the $2N+1$ orthogonal terms of both $\mathbf{C}_n$ and c_n, for $n \in \mathcal{N}$. This allows us to compute explicitly the partial sums (3.33)

$$\mathbf{C}^{\mathcal{N}} = \sum_{n\in\mathcal{N}} \mathbf{C}_n e^{in\omega_\ell t} \text{ and } c^{\mathcal{N}} = \sum_{n\in\mathcal{N}} c_n e^{in\omega_\ell t}.$$

Appendix C

Resolution of the approximate block Toeplitz system (3.46)

We consider the approximation $\mathbf{A}^{(N,J)}_{\boldsymbol{\omega}^{(0)}}$ of $\mathbf{A}^{(N,J)}_{\boldsymbol{\omega}^{(J)}}$, introduced in Section 3.4 and associated to the linear system (3.46) that we aim to solve:

$$\mathbf{A}^{(N,J)}_{\boldsymbol{\omega}^{(0)}} \boldsymbol{w}^{(N,J)}_{\boldsymbol{\omega}^{(0)}} = \mathbf{b}^{(N,J)}.$$

Let us notice that the methodology proposed below applies for block banded Toeplitz linear systems in general. The term $\mathbf{A}^{(N,J)}_{\boldsymbol{\omega}^{(0)}}$ is a block banded partial hermitian Toeplitz matrix (i.e. block banded, block partial hermitian [86] and block Toeplitz) with symmetric blocks, which is completely defined by its first block row

$$\mathbf{R}^{-J} := (\mathbf{T}_0 \ \mathbf{T}_1 \ \cdots \ \mathbf{T}_N \ \mathbf{0} \ \cdots \ \mathbf{0}),$$

where $\mathbf{T}_n = \mathbf{A}^{(n,J)}_{\omega_0}$, $0 \leq n \leq N$ (since we have $\mathbf{T}_{-n} = \overline{\mathbf{T}_n}$), and $\mathbf{0}$ is the empty matrix of order n_{dof}.

Toeplitz matrices are an important class of structured matrices arising in many areas, typically wave scattering problems containing coupled components or image processing. Inversion and decomposition of block Toeplitz matrices have been widely studied with developments based on their cyclic displacement structures [50, 54, 65] or even on block Padé approximations [15, 7]. Two important classes of direct algorithms also exist relatively to Toeplitz-like matrices, namely Levinson

type and Schur type [75]. We define the (Toeplitz) block circulant extension of $\mathbf{A}_{\boldsymbol{\omega}^{(0)}}^{(N,J)}$ as

$$\mathbf{A}_{\mathrm{Circ}}^{(N,J)} := \begin{pmatrix} \mathbf{T}_0 & \mathbf{T}_1 & \cdots & \mathbf{T}_N & \mathbf{0} & \cdots & \mathbf{0} & \bar{\mathbf{T}}_N & \cdots & \bar{\mathbf{T}}_1 \\ \bar{\mathbf{T}}_1 & \ddots & \ddots & & \ddots & \ddots & & \ddots & \ddots & \vdots \\ \vdots & \ddots & \ddots & \ddots & & \ddots & \ddots & & \ddots & \bar{\mathbf{T}}_N \\ \bar{\mathbf{T}}_N & & \ddots & \ddots & \ddots & & \ddots & \ddots & & \mathbf{0} \\ \mathbf{0} & \ddots & & \ddots & \ddots & \ddots & & \ddots & \ddots & \vdots \\ \vdots & \ddots & \ddots & & \ddots & \ddots & \ddots & & \ddots & \mathbf{0} \\ \mathbf{0} & & \ddots & \ddots & & \ddots & \ddots & \ddots & & \mathbf{T}_N \\ \mathbf{T}_N & \ddots & & \ddots & \ddots & & \ddots & \ddots & \ddots & \vdots \\ \vdots & \ddots & \ddots & & \ddots & \ddots & & \ddots & \ddots & \mathbf{T}_1 \\ \mathbf{T}_1 & \cdots & \mathbf{T}_N & \mathbf{0} & \cdots & \mathbf{0} & \bar{\mathbf{T}}_N & \cdots & \bar{\mathbf{T}}_1 & \mathbf{T}_0 \end{pmatrix}.$$

Block circulant matrices (i.e. with circulant block coefficients) belong to the class of block Toeplitz matrices and appear in many periodic problems involving, in particular elliptic equations with oscillating boundary conditions. We observe that $\mathbf{A}_{\mathrm{Circ}}^{(N,J)}$ is well defined under the condition that $N \leq J$.

Let us now introduce the permutation matrix $\boldsymbol{\sigma}$ of order $2J+1$ such that

$$\boldsymbol{\sigma} := \begin{pmatrix} 0 & 1 & & & \\ & \ddots & \ddots & & \\ & & \ddots & \ddots & \\ & & & \ddots & 1 \\ 1 & & & & 0 \end{pmatrix}.$$

Then, we have the following statement.

Proposition C.1. *If we denote the first block row of* $\mathbf{A}_{\mathrm{Circ}}^{(N,J)}$ *by*

$$\mathbf{R}_{\mathrm{Circ}}^{-J} = \left(\mathbf{R}_{\mathrm{Circ}}^{-J}(0) \ \cdots \ \mathbf{R}_{\mathrm{Circ}}^{-J}(2J)\right) := \left(\mathbf{T}_0 \ \ \mathbf{T}_1 \ \cdots \ \mathbf{T}_N \ \mathbf{0} \ \cdots \ \mathbf{0} \ \bar{\mathbf{T}}_N \ \cdots \ \bar{\mathbf{T}}_1\right),$$

then we have

$$\mathbf{A}_{\mathrm{Circ}}^{(N,J)} = \sum_{j=0}^{2J} \boldsymbol{\sigma}^j \otimes \mathbf{R}_{\mathrm{Circ}}^{-J}(j),$$

where $\boldsymbol{\sigma}^j$ *denotes* $\boldsymbol{\sigma}$ *to the power* j*.*

Proof. As for $\mathbf{A}_{\boldsymbol{\omega}^{(0)}}^{(N,J)}$, all the blocks of $\mathbf{A}_{\mathrm{Circ}}^{(N,J)}$ are present in $\mathbf{R}_{\mathrm{Circ}}^{-J}$. By definition, each row of $\mathbf{A}_{\mathrm{Circ}}^{(N,J)}$ is rotated one element to the right relatively to the preceding row. This is precisely the action of the powers $\boldsymbol{\sigma}^j$of the permutation matrix σ of order $2J+1$, $0 \leq j \leq 2J$, which satisfies

$$\boldsymbol{\sigma}^{2J+1} = \mathbf{I}_{2J+1}. \tag{C.1}$$

This ends the proof. ■

In this section, we propose a resolution approach for (3.46), which is decomposed as follows. We link $\mathbf{A}_{\boldsymbol{\omega}^{(0)}}^{(N,J)}$ to its circulant extension as described in [30], and apply the Woodbury matrix identity [91]. Then, $\mathbf{A}_{\mathrm{Circ}}^{(N,J)}$ is block diagonalized using its well-known link to DFT matrices. Let us set the following matrices

$$\mathbf{A}_{\mathrm{Circ,L}}^{(N,J)} = \begin{pmatrix} \mathbf{R}_{\mathrm{Circ}}^{-J}(N) & \cdots & \mathbf{0} \\ \vdots & \ddots & \vdots \\ \mathbf{R}_{\mathrm{Circ}}^{-J}(1) & \cdots & \mathbf{R}_{\mathrm{Circ}}^{-J}(N) \end{pmatrix}$$

and

$$\mathbf{A}_{\mathrm{Circ,U}}^{(N,J)} = \begin{pmatrix} \mathbf{R}_{\mathrm{Circ}}^{-J}(2J+1-N) & \cdots & \mathbf{R}_{\mathrm{Circ}}^{-J}(2J) \\ \vdots & \ddots & \vdots \\ \mathbf{0} & \cdots & \mathbf{R}_{\mathrm{Circ}}^{-J}(2J+1-N) \end{pmatrix} = \bar{\mathbf{A}}_{\mathrm{Circ,L}}^{(N,J)},$$

from which we build, for $K = 2(J-N)+1$

$$\mathbf{F}_{\mathrm{L}} = \begin{pmatrix} \mathbf{I}_{Nn_{\mathrm{dof}}} & \mathbf{0}_{Nn_{\mathrm{dof}}} \\ \mathbf{0}_{(K\times N)n_{\mathrm{dof}}} & \mathbf{0}_{(K\times N)n_{\mathrm{dof}}} \\ \mathbf{0}_{Nn_{\mathrm{dof}}} & \mathbf{A}_{\mathrm{Circ,L}}^{(N,J)} \end{pmatrix}$$

and

$$\mathbf{F}_{\mathrm{U}} = \begin{pmatrix} \mathbf{0}_{Nn_{\mathrm{dof}}} & \mathbf{I}_{Nn_{\mathrm{dof}}} \\ \mathbf{0}_{(K\times N)n_{\mathrm{dof}}} & \mathbf{0}_{(K\times N)n_{\mathrm{dof}}} \\ \left(\mathbf{A}_{\mathrm{Circ,U}}^{(N,J)}\right)^{\mathrm{T}} & \mathbf{0}_{Nn_{\mathrm{dof}}} \end{pmatrix}.$$

Here $\mathbf{0}_{Nn_{\mathrm{dof}}}$ and $\mathbf{0}_{(K\times N)n_{\mathrm{dof}}}$ denote respectively the null matrices of size $N\mathrm{dof}\times N\mathrm{dof}$ and $Kn_{\mathrm{dof}}\times N\mathrm{dof}$. The matrices $\mathbf{A}_{\mathrm{Circ,U}}^{(N,J)}$ and $\mathbf{A}_{\mathrm{Circ,L}}^{(N,J)}$ are block upper and lower triangular matrices of order Nn_{dof} that involve in the lower left and upper right corners of $\mathbf{A}_{\mathrm{Circ}}^{(N,J)}$, respectively. Here, the matrix $\mathbf{A}_{\boldsymbol{\omega}^{(0)}}^{(N,J)}$ is linked to $\mathbf{A}_{\mathrm{Circ}}^{(N,J)}$ through

$$\mathbf{A}_{\boldsymbol{\omega}^{(0)}}^{(N,J)} = \mathbf{A}_{\mathrm{Circ}}^{(N,J)} - \mathbf{F}_{\mathrm{L}}\mathbf{F}_{\mathrm{U}}^{\mathrm{T}},$$

and the Woodbury matrix identity gives a formulation of the inverse of $\mathbf{A}_{\mathrm{Circ}}^{(N,J)} - \mathbf{F}_{\mathrm{L}}\mathbf{F}_{\mathrm{U}}^{\mathrm{T}}$ in terms of $\left(\mathbf{A}_{\mathrm{Circ}}^{(N,J)}\right)^{-1}$, which yields

$$\begin{aligned}\left(\mathbf{A}_{\boldsymbol{\omega}^{(0)}}^{(N,J)}\right)^{-1} = \left(\mathbf{A}_{\mathrm{Circ}}^{(N,J)}\right)^{-1} + \\ \left(\mathbf{A}_{\mathrm{Circ}}^{(N,J)}\right)^{-1}\mathbf{F}_{\mathrm{L}}\left(\mathbf{I}_{2Nn_{\mathrm{dof}}} - \mathbf{F}_{\mathrm{U}}^{\mathrm{T}}\left(\mathbf{A}_{\mathrm{Circ}}^{(N,J)}\right)^{-1}\mathbf{F}_{\mathrm{L}}\right)^{-1}\mathbf{F}_{\mathrm{U}}^{\mathrm{T}}\left(\mathbf{A}_{\mathrm{Circ}}^{(N,J)}\right)^{-1}.\end{aligned} \tag{C.2}$$

In [30], $\left(\mathbf{A}_{\mathrm{Circ}}^{(N,J)}\right)^{-1}$ is computed through the resolution of $2J+1$ linear sub-systems of size n_{dof}, knowing that the inverse of a block circulant matrix is also block circulant (i.e. defined by any of its rows or columns). Alternatively, we propose here to decompose this inverse using block

diagonalization in order to decouple the system. From (C.1), $\boldsymbol{\sigma}$ has $2J+1$ eigenvalues which are the $(2J+1)$ roots of unity $\{\lambda_j\}_{0\leq j\leq 2J}$, and the corresponding jth eigenvector is of the form

$$\mathbf{e}_j = \left(1, \lambda_j, \lambda_j^2, ..., \lambda_j^{2J}\right)^{\mathrm{T}}, \text{ with } \lambda_j = e^{\frac{2i\pi}{2J+1}j}.$$

The family $\{\mathbf{e}_j\}_{0\leq j\leq 2J}$ forms an eigenbasis of $\boldsymbol{\sigma}$, whose transition matrix can be written as the normalized Vandermonde matrix

$$\mathbf{V} := \frac{1}{\sqrt{2J+1}}\left(\mathbf{e}_0 \ \cdots \ \mathbf{e}_{2J}\right) = \frac{1}{\sqrt{2J+1}}\begin{pmatrix} 1 & 1 & \cdots & 1 \\ 1 & \lambda_1 & \cdots & \lambda_{2J} \\ \vdots & \vdots & & \vdots \\ 1 & \lambda_1^{2J} & \cdots & \lambda_{2J}^{2J} \end{pmatrix}.$$

The matrix $\mathbf{V}$ is known as the DFT matrix, which is unitary and then allows to diagonalize $\boldsymbol{\sigma}$. Hence, we have $\boldsymbol{\sigma} = \mathbf{V}\boldsymbol{\Lambda}\mathbf{V}^{-1}$, and more generally

$$\boldsymbol{\sigma}^j = \mathbf{V}\boldsymbol{\Lambda}^j\mathbf{V}^*, \tag{C.3}$$

with

$$\boldsymbol{\Lambda} := \begin{pmatrix} 1 & & & \\ & \lambda_1 & & \\ & & \ddots & \\ & & & \lambda_{2J} \end{pmatrix} \text{ and } \boldsymbol{\Lambda}^j := \begin{pmatrix} 1 & & & \\ & \lambda_1^j & & \\ & & \ddots & \\ & & & \lambda_{2J}^j \end{pmatrix}.$$

Here, $\mathbf{V}^*$ designates the adjoint matrix of $\mathbf{V}$. Finally, injecting (C.3) in Proposition C.1 yields

$$\begin{aligned} \mathbf{A}_{\mathrm{Circ}}^{(N,J)} &= \sum_{j=0}^{2J} (\mathbf{V}\boldsymbol{\Lambda}^j\mathbf{V}^*) \otimes \mathbf{R}_{\mathrm{Circ}}^{-J}(j) \\ &= \sum_{j=0}^{2J} (\mathbf{V}\otimes\mathbf{Id}_{n_\Omega})(\boldsymbol{\Lambda}^j \otimes \mathbf{R}_{\mathrm{Circ}}^{-J}(j))(\mathbf{V}^*\otimes\mathbf{Id}_{n_\Omega}) \\ &= (\mathbf{V}\otimes\mathbf{Id}_{n_\Omega})\left(\sum_{j=0}^{2J} \boldsymbol{\Lambda}^j \otimes \mathbf{R}_{\mathrm{Circ}}^{-J}(j)\right)(\mathbf{V}^*\otimes\mathbf{Id}_{n_\Omega}) \\ &=: \mathbf{V}^{(N,J)}\boldsymbol{\Lambda}^{(N,J)}\left(\mathbf{V}^{(N,J)}\right)^* \end{aligned} \tag{C.4}$$

Since $\mathbf{V}$ is unitary, then this is also the case of $\mathbf{V}^{(N,J)}$, and (C.4) gives

$$\left(\mathbf{A}_{\mathrm{Circ}}^{(N,J)}\right)^{-1} = \mathbf{V}^{(N,J)}\left(\boldsymbol{\Lambda}^{(N,J)}\right)^{-1}\left(\mathbf{V}^{(N,J)}\right)^*. \tag{C.5}$$

The computation of $\left(\boldsymbol{\Lambda}^{(N,J)}\right)^{-1}$ is then obtained by solving again $2J+1$ linear systems (for each diagonal block of $\boldsymbol{\Lambda}^{(N,J)}$) of size n_{dof}, which leads to the same cost as in [30]. Finally, injecting

(C.5) in (C.2) one obtains $\left(\mathbf{A}_{\boldsymbol{\omega}^{(0)}}^{(N,J)}\right)^{-1}$ and solves (3.46) by means of successive matrix vector products starting with $\mathbf{b}^{(N,J)}$. As a consequence, the system (3.46) leads to

$$\begin{aligned}\boldsymbol{w}_{\boldsymbol{\omega}^{(0)}}^{(N,J)} &= \left(\mathbf{A}_{\mathrm{Circ}}^{(N,J)}\right)^{-1}\mathbf{b}^{(N,J)} + \\ &\quad \left(\mathbf{A}_{\mathrm{Circ}}^{(N,J)}\right)^{-1}\mathbf{F}_{\mathrm{L}}\left(\mathbf{I}_{2Nn_{\mathrm{dof}}} - \mathbf{F}_{\mathrm{U}}^{\mathrm{T}}\left(\mathbf{A}_{\mathrm{Circ}}^{(N,J)}\right)^{-1}\mathbf{F}_{\mathrm{L}}\right)^{-1}\mathbf{F}_{\mathrm{U}}^{\mathrm{T}}\left(\mathbf{A}_{\mathrm{Circ}}^{(N,J)}\right)^{-1}\mathbf{b}^{(N,J)} \\ &= \mathbf{y} + \mathbf{V}^{(N,J)}\left(\boldsymbol{\Lambda}^{(N,J)}\right)^{-1}\left(\mathbf{V}^{(N,J)}\right)^{*}\mathbf{F}_{\mathrm{L}}\mathbf{G}\mathbf{F}_{\mathrm{U}}^{\mathrm{T}}\mathbf{y},\end{aligned}$$

with

$$\mathbf{G} = \left(\mathbf{I}_{2Nn_{\mathrm{dof}}} - \mathbf{F}_{\mathrm{U}}^{\mathrm{T}}\left(\mathbf{A}_{\mathrm{Circ}}^{(N,J)}\right)^{-1}\mathbf{F}_{\mathrm{L}}\right)^{-1}$$

and where

$$\mathbf{y} = \left(\mathbf{A}_{\mathrm{Circ}}^{(N,J)}\right)^{-1}\mathbf{b}^{(N,J)} = \mathbf{V}^{(N,J)}\left(\boldsymbol{\Lambda}^{(N,J)}\right)^{-1}\left(\mathbf{V}^{(N,J)}\right)^{*}\mathbf{b}^{(N,J)}$$

is evaluated by applying successively the inverse FFT to $\mathbf{b}^{(N,J)}$ (taking $\mathcal{O}(n_{\mathrm{dof}}^{J}\log(n_{\mathrm{dof}}^{J}))$ flops), the product with the block diagonal matrix $\left(\boldsymbol{\Lambda}^{(N,J)}\right)^{-1}$ (taking $\mathcal{O}(n_{\mathrm{dof}}^{2}(2J+1))$ flops) and then the FFT. Due to the sparse block structure of $\mathbf{F}_{\mathrm{U}}$ and $\mathbf{F}_{\mathrm{L}}$, their corresponding MVP can also be performed efficiently in $\mathcal{O}((N+1)Nn_{\mathrm{dof}}^{2}/2 + n_{\mathrm{dof}}) = \mathcal{O}(N^{2}n_{\mathrm{dof}}^{2})$ flops. Finally, it remains to evaluate the term $\mathbf{G}$, for which different approaches are possible, depending on its structure, in order to preserve the advantage of the circulant extension approach. For instance we refer to [73] for the application of direct inversion formulae when $\mathbf{F}_{\mathrm{U}}^{\mathrm{T}}\left(\mathbf{A}_{\mathrm{Circ}}^{(N,J)}\right)^{-1}\mathbf{F}_{\mathrm{L}}$ is of low rank, or of recursive formulations based on the decomposition into a sum of matrices of rank 1. On the other hand, if the spectral radius of $\mathbf{F}_{\mathrm{U}}^{\mathrm{T}}\left(\mathbf{A}_{\mathrm{Circ}}^{(N,J)}\right)^{-1}\mathbf{F}_{\mathrm{L}}$ is lower than 1, on may consider the Neumann series expansion

$$\mathbf{G} = \sum_{n=0}^{\infty}(-1)^{n}\left(\mathbf{F}_{\mathrm{U}}^{\mathrm{T}}\left(\mathbf{A}_{\mathrm{Circ}}^{(N,J)}\right)^{-1}\mathbf{F}_{\mathrm{L}}\right)^{n}.$$

More broadly, we refer to [35] for a generalised Taylor expansion of matrix inverses, whose explicit formulation is proven using Cauchy's integral formula [4].

Appendix D

A weak formulation of the moving boundary problem for the EM field

The formulation in three dimensions of the multi-harmonic finite element method is straightforward. However, as mentioned in Conclusion, the treatment of the full Maxwell problem is a very interesting extension of this method since it leads to the full description of the EM field scattered in the domain. In particular, it provides its polarisation, allowing a more accurate analysis of the calculated micro-Doppler signature, and the evaluation of the target position in the car. In order to pave the way for this extension, we now state the boundary value problem satisfied by the scattered EM field in the moving domain Ω_t, and derive the corresponding weak formulation. Since we deal with different materials, both permittivity and permeability are in practice space-dependent. However, as justified in Subsection 3.5.1, we consider these coefficients piecewise constant and directly adapt the formulation at the discrete level.

Following the notations of Chapter 1 and 3, let us now state the PDE formulation of the evolution of the EM field $(\mathbf{E}, \mathbf{B})$ in the three dimensional domain Ω_t ($d = 3$). We consider Maxwell's equations (1.3)-(1.6) in source-free regions and in isotropic space. We apply the **curl** operator to (1.5) and (1.6), leading to

$$\nabla_{\mathbf{x}} \times (\nabla_{\mathbf{x}} \times \mathbf{E}) = -\partial_t \nabla_{\mathbf{x}} \times \mathbf{B} \tag{D.1}$$

and

$$\nabla_{\mathbf{x}} \times (\nabla_{\mathbf{x}} \times \mathbf{B}) = \mu_\infty \varepsilon_\infty \partial_t \nabla_{\mathbf{x}} \times \mathbf{E}, \tag{D.2}$$

for $(\mathbf{x}, t) \in \Omega_t \times \mathbb{R}_*^+$. We recall the wave velocity given by $c_\infty = (\mu_\infty \varepsilon_\infty)^{-\frac{1}{2}}$, and inject (1.6) and (1.5) in (D.1) and (D.2) respectively. This yields the following second-order forms of the Maxwell system

$$\partial_t^2 \mathbf{E} + c_\infty^2 \nabla_{\mathbf{x}} \times (\nabla_{\mathbf{x}} \times \mathbf{E}) = 0 \tag{D.3}$$

and

$$\partial_t^2 \mathbf{B} + c_\infty^2 \nabla_{\mathbf{x}} \times (\nabla_{\mathbf{x}} \times \mathbf{B}) = 0. \tag{D.4}$$

Without loss of generality, let us focus on the description of $\mathbf{E}$. The vector field $\mathbf{B}$ can be treated in a fairly similar way. We highlight, as in Chapter 1, that due to the divergence-free condition

(1.3) and the identity $\nabla_{\mathbf{x}} \times \nabla_{\mathbf{x}} \times \mathbf{E} = \nabla_{\mathbf{x}}(\nabla_{\mathbf{x}} \cdot \mathbf{E}) - \Delta_{\mathbf{x}}\mathbf{E}$, (D.3) is strictly equivalent to the vector wave equation for $\mathbf{E}$

$$\partial_t^2 \mathbf{E} - c_\infty^2 \Delta_{\mathbf{x}} \mathbf{E} = 0.$$

However, in order to derive a weak formulation for the boundary value problem, we work in the following on (D.3). According to our usual physical settings, we impose on the transmitter boundary Γ^{s} a T_{f}-periodic time dependant source term, such that

$$\mathbf{E}(\mathbf{x}, t)|_{\Gamma^{\mathrm{s}}} = \mathbf{E}^{\mathrm{s}}(\mathbf{x}) e^{i\omega_{\mathrm{f}} t} \text{ for } (\mathbf{x}, t) \in \Gamma^{\mathrm{s}} \times \mathbb{R}_*^+, \tag{D.5}$$

where $\mathbf{E}^{\mathrm{s}} \in \mathcal{C}^0(\mathbb{R}^3, \mathbb{R}^3)$. The field emitted by Γ^{s} is assumed to be TEM, which means that it has neither electric nor magnetic field along the direction of propagation (e.g. $-\mathbf{n}$, where $\mathbf{n}$ is the outwardly directed unit normal vector of the domain boundary $\partial\Omega_t$). Hence, we also have $\mathbf{E}^{\mathrm{s}}(\mathbf{x}) \cdot \mathbf{n}(\mathbf{x}) = 0$ for $\mathbf{x} \in \Gamma^{\mathrm{s}}$. In addition, the spatial and temporal components of this source term are separated, leading to a static polarisation of the field. However, more complex patterns such as circular polarisation can be introduced by a slight update of this boundary condition. Note that it is also possible to control the directivity of the antenna by appropriately adjusting $\mathbf{E}^{\mathrm{s}}$ and the shape of Γ^s. In this way, we can choose to direct the beam towards the area where the target is supposed to be located

As previously, we split the surface boundary Σ enclosing the computational domain into $\Sigma = \Sigma_0 \cap \Sigma_1$, where Σ_0 models metallic plates (PEC) supporting the reflecting boundary condition

$$\mathbf{E} \times \mathbf{n} = \mathbf{0}, \tag{D.6}$$

and Σ_1 represents transparent materials. To model absorbing boundary conditions over Σ_1, we usually use impedance-like conditions. More precisely, let us consider the Silver-Müller condition [8]

$$(\partial_t \mathbf{E} \times \mathbf{n}) \times \mathbf{n} - c_\infty (\nabla_{\mathbf{x}} \times \mathbf{E}) \times \mathbf{n} = \mathbf{0} \text{ for } (\mathbf{x}, t) \in \Sigma_1 \times \mathbb{R}_*^+. \tag{D.7}$$

Finally, we set as previously the homogeneous initial conditions $\mathbf{E}(\mathbf{x}, 0) = 0$ and $\partial_t \mathbf{E}(\mathbf{x}, 0) = 0$. For fixed $t > 0$, we designate by $\mathbf{H}(\mathbf{curl}, \Omega_t)$ the Sobolev space

$$\mathbf{H}(\mathbf{curl}, \Omega_t) := \{\mathbf{E} \in [L^2(\Omega_t)]^3 \text{ such that } \nabla_{\mathbf{x}} \times \mathbf{E} \in [L^2(\Omega_t)]^3\}.$$

Now, we can use the boundary conditions (D.5) and (D.6) to define a tangential trace of $\mathbf{H}(\mathbf{curl}, \Omega_t)$ by defining the corresponding subspace

$$\mathbf{H}_{\mathbf{E}^{\mathrm{s}}, \omega_{\mathrm{f}} t}(\mathbf{curl}, \Omega_t) := \left\{ \mathbf{E} \in \mathbf{H}(\mathbf{curl}, \Omega_t) \mid \mathbf{E}|_{\Sigma_0} \times \mathbf{n} = \mathbf{0} \text{ and } \mathbf{E}|_{\Gamma^{\mathrm{s}}} = \mathbf{E}^{\mathrm{s}} e^{i\omega_{\mathrm{f}} t} \right\}.$$

Similarly, we have

$$\mathbf{H}_{\mathbf{0},0}(\mathbf{curl}, \Omega_t) := \{\mathbf{E} \in \mathbf{H}(\mathbf{curl}, \Omega_t) \mid \mathbf{E}|_{\Sigma_0} \times \mathbf{n} = \mathbf{0} \text{ and } \mathbf{E}|_{\Gamma^{\mathrm{s}}} = \mathbf{0}\}.$$

According to these assumptions, the weak formulation in Ω_t writes, for fixed time $t > 0$: find $\mathbf{E}(\cdot, t) \in \mathbf{H}_{\mathbf{E}^{\mathrm{s}}, \omega_{\mathrm{f}} t}(\mathbf{curl}, \Omega_t)$, such that for any $\boldsymbol{\phi} \in \mathbf{H}_{\mathbf{0},0}(\mathbf{curl}, \Omega_t)$

$$\begin{aligned} &\int_{\Omega_t} (\nabla_{\mathbf{x}} \times \mathbf{E}) \cdot (\nabla_{\mathbf{x}} \times \overline{\boldsymbol{\phi}}) d\Omega_t \\ &\qquad + \int_{\Omega_t} \frac{1}{c_\infty^2} \partial_t^2 \mathbf{E} \cdot \overline{\boldsymbol{\phi}} d\Omega_t + \int_{\partial\Omega_t} [(\nabla_{\mathbf{x}} \times \mathbf{E}) \times \mathbf{n}] \cdot (\overline{\boldsymbol{\phi}} \times \mathbf{n}) d(\partial\Omega_t) = 0. \end{aligned} \tag{D.8}$$

Since $\boldsymbol{\phi} = \mathbf{0}$ on $\Sigma_0 \cap \Gamma^{\mathrm{s}}$, it remains to act on the boundary term of (D.8) using (D.7). This leads to the weak formulation

$$\int_{\Omega_t} (\nabla_{\mathbf{x}} \times \mathbf{E}) \cdot (\nabla_{\mathbf{x}} \times \overline{\boldsymbol{\phi}}) d\Omega_t + \int_{\Omega_t} \frac{1}{c_\infty^2} \partial_t^2 \mathbf{E} \cdot \overline{\boldsymbol{\phi}} d\Omega_t + \int_{\Sigma_1} \frac{1}{c_\infty} (\partial_t \mathbf{E} \times \mathbf{n}) \cdot (\overline{\boldsymbol{\phi}} \times \mathbf{n}) d\Sigma_1 = 0, \quad \text{(D.9)}$$

which corresponds to the formulation of (3.6) in the three-dimensional vector case.

Now let us consider the change of metric $\boldsymbol{\Phi}_t$ as defined in Section 3.2.1. Hence, the associated Jacobian $\mathbf{J}_t$ (and any related terms) can be expanded into Fourier series, precisely in the same way. This leads us to consider the corresponding boundary values problem in terms of the space variable $\mathbf{x}_0 \in \Omega_0$. Then, and similarly, we define the electric field in fixed domain $\mathbf{E}_0(\mathbf{x}_0, t) = \mathbf{E}_0(\boldsymbol{\Phi}_t^{-1}(\mathbf{x}), t) = \mathbf{E}(\mathbf{x}, t)$ for $(\mathbf{x}_0, t) \in \Omega_0 \times \mathbb{R}_*^+$.

Finally, let us stress that the extension to the vector case requires an adaptation of the ansatz (3.34). Hence, for any further development, we may consider the following expansion

$$\mathbf{E}_0(\mathbf{x}_0, t) = \sum_{j \in \mathbb{Z}} \mathbf{a}_j(\mathbf{x}_0) e^{i\omega_j t},$$

with $\omega_j := 2\pi(\nu_{\mathrm{f}} + j\nu_\ell)$ and where $\mathbf{a}_j : \Omega_0 \to \mathbb{C}^3$ for all $j \in \mathbb{Z}$.

List of Figures

1 Radar VitaSense (gauche). Unité de commande électronique (droite). 2
2 Signal radar réfléchi (gauche). Spectre associé (droite). 3
3 Champ incident et champ réfléchi par l'obstacle mobile. 4

1.1 Left: VitaSense device. Right: VitaSense electronic control unit (ECU). 11
1.2 Left: reflected radar signal. Right: corresponding spectrum. 12
1.3 Scattered field by moving target. 13
1.4 Fast decay of $\mathrm{J}_j(x)$ for fixed x and $j \to \infty$. 15

2.1 Bounded domain Ω_t with moving boundary ℓ. 19
2.2 Frequency spectrum $|\widehat{u}_{0,h}(0.5,\xi)|$ without ($\epsilon = 0$, in red) and with boundary motion ($\epsilon = 0.1$, in blue). This illustrates both the assumption on the decomposition (2.18) of v and the ansatz (2.30). 32
2.3 Spectrograms $|\mathrm{STFT}(u_{0,h}(0.5,t))|$, $|\mathrm{STFT}(u^{\mathcal{I}}_{0,h}(0.5,t))|$ and $\log(|\mathrm{STFT}(u_{0,h}(0.5,t))|)$ for $t \in]0, 1.2[$ and $\xi \in [-1500, 1500]$. The physical parameters are $\nu_{\mathrm{f}} = 360$, $\nu_\ell = 2$, $c_\infty = 300$ and $\epsilon = 0.1$. 33
2.4 On the top figure, time signals $u_{0,h}(0.5,t)$ in blue and $u^{\mathcal{I}}_{0,h}(0.5,t)$ in red. On the bottom figure, the absolute difference between $u^{\mathcal{I}}_{0,h}(0.5,t)$ and $w^{\mathcal{J}}_{\mathrm{gen},h}(0.5,t)]$, vs. t. The physical parameters are $\nu_{\mathrm{f}} = 360$, $\nu_\ell = 2$, $c_\infty = 300$ and $\epsilon = 0.1$. 34
2.5 Absolute difference $|\mathrm{STFT}(u^{\mathcal{I}}_{0,h}(0.5,t)) - \mathrm{STFT}(w^{\mathcal{J}}_{\mathrm{gen},h}(0.5,t))|$. The physical parameters are $\nu_{\mathrm{f}} = 360$, $\nu_\ell = 2$, $c_\infty = 300$ and $\epsilon = 0.1$. 35
2.6 Increasing the amplitude ϵ of the sinusoidal perturbation (2.15) leads to the excitation of a larger frequency band in the solution $|\widehat{u}_{0,h}(0.5,\xi)|$, with $\nu_{\mathrm{f}} = 3250$, $c_\infty = 1280$, and $\nu_\ell = 1$. 36
2.7 Top: Error $\mathrm{Err}(\widehat{u}^{\mathcal{I}^+}_{0,h}, \widehat{w}^{\mathcal{J}^+}_{\mathrm{gen},h})$ depending on ν_{f} for increasing refinement h. Bottom: cardinal $\sharp\mathcal{J}^+$ vs. ν_{f}. The vertical dashed lines correspond to the eigenfrequencies $\nu_m = mc_\infty/2$ (since $L = 1$) of the spatial domain without boundary motion. 37
2.8 Evaluation of $|\widehat{w}^{\mathcal{J}^+}_{\mathrm{gen},h}|$ for a high frequency source, with $\nu_{\mathrm{f}} = 3.2 \times 10^9$ and $c_\infty = 3 \times 10^8$. The number of bumps along the space variable directly depends on the value of the wavenumber $\kappa_{\mathrm{f}} = 2\pi\nu_{\mathrm{f}}/c_\infty$. We use $\sharp\mathcal{J}^+ = 11$, $\epsilon = 0.01$, $\nu_\ell = 1$ and $h = 0.001$. 38

2.9 Left: error $\mathrm{Err}(\widehat{u}^{\mathcal{I}^+}_{0,h}, \widehat{w}^{\mathcal{J}_1^+}_{\mathrm{gen},h})$ depending on $\sharp\mathcal{J}_1^+$. Right: $\mathrm{Err}(\widehat{w}^{\mathcal{J}^+}_{\mathrm{gen},h}, \widehat{w}^{\mathcal{J}_1^+}_{\mathrm{gen},h})$ depending on $\sharp\mathcal{J}_1^+$. The dashed line corresponds to the fixed value $\sharp\mathcal{J}^+ = 111$. The parameters are $h = 0.01$, $c_\infty = 300$, $\nu_\mathrm{f} = 500$, $\nu_\ell = 1$ and $\epsilon = 0.1$. 39
2.10 $\mathrm{Err}(\widehat{w}^{\mathcal{J}^+}_{\mathrm{gen},h}, \widehat{w}^{\mathcal{J}^+}_{h})$ for increasing values of ϵ and ν_ℓ. 40
2.11 Left: $\sharp\mathcal{J}^+$ vs. N_ℓ. Right: error $\mathrm{Err}(\widehat{u}^{\mathcal{I}^+}_{0,h}, \widehat{w}^{\mathcal{J}^+}_{h})$ vs. N_ℓ. The parameters are: $A = 1$, $c_\infty = 300$, $\nu_\mathrm{f} = 360$, and $\nu_\ell = 1$. 42
2.12 Evaluation of $|\widehat{w}^{\mathcal{J}^+}_{h}|$ in $\Omega_{0,h}$ for the square shaped modulation signal in top, and for the sawtooth signal in bottom. The parameters are: $c_\infty = 300$, $\nu_\mathrm{f} = 360$, $\epsilon = 0.05$, $\nu_\ell = 1$ and $h = 0.001$. 43
2.13 Example of a two-dimensional domain Ω_t with source boundary Γ_s and moving scatterer boundary $\Gamma(t)$. 46
2.14 Spectrogram $|\mathrm{STFT}(w^{\mathcal{I}}_h(\mathbf{x}_0, t)|$ for $\mathbf{x}_0 = (0.5, 0.5)^\mathrm{T}$, $t \in]0, 3[$ and $\xi \in [320, 400]$. The physical parameters are $\nu_\mathrm{f} = 360$, $\nu_\ell = 1$, $c_\infty = 300$ and $\epsilon = 0.1$ 47
2.15 Four components $|a_{j,h}(\mathbf{x}_0)|$ for $j = 0, 1, 2, 3$ of $\widehat{w}^{\mathcal{J}^+}_{h}(\mathbf{x}_0)$, for the physical parameters $\nu_\mathrm{f} = 360$, $\nu_\ell = 1$, $c_\infty = 300$ and $\epsilon = 0$. This case corresponds to the standard wave propagation in a fixed domain, without frequency modulation. 48
2.16 Four components $|a_{j,h}(\mathbf{x}_0)|$ for $j = 0, 1, 2, 3$ of $\widehat{w}^{\mathcal{J}^+}_{h}(\mathbf{x}_0)$, for the physical parameters $\nu_\mathrm{f} = 360$, $\nu_\ell = 1$, $c_\infty = 300$ and $\epsilon = 0.2$. 48
2.17 Four components $|a_{j,h}(\mathbf{x}_0)|$ for $j = 0, 1, 2, 3$ of $\widehat{w}^{\mathcal{J}^+}_{h}(\mathbf{x}_0)$, for the physical parameters $\nu_\mathrm{f} = 3600$, $\nu_\ell = 1$, $c_\infty = 300$ and $\epsilon = 0.02$. 49

3.1 Example of a two-dimensional ($d = 2$) computational domain Ω_t with source term on the boundary Γ^s, with moving scattering surface Γ_t and fictitious boundary Σ. . 52
3.2 Illustration of the vector flow $\mathbf{\Phi}_t$. 54
3.3 Example of a vibrating disk Ω_t with source term Γ^s and boundary Γ_t. 56
3.4 Overall scheme representing the solution of the moving boundary problem, in frequency and time domains and evaluated in both moving and fixed domains Ω_t and Ω_0. 65
3.5 Schematic description of the 2D model problem. 72
3.6 Computation of the local deformation and piecewise constant tensor $\mathbf{C}_{n,h}$ for $0 \leq n \leq 3$. 76
3.7 M_n, m_n and $\alpha_j^{(N,8)}$, for $0 \leq n, j \leq 8$ (threshold $\mathfrak{T} = 10^{-2}$). 77
3.8 Sparsity pattern of the matrix $\mathbf{A}^{(4,8)}_{\boldsymbol{\omega}^{(8)}}$. 77
3.9 $S_h(N, J)$ and $\mathrm{Err}_{j,h}(N, J)$ for $N = 4$, $0 \leq j \leq 6$ and $5 \leq J \leq 9$. 79
3.10 Amplitude $|a^{(4,8)}_{0,h}(\mathbf{x}_{0,h})|$ for $\nu_\mathrm{f} = 3 \times 10^9$. 80
3.11 Amplitude $|a^{(4,8)}_{1,h}(\mathbf{x}_{0,h})|$ for $\nu_\mathrm{f} = 3 \times 10^9$. 80
3.12 Amplitude $|a^{(4,8)}_{2,h}(\mathbf{x}_{0,h})|$ for $\nu_\mathrm{f} = 3 \times 10^9$. 81
3.13 Amplitude $|a^{(4,8)}_{3,h}(\mathbf{x}_{0,h})|$ for $\nu_\mathrm{f} = 3 \times 10^9$. 81
3.14 Amplitude $|a^{(4,8)}_{0,h}(\mathbf{x}_{0,h})|$ for $\nu_\mathrm{f} = 1.5 \times 10^{10}$. 82
3.15 Amplitude $|a^{(4,8)}_{1,h}(\mathbf{x}_{0,h})|$ for $\nu_\mathrm{f} = 1.5 \times 10^{10}$. 82
3.16 Amplitude $|a^{(4,8)}_{2,h}(\mathbf{x}_{0,h})|$ for $\nu_\mathrm{f} = 1.5 \times 10^{10}$. 83

3.17 Amplitude $|a_{3,h}^{(4,8)}(\mathbf{x}_{0,h})|$ for $\nu_{\mathrm{f}} = 1.5 \times 10^{10}$. 83
3.18 Convergence history of GMRES for solving (3.43) (black) and (3.44) with increasing J, for $\epsilon = 0.01$ (red) and $\epsilon = 0.02$ (blue). 84

4.1 2D schematic of a Renault Mégane. 89
4.2 Configuration C0. 89
4.3 Configuration C1a. 89
4.4 Configuration C1b. 90
4.5 Configuration C2a. 90
4.6 Configuration C2b. 90
4.7 Recorded breathing motion through 309 frames in blue, sine motion of amplitude 0.01 and frequency 4.3 in red. The finite length sample $\{f_k^i\}_{0\leq k\leq 8}$ is reported with black stems. 91
4.8 Locations of the five receiver positions $\Omega^{\mathrm{r},i}$, $1 \leq i \leq 5$. 92
4.9 Amplitude $|a_{0,h}^{(0,0)}(\mathbf{x}_{0,h})|$ of the field emitted from $\Gamma^{\mathrm{s},3}$ for the configuration C0. . . . 93
4.10 Amplitude $|a_{0,h}^{(0,0)}(\mathbf{x}_{0,h})|$ of the field emitted from $\Gamma^{\mathrm{s},1}$ for the configuration C0. . . . 94
4.11 Amplitude $|a_{0,h}^{(0,0)}(\mathbf{x}_{0,h})|$ of the field emitted simultaneously from $\Gamma^{\mathrm{s},1}$ and $\Gamma^{\mathrm{s},3}$, with amplitudes $A^1 = 1$ and $A^3 = 2$, respectively, for the configuration C0. 94
4.12 Amplitude $|a_{0,h}^{(4,10)}(\mathbf{x}_{0,h})|$ of the field emitted from $\Gamma^{\mathrm{s},3}$ for the configuration C1a. . 95
4.13 Magnitude $\log(|a_{0,h}^{(4,10)}(\mathbf{x}_{0,h})|)$ of the field emitted from $\Gamma^{\mathrm{s},3}$ for the configuration C1a. 96
4.14 Amplitude $|a_{1,h}^{(4,10)}(\mathbf{x}_{0,h})|$ of the field emitted from $\Gamma^{\mathrm{s},3}$ for the configuration C1a. . 96
4.15 Amplitude $|a_{2,h}^{(4,10)}(\mathbf{x}_{0,h})|$ of the field emitted from $\Gamma^{\mathrm{s},3}$ for the configuration C1a. . 97
4.16 Amplitude $|a_{5,h}^{(4,10)}(\mathbf{x}_{0,h})|$ of the field emitted from $\Gamma^{\mathrm{s},3}$ for the configuration C1a. . 97
4.17 Amplitude $|a_{10,h}^{(4,10)}(\mathbf{x}_{0,h})|$ of the field emitted from $\Gamma^{\mathrm{s},3}$ for the configuration C1a. . 98
4.18 Spectrum $|\widehat{w}_h^{(4,10)}(\Omega^{\mathrm{r},4})|$ at $\Omega^{\mathrm{r},4}$ of the field, emitted from $\Gamma^{\mathrm{s},3}$, for C0 (red) and C1a (blue). 98
4.19 Spectrum $\log(|\widehat{w}_h^{(4,10)})$ of the field emitted from $\Gamma^{\mathrm{s},3}$ in C1a, measured at positions $\Omega^{\mathrm{r},i}$ for $1 \leq i \leq 5$. 99
4.20 Amplitude $|a_{0,h}^{(4,10)}(\mathbf{x}_{0,h})|$ of the field emitted from $\Gamma^{\mathrm{s},1}$ for the configuration C1a. . 100
4.21 Amplitude $|a_{0,h}^{(4,10)}(\mathbf{x}_{0,h})|$ of the field emitted from $\Gamma^{\mathrm{s},2}$ for the configuration C1a. . 100
4.22 Amplitude $|a_{0,h}^{(4,10)}(\mathbf{x}_{0,h})|$ of the field emitted from $\Gamma^{\mathrm{s},4}$ for the configuration C1a. . 101
4.23 Spectrum $|\widehat{w}_h^{(4,10)}(\Omega^{\mathrm{r},4})|$ at $\Omega^{\mathrm{r},4}$ of the wave field in C1a, emitted from $\Gamma^{\mathrm{s},i}$, for $1 \leq i \leq 4$.101
4.24 Comparison between the spectrum of the field in C1a emitted from $\Gamma^{\mathrm{s},3}$, at $\Omega^{\mathrm{r},4}$ for $\beta^1 = 1$ (blue) and $\beta^1 = 2$ (red). 102
4.25 Amplitude $|a_{0,h}^{(4,10)}(\mathbf{x}_{0,h})|$ of the field emitted from $\Gamma^{\mathrm{s},2}$ for the configuration C1b. . 103
4.26 Spectrum $|\widehat{w}_h^{(4,10)}(\Omega^{\mathrm{r},4})|$ of the field in C1b, emitted from $\Gamma^{\mathrm{s},i}$, for $1 \leq i \leq 4$, vs. the reference spectrum for C1a at $\Gamma^{\mathrm{s},3}$. 104
4.27 Amplitude $|a_{0,h}^{(4,10)}(\mathbf{x}_{0,h})|$ of the field emitted from $\Gamma^{\mathrm{s},3}$ for the configuration C2a. . 104
4.28 Spectrum $\log(|\widehat{w}_h^{(4,10)}(\Omega^{\mathrm{r},4})|)$ emitted from $\Gamma^{\mathrm{s},3}$ in C1a (blue), in C2a (black) and from both antennas $\Gamma^{\mathrm{s},1}$ and $\Gamma^{\mathrm{s},3}$ in C2a (red). 105

4.29 Amplitude $|a_{0,h}^{(4,10)}(\mathbf{x}_{0,h})|$ of the field emitted from $\Gamma^{s,1}$ and $\Gamma^{s,3}$ for the configuration C2a. 105
4.30 Spectrum $\log(|\widehat{w}_h^{(4,10)}(\Omega^{r,4})|)$ emitted from both $\Gamma^{s,1}$ and $\Gamma^{s,3}$ in C2a, with $\varphi^1 = 0$ (blue) and $\varphi^1 = \pi$ (red). 106
4.31 Amplitude $|a_{0,h}^{(4,10)}(\mathbf{x}_{0,h})|$ of the field emitted from $\Gamma^{s,1}$ and $\Gamma^{s,3}$ for the configuration C2b. 107
4.32 Spectrum $|\widehat{w}_h^{(4,10)}(\Omega^{r,4})|$ emitted from both $\Gamma^{s,1}$ and $\Gamma^{s,3}$ in C2a (blue) and C2b (red).107

A.1 Amplitude $|u_h|$ for decreasing values of α from 1 (transparent left boundary in top, left) to 0 (reflecting boundary in bottom, right). The parameters are $\nu_f = 360$, $c_\infty = 300$, $A = 1$ and $L = 1$. 114

Bibliography

[1] IEEE Standard Definitions of Terms for Radio Wave Propagation. *IEEE Std 211-1997*, pages 1–44, 1997.

[2] M. Abramowitz and I.A. Stegun. *Handbook of Mathematical Functions, with Formulas, Graphs, and Mathematical Tables*. Dover Publications, 1964.

[3] V. Agnihotri, M. Sabharwal, and V. Goyal. Effect of frequency on micro-Doppler signatures of a helicopter. In *2019 International Conference on Advances in Big Data, Computing and Data Communication Systems (icABCD)*, pages 1–5, 08 2019.

[4] L. V. Ahlfors. *Complex Analysis: An Introduction to the Theory of Analytic Functions of One Complex Variable*, volume 177. 1953.

[5] P. Alonso, J. M. Badía, and A. M. Vidal. An efficient parallel algorithm to solve block-Toeplitz systems. *The Journal of Supercomputing*, 32(3):251–278, 2005.

[6] C.A. Balanis. *Advanced Engineering Electromagnetics*. John Wiley & Sons, 2012.

[7] S. Becuwe and A. Cuyt. On the fast solution of Toeplitz-block linear systems arising in multivariate approximation theory. *Numerical Algorithms*, 43(1):1, 2006.

[8] A. Bendali and L. Halpern. Conditions aux limites absorbantes pour le systeme de maxwell dans le vide en dimension 3. *Comptes rendus de l'Académie des sciences. Série 1, Mathématique*, 307(20):1011–1013, 1988.

[9] D. Bertaccini and M. K. Ng. Block $\{\omega\}$-circulant preconditioners for the systems of differential equations. *Calcolo*, 40(2):71–90, 2003.

[10] B. Boashash. Estimating and interpreting the instantaneous frequency of a signal. i. fundamentals. *Proceedings of the IEEE*, 80(4):520–538, 1992.

[11] H. Bohr. *Almost Periodic Functions*. American Mathematical Society, 1947.

[12] A. Borovoi, A. Konoshonkin, and N. Kustova. The physical-optics approximation and its application to light backscattering by hexagonal ice crystals. *Journal of Quantitative Spectroscopy and Radiative Transfer*, 146:181–189, 2014.

[13] Y. Boubendir, X. Antoine, and C. Geuzaine. A quasi-optimal non-overlapping domain decomposition algorithm for the Helmholtz equation. *Journal of Computational Physics*, 231(2):262–280, 2012.

[14] H.G. Brachtendorf, G. Welsch, and R. Laur. Fast simulation of the steady-state of circuits by the harmonic balance technique. In *Proceedings of ISCAS'95 - International Symposium on Circuits and Systems*, volume 2, pages 1388–1391, 1995.

[15] R.P. Brent, F.G. Gustavson, and D.Y. Yun. Fast solution of Toeplitz systems of equations and computation of Padé approximants. *Journal of Algorithms*, 1(3):259–295, 1980.

[16] D. Brooks, O. Schwander, F. Barbaresco, J.Y. Schneider, and M. Cord. Complex-valued neural networks for fully-temporal micro-Doppler classification. In *20th International Radar Symposium (IRS)*, pages 1–10, 2019.

[17] D.A. Brooks, O. Schwander, F. Barbaresco, J.Y. Schneider, and M. Cord. Temporal deep learning for drone micro-Doppler classification. In H. Rohling, editor, *2018 19th International Radar Symposium (IRS)*, 2018.

[18] A.J. Bur. Dielectric properties of polymers at microwave frequencies: a review. *Polymer*, 26(7):963–977, 1985.

[19] Z.A. Cammenga, C.J. Baker, G.E. Smith, and R. Ewing. Micro-Doppler target scattering. In *IEEE Radar Conference*, pages 1451–1455, 2014.

[20] Z.A. Cammenga, G.E. Smith, and C.J. Baker. High range resolution micro-Doppler analysis. In Ranney, KI and Doerry, A and Gilbreath, GC and Hawley, CT, editor, *Radar Sensor Technology XIX; and Active and Passive Signatures VI*, volume 9461 of *Proceedings of SPIE*, 2015.

[21] A. Cardona, T. Coune, A. Lerusse, and M. Geradin. A multiharmonic method for non-linear vibration analysis. *International Journal for Numerical Methods in Engineering*, 37(9):1593–1608, 1994.

[22] D. Censor. Scattering of electromagnetic waves by a cylinder moving along its axis. *IEEE Transactions on Microwave Theory and Techniques*, 17(3):154–158, 1969.

[23] D. Censor. Scattering of electromagnetic waves in uniformly moving media. *Journal of Mathematical Physics*, 11(6):1968–1976, 1970.

[24] D. Censor. Non-relativistic scattering: pulsating interfaces. *Progress In Electromagnetics Research*, 54:263–281, 2005.

[25] V.C. Chen. *The Micro-Doppler Effect in Radar,* 2nd Ed. Artech House, 2 edition, 2019.

[26] V.C. Chen, F. Li, S.S. Ho, and H. Wechsler. Analysis of micro-doppler signatures. *IEE Proceedings-Radar, Sonar and Navigation*, 150(4):271–276, 2003.

[27] V.C. Chen, F.Y. Li, S.S. Ho, and H. Wechsler. Micro-Doppler effect in radar: phenomenon, model, and simulation study. *IEEE Transactions on Aerospace and Electronic Systems*, 42(1):2–21, 2006.

[28] V.C. Chen, C.T. Lin, and W.P. Pala. Time-varying Doppler analysis of electromagnetic backscattering from rotating object. In *2006 IEEE Radar Conference, Vols 1 and 2*, IEEE Radar Conference, pages 807+, 2006.

[29] X. Chen, X. Yu, J. Guan, and Y. He. *High-resolution sparse representation of micro-Doppler signal in sparse fractional domain*, volume 227 of *Lecture Notes of the Institute for Computer Sciences, Social Informatics and Telecommunications Engineering*, pages 225–232. 2018.

[30] A. Chesnokov and M. Van Barel. A direct method to solve block banded block Toeplitz systems with non-banded Toeplitz blocks. *Journal of Computational and Applied Mathematics*, 234(5):1485 – 1491, 2010.

[31] W.C. Chew. Vector potential electromagnetics with generalized gauge for inhomogeneous media: Formulation. *Progress In Electromagnetics Research*, 149:69–84, 2014.

[32] I.C. Christov and C.I. Christov. On mechanical waves and Doppler shifts from moving boundaries. *Mathematical Methods in the Applied Sciences*, 40(12):4481–4492, 2017.

[33] C.W. Chuang. Backscatter of a large rotating conducting cylinder of arbitrary cross-section. *IEEE Transactions on Antennas and Propagation*, 27(1):92–95, 1979.

[34] Y. Cocheril and R. Vauzelle. A new ray-tracing based wave propagation model including rough surfaces scattering. *Progress In Electromagnetics Research*, 75:357–381, 2007.

[35] E. Deadman and S.D. Relton. Taylor's theorem for matrix functions with applications to condition number estimation. *Linear Algebra and its Applications*, 504:354–371, 2016.

[36] S. Dias Da Cruz, H.P. Beise, U. Schröder, and U. Karahasanovic. A theoretical investigation of the detection of vital signs in presence of car vibrations and radar-based passenger classification. *IEEE Transactions on Vehicular Technology*, 68(4):3374–3385, 2019.

[37] V. Dolean, P. Jolivet, and F. Nataf. *An Introduction to Domain Decomposition Methods: Theory and Parallel Implementation*. SIAM, Philadelphia, 2015.

[38] P. Dular, C. Geuzaine, F. Henrotte, and N. Legros. A general environment for the treatment of discrete problems and its application to the finite element method. *IEEE Transactions on Magnetics*, 34(5, 1):3395–3398, 1998.

[39] M. El Bouajaji, B. Thierry, X. Antoine, and C. Geuzaine. A quasi-optimal domain decomposition algorithm for the time-harmonic Maxwell's equations. *Journal of Computational Physics*, 294:38–57, 2015.

[40] A. Elhawil, L. Zhang, J. Stiens, C. De Tandt, N.A. Gotzen, G.V. Assche, and R. Vounckx. A quasi-optical free-space method for dielectric constant characterization of polymer materials in mm-wave band. In *Proceedings Symposium IEEE/LEOS Benelux Chapter*, volume 66, pages 187–190, 2007.

[41] O. Ernst and M.J. Gander. Why it is difficult to solve Helmholtz problems with classical iterative methods. In O. Lakkis I. Graham, T. Hou and R. Scheichl, editors, *Numerical Analysis of Multiscale Problems*, pages 325–363. Springer Verlag, 2012.

[42] A.S. Fokas and B. Pelloni. Method for solving moving boundary value problems for linear evolution equations. *Physical Review Letters*, 84(21):4785–4789, 2000.

[43] IT'IS Foundation. Tissue properties database v4.0, 2018.

[44] L. Fu Rong. Toeplitz-like preconditioners for the solution of block Toeplitz systems. In *Hybrid Image and Signal Processing VII*, volume 4044, pages 56–65. International Society for Optics and Photonics, 2000.

[45] Y.C. Fung, P. Tong, and X. Chen. *Classical and computational solid mechanics*, volume 2. World Scientific Publishing Company, 2017.

[46] J. Garcia-Rubia, O. Kilic, V. Dang, Q. Nguyen, and T. Nghia. Analysis of moving human micro-Doppler signature in forest environments. *Progress In Electromagnetics Research*, 148:1–14, 06 2014.

[47] D. Gasperini, H.P. Beise, U. Schroeder, X. Antoine, and C. Geuzaine. A frequency domain method for scattering problems with moving boundaries. *Wave Motion*, 102:102717, 2021.

[48] D. Gasperini, H.P. Beise, U. Schroeder, X. Antoine, and C. Geuzaine. An analysis of the steepest descent method to efficiently compute the 3D acoustic single-layer operator in the high-frequency regime. submitted, 2021.

[49] D. Gasperini, H.P. Biese, U. Schroeder, X. Antoine, and C. Geuzaine. A multi-harmonic finite element method for scattering problems with small-amplitude boundary deformations. *SIAM Journal on Scientific Computing*, 44(2):B197–B223, 2022.

[50] L. Gemignani. Schur complements of Bezoutians and the inversion of block Hankel and block Toeplitz matrices. *Linear Algebra and its Applications*, 253(1-3):39–59, 1997.

[51] A. Ghaleb. *Analyse des micro-Doppler de cibles mobiles déformables en imagerie radar*. PhD thesis, Télécom ParisTech, 2009.

[52] T.P. Gill. *The Doppler Effect: An Introduction to the Theory of the Effect*. Logos Press, 1965.

[53] C. Gu, G. Wang, Y. Li, T. Inoue, and C. Li. A hybrid radar-camera sensing system with phase compensation for random body movement cancellation in Doppler vital sign detection. *IEEE Transactions on Microwave Theory and Techniques*, 61(12):4678–4688, 2013.

[54] J. Gutiérrez-Gutiérrez and P.M. Crespo. Block Toeplitz matrices: asymptotic results and applications. *Foundations and Trends in Communications and Information Theory*, 8(3):179–257, 2011.

[55] J. Gyselinck, C. Geuzaine, P. Dular, and W. Legros. Multi-harmonic modelling of motional magnetic field problems using a hybrid finite element-boundary element discretisation. *Journal of Computational and Applied Mathematics*, 168(1-2):225–234, 2004.

[56] A. Halbach and C. Geuzaine. Steady-state nonlinear analysis of large arrays of electrically actuated micromembranes vibrating in a fluid. *Engineering with Computers*, 155(3):591–602, 2017.

[57] F. Harfoush, A. Taflove, and G.A. Kriegsmann. A numerical technique for analyzing electromagnetic wave scattering from moving surfaces in one and two dimensions. *IEEE Transactions on Antennas and Propagation*, 37(1):55–63, 1989.

[58] P. Hofmann. *Solid State Physics: An Introduction*. John Wiley & Sons, 2015.

[59] F. Ihlenburg. *Finite Element Analysis of Acoustic Scattering*. Number 132 in Applied Mathematical Sciences. Springer-Verlag, New York, 1998.

[60] X.Q. Jin and F.R. Lin. Block preconditioners with circulant blocks for general linear systems. *Computers & Mathematics with Applications*, 58(7):1309–1319, 2009.

[61] P. Ju. Global residue harmonic balance method for Helmholtz-Duffing oscillator. *Applied Mathematical Modelling*, 39(8):2172–2179, 2015.

[62] U. Karahasanovic and D. Tatarinov. Radar-based detection of thoracoabdominal asynchrony during breathing using autocorrelation function analysis. In *2018 11th German Microwave Conference (GEMIC 2018)*, pages 403–406, 2018.

[63] P. Kuchment. *Floquet Theory For Partial Differential Equations*. Birkhauser Verlag, Basel, 1993.

[64] E. Kuci, F. Henrotte, P. Duysinx, and C. Geuzaine. Design sensitivity analysis for shape optimization based on the lie derivative. *Computer methods in applied mechanics and engineering*, 317:702–722, 2017.

[65] G. Labahn, D.K. Choi, and S. Cabay. The inverses of block Hankel and block Toeplitz matrices. *SIAM Journal on Computing*, 19(1):98–123, 1990.

[66] D. Lahaye, J. Tang, and K. Vuik, editors. *Modern Solvers for Helmholtz Problems*. Birkhäuser, Cham, 2017.

[67] C. Li, J. Cummings, J. Lam, E. Graves, and W. Wu. Radar remote monitoring of vital signs. *Microwave Magazine, IEEE*, 10:47–56, 2009.

[68] J.L. Lions and E. Magenes. *Non-Homogeneous Boundary Value Problems and Applications*. Springer-Verlag, Berlin, 1972.

[69] Z. Liu, B. Peng, and X. Li. Analysis of phase noise influence on micro-Doppler feature extraction of vibrating target. *Journal of Engineering-JOE*, 2019(20):6834–6839, OCT 2019.

[70] Z. Liu, B. Peng, and Li X. Analysis of phase noise influence on micro-Doppler feature extraction on vibrating target. *Progress in Electromagnetics Research C*, 85:177–190, 2018.

[71] R. Mickens. A generalization of the method of harmonic balance. *Journal of Sound and Vibration*, 111(3):515–518, 1986.

[72] D. Middleton. Doppler effects for randomly moving scatterers and platforms. *The Journal of the Acoustical Society of America*, 61(5):1231–1250, 1977.

[73] K.S. Miller. On the inverse of the sum of matrices. *Mathematics Magazine*, 54(2):67–72, 1981.

[74] T. Mousel, P. Larsen, and H. Lorenz. Unattended children in cars–radiofrequency-based detection to reduce heat stroke fatalities. In *Proc. Int. Tech. Conf. on the Enhanced Safety of Vehicles, Detroit Michigan, United States*, pages 5–8, 2017.

[75] B.R. Musicus. Levinson and fast Choleski algorithms for Toeplitz and almost Toeplitz matrices. 1988.

[76] D.J. Newman. A simple proof of Wiener $1/f$ theorem. *Proceedings of the American Mathematical Society*, 48(1):264–265, 1975.

[77] B. Peng, X. Wei, B. Deng, H. Chen, Z. Liu, and X. Li. A sinusoidal frequency modulation Fourier transform for radar-based vehicle vibration estimation. *IEEE Transactions on Instrumentation and Measurement*, 63(9):2188–2199, 2014.

[78] H. Peng. Doppler effect for non-uniformly moving source, observer, and mirror. *Open Science Repository Physics*, (open-access):e45011870, 2018.

[79] J. Popovic and O. Runborg. Analysis of a fast method for solving the high frequency Helmholtz equation in one dimension. *BIT Numerical Mathematics*, 51(3):721–755, 2011.

[80] B. Rothenstein and A. Rothenstein. Doppler shift experiments with source in periodic motion: Parametrized Doppler shift formulas. *arXiv preprint physics/0309088*, 2003.

[81] R. Rudd, A. Prasad, D. Weston, and K. Wietholter. Functional assessment of unattended child reminder systems. Technical report, 2015.

[82] Y. Saad. *Iterative Methods for Sparse Linear Systems*. Society for Industrial and Applied Mathematics, 2003.

[83] Y. Saad and M.H. Schultz. GMRES: A generalized minimal residual algorithm for solving nonsymmetric linear systems. *SIAM Journal on Scientific and Statistical*, 7(3):856–869, 1986.

[84] E.Y. Sun and W. Rusch. Time-domain physical-optics. *IEEE Transactions on Antennas and Propagation*, 42(1):9–15, 1994.

[85] B. Thierry, A. Vion, S. Tournier, M. El Bouajaji, D. Colignon, N. Marsic, X. Antoine, and C. Geuzaine. GetDDM: An open framework for testing optimized Schwarz methods for time-harmonic wave problems. *Computer Physics Communications*, 203:309–330, 2016.

[86] Y. Tian. Completing block hermitian matrices with maximal and minimal ranks and inertias. *The Electronic Journal of Linear Algebra*, 21, 2010.

[87] J. Van Bladel. Electromagnetic fields in the presence of rotating bodies. *Proceedings of the IEEE*, 64(3):301–318, 1976.

[88] J. Van Bladel and D. De Zutter. Reflections from linearly vibrating objects: Plane mirror at normal incidence. *IEEE Transactions on Antennas and Propagation*, 29(4):629–637, 1981.

[89] U. Wijenayake and S.Y. Park. Real-time external respiratory motion measuring technique using an rgb-d camera and principal component analysis. *Sensors*, 17(8), 2017.

[90] C.W. Wong, W.S. Zhang, and S.L. Lau. Periodic forced vibration of unsymmetrical piecewise-linear systems by incremental harmonic-balance method. *Journal of Sound and Vibration*, 149(1):91–105, 1991.

[91] M.A. Woodbury. Inverting modified matrices. *Memorandum Report*, 42(106):336, 1950.

[92] H.L. Zhang, Y.X. Sha, X.Y. Guo, M.Y. Xia, and C. H. Chan. Efficient analysis of scattering by multiple moving objects using a tailored MLFMA. *IEEE Transactions on Antennas and Propagation*, 67(3):2023–2027, 2019.

[93] K. Zheng, Y. Li, S. Qin, K. An, and G. Wei. Analysis of micromotion characteristics from moving conical-shaped targets using the Lorentz-FDTD method. *IEEE Transactions on Antennas and Propagation*, 67(11):7174–7179, 2019.

[94] K.S. Zheng, J.Z. Li, G. Wei, and J.D. Xu. Analysis of Doppler effect of moving conducting surfaces with Lorentz-FDTD method. *Journal of Electromagnetic Waves and Applications*, 27(2):149–159, 2013.